Ferroelectric field-effects in high-tc superconducting devices

Laura Begon-Lours

UNIVERSITÉ PIERRE ET MARIE CURIE – PARIS VI

FACULTÉ DE PHYSIQUE

Ecole doctorale Physique et Chimie des Matériaux

THESIS

Ferroelectric Field-Effects in High-T_c Superconducting Devices

presented by **Laura BÉGON-LOURS**

to obtain the degree of

Doctor of Philosophy

defended on January, 23rd 2017 in front of the committee:

Kathrin DÖRR	Martin Luther Univesität - Halle-Wittenberg	Referee
Benjamin MARTINEZ	ICMAB-CSIC - Barcelona	Referee
Abhay SHUKLA	UPMC-IMPMC - Paris	Examiner
Jacobo SANTAMARIA	Universidad Complutense de Madrid - Madrid	Examiner
Hervé AUBIN	ESPCI-LPEM - Paris	Examiner
Manuel BIBES	Unité Mixte de Physique CNRS-Thales - Palaiseau	Supervisor
and Javier E. VILLEGAS	Unité Mixte de Physique CNRS-Thales - Palaiseau	Supervisor

Unité Mixte de Physique
CNRS-Thales
1 av. Augustin Fresnel
91767 Palaiseau
France

Ecole doctorale Physique et Chimie des Matériaux
4 place Jussieu
75005 Paris
France

Remerciements

Ces années de thèse m'ont énormément apporté sur les plans scientifique et humain. J'ai eu la chance d'évoluer dans un laboratoire exceptionnel, où j'ai pu apprendre des techniques, un savoir-faire et des méthodologies en bénéficiant de l'expérience précieuse de chercheurs et d'ingénieurs brillants et généreux. Je remercie en premier lieu mon directeur de thèse, Javier, qui m'a fait confiance et m'a accompagné jusqu'à la dernière ligne de ce manuscrit en surpassant avec moi les états d'âmes et les découragements inhérents à la recherche expérimentale, et en m'encourageant à aller de l'avant avec détermination.

Je remercie très chaleureusement les personnes qui m'ont formé, Rozenn, Karim, Cécile, Stéphanie, Yves, Victor, Eric… vous m'avez tous transmis beaucoup plus que de simples recettes ou des protocoles. Un grand merci aussi à ceux qui se sont impliqué dans mes travaux, Sophie, Vincent, Steef, Anke, Juan, Lee ainsi que Stéphane Xavier, Christian Ulysse et Maria Varela. Merci pour toutes ces heures passées sur mes – souvent pénibles – petits échantillons !

Je remercie aussi sincèrement ceux qui m'ont accordé du temps pour échanger sur mes résultats, en particulier Jérôme Lesueur qui m'a mis au contact de photons intriqués dès la sortie du berceau et qui a toujours su faire de la place dans son emploi du temps pour de longues discussions sur la physique. Merci également à Nicolas, Denis et Agnès pour m'avoir éclairé dans la compréhension de mes travaux, et surtout à Manuel pour m'avoir accompagné dès mon arrivée.

Merci aussi à ceux qui ont partagé un happy office, une pause déj, un café, une conversation à propos d'un piston ou d'un chassis, un apéro, un karting ou une épopée nocturne avec moi pendant ces longues années, vous êtes trop nombreux pour tous vous citer mais une pensée particulière à Piotr, Sophie et Alice pour être venu me témoigner votre amitié quand mes fractures m'empêchaient de me lever, Flavio, Jason et Karim pour les mégawatts de bonheur partagé sous les ondes une fois que j'étais rétablie, Sophie pour les galops à la fraiche le jeudi matin. Un doux merci aussi à Christine pour ta gentillesse, je te souhaite une retraite heureuse et reposante. Je terminerai par remercier Anne, Frédéric N.V.D. et Frédéric P. pour la direction et la canalisation des forces humaines et administratives au laboratoire, c'est une grande chance de vous avoir à la barre.

J'ai également beaucoup de reconnaissance et d'affection pour ceux qui se sont intéressé à mes travaux en dehors du labo, ma famille pour les réguliers « alors ça avance ? », ou mon papa pour son regard moderne sur la supraconductivité. Claire pour toute les fois où on a emmené notre charrette en dehors des sentiers, Max pour toutes les fenêtres qu'il a ouvert en grand dans mon cœur, et surtout ma maman qui a courageusement lu et corrigé avec amour chacune des lignes de cette thèse. Merci ♡

Ferroelectric Field-Effects in High-T_c Superconducting Devices

Abstract

In this experimental thesis, we fabricated ferroelectric field-effect devices based on high-T_c superconductors. We grew high-quality epitaxial heterostructures consisting of an ultra-thin (2 to 6 unit cells) film of YBCO and a thin ferroelectric film (BFO-Mn). We fabricated transport measurement microbridges and used a CT-AFM tip to polarise the BFO-Mn outwards or towards the BFO-Mn/YBCO interface. Due to the ferroelectric field-effect, the superconducting properties of the underlying YBCO film were consequently modified. We then used this effect locally in order to design weak links within the microbridges: two regions where the superconducting properties are enhanced are separated by a narrow region where they are depressed. We explored the conditions of existence of a Josephson coupling across this weak link.

In parallel, we fabricated ferroelectric junctions. The barrier is an ultra-thin BFO-Mn film sandwiched between a high-T_c superconducting YBCO bottom electrode and a low-T_c superconducting top electrode. Both at room temperature and at low temperature, we characterised the transport properties across the barrier and the resistive switching resulting from the polarisation of the ferroelectric barrier.

Keywords

Epitaxy, Ferroelectricity, Field-effect, Hall effect, High-T_c superconductors, Interface, Josephson effect, Lithography, Oxides, Pulsed Lased Deposition, Piezoresponse Force Microscopy, Superconductivity, Tunnel junctions, Ultra-thin films, Weak-links

Effets de champ ferroélectriques dans des dispositifs à base de supraconducteurs à haute T_c

Résumé

Les matériaux ferroélectriques possèdent une polarisation spontanée et rémanente. Lorsqu'ils sont recouverts par une électrode, des charges s'accumulent dans cette dernière, à proximité de l'interface, afin d'écranter la polarisation : c'est l'effet de champ ferroélectrique. Alors que dans les métaux cet écrantage a lieu sur une distance très courte, il s'étend sur une distance nanométrique dans les matériaux moins denses en porteurs comme les oxydes. Or, les oxydes sont des systèmes fortement corrélés, dans lesquels une petite variation du nombre de porteurs (typiquement celle induite par la proximité avec un ferroélectrique) suffit à induire de fortes modifications des propriétés physiques du matériau.

Dans cette thèse expérimentale, nous exploitons cet effet dans un oxyde supraconducteur à haute température critique, l'YBCO. Pour cela, deux configurations sont étudiées :

- En géométrie planaire, un film d'YBCO est recouvert par un film ferroélectrique (BFO-Mn). L'épaisseur du film d'YBCO est du même ordre que sa longueur d'écrantage, de telle sorte que l'effet de champ se propage dans toute la profondeur du film.
- En géométrie verticale, deux électrodes supraconductrices possédant des longueurs d'écrantage différentes sont séparées par une fine barrière ferroélectrique. En fonction de la direction de la polarisation, le profil électrostatique de la barrière est modifié.

La première partie de cette thèse a été dédiée à la croissance par ablation laser pulsée d'hétérostructures possédant les propriétés nécessaires pour ces dispositifs : dans le cas des structures planaires, il a fallu conserver la supraconductivité dans des films de quelques mailles unités seulement ; dans le cas des structures verticales, conserver de bonnes propriétés ferroélectriques dans des films nanométriques. Au terme d'un travail d'optimisation, des hétérostructures BFO-Mn (30 nm)/YBCO (2 à 5 m.u.)/PBCO//STO ainsi que des bicouches BFO-Mn (2 à 5 nm)/YBCO (50 nm)//STO d'une grande qualité ont été fabriquées.

Les procédés de lithographie ont été développés afin de fabriquer des dispositifs permettant d'étudier, dans le premier cas, les propriétés de transport dans le film d'YBCO, et dans le second cas, à travers la barrière de BFO-Mn. Les propriétés ferroélectriques de BFO-Mn sur YBCO ont été caractérisées, mettant en évidence deux résultats majeurs : premièrement, un dipôle électrique permanent est présent à l'interface BFO-Mn/YBCO, favorisant une direction de polarisation par rapport à l'autre. Deuxièmement, la polarisation est stable dans les deux directions, et peut être

modifiée dans l'air ou dans le vide, à haute et basse température, au moyen d'un simple scan AFM à pointe conductrice (CT-AFM).

Dans un premier temps, les dispositifs planaires ont été entièrement polarisés dans une direction puis une autre, et les propriétés de transport du film d'YBCO ont été mesurées dans les deux états. L'effet de champ s'est manifesté par une modification de la température critique, de la conductivité et du nombre de porteurs libres dans le film d'YBCO. L'état de basse conductivité (déplétion de porteurs dans le film d'YBCO) est obtenu pour une polarisation du BFO-Mn pointant vers l'interface BFO-Mn/YBCO, en accord avec le fait que dans l'YBCO, les porteurs sont de charge positive.

Dans un second temps, des jonctions de type lien faible ont été définies au sein des dispositifs : le ferroélectrique est polarisé vers la surface sur la plupart du dispositif (accumulation de porteurs dans le film d'YBCO) et vers l'interface BFO-Mn/YBCO sur une fine bande (déplétion de porteurs dans l'YBCO). Les différents régimes de transport ont été étudiés pour différentes températures. Des oscillations ont été observées dans les mesures de magnétorésistance et de courant critique en fonction du champ magnétique, supposément dues à un couplage Josephson de part et d'autre du lien faible.

En parallèle, les dispositifs verticaux ont été mesurés. Dans un premier temps, les propriétés ferroélectriques des films ultra-minces de BFO-Mn sur YBCO ont été étudiées à température ambiante à partir de capacités de $300\ nm$ à $1\ \mu m$ de diamètre. Plusieurs électrodes supérieures – métalliques et supraconductrices – ont été utilisées, mettant en évidence leurs influences sur les propriétés ferroélectriques des films ultra-minces.

Dans un second temps, des dispositifs verticaux avec une électrode supérieure supraconductrice ($MoSi$) ont été fabriqués. Les propriétés de transport à travers le film ferroélectrique ont été caractérisées à différentes températures, et après l'application d'une tension DC de plusieurs volts dans le but de polariser le film ferroélectrique. La résistance de la barrière s'est révélée dépendante de la tension de polarisation : un comportement hystérétique à deux états a été obtenu, typique des jonctions tunnel ferroélectriques. Les mécanismes à l'origine de cette électro-résistance, observée uniquement sous la température critique de l'électrode inférieure, sont probablement liés à l'effet de champ ferroélectrique.

Les travaux menés au cours de cette thèse ouvrent la voie pour la réalisation de dispositifs à effet de champ ferroélectrique à base de supraconducteurs, comme la réalisation de jonctions Josephson à paramètres continûment variables (en modifiant l'épaisseur de la région déplétée dans le cas des dispositifs planaires) ou à deux états (en modifiant la direction de la polarisation dans les jonctions verticales).

Contents

Introduction 1
I. Generalities 3
I.1 Superconductivity 5
I.1.1 Historical aspects 5
I.1.2 London equations 6
I.1.3 The BCS theory 8
I.1.4 Ginzburg-Landau theory 9
I.1.5 Vortices in High-T_c Superconductors 13
I.2 Josephson effect 14
I.2.1 Tunnel effect 14
I.2.2 Josephson effect 17
I.2.3 Josephson junction in a magnetic field 19
I.2.4 Josephson junctions technology 22
I.3 Ferroelectricity 24
I.3.1 Symmetry 24
I.3.2 Mechanisms of ferroelectricity 25
I.3.3 Conduction through ferroelectric oxides 26
I.3.4 Ferroelectricity in thin films 27
I.4 Materials 31
I.4.1 $SrTiO_3$ 31
I.4.2 $PrBa_2Cu_3O_{7-\delta}$ 31
I.4.3 $YBa_2Cu_3O_{7-\delta}$ 31
I.4.4 $BiFeO_3$ 32
I.4.5 $La_{1-x}Sr_xMnO_3$ 35
I.4.6 $Mo_{1-x}Si_x$ 35
II. Field-effects in correlated oxides 37
II.1 Field-Effect Transistors 38
II.1.1 Principle of the Field-Effect Transistor 38
II.1.2 Electric penetration depth and carrier modulation 39
II.1.3 Oxides field-effect transistors technologies 40
II.2 Electrostatic tuning of correlated oxides 42
II.2.1 Field-Effect in Colossal-Magneto-Resistance Manganites 42
II.2.2 Ferroelectric field-effect transistor: a prototypical model 44
II.3 Electrostatic tuning of high-T_c superconductors 47
II.3.1 Field-effect and penetration length 47
II.3.2 Field-Effect Transistors 48
II.3.3 Electric Double Layer Transistors 49
II.3.4 Ferroelectric Field-Effect Transistors 49
II.4 Some functionalities of field-effect 51
II.4.1 Local manipulation of field-effect 51

II.4.2 Tunable Josephson junctions 53
II.4.3 Ferroelectric tunnel junctions 54
III. Experimental techniques 58
III.1 Growth techniques 59
III.1.1 Pulsed Laser Deposition 59
III.1.2 Sputtering and thermal evaporation 61
III.2 Characterisation techniques 62
III.2.1 Scanning Electron Microscopy 62
III.2.2 Scanning Transmission Electron Microscopy (STEM) 63
III.2.3 Scanning Probe Microscopy (SPM) techniques 63
III.2.4 X-Ray diffraction 67
III.3 Nano and micro fabrication 72
III.3.1 Generalities on fabrication 72
III.3.2 Fabrication of planar devices 75
III.3.3 Fabrication of planar devices with a gate 80
III.3.4 Fabrication of vertical devices: matrices of pads 82
III.3.5 Fabrication of micrometric vertical devices 83
III.3.6 Measurement set-up for electrical characterisation 84
IV. Growth of epitaxial heterostructures 86
IV.1 Epitaxial heterostructures for planar field-effect devices 87
IV.1.1 Objectives 87
IV.1.2 Preparation of substrates 88
IV.1.3 Growth of $YBa_2Cu_3O_{7-\delta}$ 88
IV.1.4 Growth of *$BiFeO_3$* 90
IV.1.5 Properties of optimised BFO/YBCO/PBCO/STO 94
IV.2 Epitaxial heterostructures for ferroelectric tunnel junctions 101
IV.2.1 Objectives 101
IV.2.2 BFO/YBCO *in situ* heterostructures 103
IV.2.3 BFO-*Mn* epitaxy on YBCO films grown by PLD 104
IV.2.4 BFO-*Mn* epitaxy on YBCO commercial films 106
V. BFO/YBCO ferroelectric properties 110
V.1 Stability of the ferroelectric domains 111
V.1.1 Samples not exposed to an O_2 plasma 111
V.1.2 Samples exposed to an O_2 plasma 114
V.1.3 Asymmetry of the ferroelectric characteristics of BFO films on YBCO 115
V.1.3. a) Electrostatic interactions 116
V.1.3. b) Pinned ferroelectric layer 117
V.1.3. c) Pinned ferroelectric domains 118
V.2 Structure of the BFO-*Mn*/YBCO interface 119
V.3 Ferroelectric switching inside a cryostat 121
V.3.1 Ferroelectric switching in Helium atmosphere 121
V.3.2 Ferroelectric switching at low temperature 123
VI. Planar field-effect devices 125
VI.1 Field-effect measurements 126
VI.1.1 Characterisation of the devices 126

VI.1.2 Electrostatic modulation of the carrier density 130
VI.1.3 Experiments with a top-gate electrode 133
VI.2 Planar S/S'/S junctions 135
VI.2.1 Resistive transition of S/S'/S junctions 136
VI.2.2 Voltage-current characteristics of the junctions 138
VI.2.2. a) General shape of the voltage-current characteristics 139
VI.2.2. b) Cross-over regime from the dissipative to the non-dissipative state 140
VI.2.2. c) Voltage-current dependence on the magnetic field 141
VI.2.3 Magnetotransport 142
VI.2.4 Interpretation of the experimental observations 147
VI.3 Conclusion 151
VII. Out-of-plane field-effect devices 152
VII.1 Room-temperature measurements 154
VII.1.1 Description of the set-up 154
VII.1.2 Characterisation of *Pt*/*Co*/BFO-*Mn*/YBCO junctions 155
VII.1.3 Characterisation of *Nb*/BFO-*Mn*/YBCO junctions 158
VII.1.4 Characterisation of *NbN*/BFO-*Mn*/YBCO junctions 159
VII.1.5 Characterisation of *MoSi*/BFO-*Mn*/CMO junctions 160
VII.2 Low-temperature measurements 161
VII.2.1 Characterisation of the junctions 161
VII.2.2 Field-effect measurements 164
VII.2.3 Conclusions 166
VII.3 Conclusion 167
Appendix 170
Bibliography 174

Introduction

The richness of the phase diagram of many complex oxides is due to their strong electronic correlations. They derive, among other mechanisms, from the competition between localisation – due to Coulomb repulsions – and hopping – due to the kinetic energy – of the carriers. This competition can be tuned by changing electrostatically the carrier density: this is the keystone of Field-Effect Transistors (FETs), widely used in nowadays technology. In these devices, a voltage is applied across a dielectric gate, between a thin oxide channel and a metallic electrode. This tunes the carrier density in the channel, inducing a modification of the conductivity of the latter.

Among them, FETs with a ferroelectric gate raise a considerable interest: these materials possess a spontaneous polarisation. At their boundaries, charges accumulate close to the interface in order to screen the ferroelectric polarisation. The polarisation is remanent: the induced charge transfer remains once the electric field necessary to polarise the ferroelectric in one direction is removed.

In this experimental thesis, we use the ferroelectric field-effect to tune the electrical properties of a superconductor. The chosen material is YBCO: because of its low carrier density, the field-effect occurs over long distances in this oxide (typically one nanometre). The superconducting properties, in particular the critical temperature, are consequently modified.

We did not only focus on modifying the electrical properties of a channel, but fabricated superconducting devices based on the ferroelectric field-effect. Superconductors have unique properties; among them, the Josephson effect: this phenomenon results from the coupling of two superconductors across a weak link. It has numerous applications, from magnetometers to RSFQ digital electronics. The aim of this thesis is to open the way to ferroelectric field-effect tunable Josephson junctions, based on high-T_c superconductors. To achieve this, two kinds of devices are studied:

a) Planar devices in a transistor geometry: a ferroelectric film is grown on top of an ultra-thin superconducting channel. The polarisation is in such a way that the superconducting properties are enhanced on most of the channel, except in a thin band where it is depressed (the weak link).
b) Vertical devices in a tunnel junction geometry: an ultra-thin ferroelectric film is sandwiched between two different superconducting electrodes. The current tunnels through the ferroelectric barrier; depending on the direction of the polarisation, the electrostatic height of the latter is modified.

In the **first chapter**, one will find a description of the general concepts related to these devices: superconductivity and ferroelectricity, Josephson effect, tunnelling… The ferroelectric field-effect presented in the **second chapter**, in which a brief review of the different transistors and devices found in the literature is given. Then, the experimental techniques involved in the characterisation and fabrication of the devices are detailed in the **third chapter**.

The first step of the fabrication consists in the growth of high-quality heterostructures combining a ferroelectric film and a superconductor: this is the object of **chapter IV**. Further characterisation of the interface and ferroelectric properties of our structures can be found in **chapter V.**

Chapter VI presents the characterisation of the planar devices. In this configuration, the superconducting film is extremely thin (a few unit cells). The ferroelectric field-effect enhances the superconductivity in most of the channel, except in a thin region where it is depressed. This constitutes a weak link. The boundaries between the three regions are very faded, and the proximity effect is very strong in these kinds of devices. We investigate the signature of a Josephson coupling between the two enhanced regions, in a range of temperature where they are in a superconducting state whereas the depressed region is in a normal state. These devices are conceptually fascinating, as the length of the weak link and the strength of the coupling can a priori be of any size, and reconfigurable ad infinitum.

In the second case, the barrier is the ferroelectric film itself; the preliminary results are presented in **chapter VII**. High-T_c superconductor/Ferroelectric/Low-T_c superconductor junctions are studied in both the normal and the superconducting states. The switching of the polarisation in the ultra-thin barrier and the resulting electroresistance are characterised at different temperatures.

I. Generalities

Index

I. Generalities 3

I.1 Superconductivity 5

I.1.1 Historical aspects 5

I.1.2 London equations 6

I.1.3 The BCS theory 8

I.1.4 Ginzburg-Landau theory 9

I.1.5 Vortices in High-T_c Superconductors 13

I.2 Josephson effect 14

I.2.1 Tunnel effect 14

I.2.2 Josephson effect 17

I.2.3 Josephson junction in a magnetic field 19

I.2.4 Josephson junctions technology 22

I.3 Ferroelectricity 24

I.3.1 Symmetry 24

I.3.2 Mechanisms of ferroelectricity 25

I.3.3 Conduction through ferroelectric oxides 26

I.3.4 Ferroelectricity in thin films 27

I.4 Materials 31

I.4.1 $SrTiO_3$ 31

I.4.2 $PrBa_2Cu_3O_{7-\delta}$ 31

I.4.3 $YBa_2Cu_3O_{7-\delta}$ 31

I.4.4 $BiFeO_3$ 32

I.4.5 $La_{1-x}Sr_xMnO_3$ 35

I.4.6 $Mo_{1-x}Si_x$ 35

I.1 Superconductivity

I.1.1 Historical aspects

The study of metals at very low temperatures was for a long time limited by the ability to reach these temperatures. In 1908 in Leiden (Netherlands), Heike Kamerlingh Onnes was able to liquefy Helium gas, allowing his student Gilles Host, three years later, to observe a radical drop in the resistivity of a mercury sample at $4{,}2\ K$ (Figure I.1) [1]. Other metals such as Tin, Lead or Aluminium, behaved the same way, reaching resistivities so small that they would always be beyond the sensitivities of the measurement devices. After this first discovery of superconductivity, Meissner and Ochsenfeld showed in 1933 that when these metals were in the superconducting state, they became perfect diamagnetics, *i.e.* not only a magnetic field H is excluded from entering the superconductor, but for a superconductor that is in a normal state, the field is expelled as the sample is cooled and undergoes the normal-superconductor transition [2].

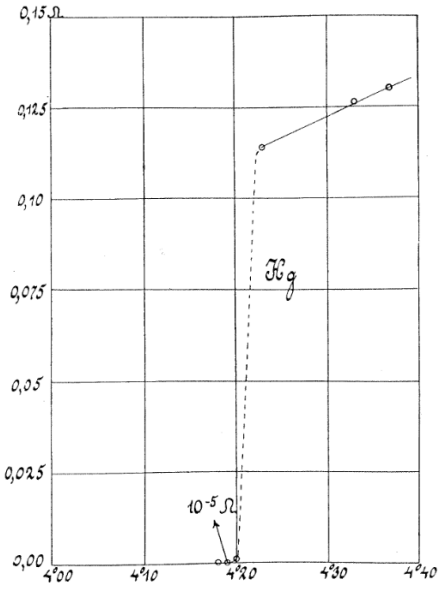

Figure I.1 : Historical resistance versus temperature measurement of a mercury wire by H.K. Onnes [1]

These effects raised the interest of the Solid State Physics community, and in 1935, the London brothers proposed an electrodynamic theory to describe the Meissner effect [3]. In 1950, Ginzburg and Landau exposed a first phenomenological theory that would describe superconductivity, assuming series expansion of the free energy and expressing it in powers of an order parameter characterising the normal / superconducting transition. Minimising this free energy leads to the Ginzburg-Landau equations, that explained magnetic properties of the superconductors.

In 1957, John Barden, Leon Cooper and John Schrieffer established a microscopic theory of superconductivity. They explained superconductivity as the formation of «Cooper pairs», pairs of

correlated electrons, created thanks to an interaction between the electrons and the phonons. This theory explains very well superconductivity in conventional superconductors like metals. Later, in 1986, Bednorz and Müller discovered a Barium and Lanthanum Copper Oxide that was superconducting with a critical temperature of $34\ K$ [4]. This was much higher than the critical temperatures measured up to then, but also very close to the upper limit predicted by the BCS theory ($35\ K$) [5].

Many other «high-T_c » superconductors were then discovered, such as $YBa_2Cu_3O_{7-\delta}$ [4], that was the first superconductor whose T_c was higher than the boiling temperature of liquid nitrogen; or copper oxides («cuprates») containing mercury like $HgBa_2Ca_2Cu_3O_{8+\delta}$ which has the highest T_c ($134\ K$ and even $164\ K$ under $31\ GPa$) ever reached for these materials [6]. Today, metallic hydrogen and compounds dominated by hydrogen are investigated, as hydrogen atoms provide strong phonon-electron coupling and high-frequency phonon modes: a T_c of $203\ K$ was obtained in a sulfur hydride system under $90\ GPa$ [7]. Iron pnictides and chalcogenides have also raised a lot of interest for their high superconducting transition temperatures [8]. In parallel, superconductivity is investigated in low-dimensional systems like the $SrTiO_3/LaAlO_3$ interface.

I.1.2 London equations

As presented in the introduction, the London equations were the first theoretical descriptions of the Meissner effect in the superconductors. The following description of the London equations is taken from [9].

From the fundamental law of dynamics applied to an electron in an electric field $E = -grad(V)$ generated by a voltage; and considering no other forces (perfect conductor):

$$m_e \frac{d\langle v \rangle}{dt} = F = qE \tag{I.1}$$

And the density of current expressed in function of the mean speed of the electrons:

$$j = nq\langle v \rangle \tag{I.2}$$

One can write the acceleration equation of the electrons:

$$\frac{dj}{dt} = nq\frac{d\langle v \rangle}{dt} = \frac{nq^2E}{m_e} \tag{I.3}$$

If we combine the Maxwell equation: $rot\ E = -\frac{\partial B}{\partial t}$, to the equation (I.3), we can obtain a relation between the derivative of the field B and the density j:

$$\mu_0 \mathrm{rot}\left(\frac{\partial j}{\partial t}\right) = -\frac{1}{\lambda_L^2}\frac{\partial B}{\partial t} \tag{I.4}$$

In this equation, where μ_0 is the permittivity of free space, a typical length λ_L appears, defined by:

$$\lambda_L = \left(\frac{m}{\mu_0 nq^2}\right)^{\frac{1}{2}} \tag{I.5}$$

In the stationary regime, the 4th Maxwell equation is $rot\ B = \mu_0 j$. Combining it to expression (I.4), and knowing that $divB = 0$, we obtain, inside a perfect conductor:

$$\Delta\left(\frac{\partial B}{\partial t}\right) = \frac{1}{\lambda_L^2}\frac{\partial B}{\partial t} \tag{I.6}$$

and:

$$\Delta\left(\frac{\partial j}{\partial t}\right) = \frac{1}{\lambda_L^2}\frac{\partial j}{\partial t} \tag{I.7}$$

In the case of a metallic plate under a parallel magnetic field, the physical solution is a decreasing exponential. This means that close to the surface, if the magnetic field changes, the conductor will induce currents to counteract these changes (Lenz law). But deeper than a distance λ_L, the field inside the conductor does not change when the field outside the surface changes.

To be able to describe the Meissner effect in the superconductors, the London brothers postulated that in the case of superconductors, because of the perfect diamagnetism, the induction equation (I.4) could be directly applied to the magnetic field and the density of current, and not to their temporal derivatives. Expression (I.4) then becomes:

$$\mu_0 \mathrm{rot} j = -\frac{1}{\lambda_L^2} B \tag{I.8}$$

and expression (I.6) and (I.7) turn to:

$$\Delta B = \frac{1}{\lambda_L^2} B \tag{I.9}$$

$$\Delta j = \frac{1}{\lambda_L^2} j \tag{I.10}$$

For a superconducting plate of a finished thickness but infinite dimensions in the x and y directions and a magnetic field parallel to Ox, equation (I.9) leads to:

$$\frac{\partial^2 B_x(z)}{\partial z^2} - \frac{1}{\lambda_L^2} B_x(z) = 0 \tag{I.11}$$

and a physical solution to this equation is:

$$B_x(z) \approx B_a exp\left(-\frac{z}{\lambda_L}\right) \tag{I.12}$$

The same calculations lead for the current to:

$$j_y(z) \approx \frac{B_a}{\mu_0 \lambda_L} exp\left(-\frac{z}{\lambda_L}\right) \tag{I.13}$$

The London equations show that the magnetic field is not completely excluded from the superconductor, but screening currents exist in a thin layer thick as λ_L, the London thickness, and decrease exponentially on this distance, as schematized on Figure I.2.

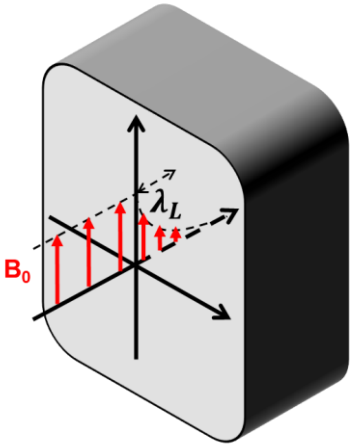

Figure I.2 : Screening of the magnetic field over a distance λ_L

I.1.3 The BCS theory

This microscopic description of superconductivity links the superconducting state to the formation of electron pairs, mediated by electron-phonons interactions. In 1956, Cooper showed that if an attractive force exists, may it be very small, between two electrons, then a state associated to a pair of electrons with an opposed momentum and an opposed spin exists and has a lower energy than two isolated electrons [10]. What could be this attraction? The interactions between electrons are always repulsive because of their negative charges. However, Frölich, in 1950, suggested that the phonons (the collective vibrations of the structure) play an important role in the apparition of superconductivity [11]: this was evidenced by experiments based on different isotopes of a superconducting metal [12]. Barden, Cooper and Schrieffer thus suggested that the attractive interaction responsible for the formation of the Cooper pairs might be mediated by electron-phonon interactions.

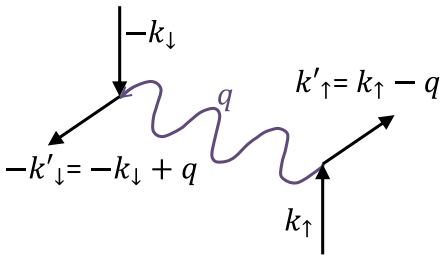

Figure I.3: Phonon mediated interaction between two electrons

When an electron moves inside a structure with polarisable ions, the lattice becomes distorted to increase the density of positive charges close to the electron. Because of the inertia of the ions, this distortion persists after the electron went by, and tends to attract another electron: this is how an attractive interaction can occur between two electrons. However, these interactions imply a transfer of impulsion from one electron to a phonon, and can only occur if:

- the two initial electrons form a pair with opposed spin and momentum, as a state $|k_\uparrow - k_\downarrow\rangle$

- the energy $\hbar q$ that it transmitted from the $k_\uparrow$ electron to the phonon is smaller than the maximum energy of a phonon $\hbar\omega_D$, which is the Debye energy; thus, the electrons have to be close to the Fermi energy
- the transition respects the Pauli exclusion and the state $|k_\uparrow - q \ \ -k_\downarrow + q\rangle$ is empty.

To make it short, if two electrons of opposed momentum and spin, close to the Fermi level, get attracted via a phonon that would interact with both, they can lower the free energy of the system by forming a pair. Of course, when considering a macroscopic number of electrons, the pairs might interact between them and the problem becomes more complex. It can still be described by the BCS theory, and solving the Schrödinger equation associated with the fundamental state corresponding to the superconducting state predicts the existence of a gap in the spectra of the electronic excitations (one can refer to the work of Thinkham [13]):

$$\Delta = \frac{\hbar\omega_D}{\sinh(1/N(0)V)} \tag{I.14}$$

Physically, this gap is the amount of energy gained by an electron when it gets paired. In the approximation of a weak interaction, and considering that under zero magnetic field the critical temperature is given by:

$$k_B T_c \approx 1.13\, \hbar\omega_D e^{-1/N(0)V} \tag{I.15}$$

We obtain a good approximation of the T_c as a function of the gap at $T = 0\ K$,

$$\Delta(0) \approx 1.76 \times k_B T_c \tag{I.16}$$

This relation is accurate for conventional superconductors. Above $T = 0\ K$, the gap can be approximated by:

$$\Delta(T) \approx 1.55\, \Delta(0) \sqrt{1 - \frac{T}{T_c}} \tag{I.17}$$

From the principle of incertitude $\delta x \delta k = 1$, we can figure out the coherence length of a Cooper pair:

$$\xi(T) = \frac{\hbar v_F}{\pi\Delta(T)} \tag{I.18}$$

I.1.4 Ginzburg-Landau theory

Prior to the microscopic description of the BCS theory, the Ginzburg-Landau theory is a phenomenological description of the superconductivity, that describes the superconducting transition with no regards to the microscopic mechanisms. Even though the Ginzburg-Landau theory is based on phenomenological results, Gor'kov showed [14] that the two theories are coherent: close to the T_c and in a material with slow variation of the order parameter ψ and of the potential vector A, ψ is proportional to the gap Δ obtained by the BCS theory, and can be thought as the wave function of the centre-of-mass motion of the Cooper pairs. The following equations are taken from [13] where the interested reader can find further details.

I.1.4. a) Free energy of Ginzburg Landau

To describe superconductivity, Ginzburg and Landau define the superconducting transition as a 2nd order phase transition. The energy of the system is expressed by a pseudo wave function $\psi(\vec{r})$ introduced as a complex parameter order, which is zero in the disordered state and non-zero in the ordered phase. In the case of a superconductor, we assume that the order parameter is small near the transition. The basic postulate of the G-L theory is that if the spatial variations are slow enough, close to the T_c the free energy can be expressed as a function of ψ and of the potential vector $\vec{A}$:

$$f = f_n + \alpha|\psi|^2 + \frac{\beta}{2}|\psi|^4 + \frac{1}{2m^*}\left|(\frac{\hbar}{i}\nabla - \frac{e^*}{c}\vec{A})\psi\right|^2 + \frac{h^2}{8\pi} \quad \text{(I.19)}$$

The analysis of this expression leads to several results on the parameters α and β below T_c, as a function of the critical field H_c, the effective penetration depth in the material λ_{eff}, the charge $e^* = 2e$ of the Cooper pair, and its mass m^* assumed to be twice the electronic mass:

$$\alpha \propto (\frac{T}{T_c} - 1) < 0 \text{ and } \beta > 0 \quad \text{(I.20)}$$

$$\alpha(T) = -\frac{e^{*2}}{m^* c^2} H_c^2(T)\lambda_{eff}^2(T) \quad \text{(I.21)}$$

$$\beta(T) = \frac{4\pi e^{*4}}{m^{*2} c^4} H_c^2(T)\lambda_{eff}^4(T) \quad \text{(I.22)}$$

Minimising the expression of the free energy leads to the two Ginzburg-Landau equations:

$$\alpha\psi + \beta|\psi|^2\psi + \frac{1}{2m^*}\left(\frac{\hbar}{i}\nabla - \frac{e^*}{c}\vec{A}\right)^2\psi = 0 \quad \text{(I.23)}$$

$$\vec{J} = \frac{e^*\hbar}{2m^* i}[\psi^*\nabla\psi - \psi\nabla\psi^*] - \frac{(e^*)^2}{m^* c}\psi^*\psi\vec{A} \quad \text{(I.24)}$$

with $\vec{J}$ the current density. The boundary conditions depend on the physical situation: for a superconductor/insulator interface, the electrons cannot leave the superconductor, *i.e.*:

$$(\frac{\hbar}{i}\nabla - \frac{e^*}{c}\vec{A})\psi|_n = 0 \quad \text{(I.25)}$$

For a superconductor/metal interface, Pierre-Gilles de Gennes showed that the condition could be expressed as [15]:

$$(\frac{\hbar}{i}\nabla - \frac{e^*}{c}\vec{A})\psi|_n = \frac{i\hbar}{b}\psi \quad \text{(I.26)}$$

where b, which depends on the normal material, is a real constant and characterises the extrapolation length at which the order parameter should go to zero if it kept the same slope at the interface. It is close to zero for a magnetic metal, and is infinite for an insulator.

I.1.4. b) Coherence length

In a superconductor that is not perfect, for example close to a defect, the order parameter is not constant anymore. Without any external field, the G-L equations can be expressed as:

$$\alpha\psi + \beta|\psi|^2\psi + \frac{\hbar^2}{2m^*}\nabla^2\psi = 0 \tag{I.27}$$

$$\frac{e^*\hbar}{2m^*i}[\psi^*\nabla\psi - \psi\nabla\psi^*] = 0 \tag{I.28}$$

With $f(x) = \frac{\psi(x)}{\psi_\infty}$ the ratio between the wavefunction close to the defect and the wave function far from it $\psi_\infty = \sqrt{-\alpha/\beta}$, and assuming that ψ is real since the differential equation has only real coefficients, we obtain:

$$\frac{\hbar^2}{2m^*|\alpha|}\frac{d^2f}{dx^2} + f - f^3 = 0 \tag{I.29}$$

This expression lets a new length parameter appear:

$$\xi(T) = \sqrt{\frac{\hbar^2}{2m^*|\alpha|}} = \sqrt{\frac{\hbar^2}{2m^*\alpha_0|T - T_c|}} \tag{I.30}$$

It is called the coherence length of Ginzburg-Landau, and represents the distance over which the system feels the defect. $\xi(T)$ constitutes, with the London thickness λ_L, one of the two characteristic lengths of superconductivity. From the expression of $\alpha(T)$ in (I.21), we find:

$$\xi(T) = \frac{\Phi_0}{2\sqrt{2}\pi H_c(T)\lambda_{eff}(T)} \tag{I.31}$$

where $\Phi_0 = hc/2e$ is the fluxoid quantum.

I.1.4. c) Ginzburg-Landau parameter

The ratio $\kappa = \frac{\lambda_{eff}}{\xi}$, named Ginzburg-Landau parameter, is independent of the temperature as the two lengths present the same temperature dependence [16] provided by the relation:

$$\lambda(T), \xi(T) \propto (1 - T/T_c)^{-1/2} \tag{I.32}$$

κ distinguishes two families of superconductors. On one hand, for $\kappa < 1/\sqrt{2}$, the type I superconductors: their surface energy is positive, and an interface with a normal material is always unfavourable. If a magnetic field is applied, it is completely expelled from the superconductor unless its value is higher than a critical field at which the superconductor will transit to a normal state, like schematized on Figure I.4–*left*. Most of the pure metals belong to this type of superconductors, and are, as we already mentioned, very well described by the BCS theory.

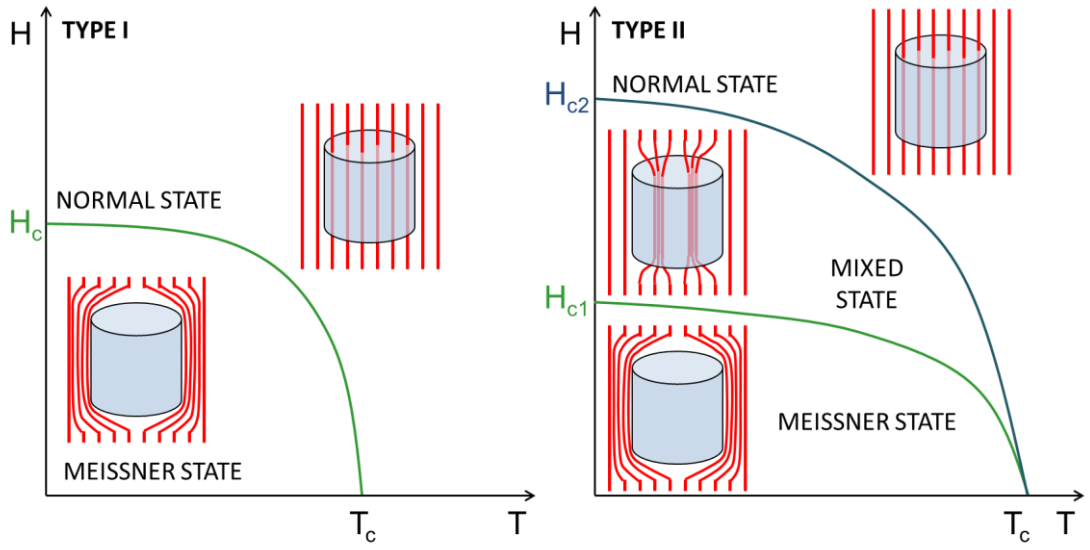

Figure I.4: General phase diagrams for type I (left) and type II (right) superconductors

On the other hand, for $\kappa > 1/\sqrt{2}$, normal/superconductor interfaces are favourable: for fields smaller than H_c, the loss in the condensation energy is compensated by a gain in the magnetic energy. The superconductor can go through three phases (see Figure I.4–*right*): for fields smaller than a first critical field H_{c1}, the Meissner effect is total. At $H = H_{c1}$, the field penetrates partially the superconductor by forming cylindrical, quantised flux lines call vortices. The penetration profiles of the magnetic field $B(x)$ into a superconductor at the interface with a normal metal as well as the density of Cooper pairs $n_c(x)$ in type I and type II superconductors are schematized in Figure I.5.

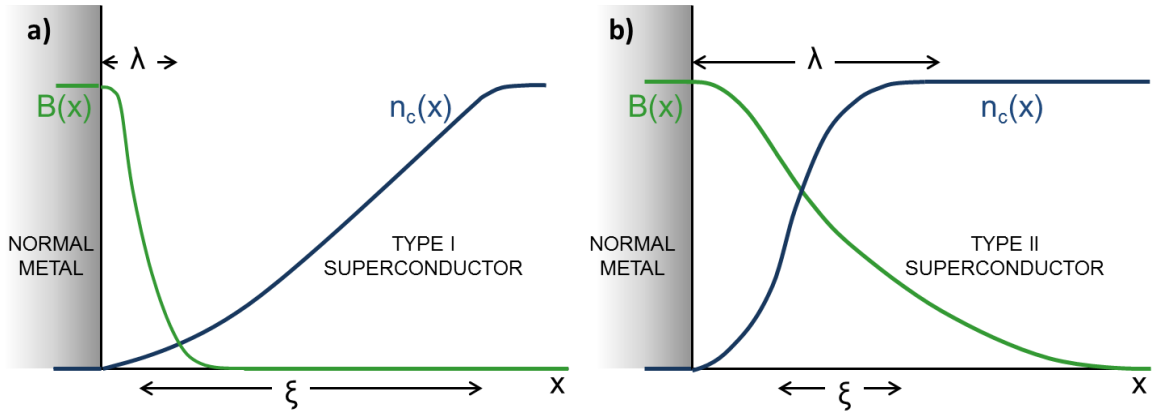

Figure I.5: Schematic representation of the coherence length and penetration depth in the boundary between a normal region and a (a) type I and (b) type II superconducting regions.

Vortices have a normal core of radius ξ where the density of Cooper pairs is zero. It is surrounded by a region of larger radius, λ, where superconducting currents are flowing generating a flux quantum of $\Phi_0 = 2.07 \cdot 10^{-15}\, Tm^2$. Figure I.6 shows a schematic representation of a vortex, where the magnetic field profile, $B(r)$ and $n_c(r)$ are shown. The more H increases, the more vortices appear; in the lack of defects, they can arrange in a regular array forming a triangular (or hexagonal) lattice, known as the Abrikosov lattice [17], in order to minimise the system total energy. When a critical value H_{c2} is reached, the superconductor becomes normal. The high-T_c superconductors like cuprates and alloys, and some pure metals like Vanadium or Niobium are type II superconductors.

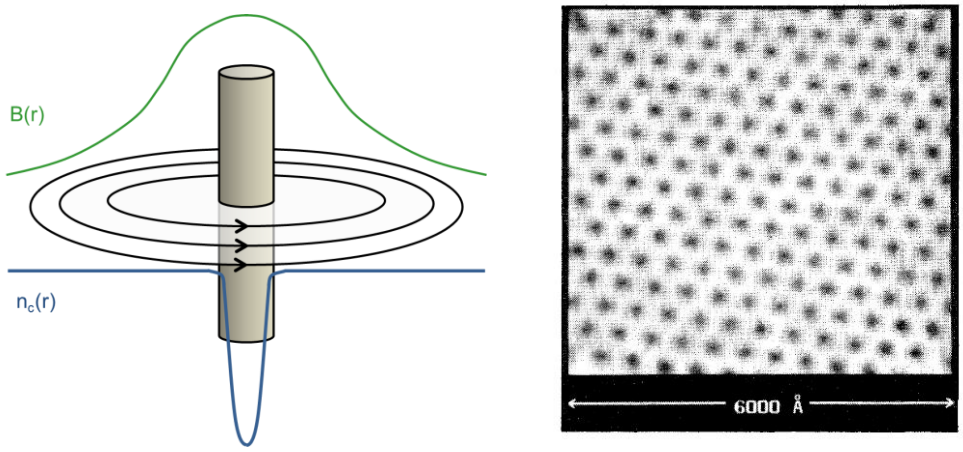

Figure I.6: Schematic representation of a vortex (left) and STM image of an Abrikosov flux lattice produced by a 1 T magnetic field in $NbSe_2$ at 1.8 K (right) taken from [17]

I.1.5 Vortices in High-T_c Superconductors

The mixed state itself can show different phases, and show a behaviour that is not always reversible magnetically: the interactions between vortices, disorder, thermal fluctuations, anisotropic behaviours of some materials can lead to very rich phase diagrams [16]. However, they always present at least two states: a magnetically irreversible zero-resistance state, called "vortex solid phase", and a reversible state with dissipative transport properties, called "vortex liquid state" [18]. In the absence of disorder, as in clean defect-free systems, the solid phase presents topological order (forming the Abrikosov lattice), and it is separated from the liquid phase, by a first order transition (melting line) [16]. In samples containing disorder (defects), a second order transition (irreversibility line) is found between the solid and liquid phases [19],[20]. Moreover, various glassy vortex states have been suggested for this solid state.

An isolated vortex carries an energy, for a unit length, of:

$$\varepsilon_1 = \frac{1}{4\pi\mu_0}\left(\frac{\Phi_0}{\lambda}\right)^2 \ln\left(\frac{\lambda}{\xi}\right) + \varepsilon_{core} \quad \text{with} \quad \varepsilon_{core} \approx \pi\xi^2\mu_0 {H_c}^2 \tag{I.33}$$

where ε_{core}, the energy of the core, is very little compared to the total energy in high-T_c superconductors. This dependence of the energy on the square of the flux quantum Φ_0 implies that it is more favourable to have many vortices each carrying one quantum of flux, than one vortex carrying many flux quanta. The first critical field H_{c1}, at which the creation of a vortex is energetically favourable, is given by:

$$H_{c1} = \frac{\varepsilon_1}{\Phi_0} = \frac{\Phi_0}{4\pi\mu_0\lambda^2}\ln\kappa \tag{I.34}$$

The second critical field H_{c2} can be expressed as the field for which the distance between two vortices becomes smaller than the coherence length:

$$H_{c2} = \frac{\Phi_0}{4\pi\mu_0\xi^2} \tag{I.35}$$

For a superconductor in which $\xi << \lambda$, the resolution of the second G-L equation gives:

$$B(r) = \frac{\Phi_0}{2\pi\lambda^2} K_0\left(\frac{r}{\lambda}\right) \text{ and } J_s(r) = \frac{\Phi_0}{2\pi\lambda^3} K_1\left(\frac{r}{\lambda}\right) \quad \text{(I.36)}$$

where K_0 and K_1 are the modified zero and first order Bessel functions. Far from the vortex, $K_0(r)$ and $K_1(r)$ behave asymptotically as $e^{-r/\lambda}$, whereas for $\xi < r << \lambda$ they vary as $\ln\left(\frac{\lambda}{r}\right)$.

Vortices in YBCO

In YBCO, different vortex solid phases are possible, depending on the type and the dimensionality of the defects. A Bose glass phase is expected when the defects are correlated [21],[22], for example if they are amorphous columns created by heavy ion irradiation, of 2D planar defects like twin boundaries. For anisotropic, random defects, a vortex glass phase is stabilised [19].

The magnetic-field *vs* temperature phase diagram of thin films of YBCO exhibits an « irreversibility line ». Below the irreversibility line, in the solid phase, vortices are pinned. The superconductor presents zero electrical resistance unless the electrical current exceeds the critical depinning current, beyond which a strongly non-linear, finite resistance is observed. Above the irreversibility line and below the critical temperature, the material is superconducting (its order parameter ψ is finite) but the temperature is high enough so that the thermal energy exceeds the pinning energy of the vortices in the material. This leads to spontaneous vortex motion and zero critical current. Since vortices carry magnetic flux, moving vortices generate an electric field and therefore cause dissipation: the material thus presents a finite electrical resistance, even though it is in a superconducting state.

I.2 Josephson effect

I.2.1 Tunnel effect

The tunnel effect is a quantum phenomenon that occurs in many physical systems, and occurs when there is a probability bigger than zero that a particle can pass through a potential barrier even though its kinetic energy is smaller than the height of the barrier. This is possible because quantum particles are described by a wavefunction: when the particle meets a barrier, it penetrates into it as an evanescent wave. If the barrier is thin enough so that the probability that the particle is present on the other side is finite, if the transfer is constant in energy and if it respects the Pauli exclusion principle, the particle can go through the barrier. The following model describing this effect is taken from [23].

The probability $W_{1\to2}$ that an electron with an energy comprised between E and $E + dE$ transits from the state $|1\rangle$ to the state $|2\rangle$, is given for small perturbations H_T of the system by the expression:

$$W_{1\to2} = \frac{2\pi}{\hbar} |\langle 2|H_T|1\rangle|^2 N_2(E)\big(1 - f(E)\big) \quad \text{(I.44)}$$

with $f(E) = \frac{1}{1+e^{\frac{E-\mu}{k_B T}}}$ the Fermi-Dirac function, and $N_2(E)\big(1-f(E)\big)$ the density of free states in the second material. The density of current from the state $|1\rangle$ to the state $|2\rangle$ is obtained by integrating relation (I.44) over the density of occupied states $N_1(E)f(E)$ in the first material:

$$J_{1\to 2} = e\frac{2\pi}{\hbar}\int |T|^2 N_2(E)\big(1-f(E)\big)N_1(E-eV)f(E-eV)dE \qquad \text{(I.45)}$$

with $T = \langle 2|H_T|1\rangle$ the matrix element that expresses the coupling between states $|1\rangle$ and $|2\rangle$. A similar expression is obtained for the current density $J_{2\to 1}$ flowing in the other direction. The current through a barrier of a surface S is then given by the sum of currents from material *1* to *2* and material *2* to *1*:

$$I = (J_{1\to 2} - J_{2\to 1}) \times S = \frac{2\pi e S}{\hbar}|T|^2 \int_{-\infty}^{+\infty} N_2(E)N_1(E-eV)[f(E-eV)-f(E)]dE \qquad \text{(I.46)}$$

This relation highlights the fact that the tunnel current depends both on the density of states of the different materials in contact $N_1(E-eV)$ and $N_2(E)$, but also on the applied potential V on which the difference $f(E-eV)-f(E)$ depends.

I.2.1. a) Metal/Insulator/Metal junctions

In the case of two metals separated by an insulating barrier of thickness s, there is no current if the two metals have the same Fermi energy. But if a voltage V is applied across the barrier, a tunnel current occurs. If the voltage is small (typically few meV), we can assume the density of state to be constant and the current is then given by:

$$I_{NN} = S|T|^2 N_1(E_F)N_2(E_F)eV = G_{NN}V \qquad \text{(I.47)}$$

In these conditions, the junctions have an Ohmic behaviour, and are characterised by a conductance G_{NN}. At higher bias, the conductance is not Ohmic, but increases with increasing voltage across the junction. Depending on the barrier height and profile (rectangular, trapezoidal…), and on the voltage range, voltage dependences that go from nearly quadratic to exponential can be observed [24]. As an example, in the case of a rectangular barrier of height φ, for very high voltages, ($V > (\varphi + E_F)/e$) the current is given by [25]:

$$J = V^2 \frac{2{,}2e^3}{8\pi h\varphi_0 s^2}\exp\left(-\frac{1}{V}\frac{8\pi s}{2{,}96he}(2m)^{1/2}{\varphi_0}^{3/2}\right) \qquad \text{(I.48)}$$

I.2.1. b) Superconductor/Insulator/Superconductor junctions

Superconductors are different from normal metals as they exhibit a gap Δ, which corresponds to the energy necessary to break the Cooper pairs. The density of states of the quasiparticles diverges at Δ and is given by:

$$N(E) = N(E_F)\frac{E}{\sqrt{E^2-\Delta^2}} \qquad \text{(I.49)}$$

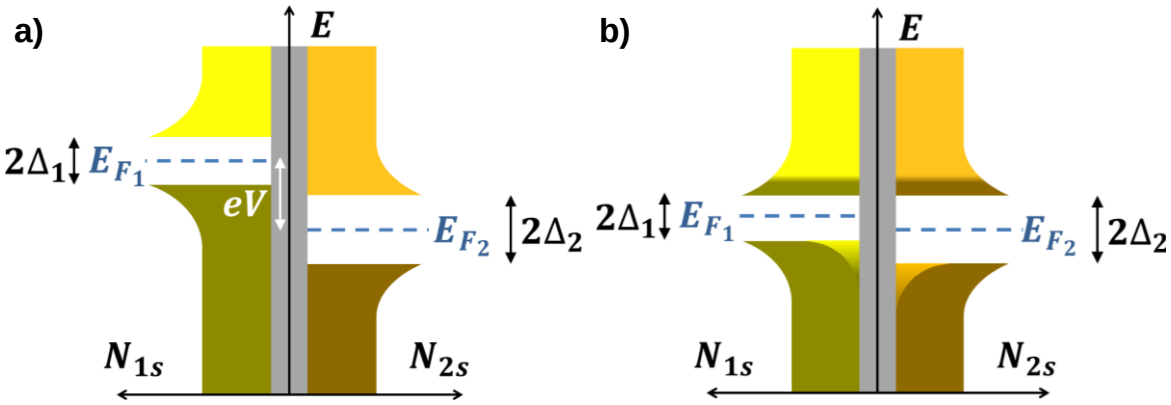

Figure I.7: Superconductor/Insulator/Superconductor junction a) at 0 K and b) at finite temperature: thermal excitation leads to electron and hole-like quasiparticles

In these junctions the tunnel current is given by:

$$I_{SS} = \frac{G_{SS}}{e}\int_{-\infty}^{+\infty} \frac{N_{1S}(E)N_{2S}(E)}{N_{1S}(E_F)N_{2S}(E_F)}[f(E-eV)-f(E)]dE \qquad \text{(I.50)}$$

At $0\ K$, there are no available states until $e \times V$ reaches the value $\Delta_1 + \Delta_2$. At this point, the current increases suddenly: as schematically represented on Figure I.7 *a),* when $e \times V$ is just higher than the sum of the two gaps $\Delta_1 + \Delta_2$, the singularities in the density of state function of both superconductors face one each other. The corresponding $I(V)$ characteristic is represented by the red curve in Figure I.8.

Case of two identical superconductors:

At $T = 0\ K$, if $|eV| < 2\Delta$, no current can go through the barrier. At $|eV| = 2\Delta$, a tunnel current occurs. At $T > 0$, because thermal excitation leads to electron and hole-like quasiparticles, a tunnel current can occur before this threshold.

Case of two different superconductors:

At $T = 0\ K$, the tunnel current starts when $|eV|$ gets higher than $\Delta_1 + \Delta_2$, the sum of the gaps of the two superconductors. At $T > 0\ K$, a finite population of electronlike (and holelike) quasiparticles exist above (below) the gap [26]. If we suppose that superconductor *1* has a smaller gap than superconductor *2* ($\Delta_1 < \Delta_2$), we can consider that a relatively higher number of quasiparticles is present in the former. Then for $|eV| < \Delta_2 - \Delta_1$, as schematically represented in Figure I.7 *b),* quasiparticles in the superconductor *1* face unoccupied electron and hole states of superconductor *2*, which yields a tunnel current. It increases until $|eV| = \Delta_2 - \Delta_1$. For higher energies, the quasiparticles face unoccupied states that are far from the gap, in an area where the density of state gets narrower, which makes the tunnel current decrease. It increases again when $|eV|$ approaches $\Delta_1 + \Delta_2$, and electrons below the gap in superconductor 1 can tunnel into empty states above that of superconductor 2. The above scenario results in the schematic I-V characteristic depicted in by the black dashed curve in Figure I.8.

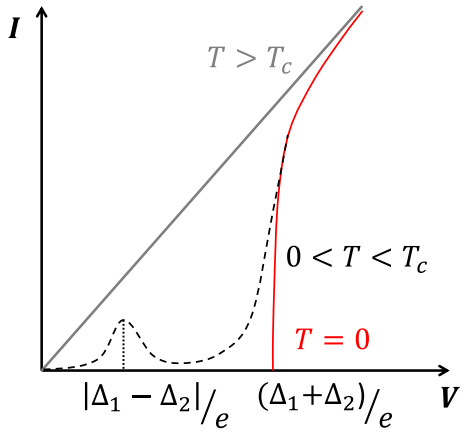

Figure I.8: Current-voltage characteristic of an S/I/S junction at 0 K (red curve) and at finite temperature (dash curve)

I.2.2 Josephson effect

In the precedent section we considered the tunnelling of a superconducting quasiparticle through a barrier. In 1962, Josephson predicted that a condensed electron pair could also tunnel from a superconductor to another, realising a phase correlation between the two superconducting blocks [27], [28]. This effect was first observed in 1963 by Anderson and Rowell in a tin/tin oxide/lead tunnel junction [29]. It was generalised to "weak links" separating superconductors, in which the conduction mechanism is not necessarily the direct tunnelling of quasiparticles. The following description of the Josephson equations are taken from [30], where the reader can find a detailed derivation of the AC and DC Josephson effect, as well as in Appendix A. Only the final expressions will be given here.

I.2.2. a) Josephson equations

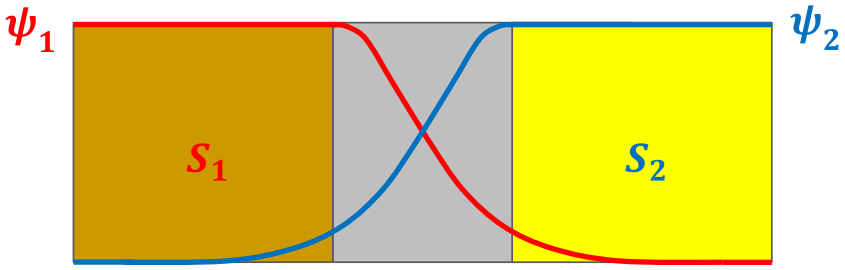

Figure I.9: Superconductor/Insulator/Superconductor junction

Considering a superconductor/insulator/superconductor junction as described on Figure I.9, each superconducting block is described by a wave function:

$$\psi_1 = \sqrt{n_1}e^{i\varphi_1} \text{ and } \psi_2 = \sqrt{n_2}e^{i\varphi_2} \quad \text{(I.51)}$$

where $n_1 = |\psi_1|^2$ and $n_2 = |\psi_2|^2$ represent the density of Cooper pairs in each superconducting part, and φ_1, φ_2 their phases. When the barrier is thin enough, the two wavefunctions overlap, and the two blocks are coupled: the probability that a Cooper pair can go through the barrier thanks to tunnel effect becomes superior to zero.

The system is then described by a linear combination of the two states:

$$|\psi\rangle = \psi_1|1\rangle + \psi_2|2\rangle \tag{I.52}$$

where ψ_i represents the probability that a Cooper pair is present in the block i. Solving the Schrodinger equation driving the temporal evolution of the system leads to the equations presented in the following paragraphs. From now, the phase difference between the two blocks will be expressed as $\varphi = \varphi_1 - \varphi_2$.

I.2.2. b) Continuous Josephson effect

The first equation describes the conservation of the total number of Cooper pairs and express the density of current that goes through the barrier, as a function of the coupling constant K between the two ground states of the two superconductors:

$$J = \frac{2K}{\hbar}\sqrt{n_1 n_2}\sin\varphi \tag{I.53}$$

The expression of the current can be obtained by integrating it along the surface S of the junction, which gives the first Josephson equation:

$$I = I_c \sin\varphi \quad \text{with} \quad I_c = \frac{2K}{\hbar}S\sqrt{n_1 n_2} \tag{I.54}$$

In this expression, I_c is the maximum current that can go through the junction without dissipating energy: it is a characteristic that is intrinsic to the system. This expression traduces the fact that in a Josephson junction, the Cooper pairs can spontaneously go through the junction and a current is induced without the application of a voltage, but because of a difference of phase between the two superconductors: it is called the continuous or DC Josephson effect.

The previous equations describe superconductor/insulator/superconductor tunnel junctions, but the continuous Josephson effect, or similar effects [31], [32] can be observed in different weak-link junctions, such as superconductor/normal metal/superconductor junctions [32], Dayem bridges [33], irradiated junctions [34], [35]...

I.2.2. c) Alternative Josephson effect

The second equation derived from the temporal evolution of the system indicates that the difference of phase is driven by the potential across the junction:

$$\frac{d\varphi}{dt} = \frac{d\varphi_1}{dt} - \frac{d\varphi_2}{dt} = \frac{2eV}{\hbar} \tag{I.55}$$

It implies that if we apply a voltage V on both sides of the junction, an AC current will be generated through the junction:

$$I = I_c \sin\left(\frac{2eV}{\hbar}t + \varphi_0\right) \tag{I.56}$$

This second Josephson effect is called the alternative or AC Josephson effect. It was first observed by Shapiro in 1963 in $Al/Al_2O_3/Sn$ junctions [36]. The frequency of the oscillations $f_J = \frac{eV}{\pi\hbar}$ is directly

proportional to the applied voltage, and the ratio $\frac{f_J}{V} = \frac{e}{\pi\hbar} = 483{,}6\ MHz/\mu V$ is constant. It does not depend on the experiment nor the system. If, on the contrary an alternative voltage is applied across the junction with hyperfrequency irradiation, the supercurrent tends to synchronise with this frequency and its harmonics. This leads to the apparition of steps in the $I(V)$ characteristic, for defined values of continuous voltage across the barrier:

$$V_n = \frac{nh}{2e} f_0 \qquad (n = \pm 1, \pm 2, \dots) \tag{I.57}$$

with f_0 the irradiation frequency. These characteristic steps are called Shapiro steps. Therefore, one of the main applications of Josephson junctions are frequency/voltage (or voltage/frequency) convertors, with a fundamental precision [27].

I.2.3 Josephson junction in a magnetic field

Josephson junctions are very sensitive to magnetic fields, as their presence induces spatial modulation of the superconductors' phases, and therefore a periodic modulation of the Josephson current. They are widely used for fine magnetic field detectors like SQUIDs [37]. The following equations are taken from [30] in which the interested reader can find further details.

I.2.3. a) Magnetic field-effects

If we consider a junction plunged into a magnetic field H along the y direction, the presence of the field, described by the vector potential $\vec{A}$, will induce a difference in the gauge invariant phase between two points of the barrier (either both on the left or both on the right of the barrier) and separated by a distance dx:

$$\nabla\varphi_{L,R} = \frac{2e}{\hbar c}\left(\frac{mc}{2e^2\rho}\vec{J_s} + \vec{A}\right) \tag{I.58}$$

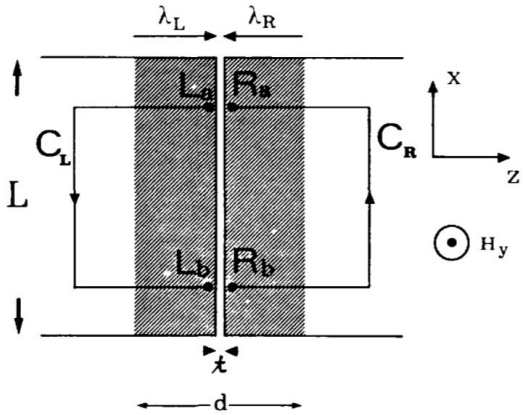

Figure I.10: Contours of integration for the derivation of the field dependence of the phase difference. The dashed areas indicate the regions where the field penetrates the superconductor. Taken from [30]

By integrating it along the contours defined on Figure I.10 – the calculations are detailed in Appendix B – and according to expression (I.54), the tunnelling current is then:

$$J(x) = J_c \sin\left(\frac{2e}{\hbar c} H_y dx + \varphi_0\right) \tag{I.59}$$

where $d = (\lambda_L + t + \lambda_R)$ represents the magnetic static thickness of the junction (t is the distance between the electrodes and $\lambda_{L,R}$ the London penetration depths). This equation implies that the current is spatially modulated along the direction parallel to the magnetic field, and that for some values of H_y, the net tunneling current in the channel is zero.

The total current in the junction is given by the integration of the density over the junction area:

$$I = \iint J_c(x,y)\sin(\frac{2e}{\hbar c}H_y dx + \varphi_0)\,dxdy = \iint J_c(x,y)\sin(kx + \varphi_0)\,dxdy \tag{I.60}$$

with $k = 2\pi d\frac{2e}{h}H_y = \frac{2\pi d}{\Phi_0}H_y$. The critical current density is given by the integration along the y direction:

$$\mathcal{J}_c(x) = \int dy J_c(x,y) \tag{I.61}$$

and the critical current is obtained by integrating $\mathcal{J}_c$ along the largest junction dimension L along x:

$$I(k,\varphi_0) = \int_{-L/2}^{L/2} dx\mathcal{J}_c(x)\sin(kx+\varphi_0) = \mathrm{Im}\left\{e^{i\varphi_0}\int_{-L/2}^{L/2} dx\mathcal{J}_c(x)e^{ikx}\right\} \tag{I.62}$$

The maximum Josephson current is obtained by maximising equation (1.62) with respect to φ_0:

$$I_{max}(k) = \left|\int_{-L/2}^{L/2} dx\mathcal{J}_c(x)e^{ikx}\right| \tag{I.63}$$

$I_{max}(k)$ is thus the Fourier transform of the critical current density $\mathcal{J}_c(x)$ [38].

I.2.3. b) Uniform and rectangular junction in a magnetic field

In the case of a rectangular and uniform junction, of length L along the x direction, and width W along the y direction, $J_c(x,y)$ is constant and the critical current density is given by:

$$\mathcal{J}_c(x) = \int dy J_c(x,y) = \begin{cases} WJ_c & |x| \le L/2 \\ 0 & |x| > L/2 \end{cases} \tag{I.64}$$

And the maximum Josephson current that can go through the junction is:

$$I_{max}(k) = \left|WJ_c\int_{-L/2}^{L/2} dx e^{ikx}\right| = I_c\left|\frac{\sin\left(k\frac{L}{2}\right)}{k\frac{L}{2}}\right| \tag{I.65}$$

with $k = \frac{2\pi d}{\Phi_0}H_y$. I_{max} can be expressed as a function of the magnetic flux through the junction $\Phi = dLH_y$:

$$I_{max}\left(\frac{\Phi_{ext}}{\Phi_0}\right) = I_c\left|\frac{\sin\left(\pi\frac{\Phi}{\Phi_0}\right)}{\pi\frac{\Phi}{\Phi_0}}\right| \tag{I.66}$$

The profile of I_{max} as a function of the field is thus a Fraunhofer pattern, with extinctions of the Josephson current for $\Phi = n\Phi_0$ with n a natural number, as represented in Figure I.11. This was observed by Rowell in 1963.

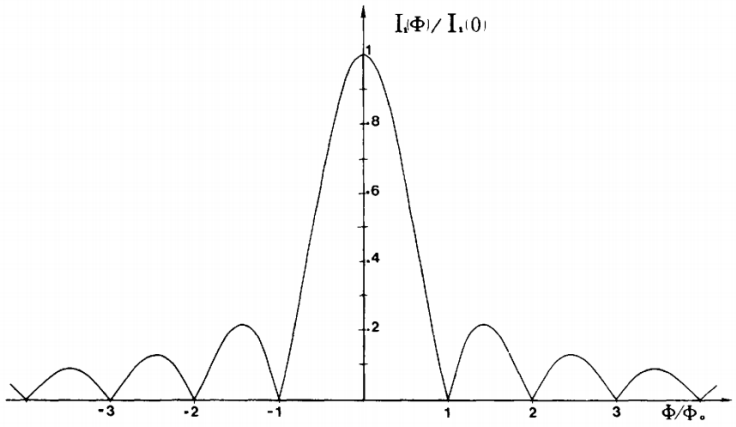

Figure I.11: Theoretical magnetic dependence of the maximum Josephson current for a rectangular junction. Taken from [30]

I.2.3. c) Electrodynamics of the junction

If we now apply a magnetic field both along the x and y direction, the same calculations that lead to equation (I.59) give:

$$\frac{d\varphi}{dx} = \frac{2e}{\hbar c} H_y d \quad \text{and} \quad \frac{d\varphi}{dy} = \frac{2e}{\hbar c} H_x d \tag{I.67}$$

In our case the Maxwell equation $\vec{\nabla} \times \vec{H} = \frac{4\pi}{c}\vec{J} + \frac{1}{c}\frac{\partial \vec{D}}{\partial t}$ reduces to:

$$\frac{\partial H_y}{\partial x} + \frac{\partial H_x}{\partial y} = \frac{4\pi}{c} J_z + \frac{1}{c}\frac{\partial D_z}{\partial t} \tag{I.68}$$

By combining this equation with equation (I.54) and equations (I.67), we obtain:

$$\frac{\hbar c^2}{8\pi e d}\left(\frac{\partial^2 \varphi}{\partial x^2} + \frac{\partial^2 \varphi}{\partial y^2}\right) = J_1 \sin\varphi + C\frac{dV}{dt} \tag{I.69}$$

where $C = \frac{\varepsilon_r}{4\pi t}$ is the junction capacitance per unit area, ε_r the relative dielectric constant of the barrier and t its thickness. Using equation (I.55), we obtain:

$$\frac{\partial^2 \varphi}{\partial x^2} + \frac{\partial^2 \varphi}{\partial y^2} - \frac{1}{\bar{c}^2}\frac{\partial^2 \varphi}{\partial t^2} = \frac{1}{\lambda_J^2}\sin\varphi \tag{I.70}$$

where

$$\bar{c} = c\left(\frac{1}{4\pi C d}\right)^{1/2} = c\left(\frac{t}{\varepsilon_r\, d}\right)^{1/2} \tag{I.71}$$

and

$$\lambda_J = \left(\frac{\hbar c^2}{8\pi e d J_c}\right)^{1/2} \tag{I.72}$$

The electrodynamics of the junctions are ruled by equation (I.70). In the stationary limit and with small φ ($\sin\varphi \sim \varphi$), this equation reduces to a London-type equation with an exponential solution: $\varphi \sim e^{-x/\lambda_J}$. The length λ_J, the "Josephson penetration depth" represents the distance over which

Josephson currents generated to screen the self-field generated by the supercurrents are confined at the edge of the junction.

I.2.3. d) "Small" and "large" junctions

The Josephson penetration depth depends on the current density J_c, which varies with the temperature and the thickness of the barrier. It also depends on the London penetration depth λ_L, which also varies with the temperature. Depending on these parameters and on the geometry of the junction, two different behaviours can be observed regarding the shielding currents. In the case of "small" junctions (if the largest transverse dimension L is smaller than λ_J), the Josephson current does not circulate and no self-field is generated. In this case, the magnetic field through the junction is equal to the external magnetic field. In the case of large junctions ($L > \lambda_J$), the Josephson currents confined to the edge of the junction generate a self-field, which is added to the external magnetic field. The main consequence is a shift of the maxima in the magnetic field pattern [39].

I.2.4 Josephson junctions technology

Technologies to fabricate Josephson junctions out of low-T_c superconductors are well-known and well controlled [40]. Their main disadvantage is that they require to be refrigerated at a very low temperature (below the temperature of liquid nitrogen). For this reason, efforts have been made to develop high-T_c Josephson junctions. The complex crystallographic structures and the small coherence length of these materials make the fabrication of reproducible Josephson junctions much more challenging. Seven main kinds of technologies are reported in the literature, and are represented in Figure I.12:

- **Grain Boundary junctions:** When the superconducting oxide grows, its crystalline orientation might not be homogeneous on the full sample and some domains can appear: at the interface between two domains, the superconductivity is depressed and this interface acts like a natural Josephson barrier. By lithographying a microbridge above the interface, the junction can be measured. The behaviour of the junction depends a lot on the disorientation between the two domains, so these "natural" junctions were soon replaced by "artificial" controllable junctions.
    - ***Bicrystal junctions*** [41], [42]*:* the disorientation can be controlled by mechanically sticking two substrates with a 20° – 40° disorientation in the plane. These junctions have achieved good critical currents and normal resistance, with an acceptable reproducibility.
    - ***Step-Edge Grain Boundary junctions*** [43]: a sharp and straight edge is designed on the substrate (for example by ion beam milling). Superconducting stripes across the step edges give two Josephson junctions at the top and at the bottom of the step, with usually rather different characteristics [44].
    - ***Bi-epitaxial junctions*** [45]–[47]***:*** here, a buffer layer is partially deposited on the substrate; it is chosen so that above the buffer layer, the high-T_c superconductor grows with a different orientation from that above the substrate. At the interface, a grain boundary barrier is formed. The interface usually exhibits a big disorder, which makes it difficult to fabricate reproducible devices. However, by reducing the width of the bridges below the micrometre, the quality of the junctions is enhanced [45].

These junctions have to be arranged along the grain boundary line, which limits the possible designs for the devices. They were widely studied: it was observed from experiments [48] that as the misorientation angle was increased, the grain boundary behaviour would change from a weak to a strong coupling; a theoretical model [49] explained this in term of oxygen (and thus holes) depletion in a region near the boundary.

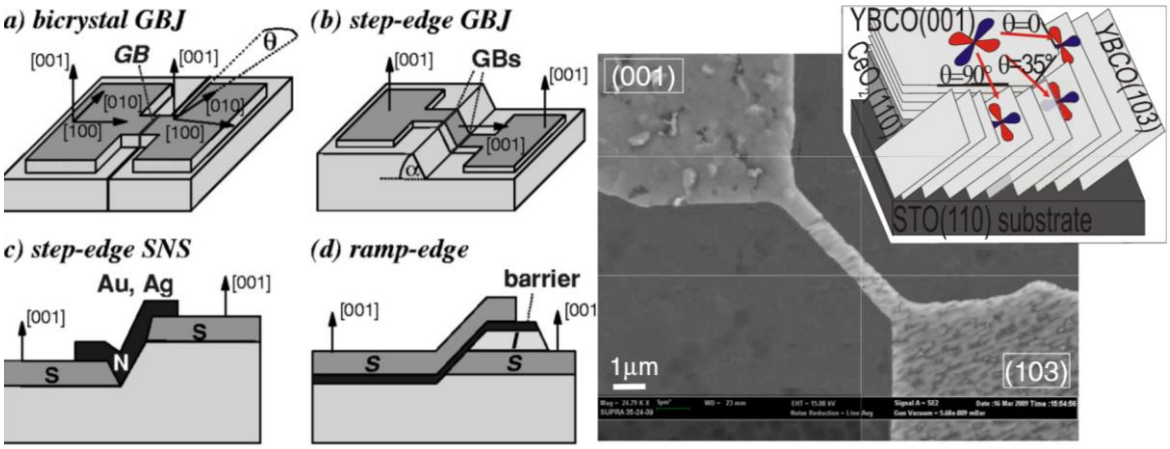

Figure I.12: Left: types of high-T_c Josephson junctions, taken from [44]; Right: SEM image of a 0.8 µm wide biepitaxial junction. The inset sketches the junction's structure. Taken from [45]

- **Interface modified junctions**: a YBCO ramp (the base electrode) is treated with Ar^+ or O^+ ions and then annealed, prior to the deposition of the top electrode. This creates barriers thick as $\sim 2-3\ nm$. Their behaviour is not well described by a S/N/S (*Superconductor / normal metal / superconductor*) model, but corresponds better to a "'*insulator / normal conductor / superconductor with a reduced critical temperature*" stack [50].

- **Junctions with an extrinsic barrier:** the barrier can also be fabricated out of another material such as a normal metal. For low-T_c superconductors, the structures of the junctions made out of an extrinsic barrier are usually "sandwich like", where an insulating layer and then a superconducting layer are deposited on top of a first superconducting layer. However, in High-T_c superconductors, the supercurrent flows in the ab plane and the coherence length in the c-axis is very small ($\xi_c \approx 0.3\ nm$) [51]. For this reason, technologies were developed to fabricate junctions in the ab-plane (in which direction the coherence length is $\xi_{ab} \approx 2\ nm$).
  - ***Step-edge*** junctions are based on the etching of a ramp in the substrate, on which the superconductor cannot grow. A metallic barrier is then deposited above the ramp, to create a link between the two superconducting plateau on both sides of the ramp.
  - ***Ramp-edge*** junctions are based on a first superconducting layer, which is covered by a thick insulator. A ramp is then etched in the structure with a small angle (10 to 20°), and a thin oxide insulator and the second superconducting electrode are grown on top of the ramp.

- **Irradiated junctions:** much more reproducible than the former technologies, the junctions based on irradiation are also less complex and better understood. They are fabricated by

irradiating small regions of a superconducting channel with ions, creating a weak link between the two sides of the channel. This technique allows to design smaller junctions, and the characteristic of the irradiation and thus of the junction can be well controlled [35], [52]–[55].

I.3 Ferroelectricity

Let us now present ferroelectric materials. They show the remarkable property of having a spontaneous electrical polarisation, which can be switched in two equivalent directions by the application of an electric field. These materials have been widely studied since the discovery of perovskite-like ferroelectric oxides (ABO_3 structure), which can reach high values of polarisation. A typical example is $BaTiO_3$, first studied in the 1950's and which widely contributed to the understanding of ferroelectricity [56].

These oxides usually have high dielectric constants – in some cases dependent on the ferroelectric state – which lead to the development of voltage-controlled capacitors. Finally, the remanent and hysteretic properties of the polarisation lead to the development of Fe-RAM (Ferroelectric Random Access Memories), faster, more durable and energy efficient than current flash memories.

I.3.1 Symmetry

Crystalline structures are sorted into thirty-two symmetry classes; among those some are not compatible with the existence of a retentive electrical polarisation: it is for example the case of the centrosymmetric structures. There are twenty-one non-centrosymmetric classes, which are all (except the 432 class) compatible with a piezoelectric effect: *i.e.* these materials are able to polarise electrically when then are mechanically solicited (compression or dilatation). The inverse piezoelectric effect manifests itself as the mechanical deformation of the material when an electric field is applied. The piezoelectric effect is for instance behind the invention of the sonar during the first world war [57], and is widely used nowadays in MEMS (electromechanical microsystems) like microengines, microvalves, accelerometers, membranes… We will see later that the piezoelectric effect is also very useful to characterise ferroelectricity.

Ferroelectricity can only occur if only one high symmetry axis exists in the crystal (it is then polar): among the twenty classes allowing the piezoelectric effect, only ten of them have this property. These materials are pyroelectric: if the temperature changes, their electric polarisation changes, which can create a difference of potential from one terminal to another. This effect is for example widely used in infrared detectors [58]. It is among the pyroelectric materials that we meet ferroelectric materials, in which the electric polarisation is retentive and can be switched between two equivalent directions by the application of an external electric field. In the same way that the magnetisation of a ferromagnet is hysteretic with respect to the applied magnetic field, the polarisation of a ferroelectric material is hysteretic with respect to the applied electric field, as represented in Figure I.13: it is because of this analogy that this property is called "ferro"electricity.

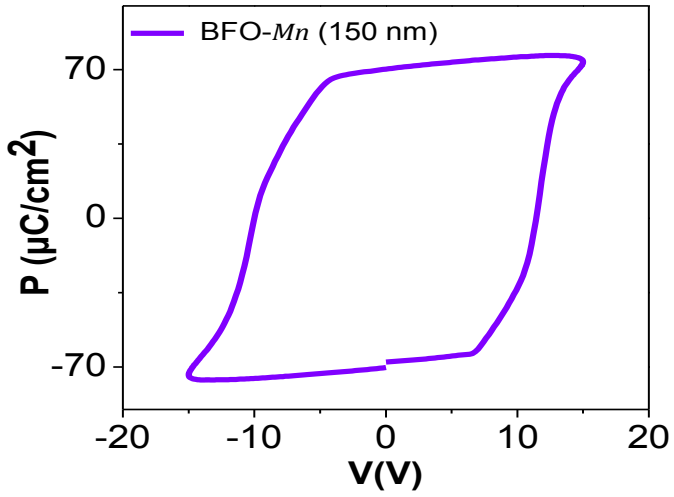

Figure I.13: Ferroelectric cycle: polarisation of a $150\ nm$ thick BFO-Mn film as a function of the applied electric field

Nevertheless, ferroelectric materials undergo a transition from the ordered, ferroelectric phase to a paraelectric phase above a certain temperature (again, by analogy, called « Curie » temperature). In this phase, the material is still able to polarise when an electric field is applied, but it is not retentive: there is no hysteretic cycle like in the ferroelectric phase.

I.3.2 Mechanisms of ferroelectricity

There are two families of ferroelectric materials, which differ by the nature of their paraelectric/ferroelectric transition. In the first case, a polarisation at the cell-scale exists above Curie temperature, but its direction is random and the mean polarisation is zero when no electric field is applied. When the temperature gets lower, a disorder-order transition occurs and it gets more energetically favourable for the dipoles to get aligned in the same direction and the same orientation than their closest neighbours: the polarisation gets coherent at macroscopic scales [59],[60].

In the other case, the paraelectric phase is cubic and the barycentres of the negative and positive charges are merged. When the so-called “distortive” transition occurs, the cell gets distorted and the barycentre of the negative charges (*i.e.* in the perovskites, the centre of the octahedron formed by the oxygen atoms [61]) separates from the barycentre of the positive charges (in perovskites, carried by the metallic ion), giving rise to a dipolar momentum in the cell. Figure I.14 *c)* schematizes this mechanism for a $BaTiO_3$ cell, which is a prototypical ferroelectric: the Ti atom and the oxygen octahedron displace along the c axis but not in the same direction. The two cases (Ti upwards and O downwards or the opposite) are energetically equivalent. The distortion is identical for a certain amount of close cells, *i.e.* the metallic ion displaces in the same direction with respect to the oxygen octahedron: a large-scale coherent polarisation is then created. More precisely, in the paraelectric phase, short range repulsive forces between the ions favour a cubic lattice. When the temperature decreases, the atomic vibrations are smaller and these short-scale repulsions are compensated by long-scale Coulomb interactions between the dipoles present in the lattice [62]. In this regime, the ions vibrate around positions different from their original position in the cubic lattice. Two equivalent potential wells exist for the energy of the ferroelectric domains, corresponding to two positions for the barycentre of the charges in the lattice, and at two opposite directions for the polarisation (see Figure I.14 *a)* and *b)*).

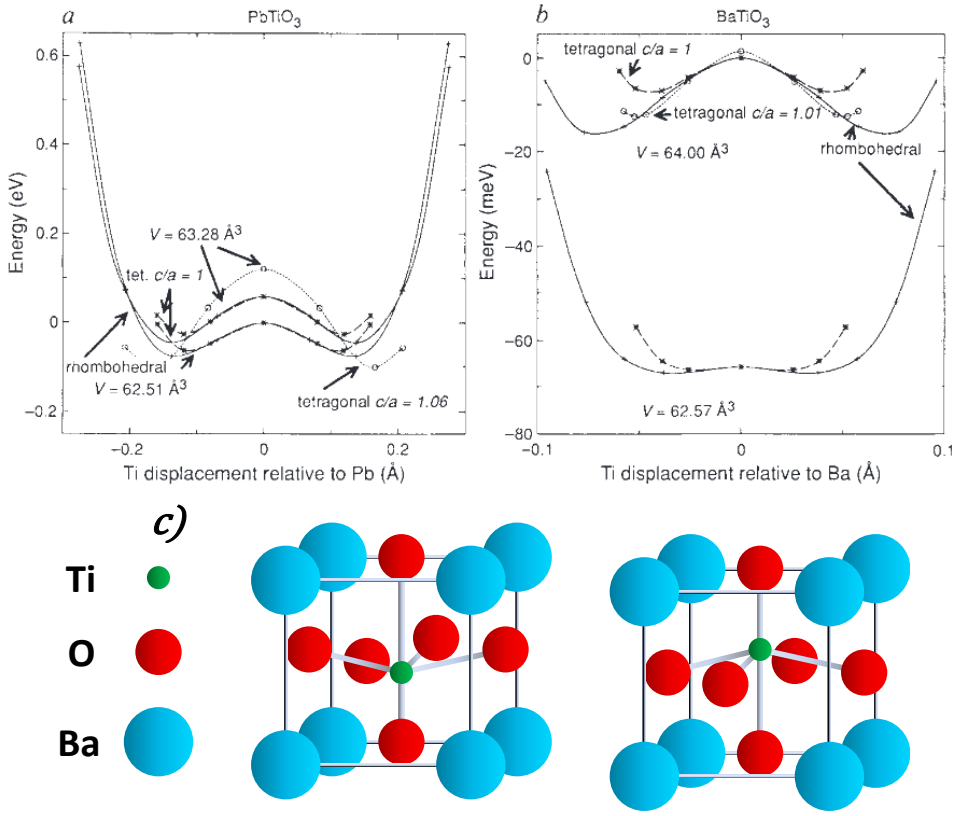

Figure I.14: Calculated energy as a function of soft-mode distortion for a) $PbTiO_3$ and b) $BaTiO_3$ [61]. c) Schematic representation of $BaTiO_3$ unit cell for the two directions of polarisation

In perovskites, competition between short range ionic restoring forces and long range Coulomb interactions is not enough to stabilise the distortion of the lattice and the ferroelectricity. An electronic reconstruction also happens in the lattice: it mainly consists in a hybridation between the empty d orbitals of the transition metal ("B" site) that displaced into the lattice, and the $2p$ orbitals of the neighbouring oxygen atoms. In some cases, when the electronic configuration of A site atoms presents $2s$ orbitals (such as Bi or Pb), hybridation can also occur with the p orbitals of oxygen, stabilising ferroelectricity.

I.3.3 Conduction through ferroelectric oxides

Ferroelectric materials are insulators. However, many conduction mechanisms can occur inside them (leakage currents), making the measurements of the polarisation difficult. Three main mechanisms are met in perovskite oxides:

- The Schottky emission: when the voltage applied across the ferroelectric is high enough for the electrons to go through the potential barrier at the interface, they can be injected in the ferroelectric. It is thus an interface effect, and the Schottky current is given by [63]:

$$J_s = AT^2 exp - \left[\frac{\Phi}{k_B T} - \frac{1}{k_B T}\left(\frac{q^3 V}{4\pi\epsilon_0\epsilon_r t}\right)^{1/2}\right] \quad \text{(I.84)}$$

where A is the Richardson constant, T the temperature, k_B the Boltzmann constant, Φ the height of the Schottky barrier, q the charge of the electron, ϵ_0 the permittivity of the free space, ϵ_r the dielectric constant of the ferroelectric and t its thickness.

- The conductive properties of the ferroelectric can locally change when the number of electrons injected into the material becomes larger than the transport itself: a zone of space charges is then created and with μ the carriers' mobility in the ferroelectric, the current varies as [64]:

$$J_{SCLC} = \frac{9\mu\epsilon_0\epsilon_r}{8}\frac{V^2}{t^3} \quad \text{(I.85)}$$

- The Poole-Frenkel emission: in ferroelectrics that present electrical defects such as Fe^{2+} ions in oxygen deficient $BiFeO_3$, the electrons can hop from an electrical trap to another. It is a thermal activated phenomenon, which is also activated with the applied tension. It is given as a function of the ionisation energy E_I of the traps by:

$$J_{PF} = cV\ exp - \left[\frac{E_I}{k_BT} - \frac{1}{k_BT}\left(\frac{q^3V}{4\pi\epsilon_0\epsilon_r t}\right)^{1/2}\right] \quad \text{(I.86)}$$

I.3.4 Ferroelectricity in thin films

Ferroelectricity is a cooperative phenomenon of long range interactions, which can only exist in a volume that is big enough. The study of perovskites and the theories of continuous medium showed that below a few nanometres, ferroelectricity disappears, eventually replaced by an antiferroelectric order [65]. This theoretical limit evolved during the XXth century, it was several hundreds of nanometres in 1972 for triglycine sulfate films [66]. The observed critical thicknesses dropped since then, as the fabrication techniques and the quality of the thin films improved.

I.3.4. a) Influence of the strain

When a thin film of a ferroelectric material is grown on a substrate whose lattice parameters differ from the lattice parameters of the bulk ferroelectric, a strain is induced in the film. This strain is compressive when the final lattice parameters of the film are smaller than the bulk and tensile when it is bigger. In epitaxial thin films, the strain is biaxial in the ab plane. The strain strongly influences the ferroelectricity in thin films. It can result in bigger values of polarisation compared to the bulk [67], [68], change the mechanisms of ferroelectricity [69], and maintain ferroelectricity in films as thick as few unit-cells [70], [71]. The case of bismuth ferrite ($BiFeO_3$) is detailed in section I.4.4. b).

I.3.4. b) Critical thickness

The coercive field E_c needed to reverse the polarisation of a ferroelectric film empirically increases when the film thickness d decreases. For thicknesses in the range $100\ nm \sim 100\ \mu m$, a semi-empirical scaling law describes the evolution of the coercive field [72]–[74]: $E_c\ (t) \propto d^{-2/3}$. This scaling does not take into account that when the polarisation charges $\rho = -\mathrm{div}\ \vec{P}$ are not perfectly compensated by free charge carriers, a depolarisation potential arises across the film [75], due to the accumulation of screening charges at the interface. This accumulation occurs over a distance λ_{eff}, typically $0{,}07\ nm$ in Au and $1\ nm$ in an oxide like lanthanum strontium manganite.

Let us consider a $M_1/FE/M_2$ junction where M_1 and M_2 are metal electrodes of Thomas-Fermi screening lengths δ_1 and δ_2, and FE is a ferroelectric film of thickness d. The z axis is taken perpendicular to the surface of the ferroelectric film, like shown in Figure I.15. For a film of thickness d comprised between two electrodes parallel to the z axis, of screening length δ_1 and δ_2 and dielectric constants ε_1 and ε_2, in a free-electron model the potential within the electrodes is related to the density of charges σ_S by a Thomas-Fermi distribution, as in Figure I.15 *a)* [76]:

$$\varphi(z) = \begin{cases} \dfrac{\sigma_S \delta_1 e^{-|z|/\delta_1}}{\varepsilon_0} & z \leq 0 \\ -\dfrac{\sigma_S \delta_2 e^{-|z-d|/\delta_2}}{\varepsilon_0} & z \geq d \end{cases} \tag{I.87}$$

According to the charge conservation condition σ_S is the same in the two electrodes. Assuming that the electric field due to the voltage drop is constant in the ferroelectric: $\varphi(d) - \varphi(0) = E \times d$, and according to the continuity of the displacement field: $\varepsilon_F E + P - \sigma_S = 0$, we obtain:

$$\varphi(0) - \varphi(d) = \frac{(P - \sigma_S)d}{\varepsilon_F} \tag{I.88}$$

where P is the absolute value of the spontaneous polarisation, and ε_F is the dielectric permittivity of the ferroelectric film. Combining equations (I.87) and (I.88), we express the screening charge density as:

$$\sigma_S = \frac{d \times P}{\varepsilon(\delta_1 + \delta_2) + d} \tag{I.89}$$

with $\varepsilon = \varepsilon_F/\varepsilon_0$ the dielectric constant of the film. When the electrodes are bad metals (large screening lengths) and when the thickness decreases, $\frac{\varepsilon(\delta_1+\delta_2)}{d} \gg 1$: from equation (I.89), in this limit σ_S tends to zero, meanwhile Shaw *et al.* [77] have shown that the depolarising field $\vec{E}$, represented in Figure I.15. *b)*, increases to saturation at $-\vec{P}/\varepsilon$. This increase might lead to the instability of the out-of-plane polarisation in ultra-thin ferroelectric films, which disappears underneath a critical thickness [78].

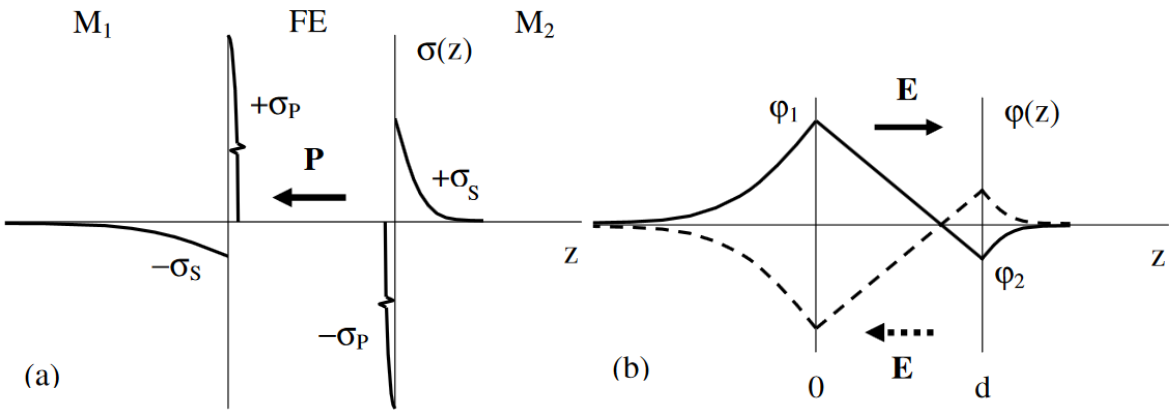

Figure I.15: a) Charge distribution and b) Electrostatic potential profiles for a metal/ferroelectric/metal capacitor, taken from [76]

I.3.4. c) Electrostatic potential across a ferroelectric film

Another consequence of the depolarising field introduced in the previous paragraph is that if the two electrodes are different – if they have different screening lengths – the electrostatic potential across the barrier is strongly asymmetric, as represented in Figure I.15 *b)*, the solid line represents the depolarising field for one direction of the polarisation, and the dash line for the other direction.

One consequence of this asymmetry is that in the case of a ferroelectric tunnel junction (FTJ), the height of the barrier and thus its resistance are different depending of the direction of the polarisation. This situation is represented in Figure I.16 taken from [79]: if we consider a barrier of an initial rectangular shape of height U with respect to the Fermi energy, the potential due to the screening will modify the profile of the barrier according to equations (I.87). The average height Φ_+ (resp. Φ_-) of the barrier when the polarisation points towards the left (resp. the right) becomes:

$$\Phi_+ = U + \frac{|\varphi(d)| - |\varphi(0)|}{2}$$
$$\Phi_- = U + \frac{|\varphi(0)| - |\varphi(d)|}{2} \quad \text{(I.90)}$$

The shift in the average height is thus:

$$\Phi_+ - \Phi_- = |\varphi(d)| - |\varphi(0)| = \frac{\sigma_S(\delta_2 - \delta_1)}{\varepsilon_0} \quad \text{(I.91)}$$

This change in the barrier height induces a change in the resistivity of the barrier, a phenomenon known as Tunnelling ElectroResistance (TER). OFF/ON resistance ratio can reach several hundreds in these metal-electrode based ferroelectric tunnel junctions [80], [81].

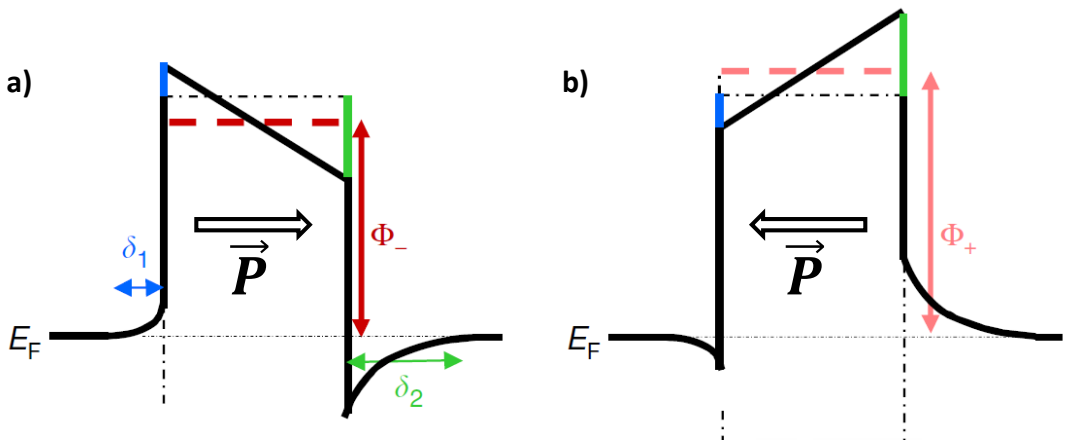

Figure I.16: Representation of the potential energy profile of a metal-ferroelectric-metal barrier with asymmetric electrodes for the polarisation pointing towards a) the left; b) the right, taken from [79]

I.3.4. d) Interface effects

The substrate used for the growth of ferroelectric thin films and the nature of the top-electrode influence the ferroelectric properties of the film. Even if the electrodes are metallic and perfectly screen the charges, a dielectric gap can exist at the interface between the electrode and the ferroelectric, generating a depolarising field [68]. It can be due to the bad quality of the interface or to its chemistry. The polarisation in an ultra-thin film may also be affected by interface effects between the film and the electrodes, either because of dipole-dipole interactions, or by short-range interactions between the closest atomic layers [82].

The chemistry of the interface also plays a role in the way the charges can be injected in the ferroelectric material when a voltage is applied. As mentioned in section I.3.3, interfaces can strongly influence the conduction inside the material. These effects are well illustrated by Figure I.17, taken from [68]. Polarisation loops (in blue) and leakage currents (in red) of a $BiFeO_3$-Mn film sandwiched between different electrodes are represented. Figure I.17 *a)* and *b)* represent the measurement for the same film grown on two different bottom electrodes: a) Lanthanum strontium manganite and b) strontium oxide, with the same top electrode (gold).

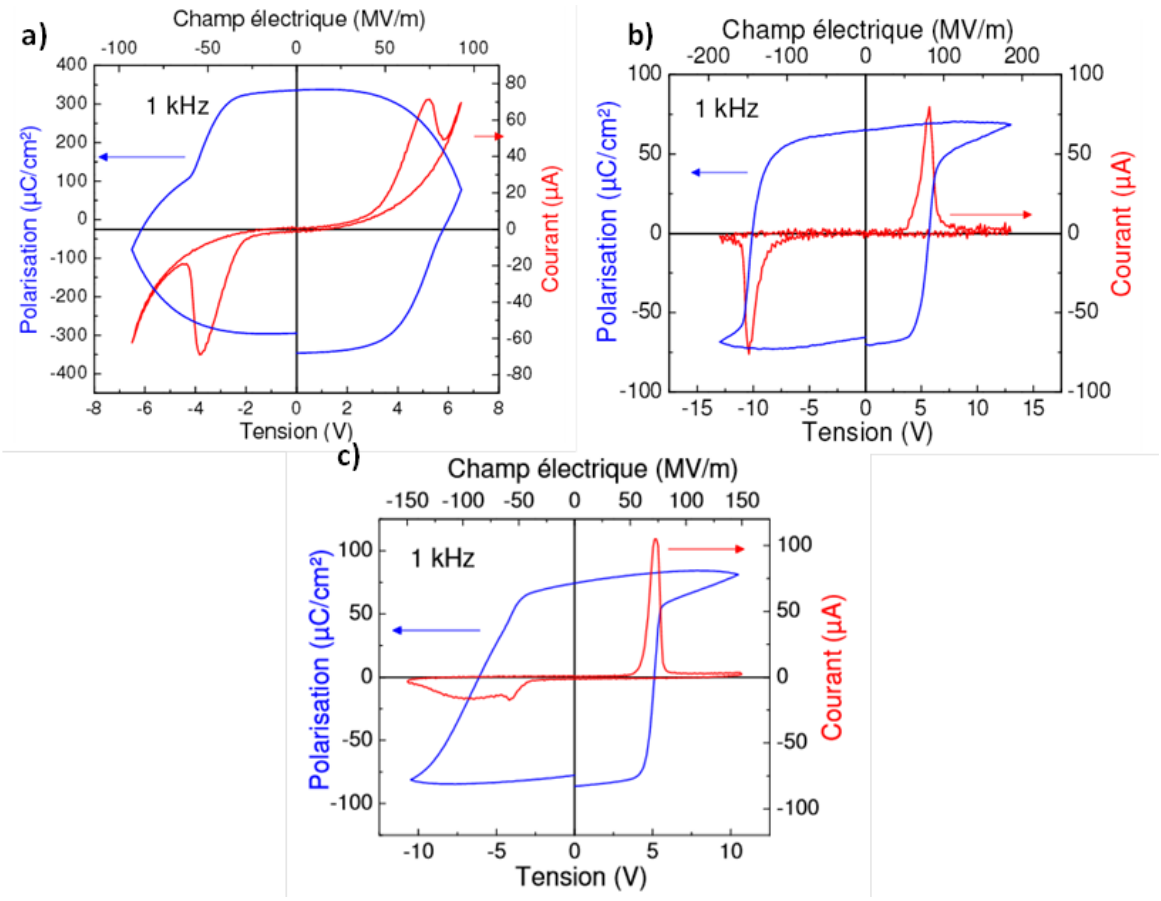

Figure I.17: Taken from [68] ferroelectric loops in current and in polarisation for a) *BFO-Mn(70 nm)/LSMO//STO(001)* with *Au* top electrode, b*) BFO-Mn(70 nm)/SRO//STO(001)* with *Au* top electrode c) *BFO-Mn(70 nm)/SRO//STO(001)* with *CoFeB* top electrode

Both the $BiFeO_3$-Mn film and the bottom electrodes are strained by the same substrate, $SrTiO_3$ (001). We can see that the value of the polarisation, the shape of the cycle and the conduction

through the film are very different depending on the bottom electrode. Similarly, Figure I.17 *b)* and *c)* represent the measurements for the same heterostructure (BFO-$Mn(70\ \mathrm{nm})$/SRO//STO(001)) coated with gold: *b)* or $CoFeB$: *c)*). Again, the properties of the film are very different from one structure to the other.

I.4 Materials

We will now present the different materials used during this thesis. Most of them are perovskite oxides. The name « perovskite » initially refers to calcium titanate, $CaTiO_3$; by extension, it refers to all "ABX_3" crystals, where A and B are cations and X are anions. B cations are small, and are localised in octahedrons formed by X anions. Bigger A cations are localised between these octahedrons. Depending on the size of the atoms, the octahedrons are more or less distorted and the interatomic distances as well as the angles between the bonds vary. This can confer electronic, magnetic, etc. properties to the perovskite.

I.4.1 $SrTiO_3$

As a substrate to grow the films studied in this thesis, we principally used strontium titanate (STO), which is a paraelectric insulator with a perovskite structure. It is cubic at room temperature, with lattice parameters $a = b = c = 0{,}3905\ nm$. It undergoes a structural phase transition at $105\ \mathrm{K}$ where it becomes tetragonal with a ratio $c/a = 1.00056$, and another one at $65\ \mathrm{K}$ where it becomes orthorhombic ($c/b = 1.0002$ and $c/a = 0.9998$).

I.4.2 $PrBa_2Cu_3O_{7-\delta}$

$PrBa_2Cu_3O_{7-\delta}$ (PBCO) is the only member of the family of $(RE)Ba_2Cu_3O_{7-\delta}$ – where (RE) is a rare-earth element – that does not present a superconducting transition whatever his doping in oxygen is. It is tetragonal for $\delta > 0{,}4$, with $a = b = 0{,}391\ nm$ and $c = 1{,}185\ nm$. It is orthorhombic for $\delta < 0{,}4$, with $a = 0{,}390\ nm$, $b = 0{,}392\ nm$ and $c = 1{,}171\ nm$.

I.4.3 $YBa_2Cu_3O_{7-\delta}$

Yttrium barium copper oxide (YBCO) has a perovskite-like structure; its unit cell is composed of three oxygen-deficient perovskite cells: a $CuYO_2$ cell between two $CuBaO_2$ or $CuBaO_{2.5}$ cells. Two formulae are thus possible for the YBCO cell: $YBa_2Cu_3O_7$ and $YBa_2Cu_3O_6$. In practice, depending on the growth conditions of the material, we meet both kind of cells in the material, and define its formula as "$YBa_2Cu_3O_{7-\delta}$" where δ is the deficit of oxygen with respect to: $YBa_2Cu_3O_7$. Figure I.18 describes the different formulae for the $YBaCuO$ cell.

Two CuO_2 plans thus exist planar to the (001) direction, separated by a plan only containing Yttrium atoms. These double CuO_2 planes have a key role for the superconductivity in cuprates, though the exact mechanisms are not well understood. The transition ions Cu^{2+} have a unique charge carrier on a d orbital: transferring an electron from a $Cu^{2+}$to another is very difficult, but the covalence is very strong with O^{2-} ions in the CuO_2 planes [84]. For small doping in oxygen ($\delta > 0.63$), the strong Coulomb repulsions between the Cu^{2+} ions freeze the electrons and the YBCO behaves as an antiferromagnetic "Mott" insulator. For higher oxygen concentrations (thus higher holes concentrations), the superconducting state appears.

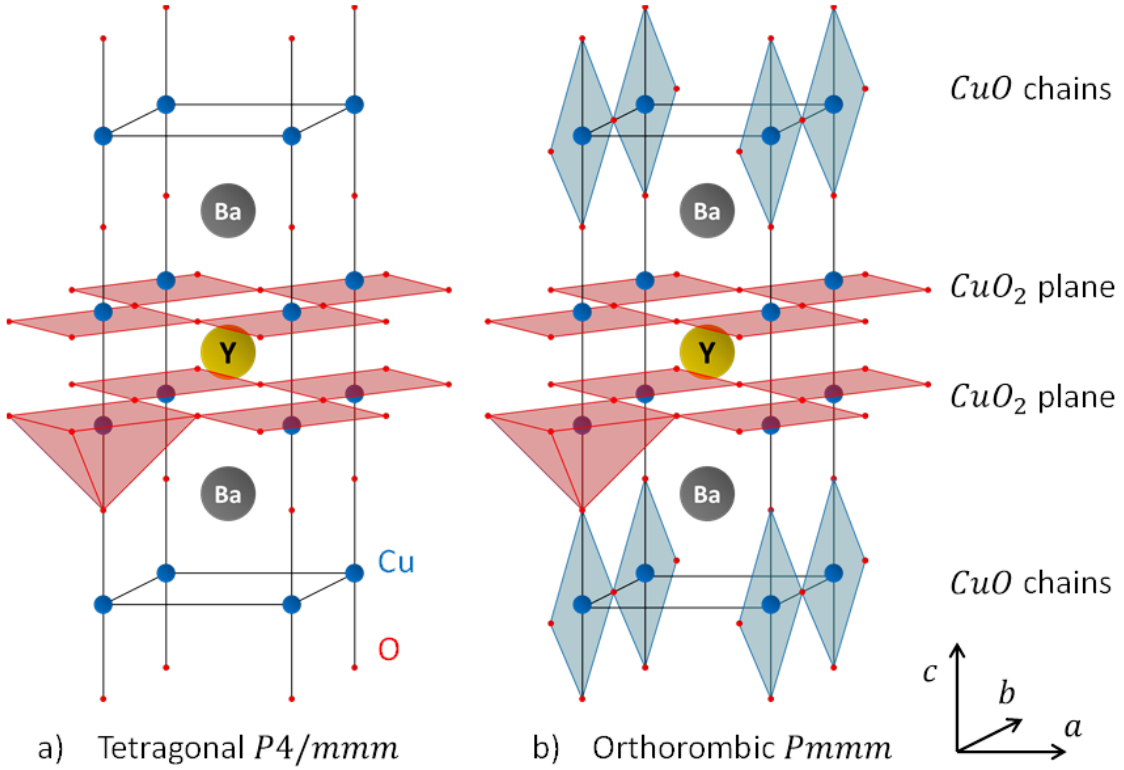

Figure I.18: The oxygen deficient perovskite structures for $YBa_2Cu_3O_{7-\delta}$ system with oxygen content: a) δ = 6; b) δ = 7

The superconducting current essentially occurs in the ab CuO_2 planes: the electronic properties and the superconducting gap are highly anisotropic. The coherence length λ and penetration depths ξ are very different along the c axis and along the a and b axes (see table I.4.1, data taken from [85]).

YBCO ($T = 0K$)	c	ab
λ (nm)	890	135
ξ (nm)	0.24	1.6

Table I.4.1: Coherence length λ and penetration depth ξ for bulk YBCO at T = 0 K

In the case of YBCO, the planes containing the CuO chains act like charge reservoirs, as the oxygen atoms between CuO_2 planes and CuO chains get ionised and attract the electrons from the CuO_2 planes [84]. It causes an indirect doping of holes in these planes, modifying the superconducting properties of the material: the critical temperature of YBCO is maximum (92 K) for $\delta = 0.08$ [86], [87]. With this stoichiometry, its structure is orthorhombic and belongs to the space group $Pmmm$. The lattice parameters are $a = 3.8227$ Å, $b = 3.8872$ Å and $c = 11.6802$ Å.

I.4.4 $BiFeO_3$

Bismuth ferrite ($BiFeO_3$, BFO) is a perovskite that raises a lot of interest, first because it is multiferroic at room temperature (it is both ferroelectric and antiferromagnetic), but also because it shows a very high remanent polarisation. The lattice of bulk bismuth ferrite is rhombohedral, slightly elongated in the $[111]$ pseudo-cubic diagonal, as represented in Figure I.19. The oxygen octahedron

(the barycentre of the negative charges) displaces itself along this direction, leading to a ferroelectric order. The Curie temperature for the ferroelectric order is very high (above $800°C$), and the polarisation in the $[111]$ direction can reach $100\ \mu C/cm^2$ in a high-quality crystal [88]. The Néel temperature for the G-type antiferromagnetic order is much lower (around $370°C$); these two properties are coupled, and the electric polarisation can eventually be enhanced in the presence of a magnetic field [89].

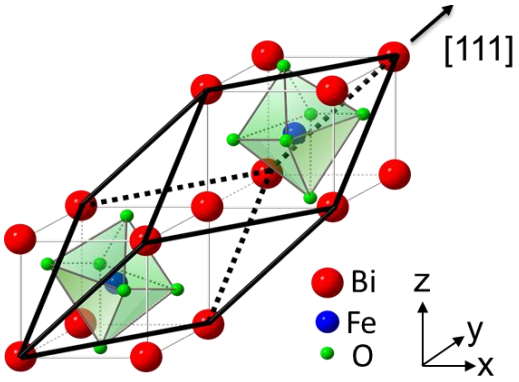

Figure I.19: Pseudo-cubic bulk bismuth ferrite lattice

I.4.4. a) Mechanisms of ferroelectricity in $BiFeO_3$

The coexistence of ferroelectricity and antiferromagnetism in $BiFeO_3$ is only possible thanks to an unusual mechanism for ferroelectricity. In most of ferroelectric perovskites, there is a hybridation between empty d-orbitals of the transition metal atom and filled p-orbitals of the oxygen atoms, in order to stabilise the system. In the case of $BiFeO_3$, the oxygen cannot hybridise with the d orbitals of Fe atoms because they are not empty (which allows the antiferromagnetic order to exist). Instead, the p orbitals of oxygen hybridise with Fe $6s$ orbitals (filled or empty) [90]. Thanks to this hybridation, the Bi-O link is partially covalent, which turns the $6s$ orbital of Bi anisotropic. It repulses the neighbouring electronic clouds, and distorts the lattice in the $[111]$ direction. Thin films of bismuth ferrite exhibit a rhombohedric or a monoclinic lattice, with an angle of distortion that is close to bulk $BiFeO_3$ ($0.7°$), and the same direction for the polarisation (the $[111]$ diagonal). A highly distorted phase of $BiFeO_3$ ("super tetragonal phase" or T-phase) was also observed [91]. This highly distorted phase differs from the intermediate one as the oxygen rotations are only allowed around the a an b axis and not in the three axes (see Figure I.20). The polarisation in thin films is rather hard to measure, since this material is very leaky. Leakage currents can be reduced by replacing a small percentage of Bi atoms with Nd or La, or Fe atoms with Mn, Ti or Cr. X-PEEM studies [92] showed that magneto-electric coupling still exists in thin $BiFeO_3$ films.

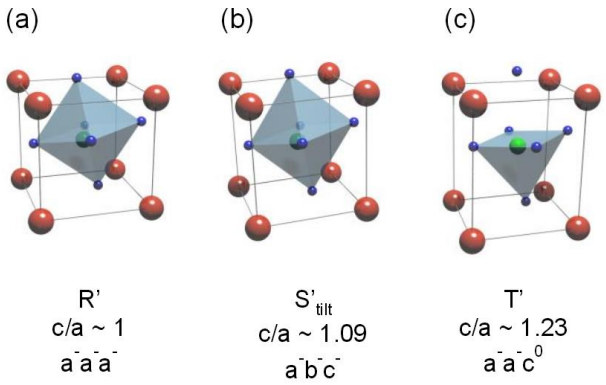

Figure I.20: a) Rhombohedral, b) intermediate tilted and c) super-tetragonal phases of BiFeO3, taken from [69]

I.4.4. b) Influence of strain

Ederer et al. [93], [94] calculated the influence of an epitaxial, mechanic strain on the magnetic and ferroelectric properties of BFO. Both theory and observation [95] show that in $R3c$ or $P4mm$ films, the mismatch did not have a big influence on the value of the polarisation in BFO. They observed that the $P4mm$ phase exhibits much bigger values of polarisation than the $R3c$ phase. The lattice parameters for the pseudo-cubic cell are $a_C = 3.96$ Å and $\alpha_C = 89.4°$, whereas the calculation gives $a_{T1} = 3.665$ Å and $c_{T1} = 4.65455$ Å for the intermediate tilted phase [93], and $a_{T2} = 3.7859$ Å and $c_{T2} = 4.8525$ Å for the super-tetragonal phase [90]. The lattice mismatch with $SrTiO_3$ (001) is given by:

	R3c: a_C=3.96 Å	*P4mm*: a_{T1}=3.665 Å	*P4mm*: a_{T2}=3.7859 Å
STO: a_C=3.905 Å	1.4	-6.1	-3.05

Table I.4.2: Lattice mismatch of different BFO phases on STO.

A complete review on BFO was made by D. Sando *et al.* [69], reporting the different lattice constants observed in the literature until then (see Figure I.21).

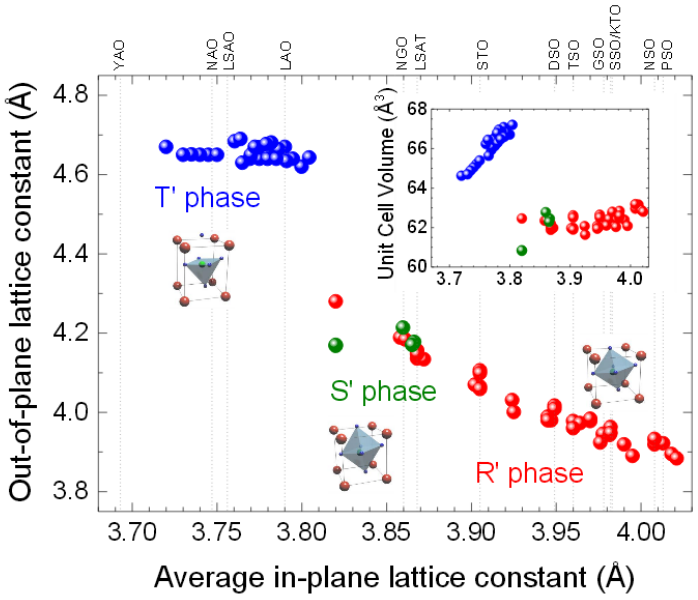

Figure I.21: Lattice constants of $BiFeO_3$ thin films collected from published data, taken from [69]

I.4.5 $La_{1-x}Sr_xMnO_3$

Lanthanum strontium manganite (LSMO) is a strongly correlated oxide that exhibits unique magnetic and electronic behaviours: colossal magneto-resistance (CMR), spin-charge-orbital ordering, spin polarisation [96]… It has a perovskite crystal structure, with lanthanum atoms (occupying the "A" sites) partially substituted by strontium atoms. Lanthanum atoms have a valence $3+$, whereas strontium has a valence $2+$: this substitution, or doping, introduces extra holes in the valence band of this oxide and modify its properties. Its phase diagram is very rich: it is represented in Figure I.22 *a)*, taken from [97], where $AFM,\ PM,\ PI,\ FM,\ FI$ and CI denote anti-ferromagnetic metal, paramagnetic metal, paramagnetic insulator, ferromagnetic metal, ferromagnetic insulator and spin canted insulator states. $La_{1-x}Sr_xMnO_3$ has a ferromagnetic metallic behaviour in the range $0{,}1 < x < 0{,}5$, and the Curie temperature is maximal (370 K) for $x = 1/3$ [98]. LSMO is rhombohedral, with lattice parameters $\alpha = 90{,}26°$ and $a = 0{,}388\ nm$.

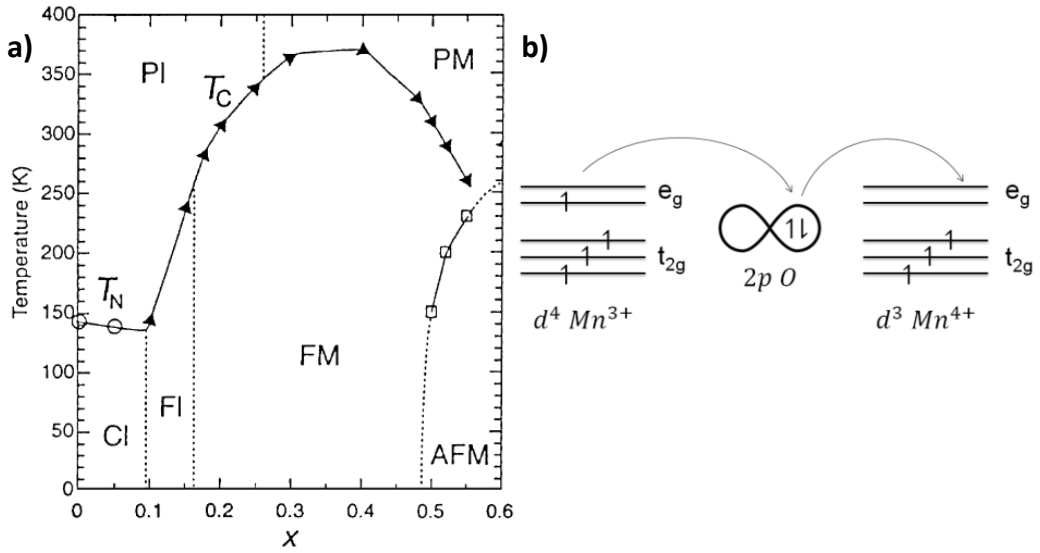

Figure I.22: a) Phase diagram of LSMO, taken from [97]. b) Principle of the double-exchange

Because of the doping, a fraction of the Mn atoms has a valence $+3$ and the others a valence $+4$. In 1951, a mechanism was proposed y Zener *et al.* to explain how a magnetic exchange could occur between Mn^{3+} and Mn^{4+} ions [99], thanks to the presence of oxygen atoms and their Mn-O-Mn $180°$ alignment. In his theory, schematized in Figure I.22 *b)*, a spin from the O $2\mathrm{p}$ orbital hops into a vacant e_g orbital of an Mn^{4+} ion. The O $2\mathrm{p}$ orbital can then be filled by a spin of the same orientation from the e_g of an Mn^{3+} ion. At the end, a spin was transferred from Mn^{3+} to Mn^{4+}.

I.4.6 $Mo_{1-x}Si_x$

Molybdenum Silicide ($Mo_{1-x}Si_x$) is an amorphous superconductor in the range $x > 15{\sim}20\%$. Its maximal critical temperature ($T_c \sim 9\ K$) [8] is one of the highest among other amorphous superconductors [100]. Figure I.23 represents the T_c as a function of the Si and Ge doping for $50\ nm$ and $200\ nm$ Mo based films grown by RF magnetron sputtering, taken from [100]. The solid straight line refers to the results of Edelstein *et al.* [101] and T_c value for pure Mo is reported by Kimhi and Geballe for a nitrogen stabilised a-Mo film [102].

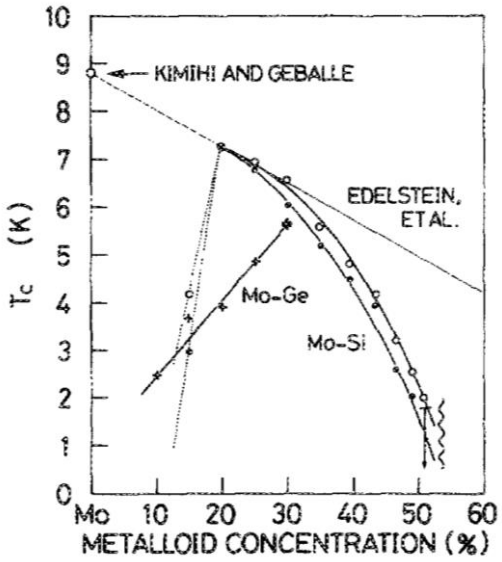

Figure I.23: Critical temperature dependencies on metalloid concentration, taken from [100]. Open symbols: $200\ nm$ films; closed symbols: $50\ nm$ films. The solid straight line refers to the results of Edelstein et al. [101] and T_c value for pure Mo is reported by Kimhi and Geballe for a nitrogen stabilised a-Mo film.

In the following chapters, STO will refer to $SrTiO_3$, BFO to $BiFeO_3$ and BFO-Mn to $BiFeO_3$ doped with 5% of Mn, PBCO will refer to $PrBa_2Cu_3O_{7-\delta}$, and YBCO to $YBa_2Cu_3O_{7-\delta}$, LSMO to $La_{2/3}Sr_{1/3}MnO_3$ and MoSi to $Mo_{0.82}Si_{0.18}$.

II. Field-effects in correlated oxides

Index

II. Field-effects in correlated oxides 37

II.1 Field-Effect Transistors 38

II.1.1 Principle of the Field-Effect Transistor 38

II.1.2 Electric penetration depth and carrier modulation 39

II.1.3 Oxides field-effect transistors technologies 40

II.2 Electrostatic tuning of correlated oxides 42

II.2.1 Field-Effect in Colossal-Magneto-Resistance Manganites 42

II.2.2 Ferroelectric field-effect transistor: a prototypical model 44

II.3 Electrostatic tuning of high-T_c superconductors 47

II.3.1 Field-effect and penetration length 47

II.3.2 Field-Effect Transistors 48

II.3.3 Electric Double Layer Transistors 49

II.3.4 Ferroelectric Field-Effect Transistors 49

II.4 Some functionalities of field-effect 51

II.4.1 Local manipulation of field-effect 51

II.4.2 Tunable Josephson junctions 53

II.4.3 Ferroelectric tunnel junctions 54

The richness of many complex oxides phase diagram (among which we find high-T_c superconductors, half-metallic ferromagnets, Mott insulators, etc.) is due to strong electronic correlations. These result, for example, from the competition between carrier localisation (due to Coulomb repulsion) and hopping (due to the kinetic energy). Electronic correlations can be tuned by changing the structure of the material [103], or by changing the carrier density. This can be done either by chemical substitution, either by electrostatic tuning, which presents the advantage of changing the number of carriers without adding any disorder in the material [103], [104]. In this chapter, we provide an introduction to the field-effects in strongly correlated oxides, with focus on the materials, approaches and early works more closely related with the work presented in this thesis.

II.1 Field-Effect Transistors

II.1.1 Principle of the Field-Effect Transistor

Electrostatic tuning is the keystone of Field-Effect Transistors (FET), which are widely used in nowadays technologies, along with other components such as resistors, capacitors, diodes... Their main application is the amplification of both analogic and digital signals. The principle, described on Figure II.1, is the following: a channel connected to two electrodes (the source and the drain) is coated by an insulating dielectric film and a gate. This channel is made out of a *n*-type or a *p*-type conductor. When a voltage is applied between the gate and the source, charges accumulate in the channel, close to the interface with the dielectric. If the accumulated charges contribute to the conduction in the material (for example electrons in an *n*-doped semiconductor), the channel is conducting and the current flows through it. In the other case, if the carriers are depleted in the channel, the conductivity of the latter is decreased.

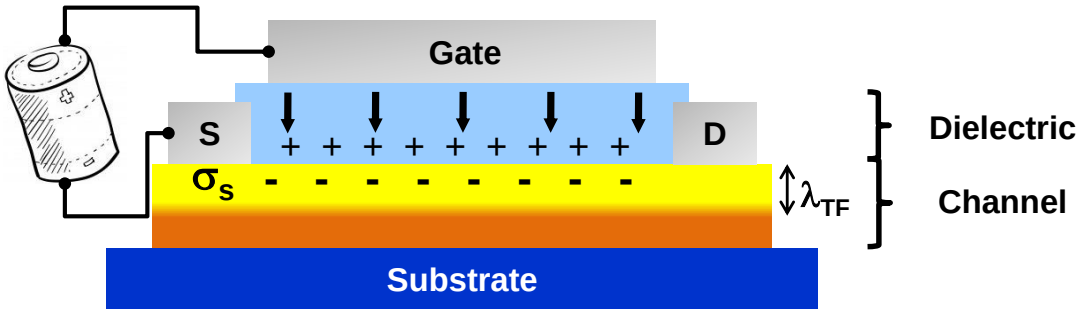

Figure II.1: Principle of a field-effect transistor. S: Source, D: Drain.

In the case of a strongly correlated oxide channel, the carrier density modulation will not only change its conductivity, but also its ground state. Figure II.2, taken from [105], shows a few examples of materials that show this type of behaviour. One can see, for instance, that Colossal Magneto-Resistance (CMR) manganites will undergo a phase transition between insulating/antiferromagnetic

and half-metallic/ferromagnetic phases upon sheet carrier density modulations of the order of 10^{13} to 10^{14} electrons per cm^2. This modulation amplitude is also sufficient to switch high-T_c cuprates between superconducting and insulator phases. Other lower carrier concentration oxides, such as $SrTiO_3$, will undergo similar phase transitions as a response to even weaker carrier density modulations. The strong sensitivity of strongly correlated oxides functionalities to the carrier density modulation opens interesting possibilities. We detail below the related physics, and the different approaches used to produce these effects.

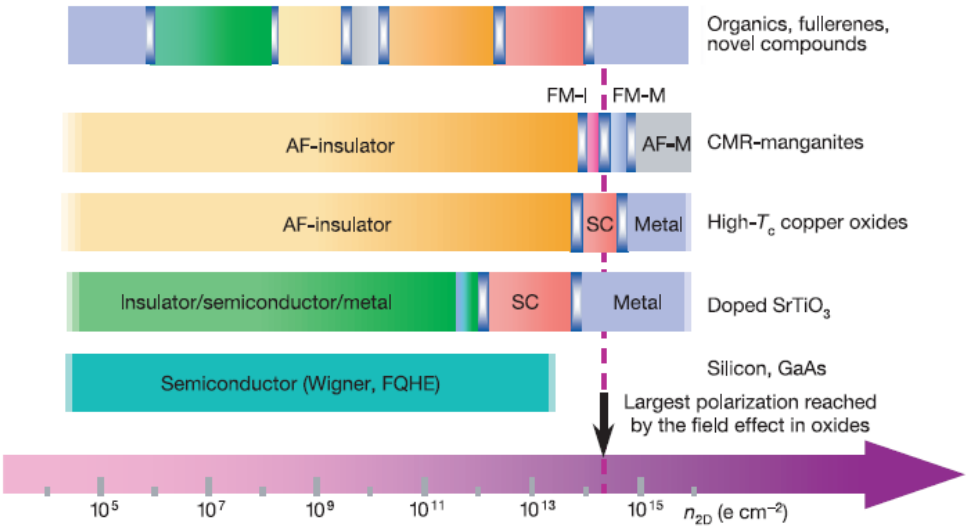

Figure II.2: Phase diagram of common compounds [105]

II.1.2 Electric penetration depth and carrier modulation

As schematized on Figure II.1, the modulation of the carrier density when a voltage is applied across the dielectric only occurs over a certain distance. For small depletions, the carrier density decays exponentially inside the conductor as described in a Thomas-Fermi approach [106] with a characteristic length λ_{TF} equal to the electric penetration depth:

$$\lambda_{TF} = \left(\varepsilon_s\varepsilon_0 / e^2 n_{eff}\right)^{1/2} \qquad \text{(III.1)}$$

where ε_s and ε_0 are the dielectric constants of the superconductor and the vacuum, e the elementary charge, and n_{eff} the effective density of electrons that screens the applied field. Correlated oxides have carrier density in the range of 10^{19}~10^{22} carriers/cm^3, intermediate between those of conventional metals and usual semiconductors. The electric penetration depth is nanometric in these materials.

This raises two main issues regarding the fabrication of FETs:

- **The thickness of the channel has to be comparable to the electric penetration depth;**
- **In order to achieve large carrier modulation, the areal charge density σ_S induced by the gate voltage has to be high (typically above 10^{13} carriers/cm^2).**

II.1.3 Oxides field-effect transistors technologies

The areal charge density σ_S – or polarisation – that can be induced across a dielectric gate is given by:

$$\sigma_S = \int_O^{V_G} \varepsilon_r \, \varepsilon_0(V)/t \, \mathrm{d}V \qquad \text{(III.2)}$$

where V_G is the gate voltage, ε_r and ε_0 are the dielectric constants of the dielectric and the vacuum, and t is the thickness of the dielectric.

High-permittivity dielectrics: To achieve large areal charge density, a simple way is thus to increase the gate voltage. However, this is limited by the breakdown field of the dielectric, which is typically $10^6\ V/cm^2$ for the universal gate dielectric SiO_2. Thus, dielectrics with high permittivity are preferred, such as $SrTiO_3$ (STO) that has the advantage of being a possible substrate for many oxides. An example of such a transistor is represented in Figure II.3, where the STO is both the substrate and the dielectric gate [107]. In this transistor, its thickness is reduced to $\sim 100\ \mu m$ and it is coated with a gold electrode. On the top of the device, the channel consists of a thin (3-4 *u.c.*) $NdBa_2Cu_3O_{7-\delta}$ (NBCO) path. In this study, induced charge densities of $\sim 7 \cdot 10^{13}$ charges/cm^2 have been achieved.

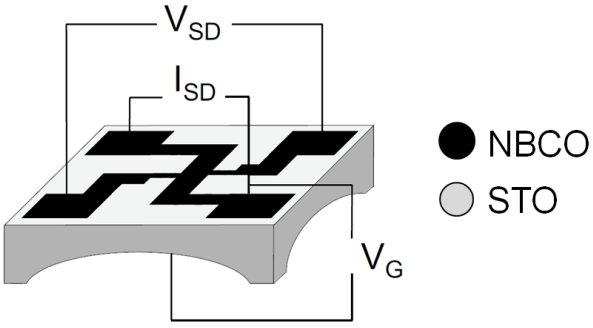

Figure II.3: Field-Effect transistor. STO is mild down to 100 μm and coated with gold. V_G: gate voltage; I_{SD} and V_{SD}: current and voltage from the source to the drain. Taken from [107]

Ferroelectric gates: Ferroelectric oxides such as $Pb(Zr,Ti)O_3$ (PZT) or $BiFeO_3$ (BFO) present three advantages as dielectric gates in FETs. First, they have a high spontaneous polarisation, up to few tens of $\mu C/cm^2$. This signifies that they could intrinsically allow very high charge transfers (typically 10^{14} charges/cm^2). Moreover, their polarisation is remanent, which means that it is not necessary to apply a voltage once the polarisation is set in one direction or the other (like schematized in Figure II.4 *a)* and *b)*). Finally, it is not necessary to use a top-gate electrode in order to switch the sign of the polarisation: this can be done by a CT-AFM scan, like schematized in Figure II.4 *c)* and described in section II.2.3 *b)*.

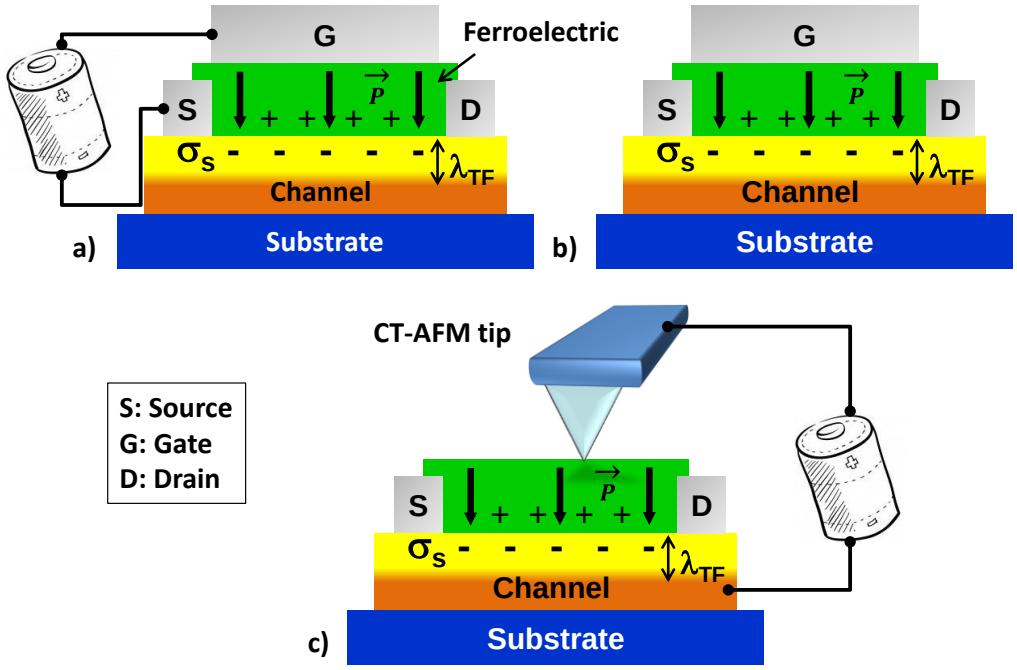

Figure II.4: Ferroelectric field-effect transistor. a) The ferroelectric polarisation is switched under an external electric field. b) The polarisation remains once the external field is removed.
c) The polarisation can be switched locally with a CT-AFM

Electric Double Layer Transistors: In the Electric Double Layer Transistors (EDLTs), both a transition metal oxide and a metallic electrode are partially immerged into an ionic liquid, as represented in Figure II.5: when a voltage is applied between them, the ions of the liquid are attracted near the surface of the electrodes. Compared to conventional dielectric gates, the distance between these ions and the surface of the oxide channel is very small and the field-effect is thus exceptionally large: charge transfer of 10^{14}~10^{15} charges/cm^2 have been reported [108].

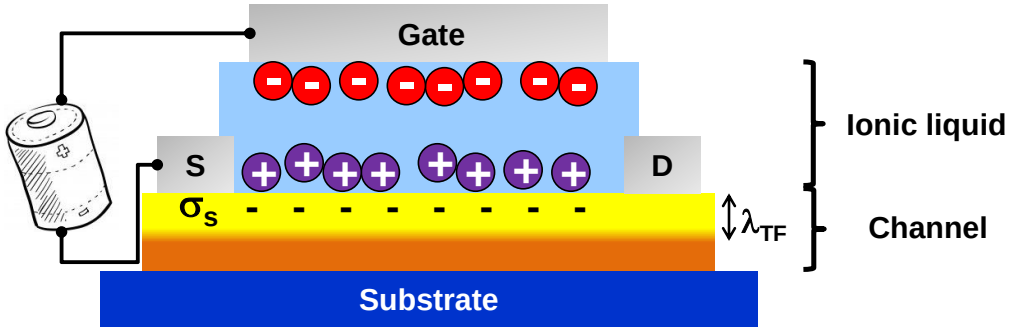

Figure II.5: Principle of the Electric Double-Layer Transistor

The broad choice of geometries and dielectric gates enables us to explore field-effect in any oxide channel. **In this thesis, the ferroelectric gate configuration is used, mostly because it allows a remanent and local manipulation of the field-effect.** The following section gives a brief review of the main field-effect experiments carried on oxides, and more specifically high-T_c superconductors.

II.2 Electrostatic tuning of correlated oxides

Tuning the electrical properties of correlated oxides using an electric field as an external control parameter has been widely developed [105], [109], thanks to the improvements in the fabrication of oxide ultra-thin films, and the technology of gates that could allow very high charge transfer (up to 10^{15} charges$/cm^2$ with the EDLT geometry) [110]–[112]. This has a technological interest: for example, the electrostatic doping of Mott insulators is considered as an alternative to silicon-based field-effect transistor, that confronts a scaling limit [109]. It also has fundamental interests, as it allows further exploration of phase diagrams: for example, Bollinger *et al*. were able to tune the superconductor/insulator transition of $La_{2-x}Sr_xCuO_4$ ($LSCO$) [113], and could observe that the critical resistance for the superconductor-insulator transition was exactly the quantum resistance for Cooper pairs, $h/(2e)^2$. This indicated that in the underdoped regime, the phase transition was not driven by pair breaking but by quantum phase fluctuations. Such information is critical to the understanding of the nature of the pseudogap and the microscopic mechanisms governing high-T_c superconductivity [114], [115].

II.2.1 Field-Effect in Colossal-Magneto-Resistance Manganites

Colossal-Magneto-Resistance manganites (CMR-manganites) also belong to a family of oxides that are highly sensitive to the doping level. As an example, Figure II.6, taken from [97], represents the phase diagram of a CMR-manganite, $La_{1-x}Sr_xMnO_3$. AFM, PM, PI, FM, FI and CI denote anti-ferromagnetic metal, paramagnetic metal, paramagnetic insulator, ferromagnetic metal, ferromagnetic insulator and spin canted insulator states. Electrostatic doping can successfully tune both electric and magnetic properties of these oxides [116]–[118]. Among the different field-effect transistors geometries, many of them are based on a ferroelectric gate [119]–[121].

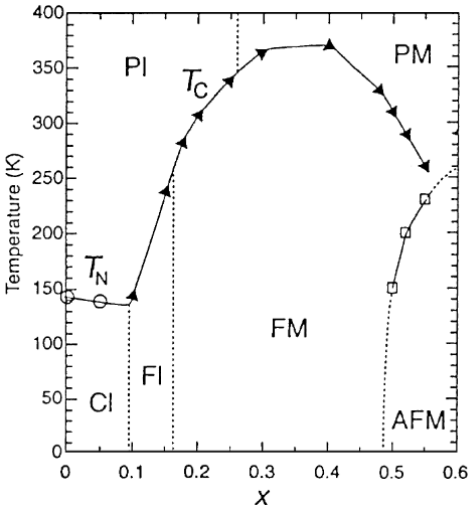

Figure II.6: Phase diagram of a CMR-manganite, $La_{1-x}Sr_xMnO_3$ taken from [97]

A typical field-effect experiment is the following: an epitaxial ferroelectric film ($BiFeO_3$ or BFO) is grown on an ultra-thin (here 4 nm) film of a CMR-manganite, $La_{2/3}Sr_{1/3}MnO_3$ (LSMO). The substrate is STO. Using a PFM (this technique is described in section II.2.3. *b)*), we image the as-

grown state of BFO: it is multi-domains, *i.e.* roughly half of the domains points downwards and the other half upwards (see inset in Figure II.7).

By measuring the resistivity as a function of the temperature, we observe the insulator/metal transition around $276\ K$ (green curve). With a PFM, we then scan the whole bridge while applying a negative voltage between the LSMO channel and the tip: this polarises the BFO downwards. At room temperature, the resistance of the channel increases by 77% (blue curve in Figure II.7): the field-effect induces a depletion of the number of carriers (holes) in the LSMO channel.

If we then polarise the BFO upwards, the resistivity of the channel drops by a factor 4 (red curve in Figure II.7), as holes are now accumulated in the channel. From these curves, we also observe that the insulator/metal transition temperature is higher when carriers are accumulated in the channel. The effect of the carrier modulation is thus similar to the effect of a chemical doping: it modifies the position of the material in its phase diagram.

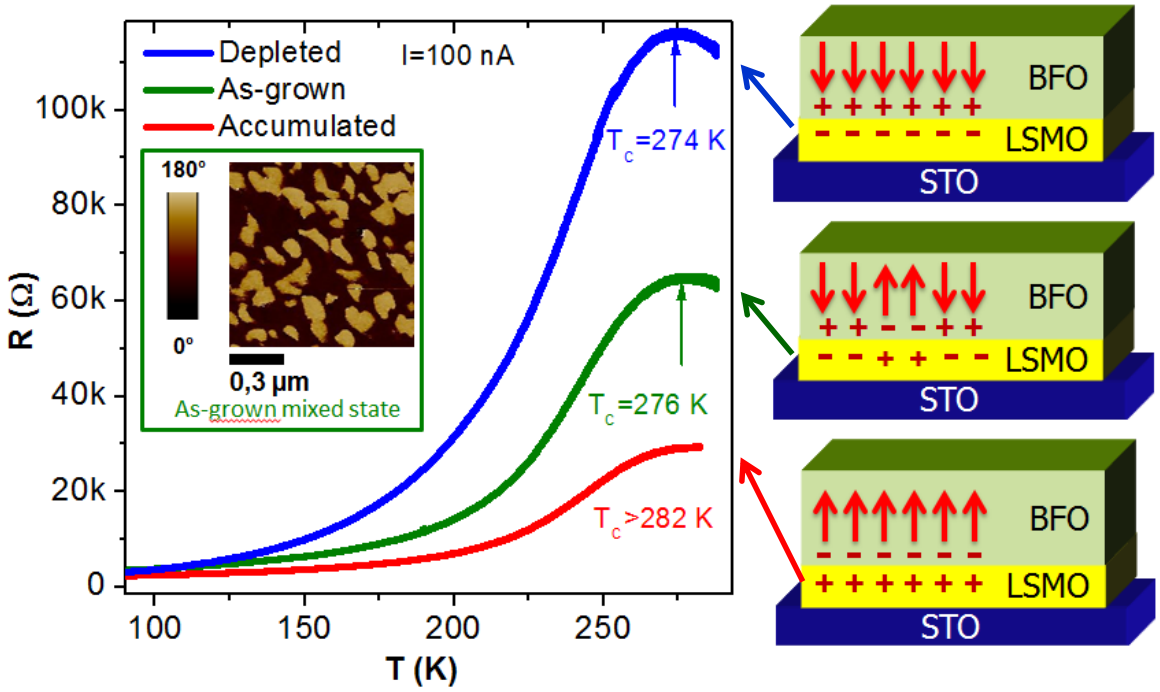

Figure II.7: Resistance vs temperature measurements for a BFO/LSMO bilayer. Green curve: the BFO is multidomain (see PFM image in inset); Blue curve: the BFO is downwards, carriers are depleted in the LSMO channel. Red curve: BFO is upwards, carriers are accumulated in the LSMO channel.

With this simple field-effect experiment, we showed that by switching the polarisation of a ferroelectric gate on the top of an oxide channel, we could tune the transport properties and browse the phase diagram of the latter.

Many other similar examples can be found in the literature. For instance, Figure II.8, taken from [117], represents a field-effect experiment on an $Au/Pb(Zr,Ti)O_3$ $(250\ nm)$/LSMO $(11,\ 12\ u.c.)$//STO structure, where $Pb(Zr,Ti)O_3$ (PZT) is a ferroelectric with a strong polarisation $(\sim 80\ \mu C/cm^2)$. By applying a gate voltage across the PZT film, carriers are either accumulated (red data in Figure II.8 *a)* and *b)*), either depleted (black data) in the thin LSMO film. The resistivity *a)* of the LSMO film is

modified by field-effect. Moreover, Kerr rotation measurements (Figure II.8 *b)*) show that the magnetic properties of the LSMO film are also modified. In a similar device, Dhoot *et al*. achieved to make a thin film of $La_{0.8}Ca_{0.2}MnO_3$ (LCMO) undergo a ferromagnetic metal to insulator phase transition [122].

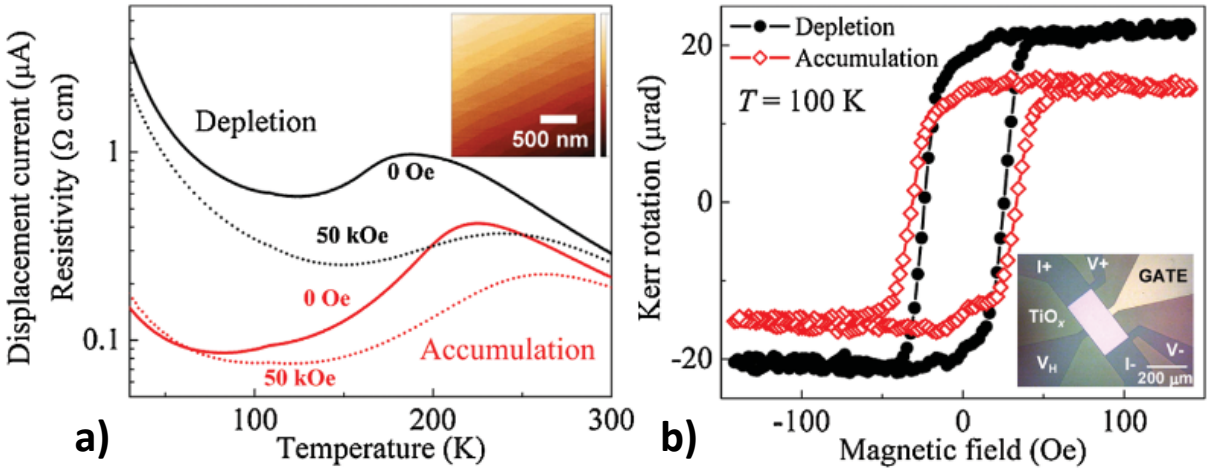

Figure II.8: a) Resistivity *vs* temperature curves for the accumulation (red) and depletion (black) states. b) Magnetic hysteresis curves of LSMO along the in-plane ⟨100⟩ direction for the two polarisation states of PZT, at 100 K. Inset: optical image of the device before Au metallisation; I+, I-, V+, V- denote the current and voltage contacts for the resistivity measurements. Taken from [117]

Field-effect is based on electrostatic interactions. In order to broaden our understanding of this effect, our group proposed a simple electrostatic model to explain the results obtained by Yamada *et al.* on $BiFeO_3/\ CaMnO_3$ bilayers of different thicknesses. This study is described in the following section.

II.2.2 Ferroelectric field-effect transistor: a prototypical model

Yamada *et al.* studied the ferroelectric field-effect in $BiFeO_3/\ CaMnO_3$ bilayers, with various thicknesses of $CaMnO_3$ (CMO). In this study, the choice of CMO is motivated by the small variation in the number of carriers needed to undergo a Mott insulator/metal transition [123]. In parallel, BFO is chosen for its strong polarisation at room temperature. The large compressive strain induced by CMO on BFO makes possible the growth of BFO in a "supertetragonal" phase, associated to a polarisation reaching $\sim 90\ \mu C/cm^2$. Further information about this phase is given in section I.4.5.

In order to measure the field-effect, *T*-BFO/CMO films are patterned into measurement bridges (see picture *a)* in Figure II.9). The direction of the polarisation of the *T*-BFO is switched by scanning the surface of the bridge with a PFM while applying a DC voltage, as represented in the PFM phases images in Figure II.9 *b)* and *c)*.

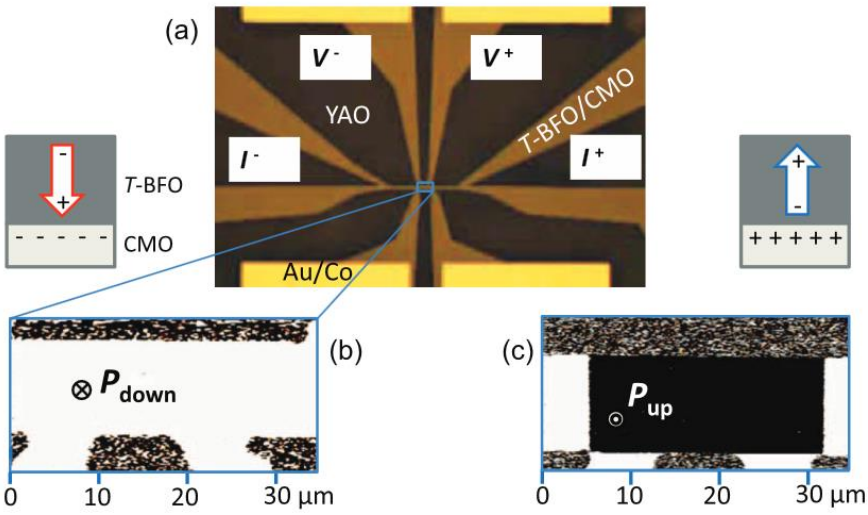

Figure II.9: a) Photograph of a patterned device for PFM and transport experiments. b) PFM phase image of the active area [blue rectangle in (a)] in the as-patterned device, showing a uniform polarisation inT-BFO pointing towards CMO (P_{down}). c) PFM phase image after writing with -8 V, demonstrating the reversed polarisation (P_{up}). Taken from [123]

These experiments were carried out on samples of various thicknesses (6 to 40 *u.c.* of CMO). As represented in Figure II.10, every film showed a higher resistivity when the polarisation pointed upwards ("OFF" state) than when the polarisation pointed downwards ("ON" state).

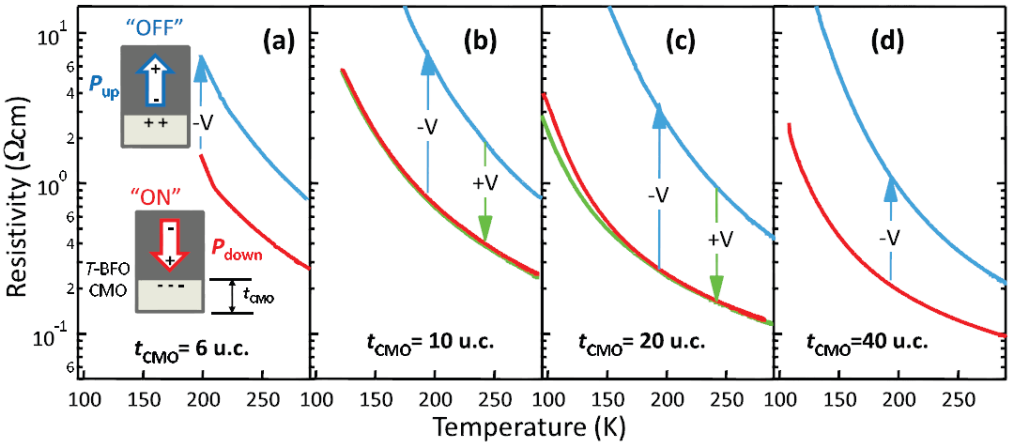

Figure II.10: Resistivity as a function of the temperature in the OFF and ON states for various thicknesses of CMO. Taken from [123]

Hall measurements were also carried on the devices, in order to estimate the carrier density in the "OFF" and "ON" states. The average carrier densities in the two states are represented in Figure II.11 *a)*: it is higher in the "ON" state than in the "OFF" state.

These two observations are consistent with an electrostatic depletion (OFF) or accumulation (ON) of electrons in the CMO channel which has a *n*-type conduction. Moreover, we observe that the modulation of the total number of carriers in the channel is bigger for the thinner films: this emphasises the fact that the field-effect only propagates close to the interface with the ferroelectric gate, and is measurable only in channels with thicknesses comparable to the Thomas-Fermi length.

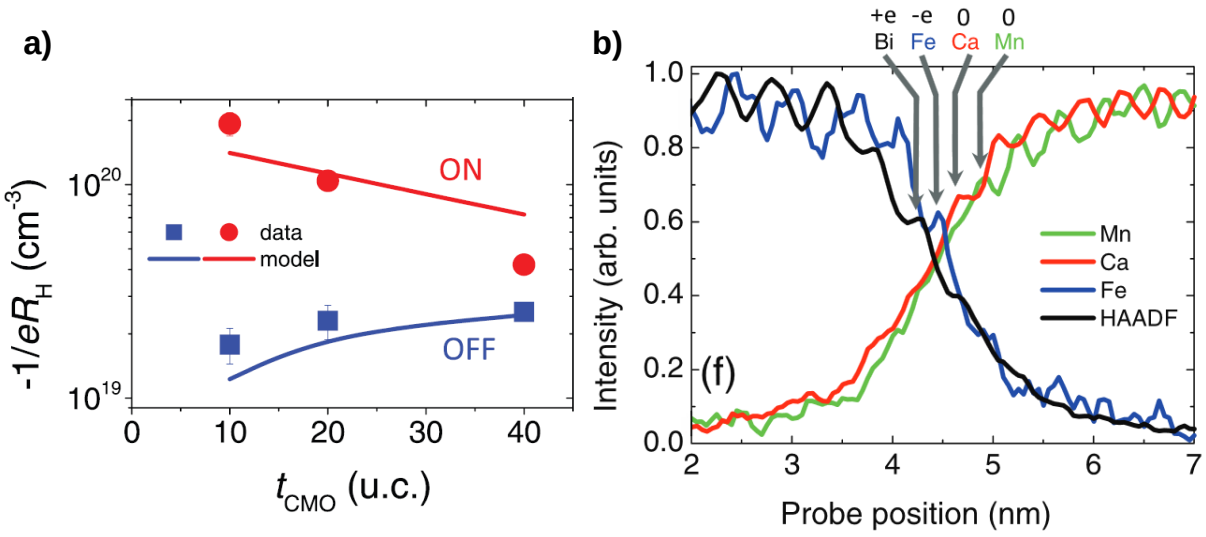

Figure II.11: a) Carrier densities in the OFF and ON states for various thicknesses of CMO. b) Average profiles of the HAADF, Mn, Ca and Fe EELS signals over a $7 \times 2\ nm^2$ rectangle. Taken from [123]

A second key observation is that the thickness dependence of the carrier densities in the two directions (n_{OFF} and n_{ON}) is asymmetric: the field-effect is weaker in the OFF state than in the ON state. CMO and BFO planes do not have the same sheet charge densities, which signify that a fixed dipole necessarily exists at their interface. Thanks to EELS maps and HAADF STEM images (these techniques are presented in section II.2.2), it was established to be pointing towards CMO: as shown in Figure II.11 *b)*, the first plane of the BFO layer is negatively charged whereas the first CMO plane is neutral. This dipole may cause an accumulation of carriers in the CMO channel, regardless of the direction of the polarisation in *T*-BFO. This could contribute in a positive way to the field-effect when the polarisation points downwards (ON state) and in a negative way when the polarisation points upwards (OFF state).

The field-effect in T-BFO/CMO was simulated by a simple electrostatic model that took into account both the screening of the polarisation and the fixed dipole at the interface. The parameter describing the distance over which the electrostatic modulation occurs in the CMO layer is the Thomas-Fermi length λ Lambda. In CMO, it can be estimated by [124]:

$$\lambda = \left(\frac{\varepsilon \hbar^2}{4me^2}\right)^{1/2} n^{-1/6} \qquad \text{(III.3)}$$

where ε is the dielectric constant of CMO ($\varepsilon \sim 20$), $\hbar$ is the reduced Planck constant, m is the electron mass, e is the elementary charge and n the carrier density ($n \sim 10^{19}\ cm^{-3}$). From this equation, $\lambda = 2 \sim 3$ u.c. is expected. The strength of the modulation is given by the value of the polarisation; Hall measurements of the carrier density in the bridge revealed that the effective polarisation acting on the channel was only about $\sim 5\ \mu C/cm^2$, whereas *T*-BFO has a polarisation of $\sim 90\ \mu C/cm^2$. Finally, the parameter taking into account the fixed dipole is expected to be of the same order of magnitude than the polarisation ($\sim 5\ \mu C/cm^2$). Figure II.12 *b)* represents the CMO channel: close to the interface with *T*-BFO, the carrier density is modulated, and is constant far from the interface. The carrier density n_s is calculated layer by layer with an exponential law: $n_s - n_{s0} \sim e^{-t/\lambda}$, where t is the distance to the interface and n_{s0} is a constant.

The experimental data (Figure II.12, left) were successfully fitted with this simple electrostatic model, in which the Thomas-Fermi length parameter was however slightly bigger than the estimated value (4,5 u.c. instead of $2{\sim}3$ u.c.). In this model, the carrier mobility was taken to be decreasing with increasing carrier concentration, in line with earlier observations [123].

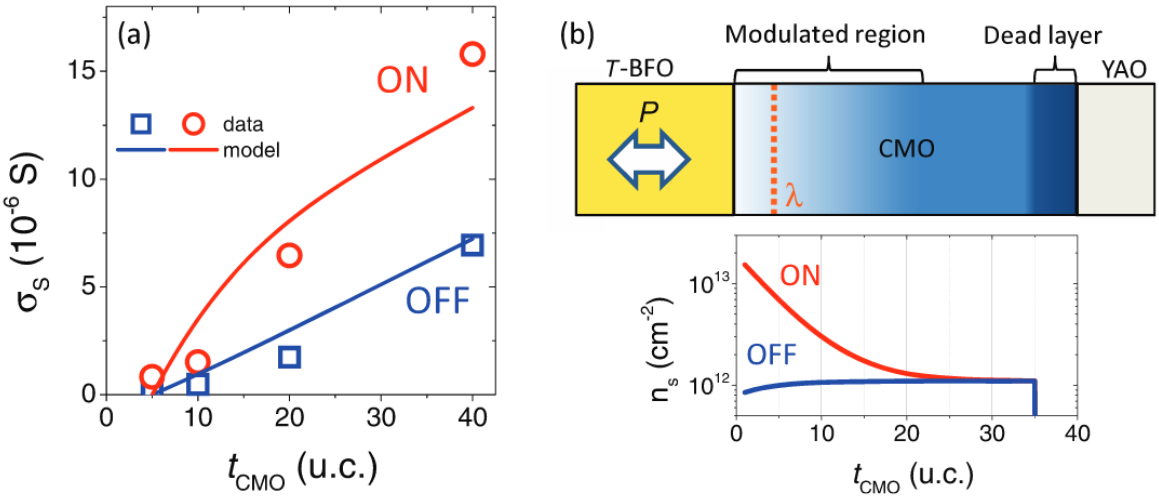

Figure II.12: (a) Sheet conductance (σ_S) at 290 K in ON (red) and OFF (blue) states plotted against the thickness t_{CMO}. The data are shown as symbols and results of the model as solid lines. (b) Depth-profile of the carrier density in the channel. λ is the Thomas-Fermi screening length. Taken from [123]

In this study, strong carrier modulations were reported. The mechanisms at the origin of the field-effect were described in terms of a simple electrostatic model, which explained accurately the obtained results. **First of all, the pinned electric dipole induced by the termination at the interface yields highly asymmetric doping effects. Moreover, the doping is not homogeneous in depth: it decreases gradually from the interface, over ~4,5 u.c..**

II.3 Electrostatic tuning of high-T_c superconductors

II.3.1 Field-effect and penetration length

Most high-T_c superconductors have the same type of phase diagram, represented in Figure II.13, with quite well-known temperature-doping relationships: in general, at low levels of doping, cuprates are antiferromagnetic insulators. At higher levels, they become superconductors; the temperature of the transition to the superconducting state as a function of carrier concentration takes a characteristic dome shape.

Chemical doping is either tuned by substitution of insulating parents (for example, in La_2CuO_4, La can be partially substitute by Sr to form $La_{2-x}Sr_xCuO_4$), or oxygen concentration (for example in $YBa_2Cu_3O_{7-\delta}$ (YBCO)). The relevant range of carrier concentrations is small, more or less $0 < x < 0.2$ carrier per unit cell (corresponding to an areal density $0 < n_{2d} < 10^{14}\ cm^{-2}$): **small changes in carrier concentration are sufficient to browse the phase diagram**.

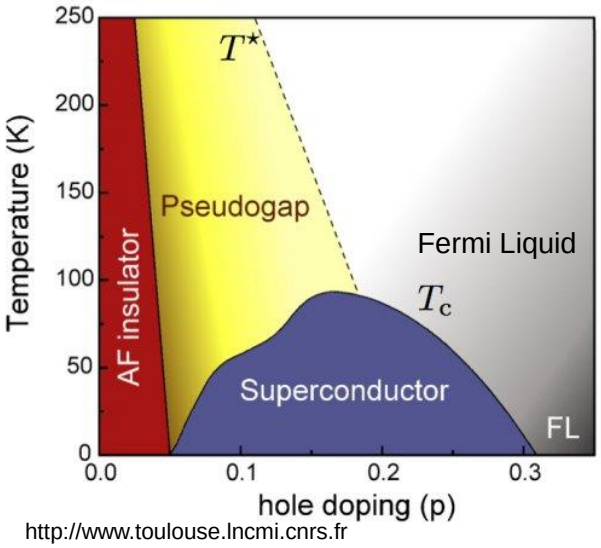

Figure II.13: General phase diagram of high T_c superconductors

As mentioned before, for small depletions, the carrier density decays exponentially inside the conductor as described in a Thomas-Fermi approach [106] with a characteristic length λ_{TF} equal to the electric penetration depth given in equation (III.1). In high-T_c superconductors, the effective density of states n_{eff} that screens the applied field can be estimated by n/e [104]. This leads to the following expression for the Thomas-Fermi length in high-T_c superconductors:

$$\lambda_{TF} = \left({}^{\varepsilon_s \varepsilon_0}/_{e \cdot n}\right)^{1/2} \qquad \text{(III.4)}$$

where ε_s and ε_0 are the dielectric constants of the superconductor and the vacuum, e the elementary charge, and n the density of mobile charge carriers in the superconductor. In these materials, $\boldsymbol{\lambda_{el} \sim 0.5 - 1\ nm}$, and when the electric field is applied along the *c*-axis, it is generally comparable or bigger than the coherence length ξ: in these conditions, the superconducting properties of the field-penetrated layers directly depend on the applied electric field [125]. **Indeed, field-effects will be measurable in ultra-thin films whose thicknesses are comparable to the electric penetration depth.** In low-T_c superconductors, for which $\lambda_{el}(T) \ll \xi(T)$ the field-effects are generally weak [126]–[128], except under certain conditions [129].

In the following sections, we give a brief review of field-effect experiments carried on high-T_c superconductors.

II.3.2 Field-Effect Transistors

Using insulators with a high-dielectric constant such as $SrTiO_3$(STO), charge transfers of order of $10^{13}\ n/cm^2$ are possible in a FET configuration [104], [130], [131]. Mannhart and Frey [104] shifted the transition temperature of a $8\ nm$ YBCO film by $8\ K$ with an STO gate insulator of $\sim 300\ nm$ (Figure II.14, left), following the work of Xi *et al*. on the same structure [132]. Similar results were obtained by Matthey *et al*. with NBCO as a superconductor (Figure II.14, right) [107].

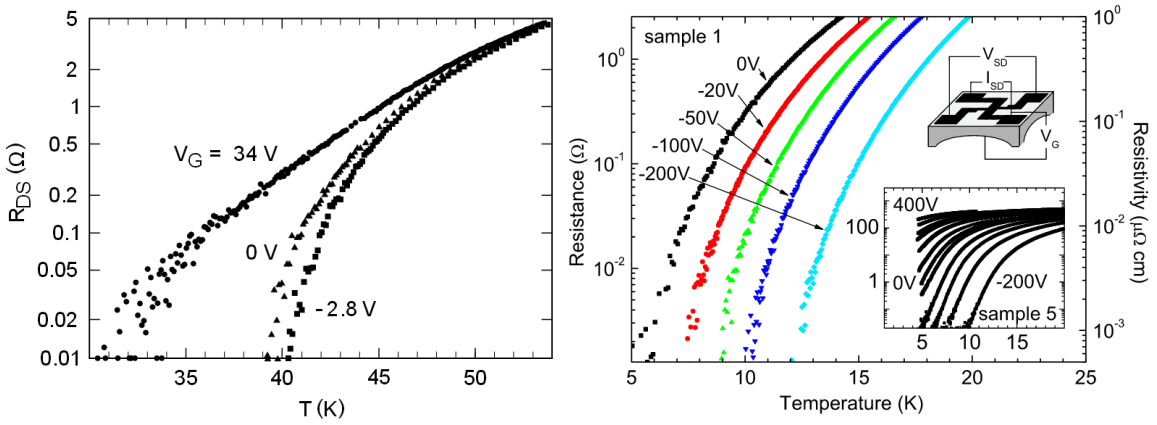

Figure II.14: Temperature dependence of : Left) a YBCO 8 nm thick channel with a ~300 nm thick STO gate, taken from [104]. Right) a NBCO 3-4 nm thick channel on a 100 µm thick STO substrate, taken from [107]

II.3.3 Electric Double Layer Transistors

Electrochemical techniques to control the electronic properties of materials have first been used by Brattain and Garrett [133] in the 1950s. Today, ionic liquids gates reached levels of charge transfer in excess of 10^{15} charges/cm^2. For example, Figure II.15 taken from [134] represents resistance vs temperature measurement for a $7\ nm$ thick YBCO channel in a ionic liquid. Depending on the applied voltage, the channel has either a superconducting either an insulating behaviour. However, it has been pointed that these techniques may induce irreversible electrochemical reduction of the superconducting layer [135].

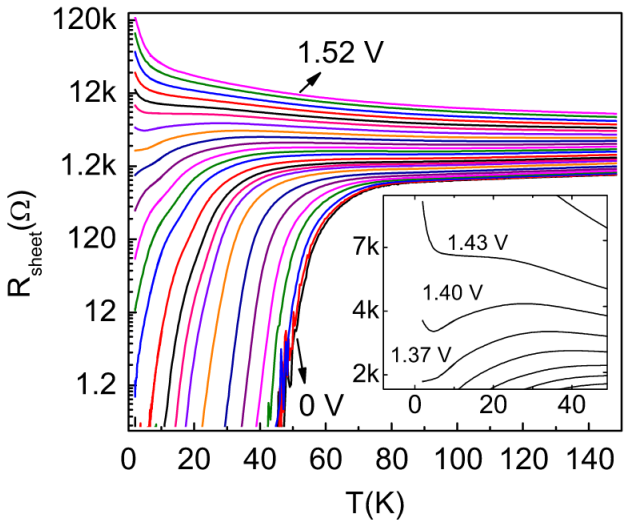

Figure II.15: Temperature dependence of a YBCO (7 nm) channel in a ionic liquid, taken from [134]

II.3.4 Ferroelectric Field-Effect Transistors

As discussed in section II.1.3, ferroelectric materials have a remanent polarisation, and the direction of their polarisation can be switched by applying temporarily an electric field [120]. They have been successfully used as gates to dope high-temperature superconductors [104], [120], [136], [137]. Early works involved a 160 Å thick Sn film grown on *triglycine sulphate*, which served both as a substrate and as the source of ferroelectric polarisation, exhibiting a shift in the T_c of Sn by

$0.0013\ K$ [138]. In $PbZr_xTi_{1-x}O_3$ (*PZT*) / $GdBa_2Cu_3O_{7-x}$ heterostructures, Ahn *et al*. observed shift in the T_c of several Kelvins induced by field-effect and superconducting to insulating transitions for more underdoped films [136]. A scheme of the device *a)* and the resistivity measurements *b)* for the two directions of the polarisation is reproduced in Figure II.16.

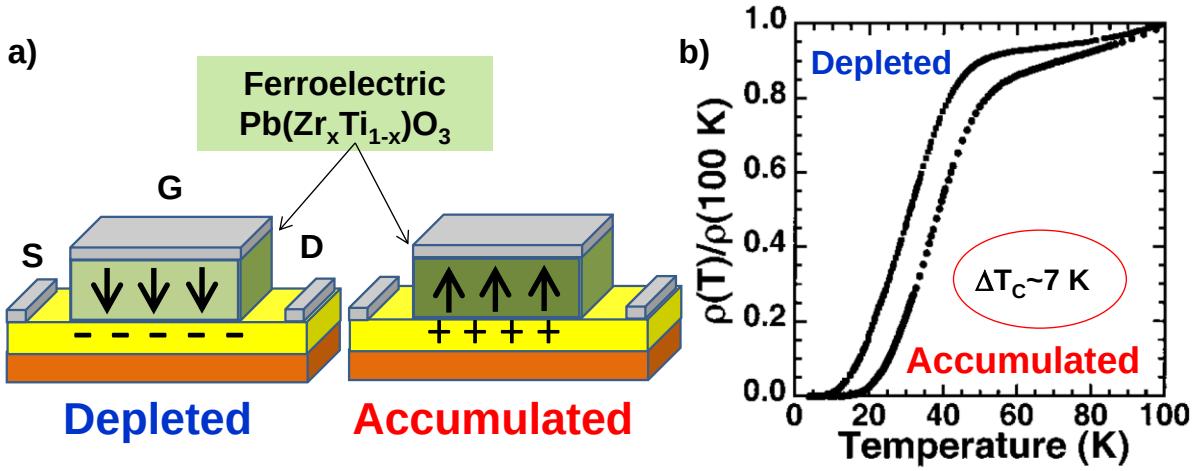

Figure II.16: a) Scheme of the ferroelectric FET. b) Resistivity (normalized at 100 K) *vs* temperature measurement for the two directions of the PZT polarisation, taken from [136]

A. Crassous *et al*. investigated field-effect in BFO/YBCO/PBCO//STO heterostructures (where PBCO stands for $PrBa_2Cu_3O_{7-\delta}$, which is an insulating cuprate). He achieved to shift the critical temperature of the superconducting channel in a reversible way by $\sim 15\ K$ for a 4 u.c. thick channel, and $\sim 30\ K$ for a 3 u.c. thick channel [139], [140]. Figure II.17, represents the resistance of the channel as a function of the temperature in the depleted state *a)* and in the accumulated state *b)*. *c)* and *d)* curves are subsequent measurements showing that the field-effect is reversible.

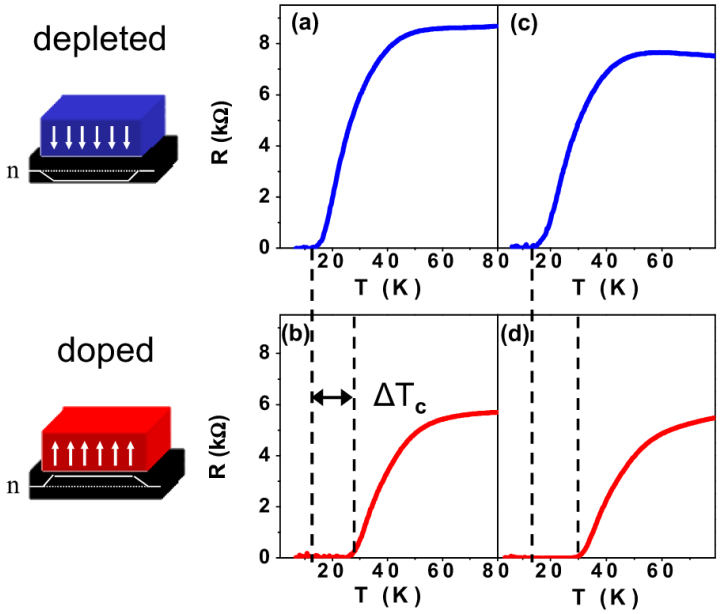

Figure II.17: Resistance vs temperature for a BFO (30 nm)/YBCO (4 u.c.)/PBCO//STO heterostructure in the as-grown state (a), and after subsequently reversing the ferroelectric polarisation outwards (b), towards (c) and outwards (d) the YBCO layer. The sketch indicates the direction of the ferroelectric polarisation and the expected variation in the carrier density within the YBCO layer. Taken from [140]

In this last experiment, contrary to the works presented earlier, the direction of the polarisation and thus the sign of the field-effect is not switched by a metallic gate, but by scanning the surface of the channel with a conductive, nanometric tip. Compared to usual transistors, it has two main advantages:

- The field-effect remains once the voltage is removed (ferroelectric gate)
- The direction of the polarisation can be controlled at the nanoscale.

These two characteristics open the way to the fabrication of ferroelectric field-effect devices, which is one of the objectives of this thesis.

II.4 Some functionalities of field-effect

Up to now, the presented experiments consisted in switching the electric and/or magnetic properties of an oxide channel. In this thesis, the manipulation of field-effect is more complex. As we will see later in the chapter VI: "Planar field-effect devices" and VII: "Out-of-plane field-effect devices":

- **In the planar devices, the ferroelectric polarisation is defined at submicrometric scales;**
- **The Josephson effect is not directly a property of the material but of the device;**
- **In the vertical devices, the current flows through physical interfaces.**

In the following paragraphs, we give a brief state of the art of related works.

II.4.1 Local manipulation of field-effect

As described in section II.2.3 *b)*, it is possible to switch locally the polarisation of a ferroelectric thin film by applying a voltage between a CT-AFM tip and the oxide channel. This raises the following question: what is the minimum size for a "field-effect" domain?

Early works involved the use of scanning probe microscopy to induce local and non-volatile field-effects in epitaxial $PbZr_{0.52}Ti_{0.48}O_3/SrRuO_3$ heterostructures [141]. In these devices, the $SrRuO_3$ (SRO) channel is $3\ nm$ thick and the PZT film has a remanent polarisation of 10 to $15\ \mu C/cm^2$. A rectangular measurement bridge is then patterned on the sample.

Using a CT-AFM tip, zones of various areas are "written" in the upwards or downwards direction. Figure II.18 represents the resistance of the channel as a function of the written area, schematically shown in the inset: "+" and "-" signs indicate if the polarisation points downwards or upwards. The staircase demonstrates local and reversible behaviour, and the sequence at the right shows the reproducibility of the poling procedure.

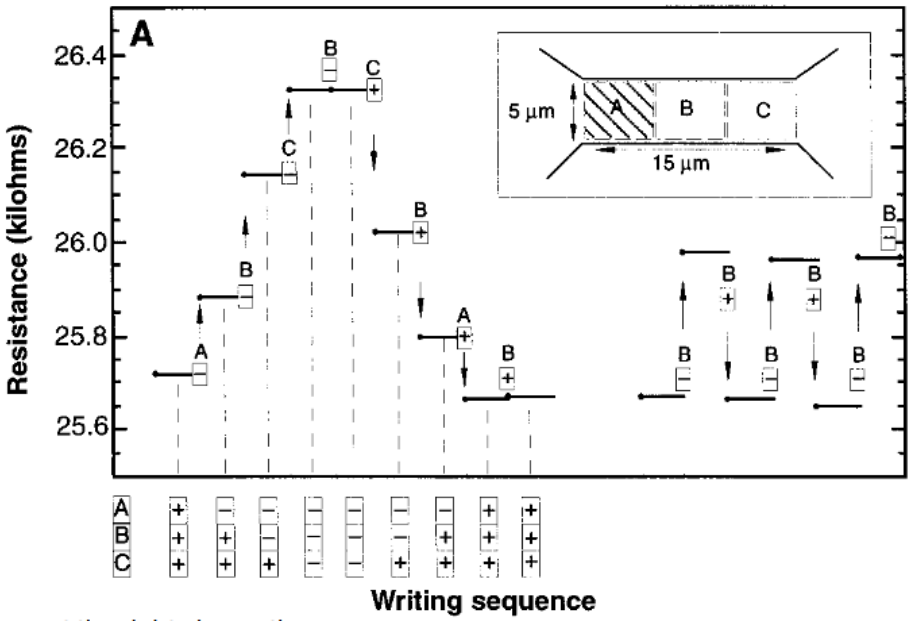

Figure II.18: Local modulation of the resistance of a channel by ferroelectric field-effect. taken from [141]

This experiment shows that field-effect is well-defined in micrometric areas. At much lower scale, the work from Crassous *et al.* shows that field-effect can be functionalised down to the nanoscale [139]. His devices consist of a BFO (30 nm)/YBCO (3 u.c.) bilayer patterned into measurement bridges. The bridge is poled upwards with a CT-AFM, and a periodic array of downwards dots is written, like represented in Figure II.19 a).

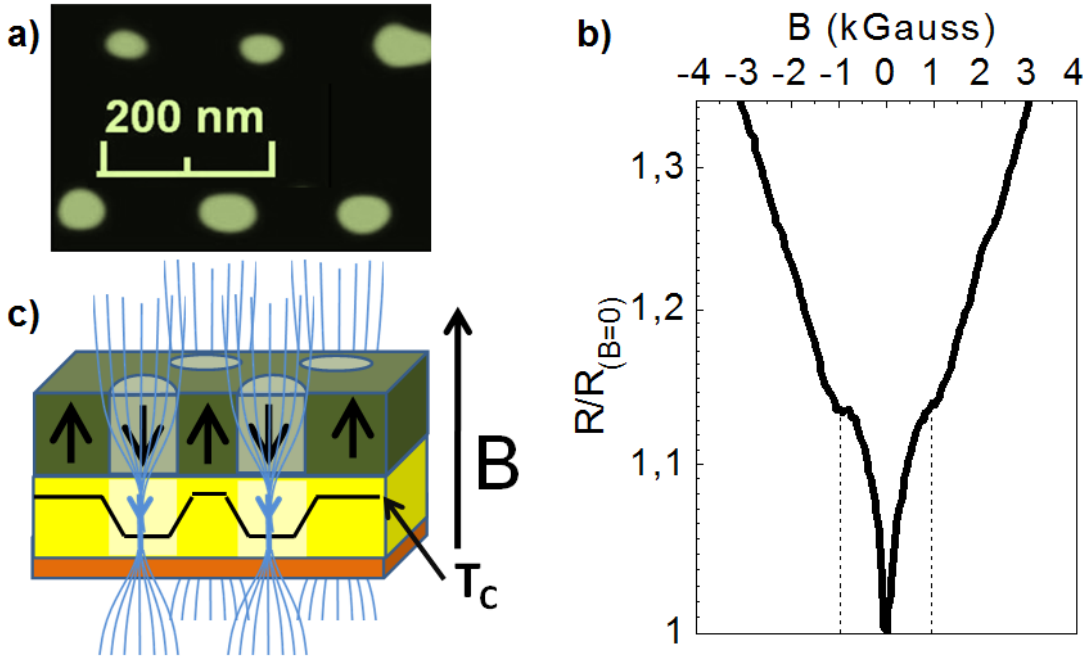

Figure II.19: a) PFM image of a periodic array of downwards ferroelectric domains. b) Magnetoresistance measurement of a BFO/YBCO channel patterned with the array in a). c) Schematic representation of flux quanta pinning by the depleted dots in the YBCO film.

The diameters of the dots is $30{\sim}80\ nm$. Evidence for the nanoscale modulation of superconductivity is obtained from the mixed-state magnetoresistance: the black curves in Figure II.19 show the resistance of the film as a function of the applied magnetic field, parallel to the c-axis of the YBCO film. Local minima appear at $H = \pm 960\ Oe$. These minima, which do not appear when the array of nanodomains is "erased", are the sign of a periodic pinning of flux quanta: underneath the BFO downwards domains, carriers are depleted in the YBCO film by field-effect and the superconductivity is locally depressed. **The field-effect is strong enough so that the flux quanta are pinned by these nanometric areas.**

II.4.2 Tunable Josephson junctions

Josephson junctions have been introduced in Chapter I, Section 2. Technologies involving low-T_c superconductors are well mastered, whereas it remains challenging to control the parameters of high-T_c Josephson junctions, which could allow the devices to operate at liquid nitrogen temperature instead of Helium. Some devices working with a number of Josephson junctions such as SQUIDs could benefit strongly from having arrays of junctions with tunable characteristics.

Some works aiming at controlling bicrystals junctions with a top-gate electrode ("JoFETs") were published earlier [142]–[147]. In 1993, Ivanov *et al*. [142] observed a strong (more than 50%) enhancement of the critical supercurrent in a YBCO 45° grain boundary junction measured via a microbridge coated by a $300\ nm$ thick STO gate. Nakajima *et al.* [147] reported a 5% modulation of the critical current in a $60\ nm$ thick YBCO grain boundary junction channel; Peterson *et al*. [146] reported a stronger modulation in a junction made out of a thinner YBCO layer ($32\ nm$).

In 1996, Mayer *et al.* obtained modulation of 8% per applied volt for an "inverted MISFET" structure based on 36,8° and 45° grain boundary junctions in ultra-thin films of YBCO ($15\ nm$) [143]. They found that for $V_G \gg 2I_cR_n$ (V_G is the gate voltage, I_c the critical Josephson current and R_n the resistance of the barrier in the normal state) the relative changes in R_n of the JoFET are at least one order of magnitude lower than the changes in the critical current. The changes in I_c as a function of the gate voltage for the two junctions are represented in Figure II.20.

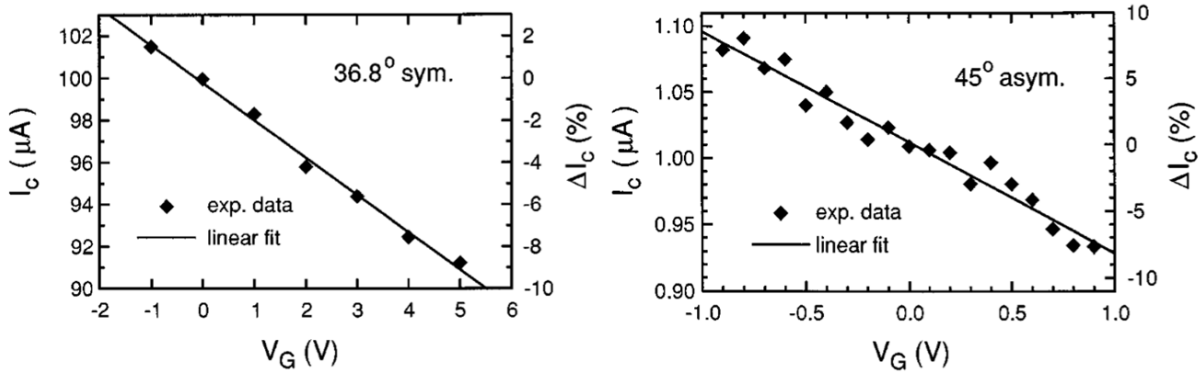

Figure II.20: Modulation of the critical current of a "JoFET" with a gate voltage, taken from [143]

They conclude that this suggested that the width of the grain boundary barrier is modulated by the applied electric field, whereas changes in the barrier height are insignificant. Betouras *et al.* proposed a theoretical model based on the Ginzburg-Landau free energy expression to describe the field-effect in grain boundary Josephson junctions [148]. They conclude that the strong field-effects

were observed because the boundary serves effectively as a proximity-effect junction which changes from S/S'/S (where S and S' are superconductors) towards S/N/S (*N* stands for normal metal) as the field is applied. **This work emphasises the strong changes that electrostatic modulation can induce in the expression of the Josephson effect.**

II.4.3 Ferroelectric tunnel junctions

Up to now, we only considered planar transistors, *i.e.* a geometry where the current flows in the channel, parallel to the surface of the gate. Ferroelectric tunnel junctions are an example of field-effect devices where the current flows through the gate, parallel to the direction of the polarisation. In these junctions, even though the ferroelectric film is thin enough to allow the electrons to tunnel through it, **the switching of the direction of the polarisation induces drastic modifications of the properties of the junction**. These changes are partially due to the modification of the thickness of the barrier after the switching (because of the inverse piezoelectric effect that occurs in ferroelectrics) and to interface effects (the bonding between the electrodes and the barrier might be modified). The electrostatic field-effects due to the partial screening of the polarisation charges by the carriers in the electrode have a large impact on the electrostatic profile of the barrier, as described in Chapter I, section I.3.5.

This effect was directly correlated to the polarisation switching in experiments using a conductive tip AFM as a top electrode on $BaTiO_3/La_{0.67}Sr_{0.33}MnO_3$ bilayers [70], [149], as well as on $BaTiO_3/SrRuO_3$ bilayers [150]. Solid-states devices with metallic top electrodes were then studied. $Ag/BaTiO_3/SrRuO_3$ nanojunctions ($\sim 20\ nm$) were fabricated by Gao *et al.*, who demonstrated that ferroelectric tunnelling was the dominating conduction mechanism in their devices [151].

Non-volatile memories with OFF/ON ratios as high as 100 based on $Au/Co/BaTiO_3/La_{0.67}Sr_{0.33}MnO_3$ were fabricated by Chanthbouala *et al.* [81]: a schematic representation of such junctions is shown in Figure II.21 *d)*. The ferroelectric characterisation of the junction (PFM phase in Figure II.21 *a)* and amplitude in *b)*) at different applied voltages V_{write} confirmed that **the resistance of the junction** (Figure II.21 *c)*) **was directly related to the direction of the polarisation of the barrier.**

Magnetoelectric coupling was demonstrated in ferroelectric tunnel junction with ferromagnetic electrodes, where the direction of the ferroelectric polarisation modifies the tunnelling spin polarisation [152]–[156]. Yamada *et al.* fabricated multilevel ferroelectric tunnel junctions based on Co/Pt/T-BFO/$Ca_{0.96}Ce_{0.04}MnO_3$ junctions, with a maximal ON/OFF ratio of 10^4. It has potential application in memory cells and memristors [157].

The reported tunnelling electroresistance (TER) is primarily attributed to the modification of the electrostatic profile of the barrier. Recent works involved phase transition at complex oxide interface, enhancing the TER effect.

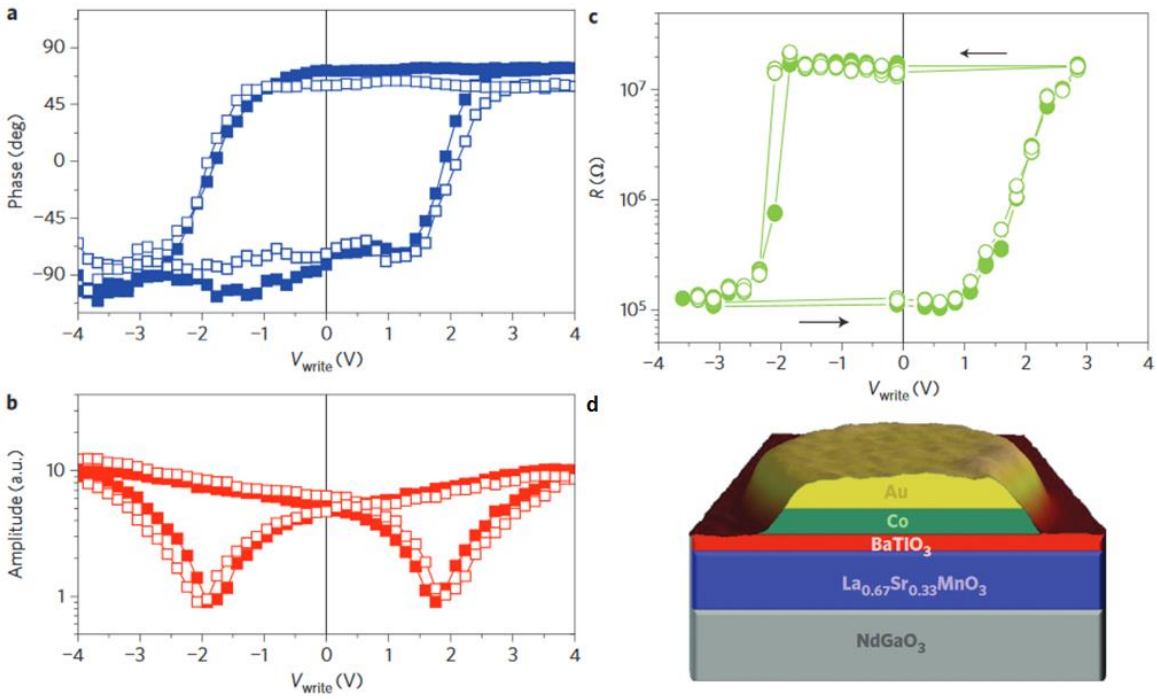

Figure II.21: PFM a) phase and b) amplitude, c) resistance of the barrier after applying DC voltage pulse V_{write}. d) Schematic of one iunction. Taken from [81]

Using electrostatic field-effect induced by polarisation switching, Yin *et al.* induced a metal-to-insulator transition in a nanometre thick $La_{0.5}Ca_{0.5}MnO_3$ (LCMO) interlayer inserted between the ferroelectric barrier ($BaTiO_3$ – BTO) and one electrode ($La_{0.7}Sr_{0.3}MnO_3$ – LSMO) [158]. By changing both the height of the barrier and its thickness, they increased the TER by several orders of magnitude. In this work, the doping ($x = 0{,}5$) of the LCMO layer is choosen at the doping boundary between the ferromagnetic-metallic phase and the antiferromagnetic-insulating phase. The device is represented in Figure II.22 *a)*.

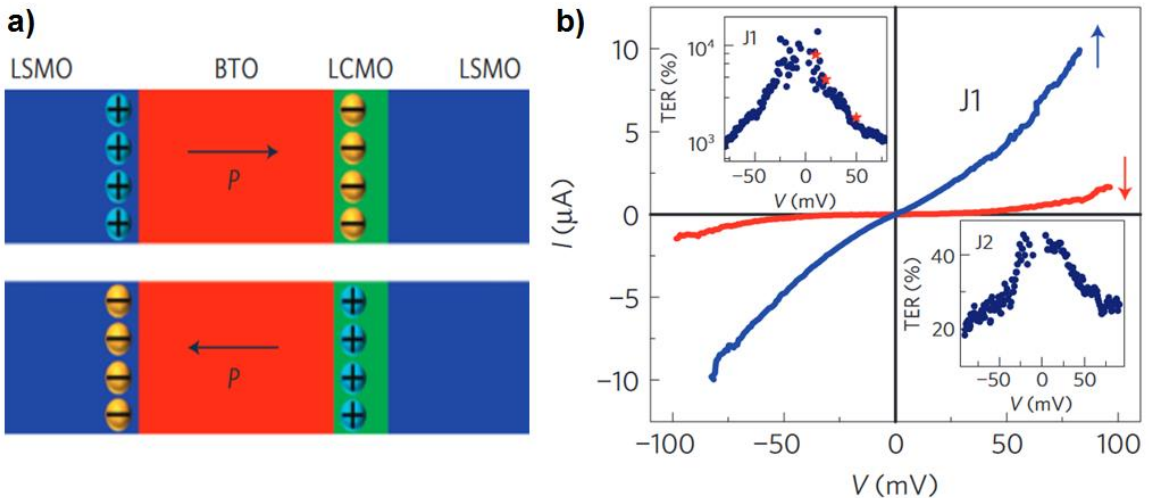

Figure II.22: a) Schematic of the LSMO/BTO/LCMO/LSMO junction for the two directions of polarisation. b) I-V characteristics of the junction in both states. Inset J1: TER ratio of the junction. Inset J2: TER ratio of a similar junction without the LCMO interlayer. Taken from [158]

Figure II.22 *b)* represents the $I - V$ characteristics of the junction for the polarisation in the two directions. The TER ratio quantifies the difference of resistance in the two states. Inset "J1" gives the

ratio for the LSMO/BTO/LCMO/LSMO junction, which reaches 10^4 for low bias. As a comparison, inset "J2" gives the TER ratio for an identical junction without the LCMO interlayer: it only reaches 40%.

The enhancement of the TER ratio is attributed to **a phase transition of the LCMO layer**: for ferroelectric polarisation pointing towards the LCMO film, the hole depletion induced by field-effect pushes the doping level towards the $x < 0{,}5$ ferromagnetic-metallic phase. In the other direction, the accumulation of holes favours the antiferromagnetic-insulating phase. **This leads to an increase in the effective thickness of the barrier, and thus an exponential enhancement of the barrier resistance.** Radaelli *et al.* found that the capacitance of $BaTiO_3/La_{0.67}Sr_{0.33}MnO_3$ junctions behaved as of an insulator/*n*-type semiconductor junction, and that it was modulated by the polarisation of BTO [159].

Similarly, metal/ferroelectric/semiconductors tunnel junctions raised a lot of interest in modulating both the height and the width of the barrier by field-effect. In these experiments, depending on the direction of the polarisation, the electrons will have to pass through a space charge region where the semiconductor is either accumulated or depleted. Wen *et al.* obtained OFF/ON ratio above 10^4 in $Pt/BaTiO_3/Nb:SrTiO_3$ junctions [160]. More recently Liu *et al.* studied the band alignment between the semiconductor and the ferroelectric using first-principle density functional theory in a similar heterostructure [161]: from the view of the electronic structure, changing the direction of the polarisation modifies the position of the conduction band minimum with respect to the Fermi level. Indeed, if the potential step created by the ferroelectric insulator is smaller than the potential drop induced by the field-effect for an accumulation of carriers in the semiconductor, then **the interfacial region in the ferroelectric layer becomes conducting** and the barrier width is reduced. This is supported by LDOS calculations, represented in Figure II.23 *b)*.

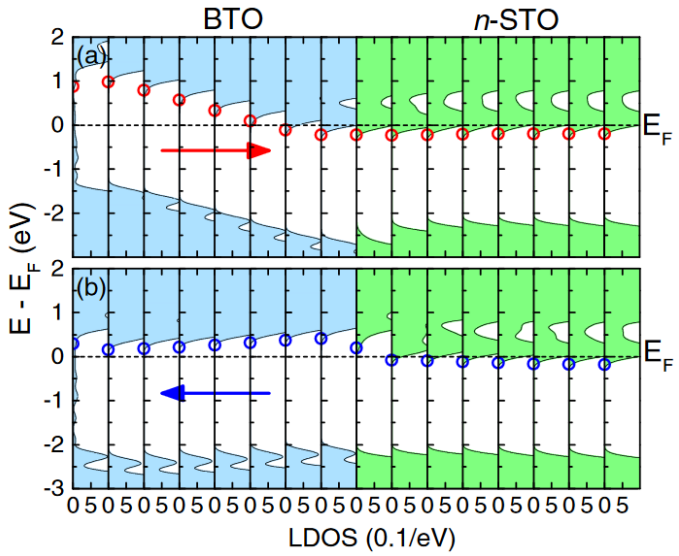

Figure II.23: Local density of states calculation in the TiO2 layers for the polarisation pointing a) towards and b) away from the BaTiO3/b-STO interface. Taken from [161]

In the other direction, the authors found that the electric field gives rise to the polar displacement in $Nb:SrTiO_3$, which increases the screening length and reduce the effect of screening by free carriers, like represented in Figure II.23 *a)*.

In the meantime Li *et al.* carried on further experiments on $Pt/BaTiO_3/Nb:SrTiO_3$ ferroelectric tunnel junctions, with $L_{1-x}S_xMO$ interlayers (heterojunctions) and without (homojunctions) [71]. They observed a strong correlation between the barrier asymmetry and the Sr concentration in the interlayer, which directly influences the Fermi level of $L_{1-x}S_xMO$. **They observed an improvement in the TER ratio for heterojunctions compared to homojunctions, and attributed it to the band offset within the ferroelectric tunnel junction, which changes both the barrier width and height.**

Ferroelectric tunnel junctions with superconducting electrodes are promising, as they can a priori switch between a superconducting state (the supercurrent tunnels through the barrier) and a normal state (the barrier width is too thick and the Cooper pairs are broken within the barrier). The density of states at the interface should be highly influenced by the polarisation direction.

The amplitude of the field-effect in BFO/YBCO/PBCO//STO heterostructures having been established, **one of the objectives of this thesis is to functionalise the field-effect in ferroelectric/superconductor structures.** More precisely, the goal is to tune electron and supercurrent transport via ferroelectric field-effects. We will seek that in in two types of devices:

- In a planar geometry, by creating a spatial variation of the critical temperature of a YBCO film. The idea, represented in Figure II.24 *a),* is to create a ferroelectric domain structure such that carriers are accumulated (leading to higher T_c) everywhere in the YBCO channel but within a narrow band perpendicular to the channel, in which charge depletion leads to relatively lower T_c. We expect that in a range of temperature comprised between the T_c in the accumulated state (T_c^{up}) and in the depleted state (T_c^{down}), the channel will behave as a superconductor/normal metal/superconductor junction and show Josephson behaviour.
- In a vertical geometry – see Figure II.24 *b)*, the concept is to create ferroelectric tunnel junctions with superconducting electrodes, in which the effective thickness of the tunnel barrier is modulated upon ferroelectric switching. We saw that in ferroelectric tunnel junctions, a strong TER is expected. One of the anticipated mechanisms is that the charge accumulation at the superconducting/ferroelectric interface may induce a superconductor/insulating transition over the screening length, leading to a variation of the effective barrier width.

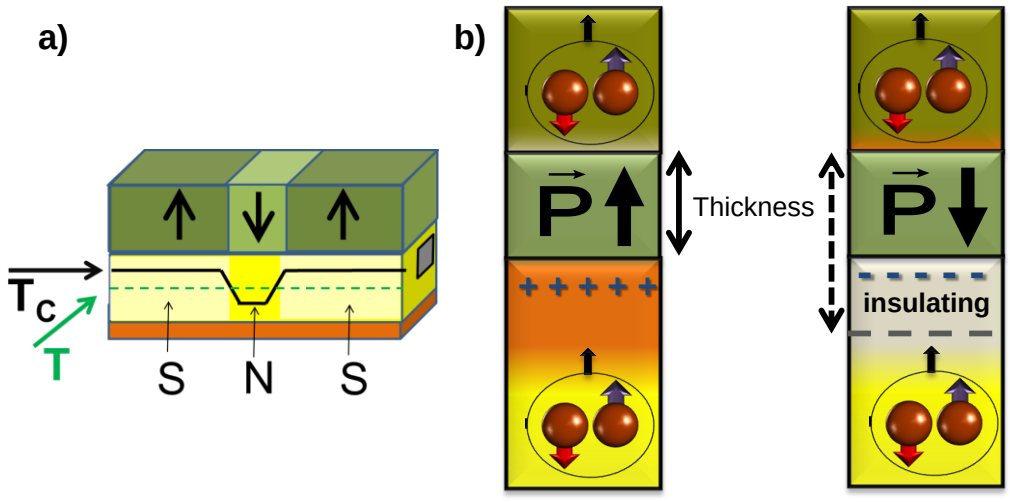

Figure II.24: Field-effect devices: a) Planar S/N/S junctions b) Vertical ferroelectric tunnel junction

III. Experimental techniques

Index

III. Experimental techniques 58

III.1 Growth techniques 59

III.1.1 Pulsed Laser Deposition 59

III.1.2 Sputtering and thermal evaporation 61

III.2 Characterisation techniques 62

III.2.1 Scanning Electron Microscopy 62

III.2.2 Scanning Transmission Electron Microscopy (STEM) 63

III.2.3 Scanning Probe Microscopy (SPM) techniques 63

III.2.4 X-Ray diffraction 67

III.3 Nano and micro fabrication 72

III.3.1 Generalities on fabrication 72

III.3.2 Fabrication of planar devices 75

III.3.3 Fabrication of planar devices with a gate 80

III.3.4 Fabrication of vertical devices: matrices of pads 82

III.3.5 Fabrication of micrometric vertical devices 83

III.3.6 Measurement set-up for electrical characterisation 84

In this chapter, we will describe the experimental techniques used for the fabrication and the characterisation of the films. We will also describe the lithography recipes optimised for the fabrication of our devices, and present the atomic force microscopy techniques that we use both to characterise our samples and manipulate the ferroelectricity at the nanoscale.

III.1 Growth techniques

III.1.1 Pulsed Laser Deposition

Pulsed Laser Deposition (PLD) is a Chemical Vapour Deposition technique that consists of sending short ($\sim 10\ ns$) laser pulses on a target of sintered materials. When the laser pulse impacts the target, and if the energy is high enough (this depends on the vaporisation enthalpy of the material and the local heating), the target is ablated: atoms and ions react and collide together, heat up, and form a plasma (the *plume*). This process is represented in Figure III.1.

PLD under oxygen atmosphere is one of the preferential techniques to grow oxides: unlike sputtering or evaporating that occur in a neutral atmosphere, here the target does not contain the materials in the desired stoichiometry, but it is in the plume that the species get oxidised before being adsorbed by the substrate.

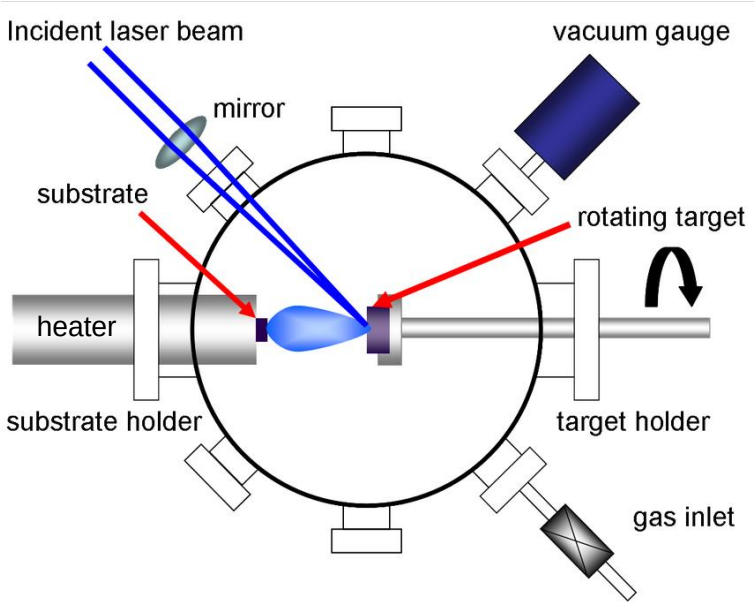

Figure III.1: Schematic representation of a PLD chamber

It is a complex growth technique, because the composition of the plume depends on many parameters: composition of the target, temperature, oxygen pressure, shape, density and profile of the laser pulse… Moreover the composition of the plume is not homogeneous; the species react with the oxygen as they travel through it: the target-to-substrate distance impacts the composition of the film. Adjusting these parameters is tricky since from one deposition to the other, some ageing occurs: the laser energy varies, the optics of the laser path blacken, the windows of the chamber get opaque (especially for low pressure deposition), the target composition changes locally in ablated areas…

In order to ensure the best quality and reproducibility for the depositions, many precautions were taken to grow the heterostructures studied in this thesis:

- The laser beam is cropped by a slit next to the lens, and an image of the spot is taken with thermic paper to check if the energy density profile is homogeneous and constant from a deposition to another.
- The energy of the spot is measured with a calorimeter, and is adjusted with an attenuator (the energy is usually high just after a gas refill, and decreases with the time).
- The lenses and windows are regularly cleaned with optical paper or replaced.
- In order not to etch the target always in the same spot, during one deposition the target draws a $6 \times 8\ mm^2$ zone, preablated for three minutes at the same rate and pressure than during the growth, in order to strip a layer that could have oxidise or been polluted.
- After a couple of depositions the target is sanded until it appears homogenous again.
- The plume is monitored with a camera, in order to check its shape, its size and its colour.
- The pressure is measured by a sensor in the deposition chamber.
- The temperature is measured on the substrate and on the sample holder with a pyrometer.

Growth modes

PLD works with a very high instantaneous rate, but with intermittence. In our PLD, the deposition is only homogenous over a cm^2. There are four main growth modes in PLD, represented on Figure III.2.

- *Step Flow*: each atom, when it reaches the surface, diffuses in a lateral way to the border of the step, which ensures a layer-by-layer growth mode, as each border grows parallel to the surface of the step.
- *Step Bunching*: this mode is close to the Step Flow mode, but some new steps appear before the steps underneath are fully covered by new atoms. It makes bunches of steps.
- *2D growth (Frank-van der Merwe)* [163]: many one-atom-thick islands appear on the surface; incident atoms diffuse either towards a step border, either towards an island border. Once the layer is completely covered, new islands grow on the upper layer.
- *3D growth (Volmer-Weber)* [164]: in this mode, new islands start to appear before the islands below merged into a layer.

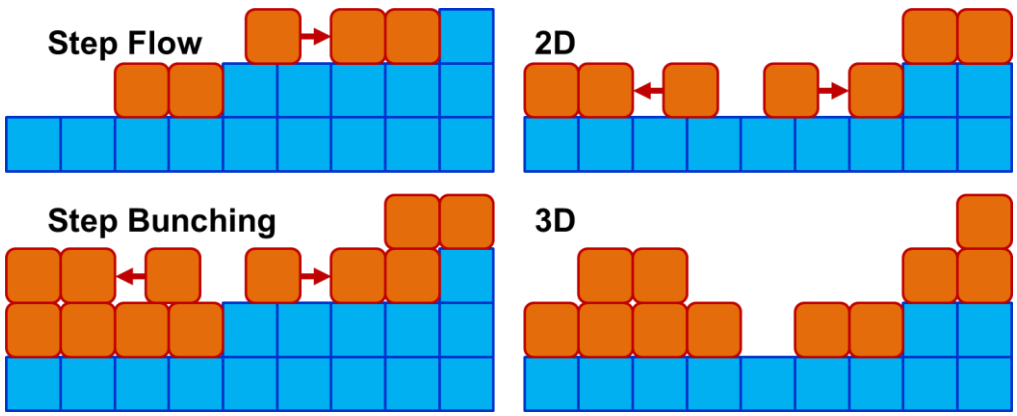

Figure III.2: Growth modes in PLD

III.1.2 Sputtering and thermal evaporation

Sputtering is a common deposition technique for thin films of metals. It consists in applying a voltage between a target (negatively polarised) and the walls of the chamber (positively polarised), in a low pressure atmosphere of Argon. The gas is ionised by the electric field, and the Ar^+ ions, attracted by the target, collide into it. If their energy is higher than the binding energy of the surface, atoms from the target are ejected, creating a cold plasma that condensates when it reaches the substrate.

Thermal evaporation, which is also used for the deposition of metallic films, is based on thermic phenomena. This technique consists of heating the target until the matter evaporates, in an ultra-low pressure chamber in order to lower the vaporisation temperature of the material.

In this thesis, evaporation and sputtering are used for the deposition of thin metallic films during the lithography process. They are two techniques that require neither cooling nor heating, but have several differences that have to be considered. First of all, evaporation is more directional, as represented in Figure III.3. This is an advantage for lift-off process: the metal is deposited in the bottom of the pattern and not on the borders, which can leave bulges once the resist gets removed.

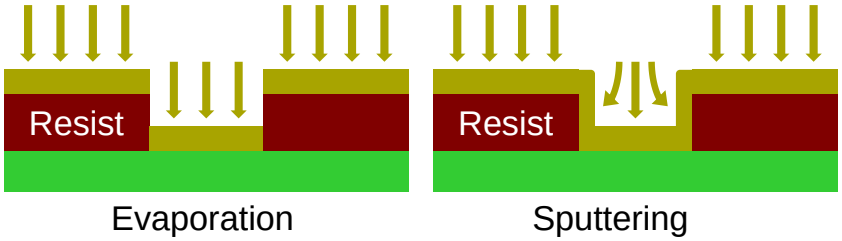

Figure III.3: Directionality: evaporation vs sputtering

When a metal is deposited on our films by one technique or the other, local heating of the substrate is induced, at least because of the heat of condensation during the deposition. For evaporation, the radiant heating also contributes, and for sputtering, the kinetic energy of the incident atoms and ions. The heating is comparable for small deposition rates, but sputtering heats more the substrate at higher rates [162]. To limit this effect, samples are usually stuck to a cooled sample holder with some grease or a resist that evacuates the heat. In the case of ultra-thin films of YBCO, it is better to avoid such uncontrolled heating: it can help the oxygen to migrate from the YBCO layer to the substrate or the BFO layer, which depresses the superconducting properties of the film. Finally, the adhesion is usually better for layers grown by sputtering compared to evaporation, because the atoms are more energetic when they arrive on the surface ($\sim 10\ eV$ compared to $\sim 0{,}1\ eV$), so they make better bonds with the atoms of the substrate.

III.2 Characterisation techniques

III.2.1 Scanning Electron Microscopy

A Scanning Electron Microscope (SEM) operates this way: an electron beam bombards the surface of the sample; like with classic optical microscopy, the electrons interact with the atoms of the surface, by reemitting electrons with a different energy. The fundamentals of this technique are well popularised in the review by K. D. Vernon-Parry [165], from which is taken Figure III.4 that represents the interactions between the electrons observed with the SEM and the atom:

- The retro-diffused electrons: they are primary electrons the trajectories of which were deflected by a quasi-elastic interaction with an atom kernel (Figure III.4 *a)* and *b)*). They are very sensitive to the atomic number of the atom they interacted with. They allow good contrast between the different observed phases.

- The secondary electrons: they are emitted when a primary electron transfers energy to an electron that belongs to the conduction band of the atom: it is thus ejected (Figure III.4 *c)* and *d)*). They are less energetic than the retro-diffused electrons. Their electrons give good indications on the topography of the sample.

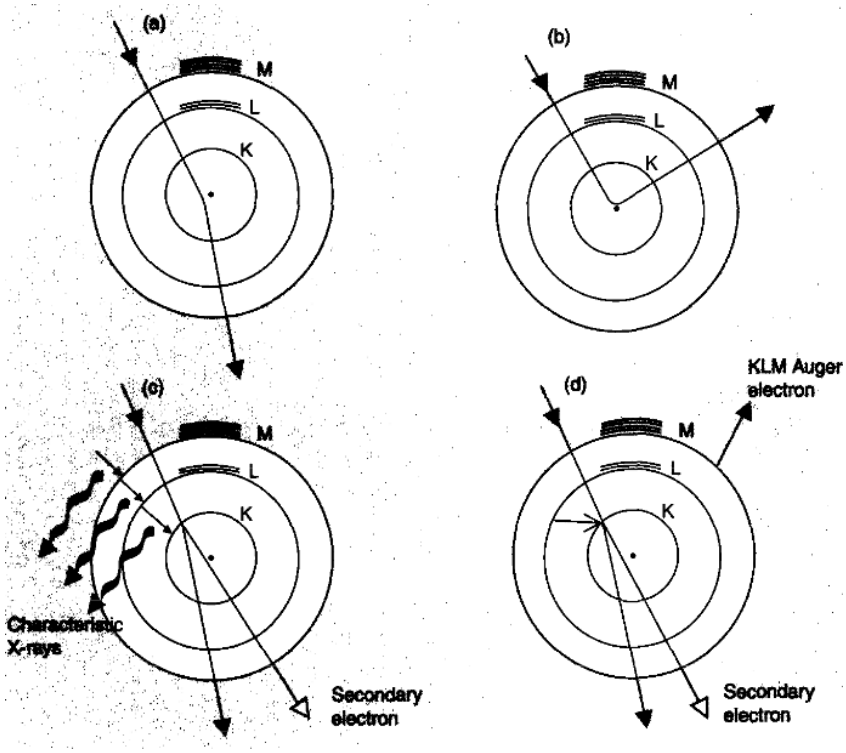

Figure III.4: Atom-electrons interactions. K, L, M… stand for the inner shells of the atom. a) Low-angle scattering - electrons scattered in this way pass to the next layer of atoms with very little loss of energy (b) Back (or high-angle) scattering; (c) Emission of a secondary electron and characteristic x-rays; (d) Emission of a secondary electron and an Auger electron. Taken from [165]

The resolution of a SEM is nanometric. It is a technique that allows a sample to be observed under different angles. It is very useful for example in growth or lithography optimisation processes, to observe the surface of the sample, the eventual parasite phases, the aspect of the devices…

III.2.2 Scanning Transmission Electron Microscopy (STEM)

A Scanning Transmission Electron Microscope (STEM) operates the same way as a SEM, but in transmission (not in reflection). Samples are thinned by polishing and ion milling to allow electron transparency. An electron beam is focused into a narrow spot which scans the sample. Along with a high-angle detector, it is possible to form atomic resolution images where the contrast is a function of the atomic number. Aberration correctors allow the resolution of STEM to reach the angstrom.

In traditional dark-field imaging, the Bragg scattered electrons are separated from the main beam by an aperture placed in the diffraction plane. High-Angle Annular Dark-Field imaging (HAADF) is a STEM technique that uses an annular dark field detector in order to collect electrons not only though an aperture but also scattered electrons around the beam, in the shape of an annulus. The signal is significantly increased, and in the meanwhile the main beam can be analysed though an EELS detector. Thanks to an electron spectrometer, the EELS detector measures the amount of energy lost by each electron when it interacted with the sample. This loss depends on the atoms, chemical bonding, valence and conduction band electronic properties, surface properties, and element-specific pair distance distribution functions, which allows the identification of atoms. These two simultaneous measurements, HAADF and EELS, provide high-resolution imaging of the sample and identification of the atoms.

III.2.3 Scanning Probe Microscopy (SPM) techniques

Many microscopy techniques were developed in order to image objects much smaller than the visible wavelength, like SEM that can reach a resolution of a few nanometres, or STEM that can spatially discern atoms. Imaging with SPM is conceptually different, because it is a near field microscopy based on scanning tip, able to probe the topography of the surface, but also many other physical properties (conducting, ferroelectric or magnetic properties…). Vertical resolution is subnanometric, and horizontal resolution, limited by the tip sharpness, can reach few nanometres.

III.2.3. a) AFM (Atomic Force Microscopy)

The principle of this technique, represented in Figure III.5, is the following: the tip is carried by a horizontal cantilever on which a laser beam is reflected towards photodiodes. A piezoelectric actuator enables the tip to approach the surface, and two others to move horizontally and scan an area (typically from $100\ nm$ to $50\ \mu m$). The height of the cantilever with respect to the sample holder is kept constant: when the tip encounters asperities at the surface of the probed area, it deflects the cantilever and displaces the reflection of the laser beam on the photodiodes. A feedback loop drives the vertical piezoelectric actuator in order to maintain the deflection constant. From this signal, the profile of the scanned surface is reconstituted.

There are two main interaction modes between the surface and the tip:

- In «contact mode», the interactions between the surface and the tip are repulsive, and there is a retroaction on the cantilever deformation so that it always stays in contact with the surface.
- In «non-contact» mode, the tip is just flying above the surface and is attracted by long range Van de Waals interactions. The microscope electronics determine the eigenfrequency of the cantilever/tip system ($\sim 300\ kHz$). Once the tip approaches the surface of the sample, the

cantilever is excited at this frequency, with an amplitude setpoint determined by the user. In this “non-contact” mode, the interactions between the tip and the surface modify the resonance frequency of the cantilever, and thus reduce the amplitude of the oscillation. A feedback loop maintains the constant reduced amplitude of the oscillation, or tip-sample interaction while scanning.

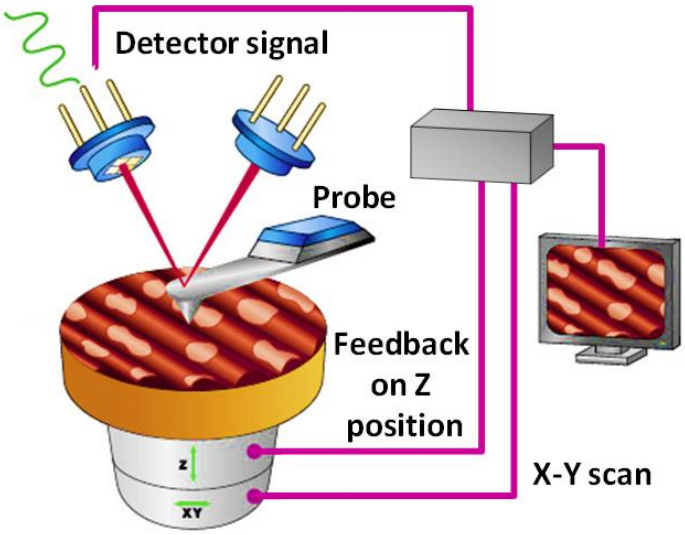

Figure III.5: Principle of SPM imaging

The mode of imaging that gives the best representation of the topography of the sample is the intermittent contact / non-contact mode (« tapping »). It takes advantages of both techniques: most of the time (the tip only stays in contact mode during a few dozens of microsecond at each pixel), the tip interacts in non-contact mode, thus preserving the tip sharpness, without modifying the surface. In constant contact mode, the shape of the tip could quickly get blurred, or might damage the film surface. It is widely used to study thin films, for the optimisation of the growth, to get information on the film quality, the smoothness of the surface, the shape of potential parasitic phases or rocks. It is an easy, fast and non-destructive technique.

III.2.3. b) PFM (Piezoresponse Force Microscopy)

PFM (Piezoresponse Force Microscopy) is by far the most popular technique to study ferroelectric thin films. This technique is based on the converse piezoelectric effect and requires the presence of a metallic bottom electrode: a voltage is applied across the layer, between the tip – in contact mode – and the bottom electrode. As it is not easy to define a potential in a sharp object, the tip is usually grounded and the potential is applied to the bottom electrode. To image domains, an AC excitation (typically $1\ V_{PP}$) is applied: as depicted in Figure III.6 *a)*, in the tip-grounded configuration, domains that point up respond in phase with the excitation (they expand when the tension is positive) whereas the downwards domains are in opposition of phase.

The set-up is schematised on Figure III.6 *b)*: this mechanical vibration is transmitted to the tip and the cantilever, and is measurable by the vibration of the reflected laser beam into the photodiodes; this signal contains both the low frequency contribution of the topological signal and

the piezoelectric response (typically at $35\ kHz$) which is then analysed by a lock-in to extract the phase and the amplitude of the signal in any points of the scanned area.

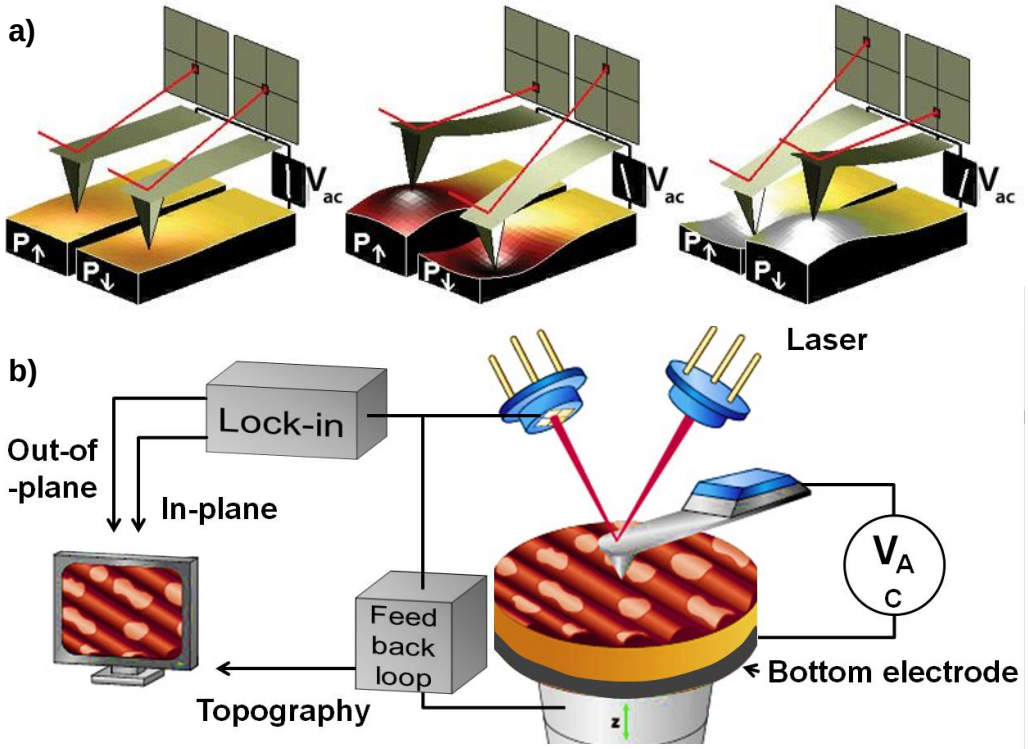

Figure III.6: a) Piezoelectric effect under the tip (figure courtesy of S. Jesse, ORNL); b) Principle of the PFM set-up

Very easy to implement, it is also a technique that is not very sensitive to the topography of the sample and that can be used on many kinds of crystals or thin films. It can spatially resolve ferroelectric domains, bring quantitative and comparative information on these domains but also on the domain walls. PFM can also be used to write ferroelectric domains, measure their temporal and/or thermal evolution, measure local hysteresis cycles, access to the piezoelectric coefficients of the material etc.

As an illustration, Figure III.7 is a PFM image of a 70 *nm* BFO film (the bottom electrode is $SrRuO_3$):

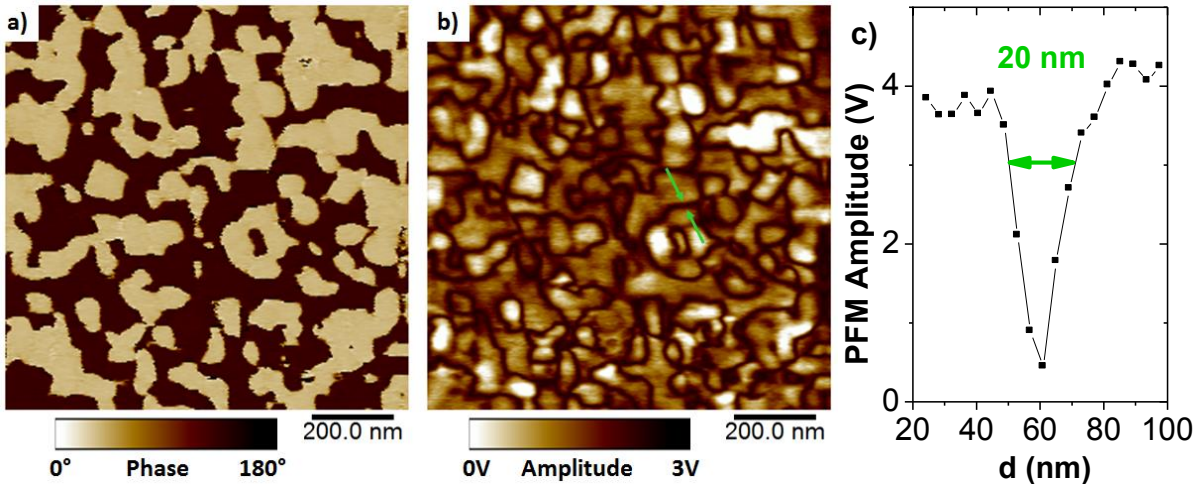

Figure III.7: PFM image of a BFO (70 nm)/SRO film. a) Phase and b) Amplitude of the signal. c) Amplitude of the signal across the domain wall between the two arrows in b).

Figure III.7 *a)* is the phase of the signal: white domains polarisation points towards the SRO film and black domains outwards. Figure III.7 b*)* is the amplitude of the piezoelectric signal: we can see that between two domains, it falls to zero. The width of the domain wall, here $\sim 20\ nm$ (see Figure III.7 c*)*) depends on the sharpness of the tip and the noise of the setup.

It is also possible to access the lateral components of the polarisation, because the mechanical vibrations of the ferroelectric domains in the plane twist the cantilever. In practice, to image these components we use longer and more flexible cantilevers than for vertical PFM, but in-plane and out-of-plane polarisation can be imaged simultaneously. PFM is a very powerful tool, as it can image ferroelectric domains but also write them, by using the tip as a top-electrode. To do this, it is no longer an AC voltage but a DC voltage that is applied, higher than the coercive field of the ferroelectric. Thin films are sometimes very heterogeneous, and it happens that the coercive field changes from one domain to the other. It is useful to determine the mean coercive field of an area, by scanning zones with different voltages and then imaging the area to determine which zones correspond to a complete switching of the polarisation. Figure III.8 represents the PFM image (phase and amplitude of the signal) of a BFO-Mn $(30\ nm)$/YBCO/PBCO//STO structure on which a large square was first written by applying a positive voltage $(+6\ V_{DC})$ between the YBCO layer and the tip, then a smaller square was written by applying $-6\ V_{DC}$. The polarisation is then imaged by applying an AC voltage.

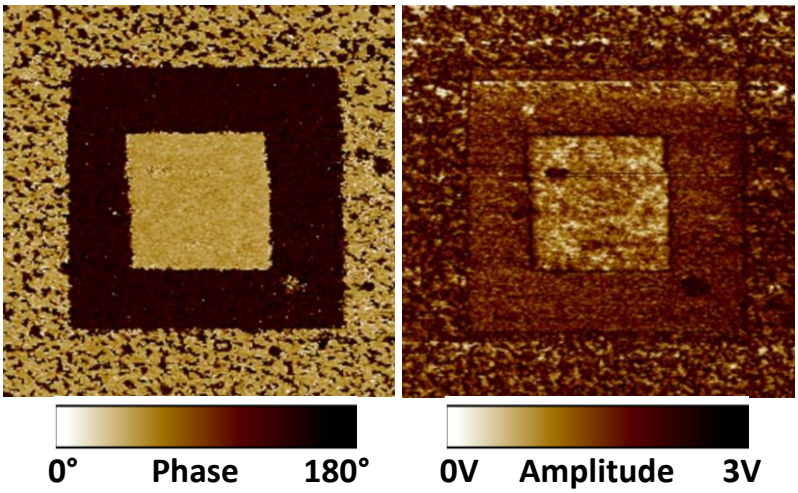

Figure III.8: PFM image of a BFO-*Mn* (30 nm)/YBCO/PBCO//STO structure

III.2.3. c) Conductive-tip AFM

The topographic images of thin films can reveal the presence of parasite phases or precipitates at the surface of the sample. It is sometimes possible to identify them by their characteristic shape, or by X-rays diffraction techniques. The CT-AFM can give additional information, as it can measure the local resistivity of a thin film. It is useful during growth optimisation, for example in the case of ultra-thin layers for tunnel junctions applications. Indeed, CT-AFM imaging can figure out whether eventual parasite phases are short-circuiting the insulating layer or assess the expected exponential dependence of the tunnelling current with the barrier thickness [24], [25].

Like PFM, this technique uses a conductive tip in contact mode, and needs a conductive bottom electrode below the insulating layer. A voltage is applied between the tip and the electrode, and an amperemeter measures the current necessary to reach the voltage setpoint. As the current is very small under the AFM tip, a current amplifier is implemented in the circuit (logarithmic amplifier for the CT-AFM). A cartography of the local resistance of the sample is thus obtained, as in Figure III.9 *b)*.

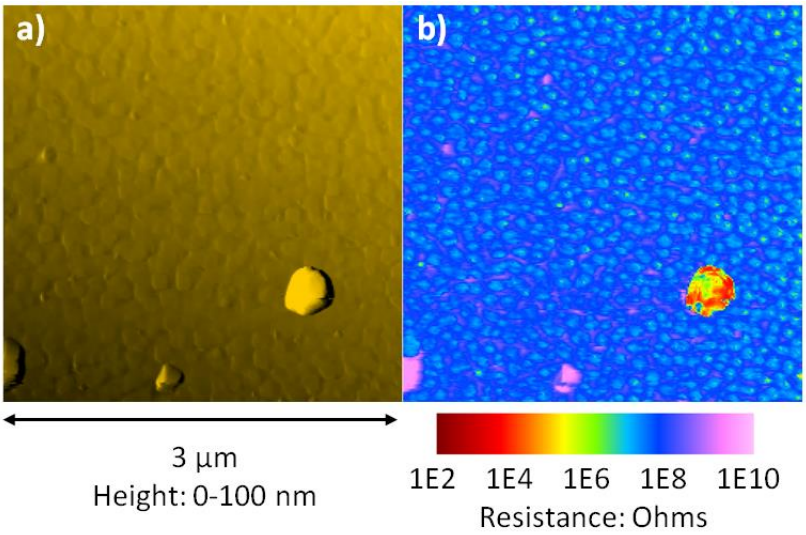

Figure III.9: a) Topography and b) CT-AFM images of a BFO-Mn/YBCO/PBCO//STO structure

This technique is limited by the serial resistance of the tip for poorly insulating layers, and by the compromise on the low-currents sensitivity of the amperemeter for highly insulating layers. In addition, applied voltages should be below some threshold value to avoid dielectric breakdown and damage of the studied layer.

III.2.4 X-ray diffraction

X-ray diffraction is a characterisation technique based on the interaction between X-rays and the electronic clouds of a material. X-rays are electromagnetic radiation of wavelength ranking from $0{,}01$ to $10\ nm$. X-rays with wavelength comparable to the size of the atom ($0{,}1\ nm$) are convenient to study crystallised material, as they provide information on the structure of lattice matched thin films:

- Crystalline structure of the material, and possible parasite phases
- Measurement of the lattice parameters of the crystal, and the thickness of the films (in practice, from a few to hundreds nanometres)
- Measurement of the broadening of the rocking curve due to crystal imperfections.

When the X-rays arrive at the surface of the sample, they induce (like any electromagnetic wave) a displacement of the electronic cloud with respect to the shell of the atoms. This is followed by the reemission of electromagnetic waves in the whole space, of the same wavelength and energy (Rayleigh diffusion). This technique suits very well the study of crystals, because the waves emitted by the regularly spaced atoms interfere either constructively or destructively depending on the direction of the rays.

Production of X-rays

X-rays are produced by bombarding a metal target (Cu, Mo…) with a beam of electrons emitted from a hot filament (usually tungsten). The incident beam ionises electrons from the K-shell ($1s$) of the target atom and X-rays are emitted as the resultant vacancies are filled by electrons dropping down from the L ($2p$) or M ($3p$) levels. This gives rise to K_α and K_β lines, as well as a broad background. Filters and monochromators can be used to select a wavelength. In our case, the incident beam has two wavelengths ($\lambda_1 = 1{,}5406$ Å and $\lambda_2 = 1{,}5439$ Å) coming from the K_{α_1} and K_{α_2} lines of Cu.

Principle

We define the diffraction plane as the plan containing the incident and the refracted beams, as represented in Figure III.10. An atomic plan will diffract if the angle θ between the incident beam and the atomic plane satisfies the Bragg condition:

$$2d_{hkl} \sin\theta = n\lambda \qquad \text{(II.1)}$$

with d_{hkl} the interreticular distance between the diffracting planes, n the order of diffraction and λ the wavelength of the incident X-rays.

We define $\overrightarrow{n_s}$ the normal to the surface and $\overrightarrow{n_p}$ the normal to the diffracting planes, ω the angle between the incident beam and the intersection between the diffraction plane and the surface of the sample, Ψ the angle between $\overrightarrow{n_s}$ and the diffraction plane, and Φ the angle defining the rotation of the goniometer around the direction $\overrightarrow{n_s}$.

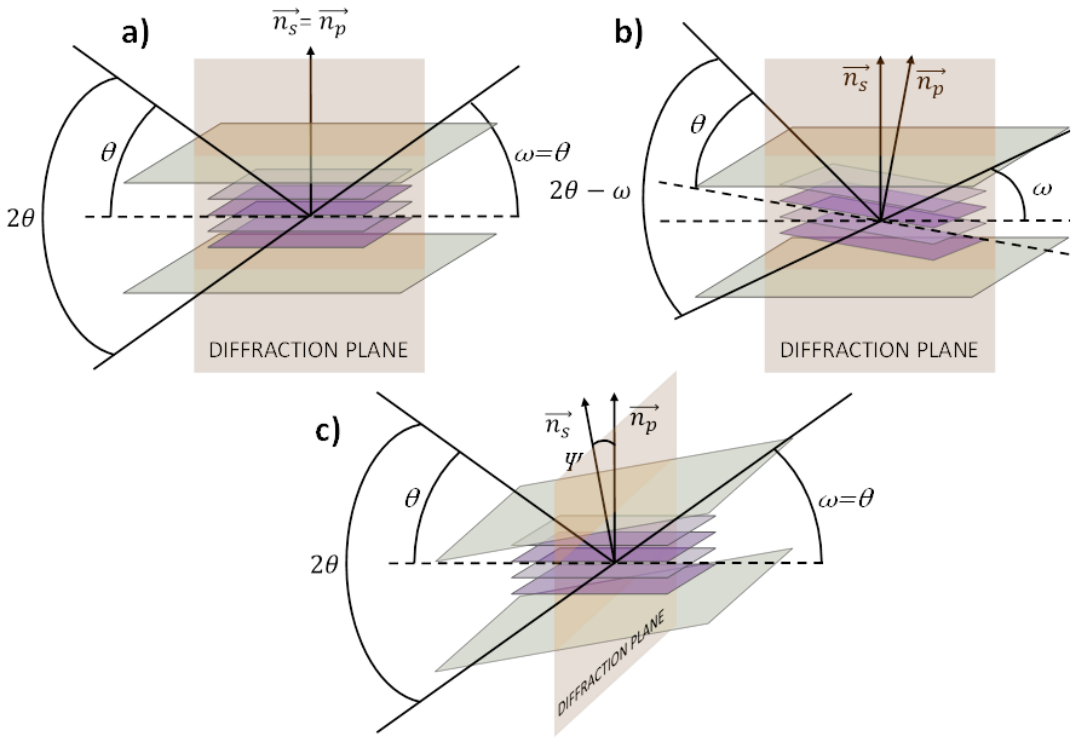

Figure III.10: Representation of the a) symmetric with $\Psi = 0°, \theta = \omega$ b) asymmetric with $\Psi = 0°, \theta \neq \omega$, c) asymmetric with $\Psi \neq 0°, \theta = \omega$.

Depending on the studied planes, different configurations are possible:

- If the diffracting planes are parallel to the surface, we can use the symmetric configuration ($\theta = \omega$ and $\Psi = 0°$).
- If the diffracting planes are not parallel to the surface, two asymmetric configurations are possible: either by uncoupling the movements of the beam and the detector ($\theta \neq \omega$ and $\Psi = 0°$), or by moving the sample holder to bring the diffracting planes in the Bragg conditions ($\theta = \omega$ and $\Psi \neq 0°$).

Structural analysis

Scans of crystalline layers exhibit a diffraction peak when the Bragg conditions are fulfilled. The position of the peak is directly linked to the lattice parameters, according to a relation that depends on the symmetry of the crystal. Table III.1 gives these relations for the principal symmetries.

The strain and the homogeneity of the film or crystal will highly influence the position and the width of the peak: a film that is strained by its substrate will exhibit a shift of the diffraction peak (to the left for a compressive strain, to the right for a tensile strain). A film that relaxes and has different strains, or a film that has dislocations, will exhibit a large peak as the sum of the different contributions.

"$\boldsymbol{\theta - 2\theta}$" scan: The source is immobile and both the detector and the sample rotate, in order to maintain an angle equal to 2θ, typically from 10 to 110°.

"$\boldsymbol{\theta - \theta}$" scan: The sample is immobile and both the source and the detector rotate, in order to maintain an angle equal to 2θ, typically from 10 to 110°. This is the configuration used for the structural analysis of the samples presented in this thesis, either in a Bragg-Brentano geometry, either with an hybrid parallel beam.

In these two equivalent configurations, if we scan for example a film on a substrate oriented along the 001 direction, the $(00l)$ diffraction peaks of the substrate will be measured. If $(00l)$ diffraction peaks are also obtained for the film, it means that the film grew in a textured way at least along the out-of-plane axis. As an example, Figure III.11 represents a $\theta - 2\theta$ scan for a BFO-Mn (30 nm)/YBCO (4 $u.c.$)/PBCO (4 $u.c.$)//STO heterostructure. BFO-Mn and STO peaks are indexed by blue and green arrows. YBCO and PBCO signals are merged, as their atomic structures are very close. They are indexed by the black arrows in Figure III.11; because of the bigger $c = d_{001}$ lattice parameter, the peaks are nearer compared to BFO and STO. The positions of the peaks allow the determination of the out-of-plane lattice parameter c, thanks to the Bragg formulae (II.1). If the quality of the film is good, the diffraction peaks are surrounded by fringes. The thickness of the film can then be estimated from the angular spacing of these fringes ($\Delta\omega$) by a relation derived from the Bragg law:

$$t = \frac{\lambda \sin(\theta + \Psi)}{\Delta\omega \sin(2\theta)} \qquad \text{(II.2)}$$

"$\boldsymbol{\omega}$" scan – Rocking Curve: the diffraction conditions are fulfilled and 2θ is fixed. ω varies around $\omega = \theta$. The width of the peak gives an indication of the orientation distribution of the studied plans and thus on the quality of the epitaxy.

Symmetry	Axis and angle	d-spacing
Cubic (1)	$A = B = C$ $\alpha = \beta = \gamma = 90°$	$\frac{1}{d^2} = \frac{h^2 + k^2 + l^2}{a^2}$
Tetragonal (2)	$A = B \neq C$ $\alpha = \beta = \gamma = 90°$	$\frac{1}{d^2} = \frac{h^2 + k^2}{a^2} + \frac{l^2}{c^2}$
Orthorombic (3)	$A \neq B \neq C$ $\alpha = \beta = \gamma = 90°$	$\frac{1}{d^2} = \frac{h^2}{a^2} + \frac{k^2}{b^2} + \frac{l^2}{c^2}$
Hexagonal (4a)	$A = B \neq C$ $\alpha = \beta = 90°,$ $\gamma = 120°$	$\frac{1}{d^2} = \frac{4}{3}\frac{h^2 + hk + k^2}{a^2} + \frac{l^2}{c^2}$
Rhombo-hedral (4b)	$A = B = C$ $\alpha = \beta = \gamma \neq 90°$ $< 120°$	$\frac{1}{d^2} = \frac{(h^2 + k^2 + l^2)\sin^2\alpha + 2(hk + kl + hl)(\cos^2\alpha - \cos\alpha)}{a^2(1 - 3\cos^2\alpha + 2\cos^3\alpha)}$
Monoclinic (5)	$A \neq B \neq C$ $\alpha = \gamma = 90°,$ $\beta > 90°$	$\frac{1}{d^2} = \frac{1}{\sin^2\beta}\left(\frac{h^2}{a^2} + \frac{k^2\sin^2\beta}{b^2} + \frac{l^2}{c^2} - \frac{2hkl\cos\beta}{ac}\right)$

Table III.1: d spacing for different symmetries

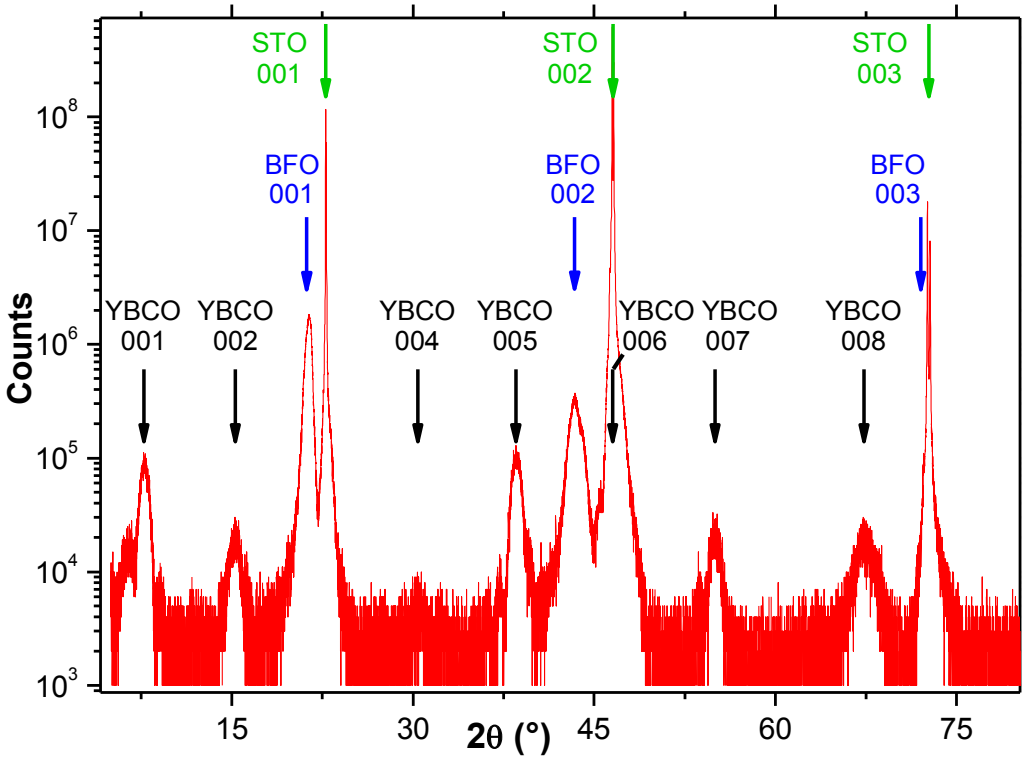

Figure III.11: $\theta/2\theta$ XRD scan of a BFO/YBCO/PBCO//STO heterostructure

Structure Factor

In a simple cubic lattice, the scattered intensity scales with the charge of the only atom in the unit cell; when considering more complex structures, the charge distribution of the whole cell contributes to the intensity. How the material scatters the incident radiation is described by a structure factor F, given by:

$$F = \int_{u.c.} \rho_e(\boldsymbol{r}) e^{-i\boldsymbol{Q}\boldsymbol{r}} d\boldsymbol{r} \tag{II.3}$$

with $\boldsymbol{r}$ a distance vector, $\rho_e(\boldsymbol{r})$ the charge distribution, and $\boldsymbol{Q}$ the scattering vector. For a perfect crystal, F is the vector sum of waves from all the N atoms within the unit cell and is expressed as:

$$\boldsymbol{F}_{hkl} = \sum_{j=1}^{N} f_j e^{-2i\pi(hx_j+ky_j+jz_j)} \tag{II.4}$$

where x_j, y_j and z_j are the position coordinates of the j^{th} atom and f_j the scattering factor of this atom. $\boldsymbol{F}_{hkl}$ and thus the scattered intensity depend on the Miller indices h, k and l. As an example, the expression of the structure factor for a face-centered cubic crystal is:

$$\begin{aligned} \boldsymbol{F}_{hkl} = f \sum_{j=1}^{4} e^{-2i\pi(hx_j+ky_j+jz_j)} &= f\left[1 + e^{-i\pi(h+k)} + e^{-i\pi(k+l)} + e^{-i\pi(l+h)}\right] \\ &= f[1 + (-1)^{h+k} + (-1)^{k+l} + (-1)^{l+h}] \end{aligned} \tag{II.5}$$

with the result:

$$\boldsymbol{F}_{hkl} = \begin{cases} 4f, & h,k,l \text{ all even or all odd} \\ 0, & h,k,l \text{ mixed parity} \end{cases} \tag{II.6}$$

It appears that when the Miller indices h, k and l do not have the same parity, the intensity of the peak is expected to be zero. The calculations for the perovskites studied in this thesis can be found in references [166] and [167]. As an example in Figure III.11, the 004 diffraction peak of YBCO undergoes a complete extinction.

X-ray reflectometry:

X-ray reflectometry can measure the thickness of thin films from a few to hundreds of nanometres. Based on the interference between the reflected waves at the different interfaces of the structure, it is a technique that is able to discriminate several layers in the same heterostructure, as long as the electronic densities of the layers are different enough. These measurements are done at very low angle (typically below $2\theta = 5°$). For an angle θ smaller than the critical angle θ_C, the beam is totally reflected by the surface of the sample. This angle depends on the optical index of the film, *i.e.* from its electronic density. For higher angles, the beam penetrates the film and is partially reflected at each interface. Depending on the phase difference between the reflected waves, they interfere either constructively or destructively, giving rise to oscillations in the $\omega - 2\theta$ scan. The period of these oscillations is directly related to the spacing between the two reflecting interfaces, *i.e.* to the thickness of the layer.

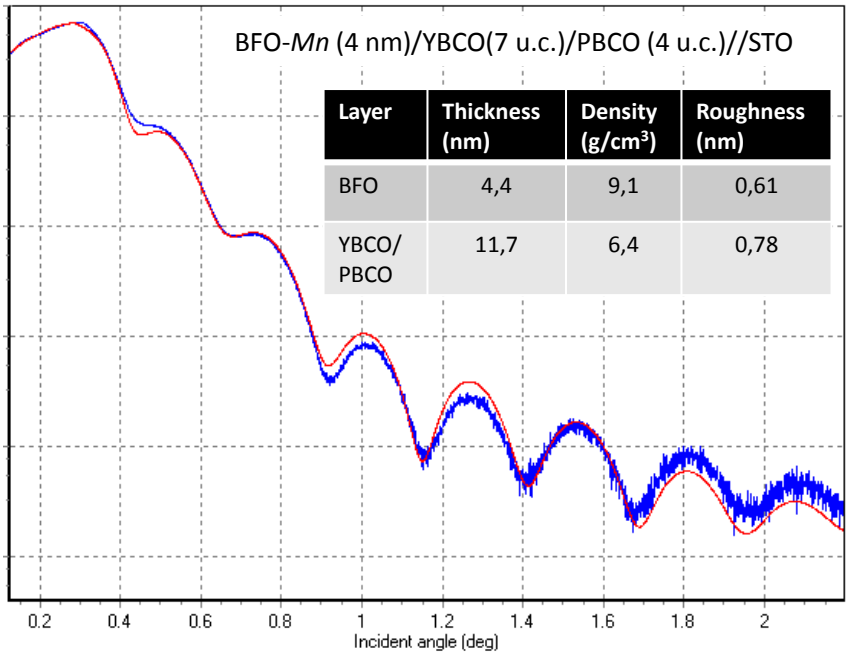

Figure III.12: XRD reflectometry scan of a BFO/YBCO/PBCO//STO heterostructure

As an example, Figure III.12 represents a reflectometry scan for a BFO-Mn $(4\ nm)$/ YBCO ($7\ u.c.$)/ PBCO $(4\ u.c.)$//STO heterostructure. The electronic densities of YBCO and PBCO are very close and no reflection occurs at their interface. The contributions of the BFO-Mn film and of the YBCO/PBCO bilayer are convoluted; the oscillations can be fitted with a simulation program such as X-Pert Reflectivity in order to estimate the thickness of the layers and their electronic densities. These oscillations are based on the interference of several waves; indeed, if the interfaces are too rough, the oscillations disappear.

III.3 Nano and micro fabrication

We now present the basic techniques for the lithography of the samples. The fabrication of micrometric electronic devices is based on two main kinds of process: the first one consists in etching layers to design the device, the second option consists in filling a negative of the device in an amorphous matrix with the desired materials. In both cases, the masks are reproduced on the device using photoresist.

III.3.1 Generalities on fabrication

Cleaning the sample:

The sample has to be perfectly clean; most of the impurities like glue or dust can be removed by simply rinsing it with acetone or propanol. In some case it is necessary to use a pressurised beam, or ultrasounds bath if the sample is robust. To desorb an organic material or water at the surface of the sample, it is useful to dry it one minute at 90°C, which helps a lot the resist to wet the surface. Another option is to use a primer, *i.e.* a solution of molecules that have both hydrophilic and hydrophobic parts, to help the resist to wet the sample.

Choosing the resist:

Resists are made out of a solvent (that is mainly responsible for the viscosity of the resist), a matrix (that gives to the film its mechanical and thermal properties after polymerisation) and a photosensitive component (that will modify the chemistry or the polarity of the matrix after insulation, and thus its solubility). Depending on their composition, the minimum size of the pattern (holes or islands), the shape of the borders after revelation of the pattern varies. Other criteria have to be taken into account, such as the compatibility between the resist and some solvents used during the process, the compatibility between the sample and the developer, and with the temperatures needed to work with the resist.

Resist coating:

To spread the resist on the surface of the sample, it is placed at the centre of a rotary sample holder that maintains the sample with vacuum. A small quantity of resist is dropped in order to form a meniscus that covers the whole sample but that does not leak on the borders. The resist in then spread by spin-coating: the duration, the acceleration and the rotating speed defines the thickness of the resist film but also its homogeneity at the surface of the sample. What is the compromise on this thickness? Spin coating is quite tough for little samples (few mm), because a bulge of $\sim 1\ mm$ forms at the border, which reduces a lot the exploitable surface. For big samples ($> cm$) the very first step is crucial: the resist has to wet the whole sample, but homogenously enough so that its thickness is the same everywhere after the spin-coating.

Annealing:

The resist is liquid enough to be coated easily. A first annealing is necessary to evaporate the solvents and stabilise the film.

Insolation:

Optical lithography: A mask made out of glass is approached in contact with the surface, and aligned with the sample. In practice, it is the corners of the sample that touch the mask first, where the resist is the thickest (as represented in Figure III.13). Interference fringes are observed in the contact areas and enable us to control the space between the sample and the mask. If the bulges are too thick, the mask might stay far from the surface of the sample and it can lower the resolution of the pattern, because UV will diffuse between the mask and the sample. In this case, the borders can be removed by a first insolation / development step.

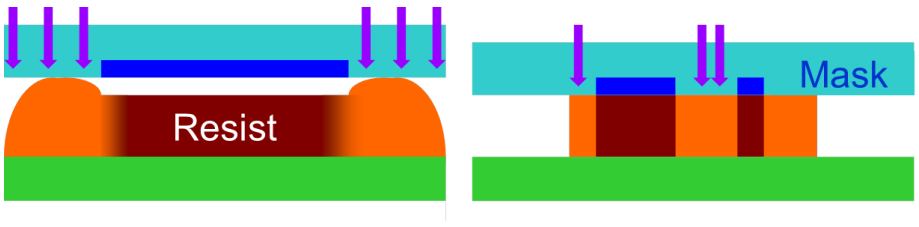

Figure III.13: Removing the resist borders from the sample

The resist is photosensitive: when it is insulated with UV, it polymerises. The beams diffuse in the resist underneath the patterns of the mask: the insolation time is a compromise between the minimum amount of energy to polymerise completely the resist and the maximum amount to keep a good resolution. It depends on the resist, its thickness, and the resolution needed.

Electron beam lithography:

Optical lithography is a fast and easy technique because a large surface can be insulated at the same time, but it is difficult to obtain submicrometric resolution. An alternative to optical lithography is electronic lithography: a focused beam of electrons scans a surface determined by a mask which is encoded in the computer that monitors the beam. It is a technique that is much slower than photolithography, as the "insulation" is made pixel by pixel, but it can reach a resolution of $\sim 10\ nm$ and the mask can be very easily modified. The resists used for e-beam lithography have different chemical compositions from those used for optical lithography.

Development:

The resist is associated to a developer, solution in which it is soluble (resp. insoluble) if it is polymerised and insoluble (resp. soluble) in its basic formulation: we talk of positive (resp. negative) photoresist. The concentration of the developer, the mechanic agitation, and the development time define the resolution of the patterns. The development is stopped by rinsing the sample in another solution. In some cases, heating the resist at very high temperature and for a long time, or insulating a negative resist for a very long time can turn it insoluble to the developer or to acetone.

Once the resist is developed, the following step in the process can be the etching of the material that is not covered by the resist. Many «dry» etching techniques exists, such as Ion Beam Etching, plasma etching, Reactive Ion Etching, or «wet» etching that is based on chemical reactions.

Ion Beam Etching (IBE):

IBE is a very convenient way to etch thin films; it consists in bombarding the surface of the sample with Argon atoms ionised in a plasma. The power of the plasma, the angle between the beam and the surface of the sample define the etching rate and the shape of the borders. The etching can be monitored with a SIMS spectrometer (Secondary Ion Mass Spectrometry) that identifies the etched species with their atomic masses, and enables a very precise control of the advancement of the etching.

Removing the resist:

Resists are usually soluble in acetone; however it can happen that a hardened layer forms at the surface. This "crust" can be stripped with a cold O_2 plasma.

Oxygen plasma:

Oxygen plasma, combined or not with other gases such as Argon or CF_4, has three main applications:

- Cleaning non-metal materials by removing organics and water.
- Modifying the surface chemistry (for example prior to bonding, to improve wettability).
- Reactive ion etching.

Lift-off :

Lithography can also be used to print a mask on the device prior to the deposition of another material. The deposited material might not stick well to the surface and lift with the resist when it is removed. To solve this problem, the profile of the resist is etched in such a way that the borders of the pattern form a cap, as schematized in Figure III.14. To do this, the surface of the resist is hardened in a chlorobenzene bath for ten minutes, before insulating and developing it [168]. Because the surface is harder, the resist is more developed below. Thanks to this profile, during the

deposition the material will be deposited on the surface of the resist and inside the patterns, but not on the borders and will lift-off more easily.

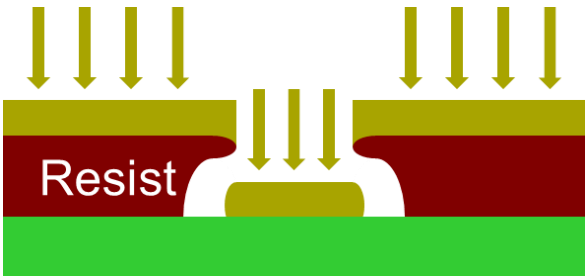

Figure III.14: "Casquette" lithography

We now detail the lithography processes optimised for the fabrication of the different devices studied during this thesis.

III.3.2 Fabrication of planar devices

The planar devices are made from $5 \times 5\ mm^2$ BFO-Mn ($30\ nm$)/YBCO ($2{\sim}5$ u.c.)/PBCO//STO heterostructures; their growth is detailed in chapter IV. Planar devices consist in a long and thin measurement bridge as schematized in Figure III.15, in the middle of which a junction is defined. Hall bar geometry is used, in order to perform carrier density measurements as well as to measure the resistivity through the junction. The width of the channel is a compromise between keeping good superconducting properties and handling big devices. Thin channels with width below $5\ \mu m$ have usually very low T_cs: close to the borders of the bridge, the YBCO is damaged and only the core of the channel is superconducting. Thick channels (with widths larger than $20\ \mu m$) are not easy to work with: we will see later that in order to control the polarisation of the ferroelectric film, we scan the measurement bridge with a nanometric probe. Such scans take a long time to go through all the surface of the bridge. Therefore, $10{\sim}15\ \mu m$ is a good compromise for the width of the bridge.

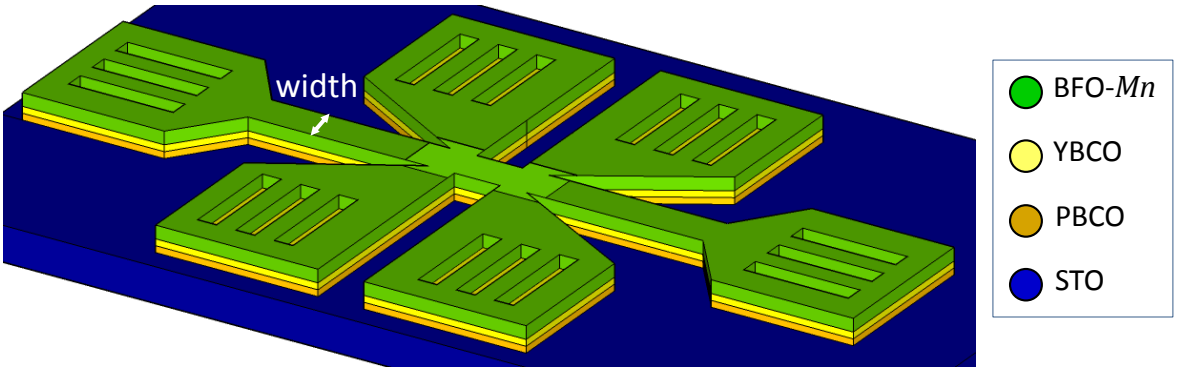

Figure III.15: Scheme of a measurement bridge

The lithography process has been optimised to favour good contacts and to minimise the damages caused to the superconducting layer. It underwent two main evolutions during this project: first of all, we investigated how to improve the robustness of our devices with regard to ageing. For this, we focused mainly on the IBE parameters and studied the impact of a step implying an O_2 plasma. In parallel, we modified the technology process in order to improve the quality of the contacts and reduce the noise during the measurements.

Robustness of the devices:

The planar devices do not have any top-electrode: this allows us to define the ferroelectric polarisation with a PFM tip, and to "write" junctions of any possible width. This implies that to fully characterise the device, it has to be taken in an out of the cryostat each time the ferroelectric state is modified. We faced a drastic problem of ageing of the samples: as explained in chapter VI, the superconducting properties were depressed after each introduction in the cryostat. Several observations allowed us to understand that the IBE step during the lithography was mostly responsible for this ageing. We decreased the power of the IBE to the minimum possible value in order to reduce the local heating of the sample. Moreover, we investigated the role of a cold O_2 plasma, which is a common technique used after IBE to help removing the resist.

In order to figure out if this step could have a positive (re-oxygenation of our samples) or a negative (local heating and eventual damage during the plasma) effect, we compared two pieces from the same sample, one that had an O_2 plasma after the IBE etching (Figure III.16; right) and one that did not (Figure III.16, left). We proceeded to a resistance versus temperature measurement of the two devices simultaneously a first time, then bring them back to room temperature and measured them from low temperature again. We observed that the sample that had not been exposed to the plasma had a lower critical temperature, a higher resistivity, and that the superconducting properties deteriorated from one cycle to the other (blue curves in Figure III.16). On the contrary, the sample that had been exposed to the plasma show no ageing (green curves in Figure III.16): this suggest that the plasma has a role of reoxygenating both YBCO, PBCO, STO and BFO-Mn, preventing YBCO very mobile oxygen atoms from migrating to the other oxides.

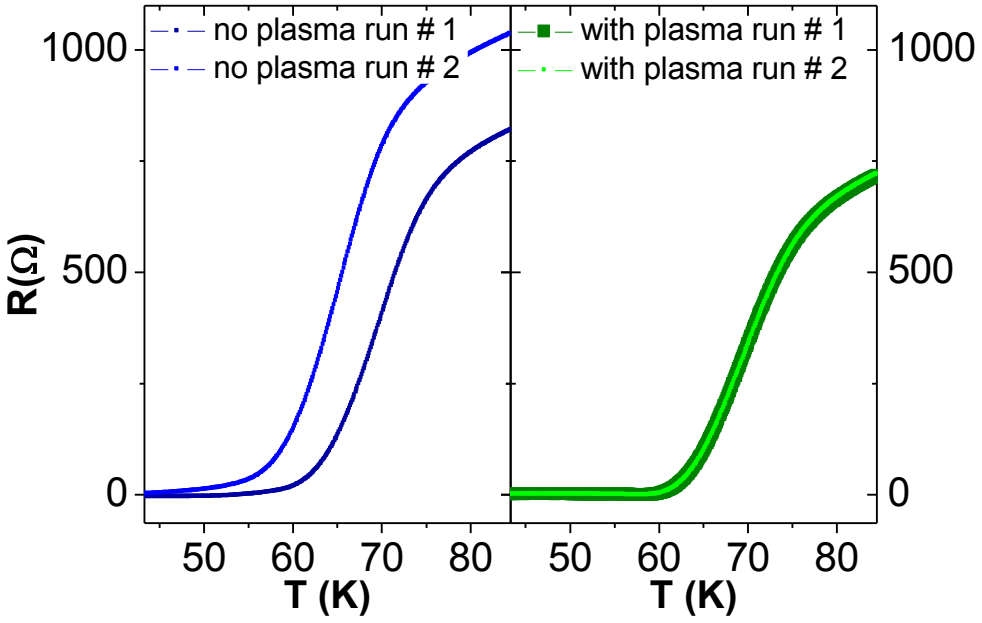

Figure III.16: Incidence of a cold O_2 plasma after IBE on the thermal cycling of YBCO layers

Electrical contacts

We then figured out a way to improve the electrical contact of the YBCO layer. The contact pads are bonded to the gold pads of a measurement chip with wires. To contact the YBCO layer through the

BFO-Mn film, an easy technique consists in wedge-bonding directly the wire to the structure with a rather big force: the wire smashes both the BFO-Mn and the YBCO films, but some contacts exist between the damaged YBCO layer, the wire and the undamaged YBCO film. The use of aluminium wire, which reacts with the oxides it is bonded with, ensures good electrical contact and mechanical properties. However, we observed that with this technique the contacts would soon become very noisy. We suspect the Al to react with the YBCO film and create an insulating shell between the wire and the YBCO layer. This was confirmed by microscope images: as an example, Figure III.17 is a picture of a sample bonded with both Al wires (in black) and Au wires (in yellow).

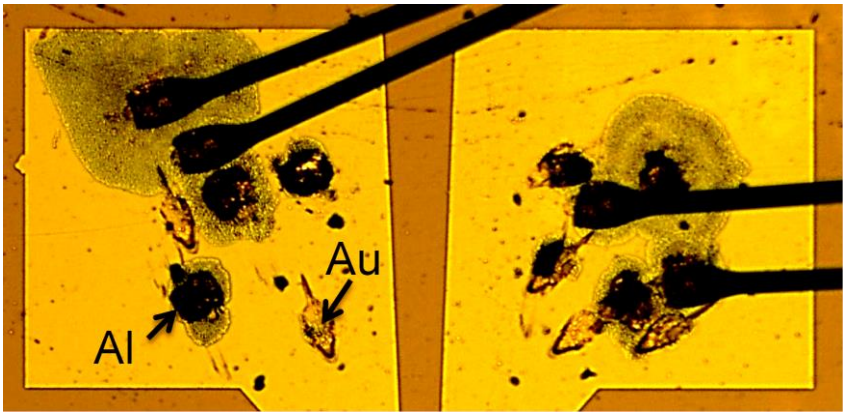

Figure III.17: Oxidation of BFO/YBCO/PBCO//STO by aluminium wires

We can see that around the aluminium contacts, there is a large area (in green) where the chemistry of the sample is modified. Au wires were considered as an alternative to Al wires, as this metal is inert. However, the mechanical properties of the contact where not good enough: the wires usually lift after a few thermal cycles. We thus developed a new lithography step in order to create contact pads. The metallic pads cannot be directly deposited on the insulating BFO-Mn, and in the meantime the YBCO layer is too thin to let us etch the BFO-Mn and stop into the YBCO layer. An alternative was to design stripes, to maximise lateral contact between gold and YBCO (see Figure III.18).

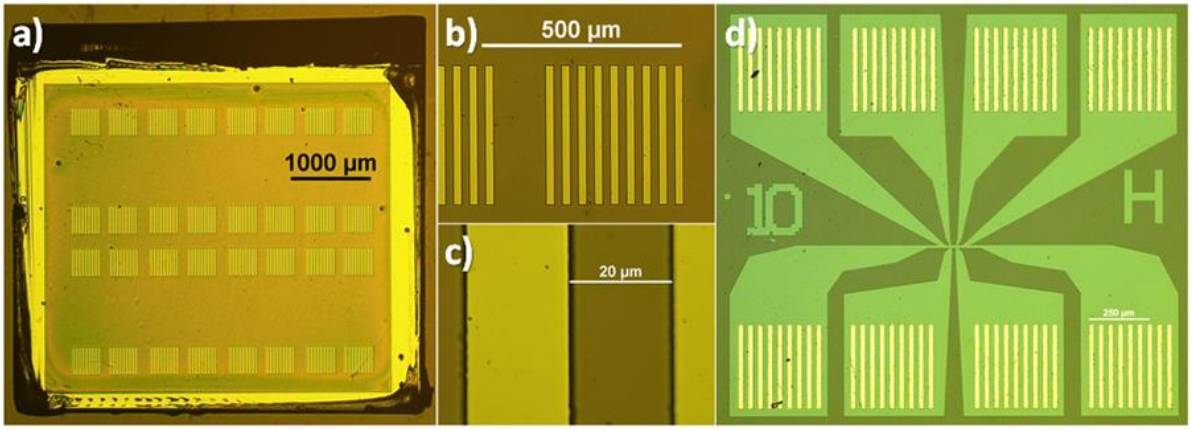

Figure III.18: Pictures of a 5x5 mm^2 devices after designing the contact stripes a) x1, b) x5 and c) x100 and d) after designing the bridge

Technology

The fabrication consists in:

- A lithography step to define gold contacts on the pads
- The deposition of gold and lift-off
- A lithography step to define measurement bridges
- The etching of the bridges.

- **1. Cleaning the sample**: the sample is first cleaned with acetone, then propanol; no ultra-sounds are used to clean the sample because this could damage the heterostructure. Still, if the surface is dirty, the gentle use of a cotton bud does not damage the oxide. The sample is heated one minute at $90°C$ to desorb the organic materials from the surface and then thermalised at room temperature.

- **2. Definition of the contacts:**
  - 2.1. Spin-coating: the sample is spin-coated $30\ s$ at $4000\ rpm$ with *S1813 G2* microposit positive photoresist, which corresponds to a layer as thick as $1{,}5\ \mu m$. Resist is baked one minute at $90°C$ on a hot plate.
  - 2.2. Insulation: the sample is exposed with $40\ mJ$ using an *MJB3* UV lamp ($365\ nm$)
  - 2.3. Development: the patterns of the contacting pads are developed $30\ s$ in *MF-139* under agitation, rinsed $30\ s$ in deionised water and dried with nitrogen. Stripes are chosen instead of usual pads in order to ensure the maximum surface of contact between gold and undamaged YBCO.
  - 2.4. Etching: the BFO-Mn layer inside the stripes is etched by Ion Beam Etching, with rotation and an inclination of $30°$ with respect to the beam. The etching is very soft, with an acceleration of only $240\ V$ and $50\ mA$ to avoid any heating of the sample, which is stuck to a $5°C$ water-cooled sample holder with thermal grease. The etching process is monitored with a SIMS (Secondary Ion Mass Spectroscopy) analyser, and is stopped when the YBCO signal starts to rise. The ions detected and the etch rates are given in Table III.2:

Oxide	Ion detected	Etch rate at $240\ V$ and $50\ mA$
BFO	Bi^{3+}	$0.95\ Å/s$
YBCO	Ba^{2+}	$0.17\ Å/s$
PBCO	Pr^{3+}	$0.17\ Å/s$
STO	Sr^{2+}	

Table III.2: Ions detected by SIMS and corresponding etching rates

  - 2.5. O_2 plasma: Room-temperature plasma ($1000\ W$, 10' under $100\ sccm$ of O_2 and $14\ sccm$ of Ar). *NB: Initially, this plasma was used to help to remove the resist that have been "cooked" and hardened by the etching: it was not needed as the etching is*

very soft, but we observed that the plasma had a major role in the aging of the samples.

- 2.6. Metallisation: $200\ nm$ of gold are then sputtered on the sample. Sputtering is preferred to evaporating because it makes better contacts between gold and YBCO.
- 2.7. Lift-off: the sample is then soaked into acetone for a few hours to proceed to the lift-off of the contact pads, and rinsed in propanol. A *cap* lithography could have been used here instead of a classic lithography, but it was not necessary to have a good quality of lift-off for these large patterns, and it requires tougher steps such as $110°C$ hard bake or ten minutes soak in chlorobenzene.

- **3. Definition of the bridge:**
  - 3.1. Spin-coating: step *2.1* is repeated.
  - 3.2. Insulation: the mask with the bridge design is aligned on the top of the pads. The parameters are the same ($40\ mJ$) as described in step *2.2*.
  - 3.3. Development: step *2.3.* is repeated.
  - 3.4. Etching: the sample is etched with the same parameters than described in step *2.4.* but the etching lasts until the substrate is reached (when the PBCO signal vanishes, as represented in Figure III.19).
  - 3.5. O_2 plasma: step *2.5.* is repeated.
  - 3.6. Cleaning: the remaining resist is dissolved in acetone. The sample is rinsed with propanol.

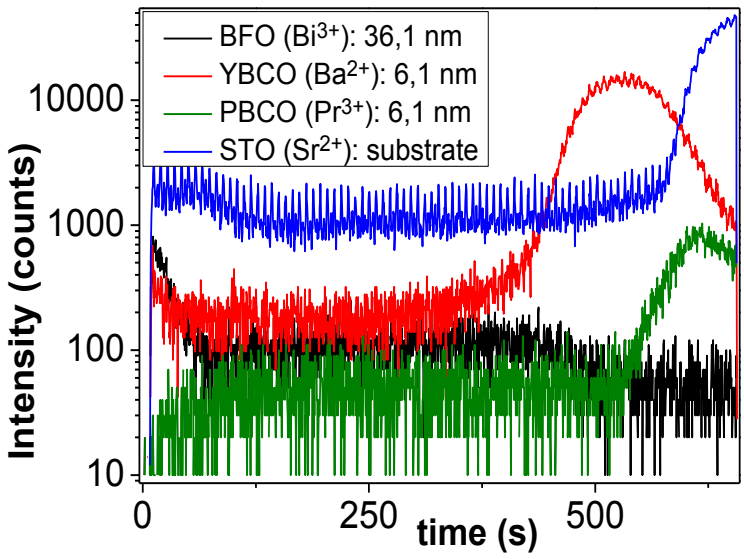

Figure III.19: SIMS monitoring of a BFO/YBCO/PBCO//STO ion beam etching.

III.3.3 Fabrication of planar devices with a gate

In order to compare the field-effect obtained with the ferroelectric polarisation and the field-effect obtained with a top-gate electrode, we fabricated devices with BFO-Mn as a dielectric, gated by a layer of Au. To insure the best contacts between each layer, we grew Au/BFO-Mn/YBCO/PBCO//STO heterostructures by PLD. The thickness of the BFO-Mn was chosen to be 200 nm, which is in principle thick enough not to be leaky. Note that as explained in section VI.1.3, this lithography did not allowed us to obtain devices in which we could switch entirely the ferroelectric polarisation. The structure is represented in Figure III.20: on the left is an optical microscope image of the device, on the right the schematic representation.

The lithography process consists in:

- A lithography step to design the measurement bridge
- The definition of the gated area
- The deposition of an insulating layer to protect the bridge from the top-electrode
- The definition of the top electrode.

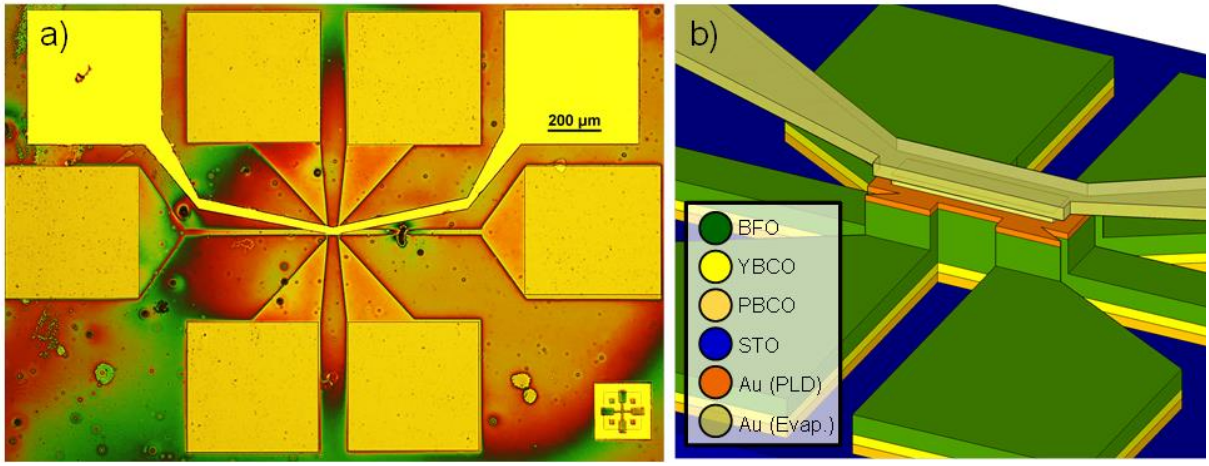

Figure III.20: a) Microscope image and b) Scheme of the top-electrode planar device

- **1. Cleaning the sample**: the sample is first cleaned with acetone, then propanol. It is heated one minute at $90°C$ and then thermalised at room temperature.

- **2. Definition of the bridge:**
  - 2.1. Spin-coating: *S1813 G2* microposit positive photoresist is spin-coated 30 s at 4000 $krpm$, then baked one minute at $90°C$ on a hot plate.
  - 2.2. Insulation: sample is exposed with 40 mJ of UV using an *MJB3* mercury lamp (wavelength 365 nm).
  - 2.3. Development: resist is developed 30 s in *MF-139* under agitation, rinsed 30 s in deionised water and dried with nitrogen.
  - 2.4. Etching: the heterostructure is etched by Ion Beam Etching, with rotation of the sample holder and an inclination of $30°$ with respect to the beam. Beam is accelerated under 240 V and 50 mA. Sample is stuck to a $5°C$ water-cooled sample

holder with thermal grease. The etching process is monitored with a SIMS analyser, and is stopped when the PBCO signal vanishes.

- 2.5. O_2 plasma: $1000\ W$, $30°C$, $10'$ under $100\ sccm$ of O_2 and $14\ sccm$ of Ar.
- 2.6. Cleaning: Remaining resist is dissolved in acetone. Sample is rinsed with propanol.

- **3. Definition of the gated area**
  - 3.1. Spin-coating: SU8 2002 resist is spin-coated $30\ s$ at $6000\ rpm$.
  - 3.2. Ramp bake: Sample is left $1'$ on a piece of filter paper on a hot plate at $65°C$, then $1'30''$ directly on the hot plate at $65°C$. It is then transferred on a hot plate at $95°C$ and left $1'30''$ on a filter paper and $1'$ directly on the plate.
  - 3.3. Insulation: $40\ mJ$ with an MJB3 UV lamp to open windows over the gated areas.
  - 3.4. Development: $30\ s$ in SU8 developer under agitation. Rinsed $30\ s$ in propanol.
  - 3.5. Polymerisation of the SU8 layer: the SU8 layer is exposed with $800\ mJ$ in order to induce chemical changes in its structure and let it become insoluble in common solvents such as acetone or propanol, and developers that will be used in the following steps such as MF-319. A hard-bake at $170°C$ would be equivalent but might damage the ultra-thin YBCO film.

- **4. Definition of the gate electrodes**
  - 4.1.Spin-coating: The sample is spin-coated $30\ s$ at $4000\ krpm$ with *S1813 G2* microposit positive photoresist, then baked one minute at $90°C$ on a hot plate.
  - 4.2. Insulation: the sample is exposed with $40\ mJ$ of UV using an *MJB3.*
  - 4.3. Development: the resist is developed $30\ s$ in *MF-139* under agitation, rinsed $30\ s$ in deionised water and dried with nitrogen.
  - 4.4. Metallisation: a thick layer of $200\ nm$ of Au is deposited by evaporating.
  - 4.5. Lift-off: the gold is removed by a lift-off in acetone, and the sample is rinsed with propanol.

III.3.4 Fabrication of vertical devices: matrices of pads

The properties of tunnel barriers strongly depend on the thickness of the film on one hand, and on the presence of defects across the barrier on the other hand. Considering Josephson coupling between two superconductors across a barrier, it can occur somewhere in the junction where the barrier is thinner but might disappear somewhere else where the barrier is thicker. A far as ferroelectric tunnel barriers are concerned, the presence of leakage paths through defects can prevent the switching of the polarisation when an electric field is applied, which can eventually breakdown and destroy the junction. It is thus important to be able to measure a large number of them. The following technology, developed at the laboratory to study similar ferroelectric junctions (see for example ref. [81], [169]) consists in defining thousands of top-electrode circular pads by electron-beam lithography and lift-off on the unpatterned barrier/bottom electrode bilayer. The bottom electrode is connected to a CT-AFM set-up (see section III.2.3. c)) and the junction is measured by contacting the top electrode with the conductive tip. This technology has several advantages:

- It is simple and reproducible.
- It allows to fabricate and measure a large number of junctions on a small (down to $5 \times 5\ mm^2$) sample.
- E-beam lithography allows to fabricate junctions with diameters between $100\ nm$ and $1\ \mu m$.
- The ferroelectric state of the barrier can be switched and read with the CT-AFM tip through the top-electrode (PFM mode).
- The resistance of the barrier can be read with the same tip without removing the sample (CT-AFM mode) as schematized in Figure III.21.

The lithography on the barrier/bottom electrode bilayer consists in:

- The definition of circular holes by electron-beam lithography on a standard PMMA resist
- The deposition of the top electrode by sputtering
- A lift-off step to define the circular pads.

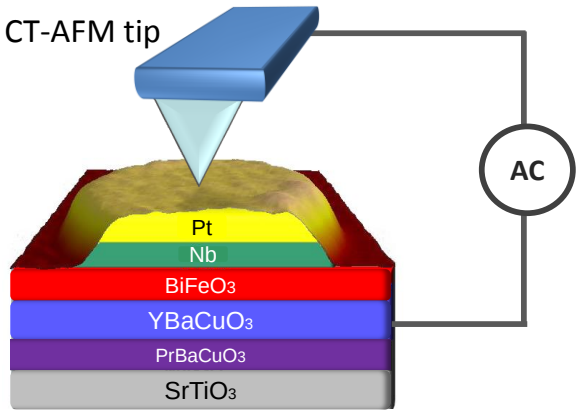

Figure III.21: Scheme of a Pt/Nb/BFO-Mn/YBCO/PBCO//STO nanodevice

III.3.5 Fabrication of micrometric vertical devices

The following technology was developed in order to obtain micrometric solid-state devices measurable at low-temperature. To do so, an insulating photoresist mask is deposited on an unpatterned BFO-Mn/YBCO//STO film. Micrometric windows are opened in the mask, and the top-electrode (here $MoSi$) is then deposited, as represented on Figure III.22. The top-electrode is contacted to the measurement chip by wire-bonding.

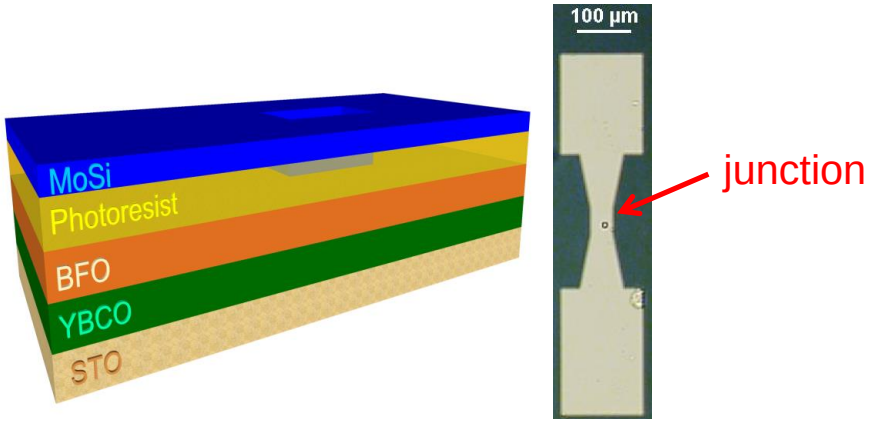

Figure III.22: Scheme of a MoSi/BFO-*Mn*/YBCO/PBCO//STO pillar and microscope picture of one junction

This technology has several advantages:

- It is simple and reproducible.
- It allows to fabricate a reasonable number of junctions (up to 98) on a small (down to $5 \times 5\ mm^2$) sample.

The lithography process on the barrier/bottom electrode bilayer consists in:

- Coating the sample with a thick insulating film and opening micrometric windows into it
- The deposition of the top-electrode
- The etching of the top-electrode to remove the short-circuits between one contact to the other
- The connection of the junctions to a chip.

- **1. Cleaning the sample**: the sample is first cleaned with acetone, then propanol.

- **2. Optical lithography: definition of the windows**
  - 2.1. Spin-coating: primer is spin-coated $30\ s$ at $4000\ rpm$. S1805 diluted with thinner (50/50) is spin-coated $30\ s$ at $4000\ rpm$.
  - 2.2. Soft bake: sample is left $1'$ on a hot plate at $60°C$.
  - 2.3. Insulation: exposition: $60\ mJ$ with an MJB3 UV lamp to open $1{\sim}10\ \mu m$ wide windows.

- 2.4. Development: $7\ s$ in MF319 developer under agitation. Rinsed $15\ s$ in deionised water. Dried with N_2.
- 2.5. Hard bake: 1' on a hot plate at $170°C$.

- **3. "Casquette": top electrodes**
  - 3.1. Spin-coating: SPR700 is spin-coated $30\ s$ at $6000\ rpm$.
  - 3.2. Soft bake: sample is left $1'$ on a hot plate at $110°C$.
  - 3.3 Hardening bath: $10'$ in chlorobenzene to harden the surface of the resist. Rinsed $30\ s$ in deionised water. Dried with N_2.
  - 3.4. Insulation: the sample is exposed with $100\ mJ$ with an MJB3 UV lamp.
  - 3.5. Development: the resist is developed $20\ s$ in MF-139 under agitation, rinsed $30\ s$ in deionised water. Dried with N_2.
  - 3.6. Metallisation: a thick layer of $100\ nm$ of $MoSi$ is deposited by sputtering under $2{,}5 \cdot 10^{-3}\ mbars\ O_2$.
  - 3.7. Lift-off: the gold is removed by a lift-off in acetone, and the sample is rinsed with propanol.

III.3.6 Measurement set-up for electrical characterisation

The samples are measured in a two-stage cryostat filled with Helium as the exchange gas and cooled via a compressor. It can reach temperatures down to $6\ \mathrm{K}$. Compared to He flow cryostats, it presents the advantage of leaving the surface of the sample cleaner after a run of measurements, which is important as the samples are regularly transferred from the cryostat to the PFM setup. The set-up is schematized in Figure III.23.

The sample is stuck with low-temperature resistant tape to a measurement chip. The contact pads are wedge-bonded with Aluminium wires to the pads of the chip, each linked to pins that connect to the sample holder of the measurement set-up. This sample holder is directly linked to a BNC box that can be connected to any device: we used a Keithley 2182A nanovoltmeter and a Keithley 6221 current source. The resistivity is always measured with four probes geometry, *i.e.* two pads are used to inject the current and two other pads are voltage probes. This configuration allows the measurement of the oxide channel without measuring the contacts in series.

The sample holder is introduced in a cryostat with $1.1\ \mathrm{PSI}$ of Helium, and a compressor cools a cavity surrounding the cryostat. The temperatures of the cavity, the cryostat and the sample holder are monitored by three sensors. They work in pair with two heaters (one in the cryostat and one on the sample holder), to stabilise any temperature between 6 and $300\ K$ via a temperature controller. The sample holder and a gaussmeter are positioned in the middle of two copper coils that generate a magnetic field, driven by a source operating under $150\ V$. The orientation of the sample holder with respect to the magnetic field can be controlled by a step-by-step motor.

Planar devices with no gate

Unlike three terminals transistors on which the field-effect can be directly controlled by a gate voltage, in our samples the devices have to be measured for one direction of the polarisation, then removed from the cryostat, switched with a PFM and introduced in the cryostat again to be measured in the other direction.

Planar devices with top gate electrode

In the case of the planar devices with thick BFO-Mn films ($150\ nm$) and an Au top gate electrode, an additional Keithley 2400 sourcemeter is connected to a current pad and the gate. It can simultaneously apply a voltage across the film and measure the leakage current.

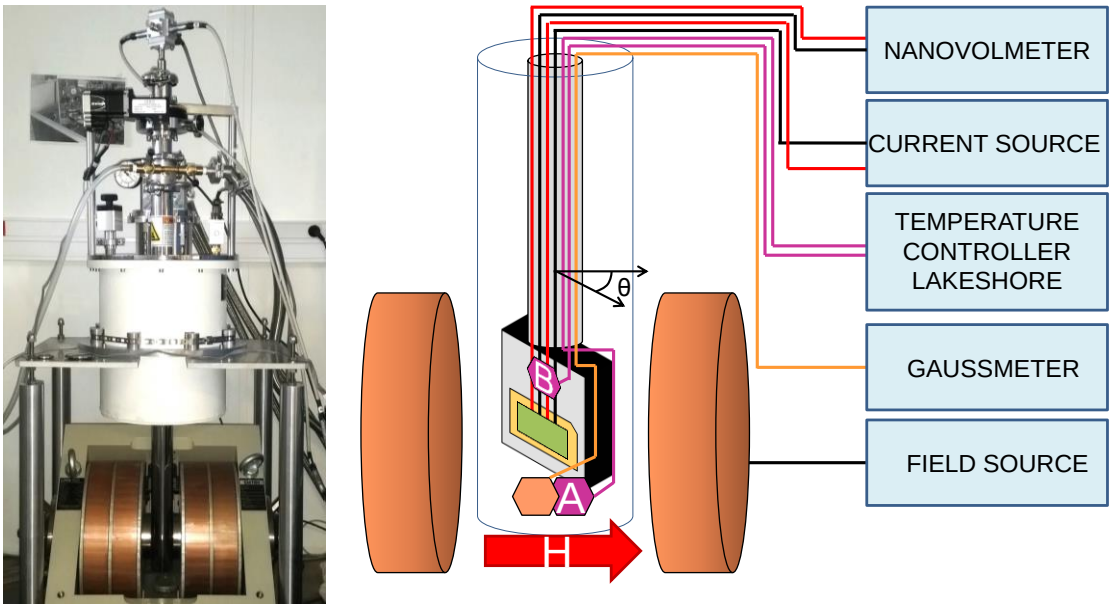

Figure III.23: Measurement setup for planar devices

IV. Growth of epitaxial heterostructures

Index

IV. Growth of epitaxial heterostructures 86

IV.1 Epitaxial heterostructures for planar field-effect devices 87

IV.1.1 Objectives 87

IV.1.2 Preparation of substrates 88

IV.1.3 Growth of $YBa_2Cu_3O_{7-\delta}$ 88

IV.1.4 Growth of $BiFeO_3$ 90

IV.1.5 Properties of optimised BFO/YBCO/PBCO/STO 94

IV.2 Epitaxial heterostructures for ferroelectric tunnel junctions 101

IV.2.1 Objectives 101

IV.2.2 BFO/YBCO *in situ* heterostructures 103

IV.2.3 BFO-*Mn* epitaxy on YBCO films grown by PLD 104

IV.2.4 BFO-*Mn* epitaxy on YBCO commercial films 106

IV.1 Epitaxial heterostructures for planar field-effect devices

IV.1.1 Objectives

The planar devices are constituted of a ferroelectric material (in green in Figure IV.1) grown on top of a superconducting film (in yellow in Figure IV.1), in which charges accumulate close to the interface in order to screen the ferroelectric polarisation. Depending on the direction of the polarisation, carriers (holes) will be accumulated or depleted in the superconducting film close to the interface, and the superconducting properties will be modified.

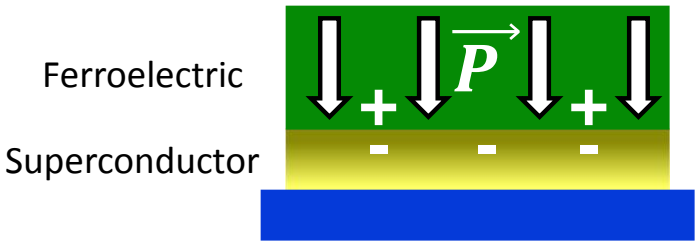

Figure IV.1: Field-effect in a superconducting channel.

The field-effect only propagates over a distance of the order of the Thomas-Fermi length, which is longer in high-T_c superconductors ("bad metals") than in low-T_c superconductors, as discussed in section II.4.1. In order to observe the field-effect in the superconducting film, its thickness has to be comparable to this length. This leads to the following issues regarding the growth:

- Produce a robust, ultra-thin, high-T_c superconducting film.
- Grow a ferroelectric film with a strong, switchable, out of plane polarisation.
- Obtain a defect-free, unscreened, epitaxial interface between the two layers to let the field-effect propagate into the superconducting layer (localised electronic states due to defect might screen the electric field [105]).
- Obtain a smooth surface that can be scanned by the PFM tip in contact mode.
- Avoid conductive defects that could lead to current leakage during the poling process and that could damage the thin superconducting film.
- Choose a substrate that has:
    - a small lattice mismatch with the materials to limit the formation of defects;
    - a thermal dilatation coefficient close to those of the materials, to avoid thermal strains during the cooling;
    - a surface with no twinning.

The heterostructure BFO/YBCO//STO appeared to be among the best candidates for such devices: these are three perovskites that can grow epitaxially one on another. YBCO, STO and BFO lattice parameters are very close ($a_{YBCO} = 3.82$ Å, $a_{STO} = 3.90$ Å, and $a_{BFO} = 3.96$ Å). BFO has a strong out-of-plane polarisation, reaching values up to $70\ \mu C/cm^2$ (see section IV.1.5. c)). YBCO is a very robust high-T_c superconductor, with a large Thomas-Fermi length ($\sim 1\ nm$) [170] that can in

principle remain superconducting for thickness down to one unit cell [171]. To fabricate these heterostructures, we use the *Pulsed Laser Deposition* (PLD) technique. The principle of this growth technique is described in section II.1.2. The PLD used in the following section operates with a KrF LPX 200 Excimer laser ($\lambda = 248\ nm$).

IV.1.2 Preparation of substrates

We use $SrTiO_3$ (STO) substrates with (001) orientation. They are chemically etched with fluorhydric acid and annealed at $1000°C$ and in O_2 to reveal atomic steps at the surface (see Figure IV.2). This treatment etches the substrate in such a way that the termination is always a $Ti - O_2$ plane, which ensures a better reproducibility for the growth of ultra-thin films. The atomic steps help a *Step Flow* mode of growth, which favours smooth and uniform layers [172]. The other face of the substrate is unpolished in order to ensure a more reproducible and more homogenous sticking: the substrates are stuck to Heinsblocks holders with silver-paste based epoxy glue. They are then annealed at $\sim 300\ °C$ in the atmosphere to remove the solvents present in the glue.

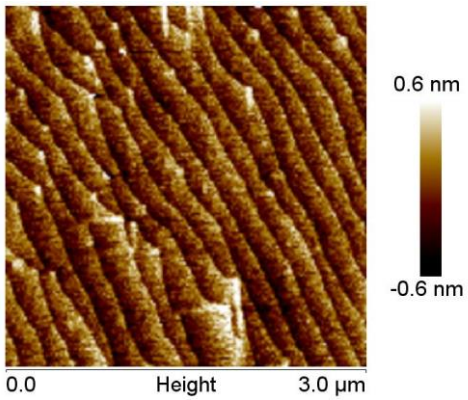

Figure IV.2: AFM topography of Ti-O_2 terminated $SrTiO_3$ substrate

IV.1.3 Growth of $YBa_2Cu_3O_{7-\delta}$

STO is cubic with an in-plane lattice parameter of $0.3905\ nm$ at room temperature whereas YBCO lattice parameters are $a = 0.382\ nm$ and $b = 0.388\ nm$ in the orthorhombic superconducting phase. To enhance YBCO superconducting properties, we grow a buffer layer of $PrBa_2Cu_3O_{7-\delta}$ (PBCO), which is an insulator that has the same structure as YBCO, but with slightly bigger lattice parameters: $a = 0.3902\ nm$ and $b = 0.3916\ nm$. **The smaller lattice mismatch with YBCO (compared to STO) and the presence of CuO chains allow ultra-thin YBCO films grown on a PBCO buffer down to 2 u.c. to be superconducting** [137]**.**

YBCO and PBCO layers are grown under the same conditions: $0.35\ mbars$ of O_2 and $690°C$ measured by a pyrometer at the center of the substrate after fifty minutes (approx. twenty minutes to reach the temperature and thirty minutes of stabilisation). **To allow a homogenous deposition, the substrate rotates around an axis slightly different from the axis of the plume** (see Figure IV.3, left). This misalignment is adjusted during the pre-ablation of the target with a special holder and monitored with a camera.

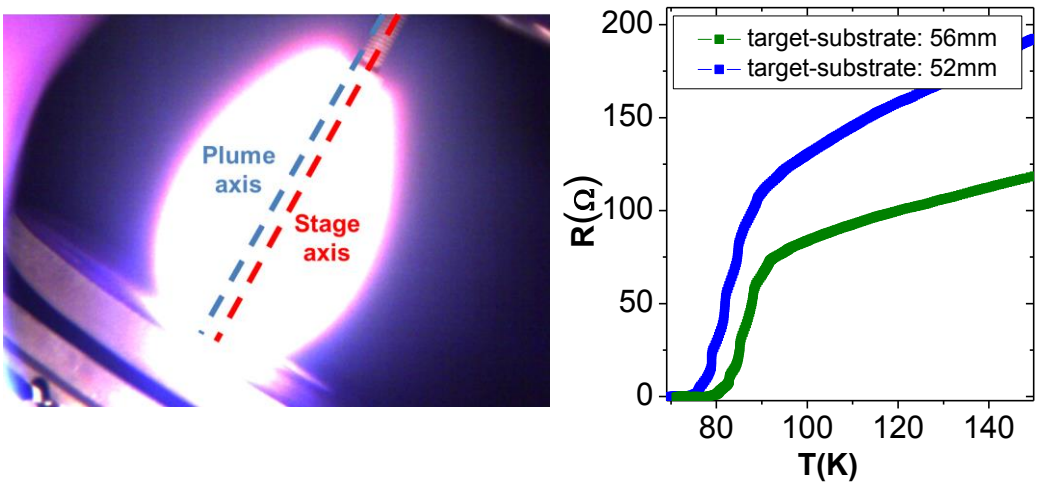

Figure IV.3: Left: Shift between plume and stage axis. Right: Influence of the target to substrate distance on the critical temperature of YBCO

We found that the YBCO film quality is very sensitive to *target to substrate* distance: if the plume is close to the substrate, the film will have a smooth surface and a limited number of defects, at the expense of a slightly reduced T_c (Figure IV.3, right, blue curve). **A bigger distance will enhance superconductivity, *i.e.* a high critical temperature and a sharp transition** (Figure IV.3, right, green curve) are obtained, but a rougher surface with a higher density of defects is obtained.

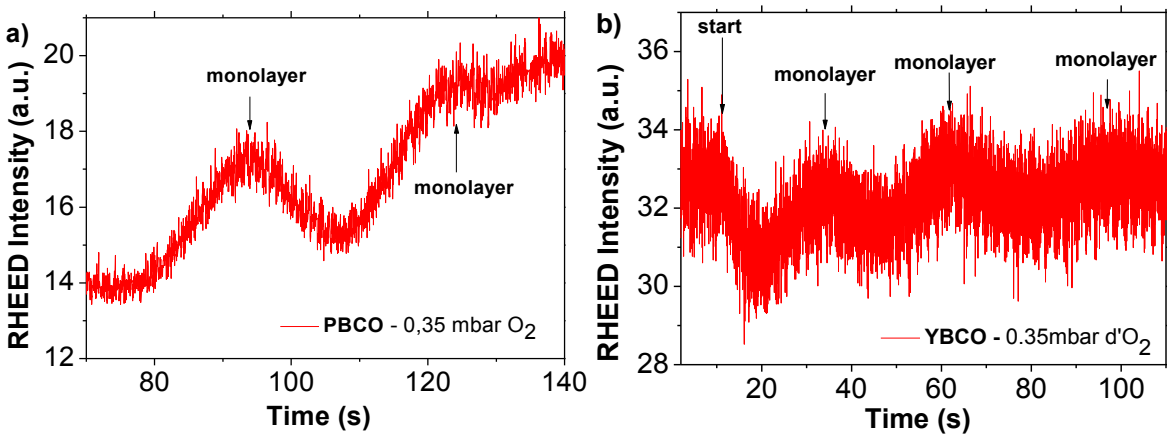

Figure IV.4: RHEED during the growth of a) a PBCO film and b) a YBCO film

The growth speed is directly influenced by all these parameters; RHEED is commonly used to monitor the number of monolayers grown, but it is not possible to use it while the sample is rotating. Calibration samples were made without rotation in order to give precise measurement of the growth rate (see Figure IV.4). A second calibration is obtained by measuring the thickness of ultra-thin YBCO//STO and PBCO//STO films by X-rays reflectivity. During the growth, the pulses frequency is reduced to $1\ Hz$ to control accurately the pulses number.

The optimisation process of this full range of parameters (pressure, temperature, target to substrate distance, shape and energy of the laser spot, misalignment of the rotation axis of the sample with respect to the plume) relies on:

- Resistance versus temperature measurements to seek a high T_c and a sharp transition,
- *AFM* and *MEB* images to check the smoothness of the layer and observe the number and shape of defects,
- X-rays reflectivity and diffraction scans to measure the thickness and the crystalline quality,
- RHEED patterns at the end of the growth to have an indication on the quality of the film: stripes indicate a 2D growth, while dots are the signature of a strong 3D contribution (see Figure IV.5, left).

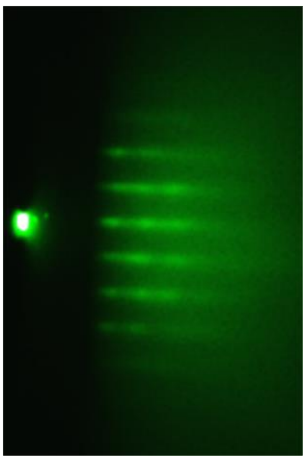

Figure IV.5: RHEED image of a YBCO (5 u.c.)/PBCO (4 u.c.)//STO heterostructure.

YBCO and PBCO are two materials that had been previously developed at the laboratory, but on another PLD system. **We successfully optimised the growth conditions on this set-up and achieved to grow ultra-thin, epitaxial YBCO/PBCO//STO heterostructures with a high critical temperature**. Results and growth conditions are detailed in section IV.1.5. e). We now discuss the epitaxial growth of BFO on these films.

IV.1.4 Growth of $BiFeO_3$

We then optimised the growth conditions for BFO on YBCO. In order to limit the risk of leakage during the poling process (*i.e.* during the application of a DC voltage in order to switch the polarisation of the ferroelectric), we choose a target doped with 5% of manganese, BFO-Mn [173]. Like YBCO, this material had never been developed in the PLD ("Real"), but had been developed earlier on a similar PLD ("LDM"). Both "Real" and "LDM" operated with a KrF LPX 200 Excimer laser ($\lambda = 248\ nm$). However, contrary to YBCO, this material was developed in a third PLD ("Abla") working with a Nd^{3+}: YAG laser. The two lasers have different wavelengths ($248\ nm$ for the KrF and $355\ nm$ for the YAG), they thus interact differently with the target. In particular, in the same conditions, we observed that the growth speed with a YAG was one order of magnitude bigger than with the KrF (typically 0.7 Å/pulse compared to 0.08 Å/pulse for a target to substrate distance of $\sim 5\ cm$, at 470°C under $0.35\ mbars$ O_2). With this in mind, we investigated two ways of growing BFO:

- BFO-Mn/YBCO/PBCO//STO heterostructures grown $in\ situ$ in "Real" with an Excimer KrF laser.

- YBCO/PBCO//STO heterostructures grown with in "Real" with a KrF laser, then transferred to "Abla" (the PLD operating with a Nd^{3+}: YAG laser) to grow *BFO-Mn* on the top of the structure.

We based our optimisation process on three main characterisations:

- AFM tapping images to control the roughness of the film and the absence of large defects that would damage the PFM tip;
- PFM writing and reading to verify the stability of the out-of-plane polarisation in both direction;
- X-rays diffraction to verify the quality of the epitaxy between the films.

Comparison between the two process

On the PLD "Abla", BFO-Mn was already optimised on other substrates such as LSMO. In the same conditions, the BFO-Mn did not grow in a textured way on YBCO films and the conditions had to be optimised again for the substrate. Finally, the quality of the BFO-Mn films on YBCO was not satisfying compared to the "*in situ*" films. As an example, Figure IV.6 shows the X-rays diffraction scans of two heterostructures.

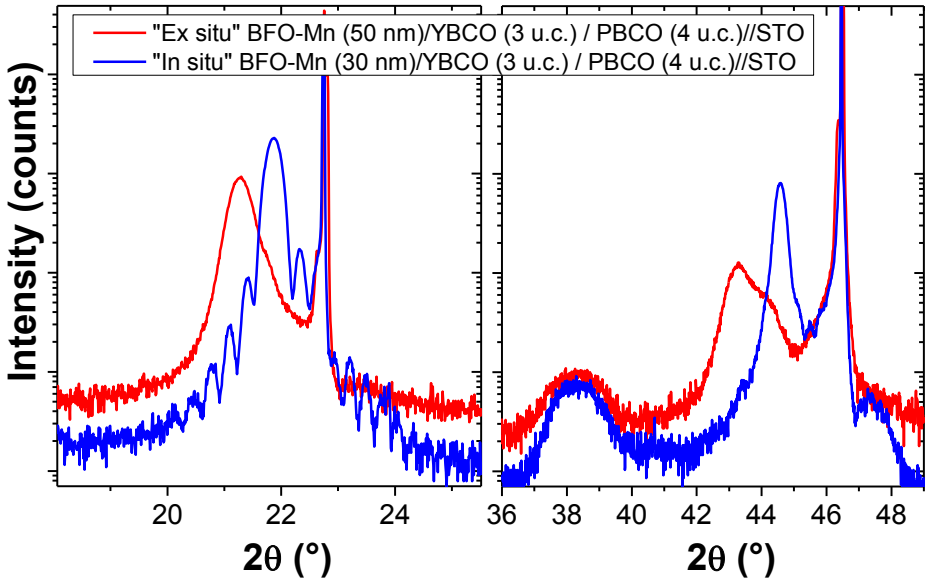

Figure IV.6: AFM and CT-AFM images of the surface (aged (top inset) and scratched (bottom inset)) of a YBCO layer

The blue curve corresponds to a BFO-Mn $(30\ nm)$/YBCO $(3\ u.c.)$/PBCO $(4\ u.c.)$//STO *"in situ"* heterostructure: the peak of the BFO-Mn is sharp and the satellite peaks are the sign of a homogenous layer. In contrast, the red curve – corresponding to a BFO-Mn $(50\ nm)$/YBCO $(3\ u.c.)$/PBCO $(4\ u.c.)$//STO heterostructures grown *"ex situ"* – shows no finite size oscillations, and a much broader BFO-Mn peak that is shifted to lower angles. These features imply a rougher BFO-Mn film and lower crystalline quality overall.

Furthermore, the superconducting properties of the YBCO films which undergo the *"ex-situ"* process are degraded as compared to the nominally identical samples grown in the *"in-situ"* process. In particular, initially a lower T_c is observed is *"ex situ"* samples which further degrades over time. This

behaviour could be due to two effects that result in deficient, inhomogeneous degradation of the YBCO layer:

- During the transfer between PLD systems, the surface of the ultra-thin YBCO (few u.c.) / PBCO (4 u.c.)//STO film is exposed to water contained in the atmosphere. We observed that for YBCO films that stayed in the atmosphere for a long time (many weeks) a very resistive layer formed at the surface of the sample: Figure IV.7 shows the difference of resistivity of the surface of the YBCO exposed to the air for a long time (upper rectangle) compared to an area where the surface of the film was scratched with a hard tip (lower rectangle).

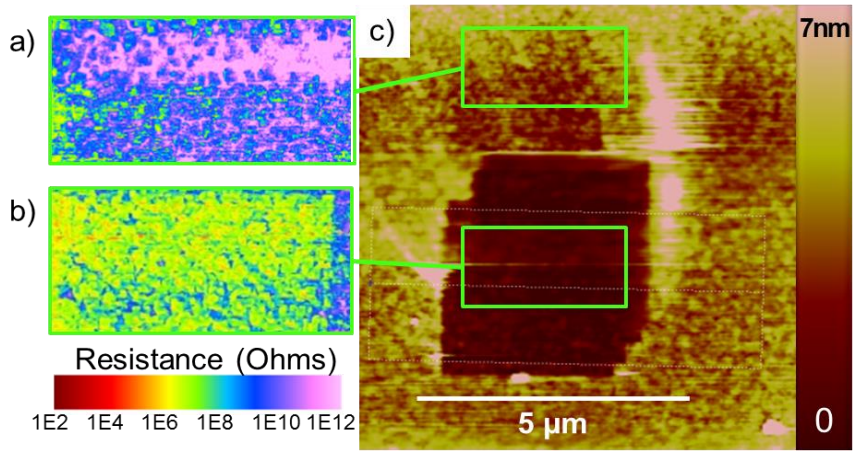

Figure IV.7: AFM and CT-AFM images of the surface (aged (top inset) and scratched (bottom inset)) of a YBCO layer

We observe that the aged surface of the YBCO is four to six orders of magnitude more resistive than the YBCO underneath. We do not know the exact time-scale of this reaction and if a few minutes are enough for this insulating layer to form at the surface of the YBCO/PBCO//STO films.

- Another incertitude is the effect of the thermal process (cooling down from $690°C$, under 800 $mbars$ of O_2 and subsequently and heating up up to $430°C$ under 0.5 $mbars$ of O_2 prior to the deposition of the BFO-Mn) on the oxygen content of the YBCO layer.

In summary, we found that **the *in-situ* process produced both BFO-Mn and YBCO films with higher quality than the *ex-situ* process.**

Cooling

Figure IV.8 shows a comparison between two BFO-*Mn*/YBCO/PBCO//STO heterostructures fabricated under the same conditions but cooled down differently:

- The blue curves represent the resistance vs temperature measurement and XRD spectra of a sample cooled with the following procedure: just after the growth of the BFO-Mn film (the sample is at $560°C$), 800 $mbars$ O_2 are introduced and the heater is shut down immediately.
- The red curves show the same measurements for an "annealed" sample: after the growth of the BFO-Mn film (the sample is at $560°C$), 800 $mbars$ O_2 are introduced. The heater is kept switched on with the same current setpoint (note that it is not a temperature setpoint)

during twenty minutes. This induces a slow cooling of the sample, whose temperature goes from $560°C$ to $460°C$ during these twenty minutes. The heater is then shut down.

Figure IV.8 *a)* shows that the "annealed" sample (red curve) has a lower critical temperature and a larger transition that the sample cooled down as soon as the deposition was over (blue line). From the XRD spectra (Figure IV.8, *b)*) we can see that the BFO-Mn peak is less sharp in the case of the annealed sample – which is the sign that it is not homogeneously strained.

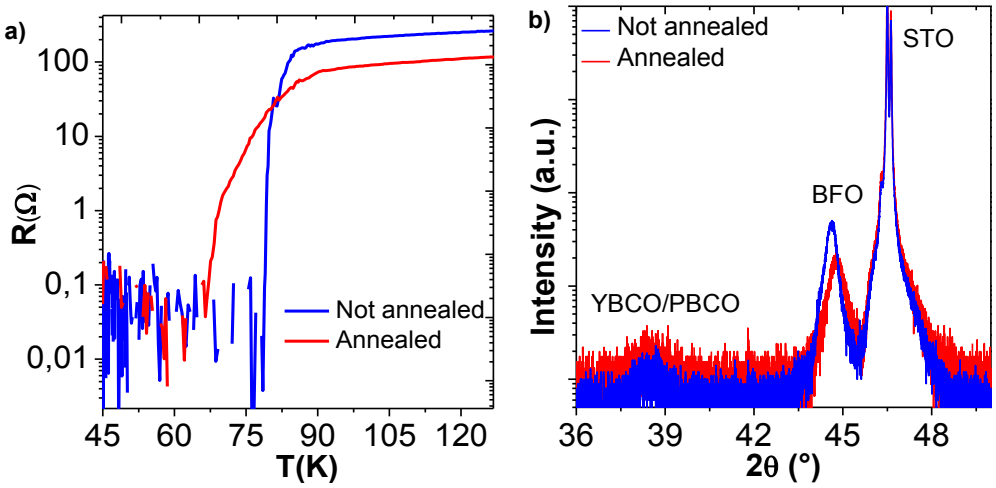

Figure IV.8: Comparison between not annealed (blue) and annealed at 460°C under 800 mbars O_2 (red) structures of BFO-Mn (30 nm)/YBCO(5 m.u.)/PBCO(4m.u.)//STO : a) Resistance *vs* temperature and b) XRD θ/2θ scans

This peak is shifted to the right compared to the "not annealed sample", which could be the sign that the compressive strain induced by the substrate is partially released (the lattice parameter of BFO is 3.96 Å whereas STO is 3.90 Å). This is consistent with a rougher topography (see Figure IV.9), where many outgrowths appeared in the annealed film (right) compared to the not annealed film (left).

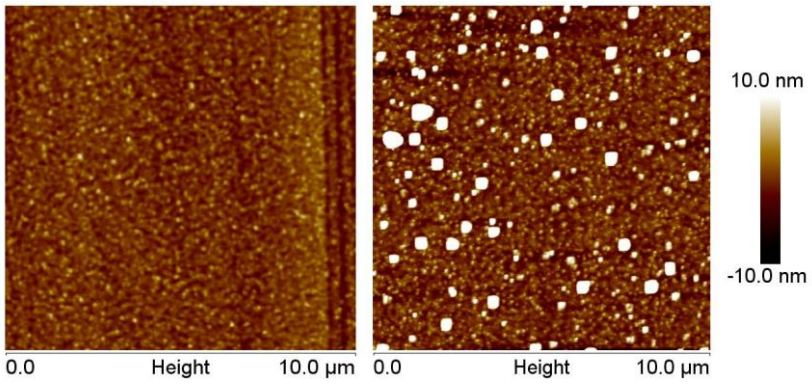

Figure IV.9: Topography of not annealed (left) and annealed (right) BFO-Mn/YBCO/PBCO//STO structures

From the above results, we found that better YBCO/BFO bilayers are obtained if the oxygenation protocol consists of **introducing 800 $mbars$ of pure O_2 and turning off the heater right after the films deposition.**

To conclude, we achieved to grow epitaxial, flat, ferroelectric BFO-Mn films on YBCO/PBCO//STO structures after optimising the growth conditions on both PLDs. In the following section, we detail the properties of the in situ heterostructures obtained at the end of the optimisation process.

IV.1.5 Properties of optimised BFO/YBCO/PBCO/STO

IV.1.5. a) Superconductivity of the YBCO layer

The lattice mismatch between the film and the substrate and the presence of steps on the substrate surface are two factors that reduce the critical temperature of ultra-thin films [171], [174]. By using a few unit cells of PBCO buffer layer, these imperfections heal out, and the YBCO can grow on a flat substrate. Moreover, PBCO shares CuO chains with YBCO at their interface. This results in better doping of the interfacial YBCO unit cell, and makes that ultrathin (2 to 6 unit cell) YBCO shows superior superconducting properties when grown on a PBCO buffer layer than when grown directly on STO [174].

BFO-Mn/YBCO/PBCO//STO heterostructures had already been developed on another PLD several years before. The critical temperature of these films (green triangles) and the onset of the transition (green squares) are represented on Figure IV.10 as a function of the YBCO thickness:

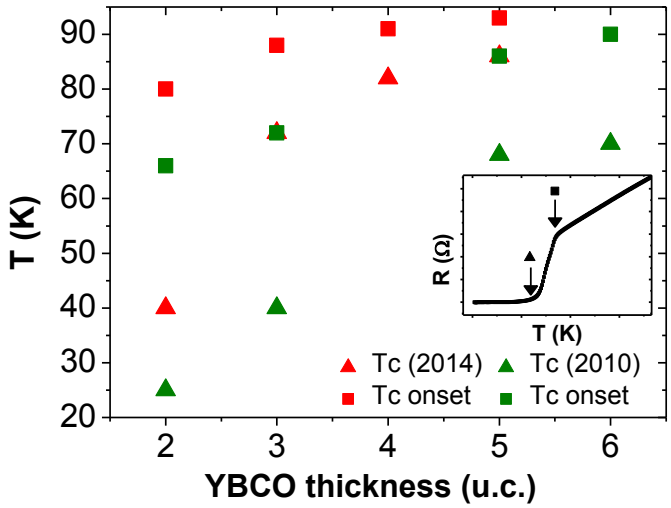

Figure IV.10: Critical temperatures and temperature at which transition begins for 2014 and 2010 samples

The critical temperature and onset of the transition of the films optimised for the work presented in this thesis are represented by the red symbols: **we achieved to improve the superconducting properties (width of the transition and critical temperature) compared to earlier standards in the laboratory.**

HAADF images revealed a very good epitaxy of the three films and the substrates. They also revealed the presence of several typical defects in YBCO, such as occasional unit-cell steps (Figure IV.11, left) and double CuO chains (Figure IV.11, right).

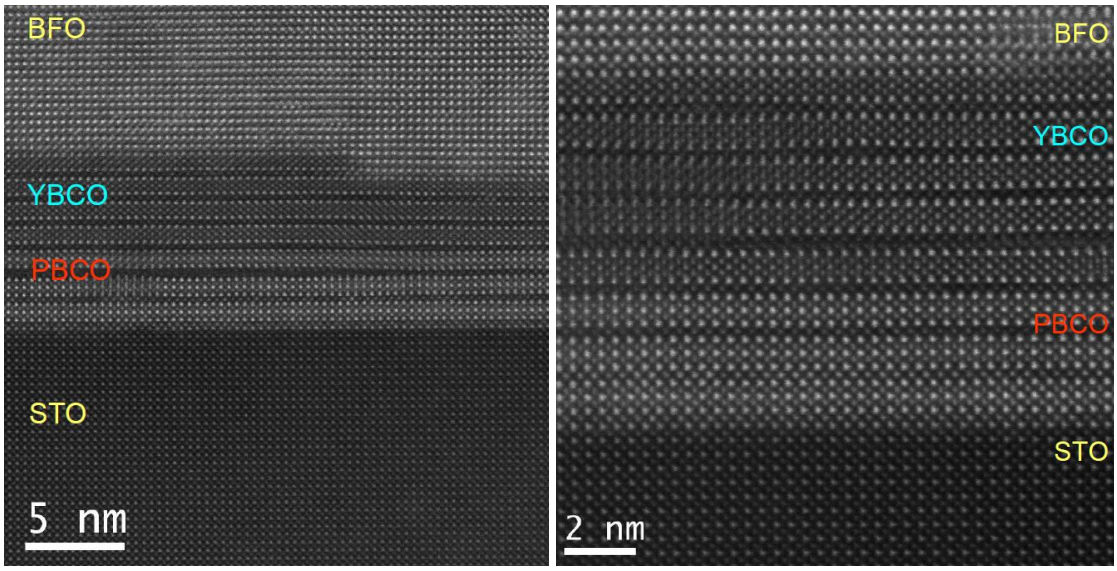

Figure IV.11: Occasional unit cell step (left) and double CuO chain (right)

IV.1.5. b) Epitaxy and interfaces

X-rays $\theta/2\theta$ diffractions scans were carried on our heterostructures to analyse the crystallinity of the films, on an Empyrean diffractometer. Due to the small thickness of both the YBCO and the PBCO films, the peaks are quite large and not well defined: a large integration time ($4\ s$ for a step of $0.01°$) was needed to reduce the noise. Figure IV.12 represents $\theta/2\theta$ scans for BFO-Mn ($30\ nm$)/YBCO (n u.c.)/PBCO (3 u.c.)//STO samples with n=2, 3, 4 and 5.

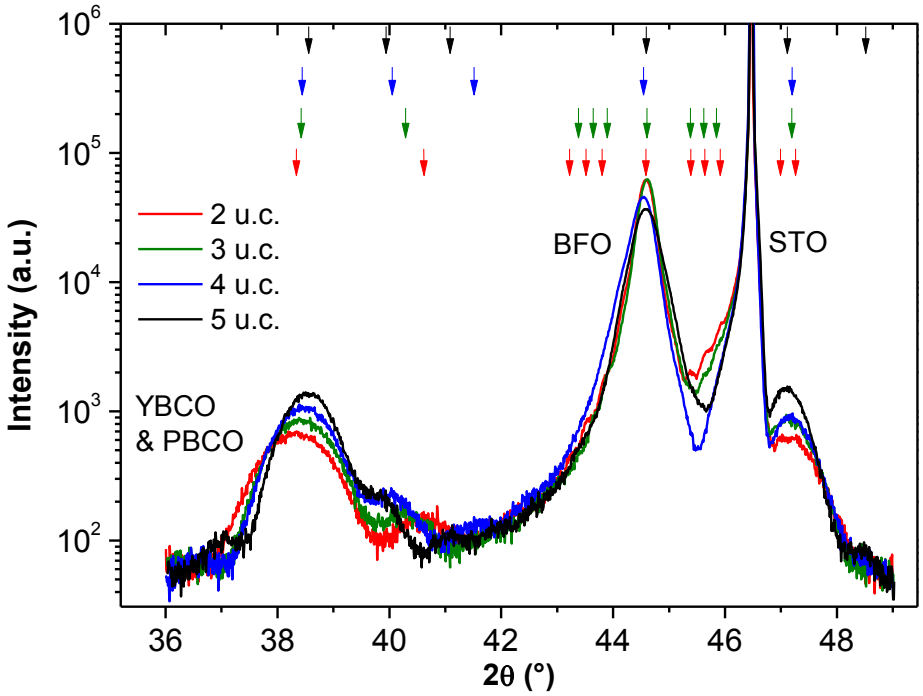

Figure IV.12: X-rays diffraction scans for BFO-Mn ($30\ nm$)/YBCO(n u.c.)/PBCO(3 u.c.)//STO

We observe additional peaks around the main reflections of the structure. These peaks, along with the broadening of the main diffracted peaks, are related to the finite number of diffracting cells. Their period is related to the number of diffracting planes by the Laue formula (see for example ref.

[95]): $L_N = \left[\frac{\sin(N\times c\times Q)}{\sin(c\times Q)}\right]^2$ with $Q = \sin(\omega) \times \frac{4\pi}{\lambda}$ the modulus of the dispersion vector, $\lambda = 1{,}5419$ Å the wavelength of the diffractometer and N the number of coherently diffracting planes. The lattice parameters c were determined from the $(00l)$ reflections with the Bragg law: $2c \sin\theta_B = \lambda l$.

We could determine the thickness of the BFO-Mn layer out of the satellite peaks of the (001) reflection, and the total thickness of the YBCO and PBCO layers out of the satellite peaks of the (005) reflection: because of their close structures, X-rays diffractometry cannot distinguish PBCO from YBCO. Figure IV.13 shows an example of the Laue oscillations for a sample with 4 u.c. of YBCO:

- In a) is represented the experimental data (in blue) and the fit for the BFO-Mn layer around the (001) reflection (in red).
- In b) are represented the experimental data (in blue), the fit for the $(3{+}4)$ u.c. thick YBCO/PBCO bilayer around the (005) reflection (in red) and the fit for the BFO-Mn layer around the (002) reflection (in grey). The parameters are consistent with the fit of the (001) reflection.

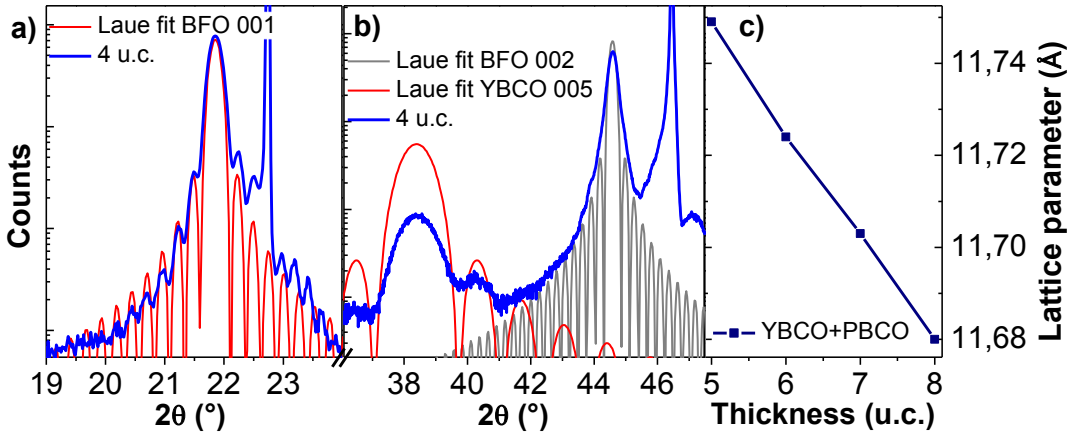

Figure IV.13: XRD θ/2θ diffraction scan of a BFO-Mn (30 nm)/YBCO (4 u.c.)/PBCO (3 u.c.)//STO heterostructure around a) the 001 and b) the 002 reflection of BFO-Mn. The red and grey lines are fit simulated according to the Laue theory. c) lattice parameters calculated from the position of the YBCO/PBCO peak as a function of the total YBCO+PBCO

Four samples of targeted thicknesses 2, 3, 4 and 5 u.c. for YBCO were analysed. The PBCO buffer thickness was targeted to be 3 u.c. and the BFO-Mn $\sim 30\ nm$. We measured a total number of unit cells $N(YBCO{+}PBCO)$ (third column of Table IV.1) consistent with the expected values.

N (YBCO) targeted	N (PBCO) targeted	N(YBCO + PBCO)	YBCO/ PBCO $\langle c \rangle$	YBCO + PBCO t	BFO-Mn c	BFO-Mn t targeted	BFO-Mn t
2	3	**5**	11,75 Å	5,9 nm	4,07 Å	30 nm	33 nm
3	3	**6**	11,72 Å	7,0 nm	4,07 Å	30 nm	35 nm
4	3	**7**	11,70 Å	8,2 nm	4,07 Å	30 nm	35 nm
5	3	**8**	11,68 Å	9,3 nm	4,07 Å	30 nm	36 nm

Table IV.1: Structural properties extracted from XRD scans for four BFO-*Mn*/YBCO/PBCO//STO films

The mean c-axis lattice parameter (4th column of Table IV.1) decreases when the thickness of YBCO layer increases (see Figure IV.13, right). This is consistent with the fact that the c-axis lattice parameter of YBCO ($c = 11.68\,Å$) is smaller than the c-axis lattice parameter of PBCO ($c = 11.71\,Å$). The c-axis lattice parameter for the BFO-Mn was constant for the four films ($c = 4{,}07\,Å$), and the thickness t of the film close to the targeted value (last column of Table IV.1).

From the X-rays diffraction scans, we verified that the thicknesses of our films were homogeneous and equal to the targeted values. The diffraction scans showed that the films were highly textured along the (001) axis, that there was an excellent epitaxy between the films and no parasite phases.

This was confirmed by STEM images. Figure IV.14 shows low magnification images of a BFO-Mn ($30\ nm$)/YBCO (2 u.c.)/PBCO (4 u.c.)//STO sample:

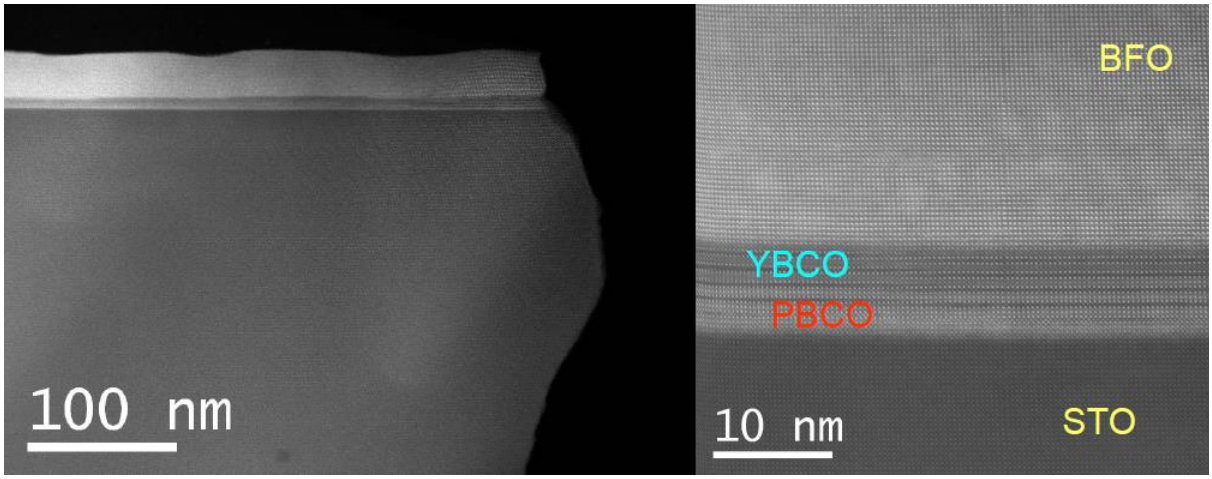

Figure IV.14: STEM images of a BFO-Mn ($30\ nm$)/YBCO (2 u.c.)/PBCO (4 u.c.)//STO heterostructure

From this image we can see that the layers are flat over long lateral distances, that there are no secondary phases. As said before, unit cell high steps are occasionally observed in the YBCO layer.

IV.1.5. c) Ferroelectricity of the BFO-Mn layer

The *BFO-Mn* layers obtained by PLD were ferroelectric, with an out-of-plane polarisation easily switchable with small tip-biased voltages (typically $2{\sim}4\ V$). Figure IV.15 represents a typical PFM image of a film after writing areas with different DC voltages (indicated by the yellow and red numbers). The area is then read with an AC voltage (here $1\ V_{PP}$). The as-grown polarisation of the samples was usually predominantly downwards, like in the background of Figure IV.15. The coercive fields are asymmetric (a smaller electric field is necessary to switch the polarisation from up to down than from down to up): for example in Figure IV.15, the coercive field to switch upwards (black areas) is $+3\ V$ whereas only $-2\ V$ is needed to switch downwards (white areas).

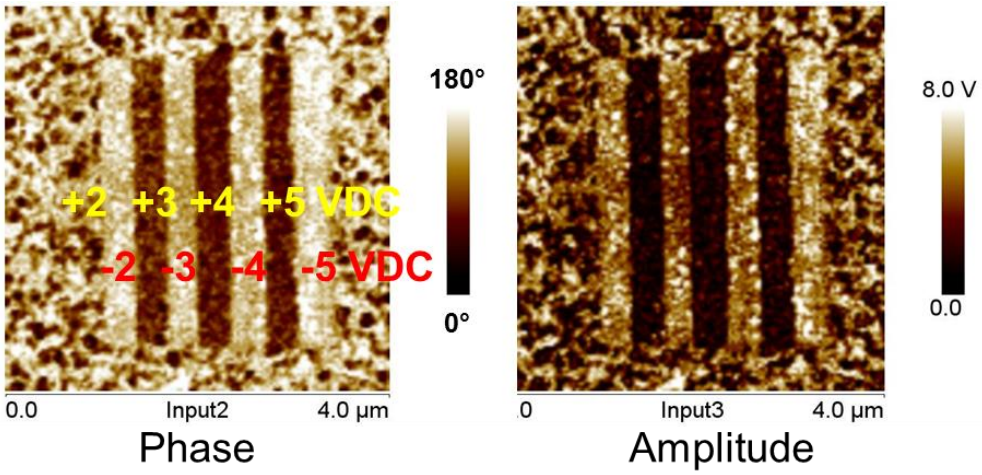

Figure IV.15: Local modification of the polarisation of a BFO-*Mn* $(30\ nm)$/YBCO layer with PFM (read with 1 V_{pp} AC)

In order to estimate the value of the polarisation in our BFO-Mn films, we grew a BFO-Mn/YBCO 4 u.c./PBCO//STO multilayer with $150\ nm$ of BFO-Mn in the conditions optimised for the planar structures. We then deposited square pads of Co (this metal was chosen because it bonds well to the BFO-Mn) coated with Pt to ensure a good contact with the measurement tip. The pads are contacted with a conductive tip AFM and a voltage is applied between the YBCO electrode and the tip, in order to measure polarisation loops; such experiments cannot be carried on thinner films, because of the risk of leakage current in these capacitors. Two typical polarisation loops on $\sim 50 \times 50\ \mu m^2$ pads are reproduced in Figure IV.16 *a)*.

The exact surface of the pad, necessary to determine the exact value of the polarisation, is determined from a CT-AFM scan (Figure IV.16 *b)*) where the green area is the unpatterned BFO-Mn surface and the yellow area is the pad. The measured polarisation reaches $70\ \mu C/cm^2$, the maximal value for the vertical polarisation in orthorhombic BFO-Mn. By measuring the current flowing through the capacitor during the application of the voltage, we determine that 90% of the BFO-Mn underneath the pad is switchable whereas 10% is leaky.

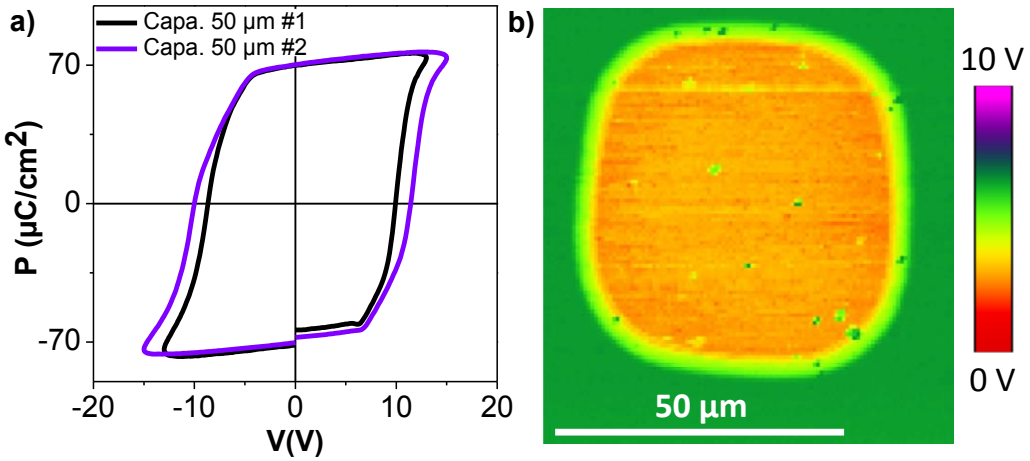

Figure IV.16: a) Polarisation vs applied voltage loop on a Co/Pt/BFO-Mn $(150\ nm)$/YBCO/PBCO//STO capacitor. b) CT-AFM image of the capacitor.

IV.1.5. d) Topography

The topography of the samples was quite different from a set of growth conditions (energy of the laser spot, target-to-substrate distance, etc.) to another: the background was either rather flat ($+/-\ 2\ nm$) either much rougher ($+/-\ 7\ nm$) over distances of $10{\sim}100\ nm$. Topographic images of two BFO-Mn ($30\ nm$)/YBCO (5 u.c.)/PBCO//STO films can be found in Figure IV.17. Defects had different shapes and origins: sharp defects, visible both on YBCO/PBCO//STO and BFO-Mn/YBCO/PBCO//STO heterostructures are attributed to YBCO. Bigger defects like insulating squares represented on the CT-AFM image in Figure IV.18 are typical defects found in BFO-Mn films. Even though defects are usually not ferroelectric (yellow arrows in Figure IV.19: the phase is not defined and the PFM amplitude is zero), some defects eventually had a PFM response (white arrow in Figure IV.19).

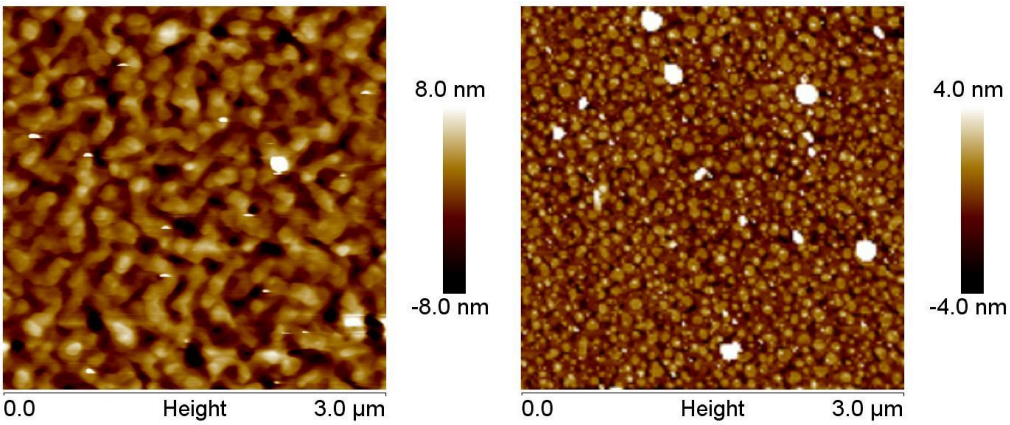

Figure IV.17: Topography of two BFO-Mn ($30\ nm$)/YBCO (5 u.c.)/PBCO (5 u.c.)//STO samples

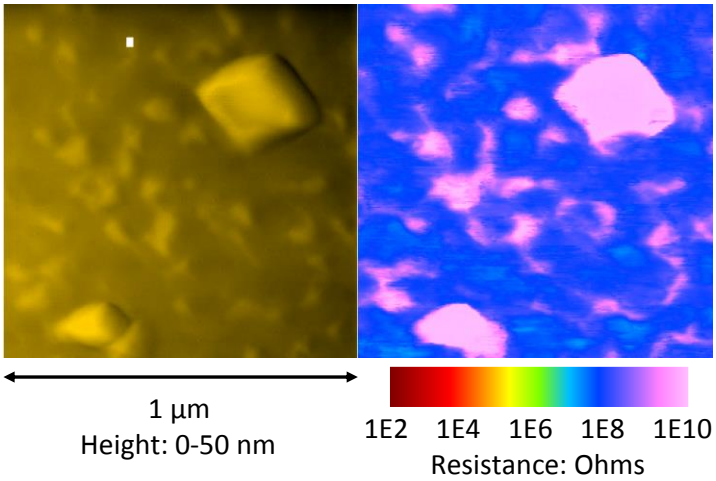

Figure IV.18: Square defect on a BFO-Mn /YBCO/PBCO//STO structure

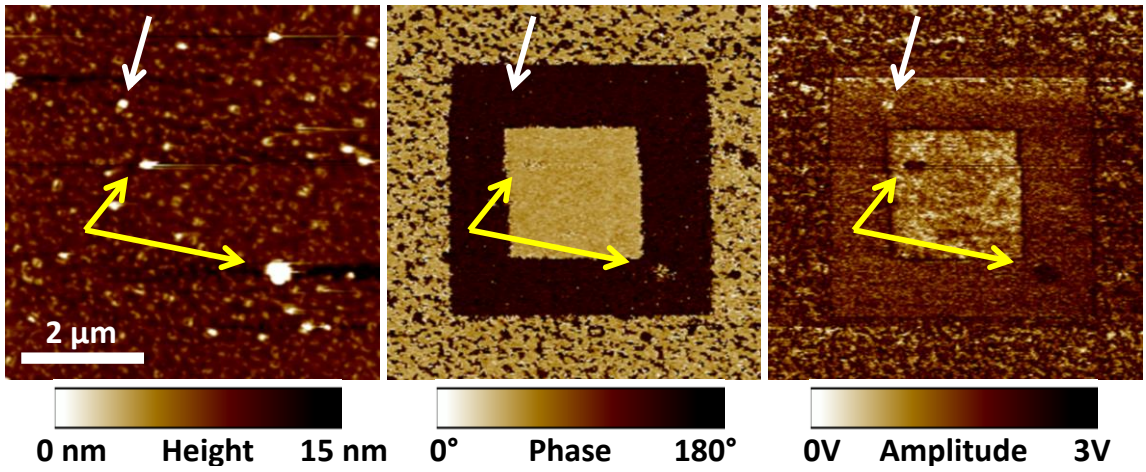

Figure IV.19: Ferroelectric (white arrows) and non-ferroelectric (yellow arrows) defects on a BFO-*Mn* /YBCO/PBCO//STO structure

Defects thus have different shapes and origin. Their presence and their moderate size is not a problem for the planar device application.

Optical microscope images also showed microscopic precipitates: they might damage SPM tips, and prevent the resist to spread homogeneously during the lithography process. Microscopic precipitates could result from projection of matter during the growth, in which case their presence should increase with the duration of the deposition. Figure IV.20 represents the number of defects observable with a microscope per unit area, as a function of *a)* the duration of the growth (in number of laser pulses) of the YBCO film and *b)* the duration of the growth of the BFO-*Mn* film. In both cases the dots colour represents the target-to-substrate distance. We observed no clear correlation between these parameters. We then compared the density of defects to the roughness of the layer, measured with AFM topographic images, in order to figure out if the defects were correlated to the quality of the film (Figure IV.20 *c)*) but, again, no clear tendency was observed. We did not identify the cause of these precipitates.

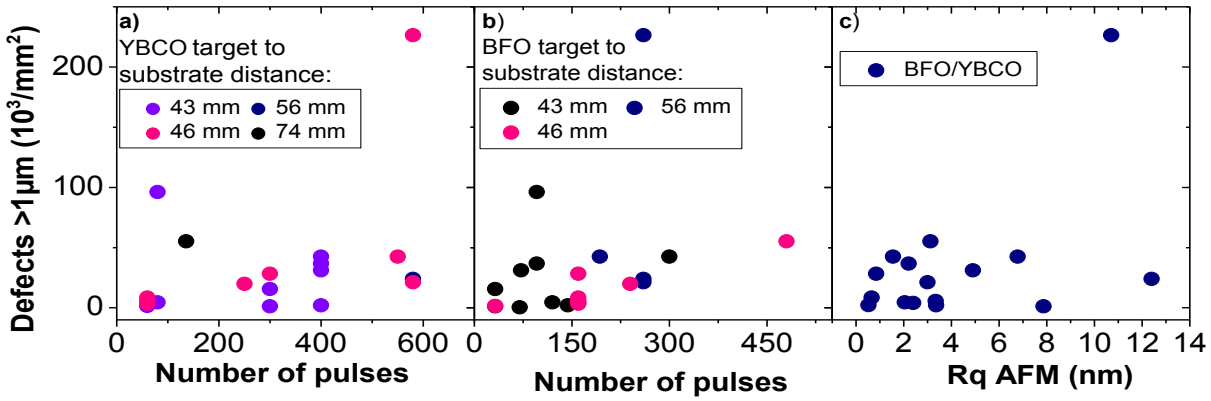

Figure IV.20: Density of microscopic defects with respect to a) YBCO thickness for different YBCO (left) and BFO-*Mn* (right) target to substrate distances on BFO-*Mn*/YBCO/PBCO//STO structures

IV.1.5. e) Optimised growth parameters

To conclude, optimisation work led to **high-quality BFO-Mn /YBCO/PBCO//STO heterostructures, with high critical temperatures and excellent epitaxy between different layers** according to X-Rays diffraction and STEM images. The optimisation process lead to the following parameters for the growth of BFO-Mn/YBCO/PBCO//STO heterostructure: the chamber is pumped down to $2 \cdot 10^{-6}\ mbars$ after introduction of the sample. The pressure is then stabilised at $0{,}35\ mbars$ of O_2.

Growth of PBCO and YBCO:

- Temperature is stabilised at 690°C (after ~ 50' heating);
- Target to substrate distance is $56\ mm$;
- Sample holder rotates;
- PBCO target is ablated during $2'26"$ at $1\ Hz$ with a step of $0{,}25\ mm$;
- YBCO target is ablated at $1\ Hz$ with a step of $0{,}25\ mm$ (duration depends on targeted thickness, deposition rate is identical to PBCO).

Growth of BFO-Mn:

- Temperature is stabilised at 570°C;
- Target to substrate distance is $52\ mm$ measured;
- Sample holder rotates;
- BFO-Mn target is ablated during $12'$ at $5\ Hz$ with a step of $0{,}5\ mm$.

$800\ mbars$ of O_2 are then introduced in the chamber and the heating is turned off.

IV.2 Epitaxial heterostructures for ferroelectric tunnel junctions

IV.2.1 Objectives

In this section we discuss the growth of heterostructures for asymmetric superconductor / ferroelectric / superconductor tunnel junctions. In these devices, we explore two mechanisms modifying the Tunnelling Electro-Resistance (TER) of the barrier:

- If the screening lengths of the two electrodes on both sides of a ferroelectric barrier are different, the electrostatic height of the barrier changes when the polarisation points towards one interface or the other. This mechanism is detailed in section I.3.5 and examples of ferroelectric tunnel junctions with asymmetric electrodes are given in section III.5.3.
- If carriers are depleted at the interface because of the screening, an insulating layer can arise at the interface with the ferroelectric, like represented on Figure IV.21, right. If the polarisation points towards the opposite direction, carriers are accumulated at the interface and the layer is no longer insulating (Figure IV.21, left). The effective width of the barrier is thus modified by the direction of the polarisation.

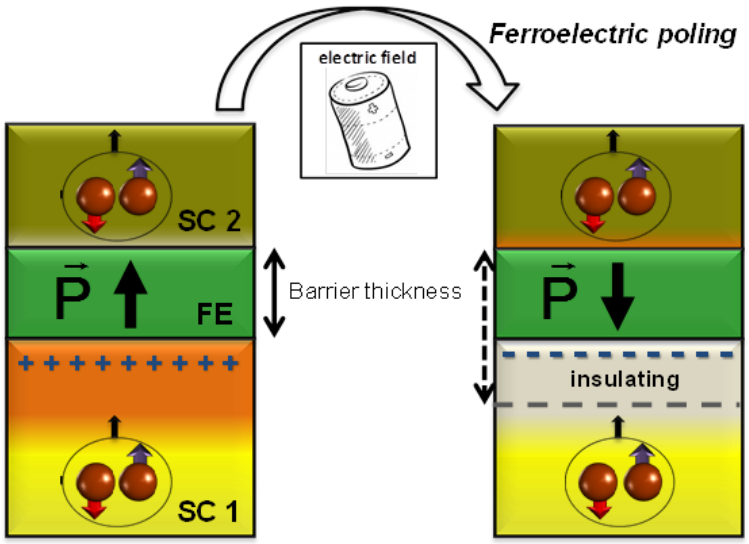

Figure IV.21: Schematic representation of the vertical devices

To obtain such devices, the bottom electrode has to:

- Be sensitive to field-effect, *i.e.* a small variation of the carrier density induces a strong modification of the T_c.
- Have a long screening length to ensure a large modulation of the junction width.
- Have a long coherence length to have Josephson coupling across the barrier.
- Grow flat so that the ferroelectric barrier can grow homogeneously.
- Grow defect-free in order to prevent any eventual screening of the field-effect by the defects or some short-circuit of the barrier.

The ferroelectric barrier has to:

- Have a strong *c*-axis polarisation and be thin enough to allow tunnelling and Josephson coupling.
- Have a good-quality interface with the bottom electrode, in order to minimise the screening of the electric field by the defects.

The top electrode must not be identical to the bottom electrode, and has to:

- Have a small screening length compared to the bottom electrode.
- Have a chemical composition stable at the contact with an oxide, so that an insulating layer does not appear at the interface between it and the ferroelectric layer.

Like for the planar devices, we focused on the structure BFO-Mn/YBCO: YBCO has lattice parameters slightly smaller than BFO-Mn, which has a large out-of-plane polarisation on substrates inducing a compressive strain [69]. For the top-electrode, we investigated several conventional superconductors, in which no large field-effect doping is expected [175]. We considered materials with a rather high T_c, such as Nb, NbN and $MoSi$.

IV.2.2 BFO/YBCO *in situ* heterostructures

In the precedent section (IV.1.1), the main challenge regarding YBCO was to keep good superconducting properties down to few unit cells. For the vertical devices, YBCO has to be flat and defect-free; as explained in section IV.1.3, the deposition conditions required for this are usually to the detriment of the superconducting properties. We were able to obtain very flat YBCO surfaces; however, even in the best conditions, we were not able to have a defect-free surface, and in most of the films some defects higher than tens of nanometres where present. These defects might not be superconducting, but they can short-cut the barrier and cause voltage leakage across the insulating film. In order to reduce the height and the density of defects, we reduced the thickness of the YBCO films down to $7{\sim}8$ unit cells, used a PBCO buffer layer and chemically etched the STO substrate to obtain flat terraces. The surface of a typical YBCO film obtained in these conditions is shown in Figure IV.22 *a)*.

In order to improve the quality of the YBCO films, we increased the frequency at which we sand the target (up to every three depositions) during the optimisation process. By doing this, we obtained films with very little roughness: Figure IV.22 *b)* is a topography image of a YBCO ($50\ nm$) film with an average roughness of $0{,}66\ nm$ and a root mean square roughness of $0{,}46\ nm$. The films were grown at $695°C$ under $35\ mbars\ O_2$, and the target ablated at $1\ Hz$ with a step of $0{,}25\ mm$.

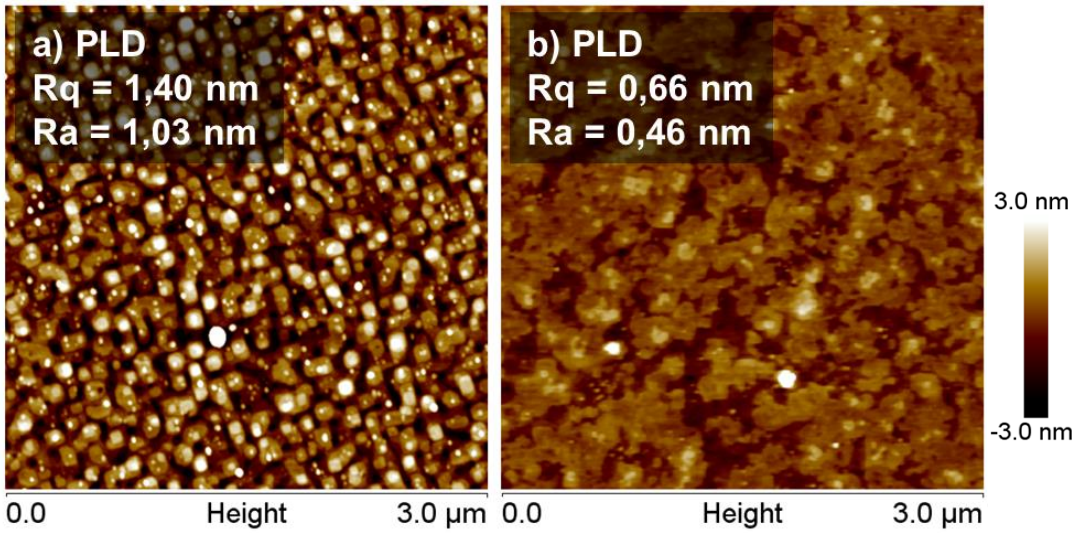

Figure IV.22: YBCO films grown by PLD a) YBCO (10 nm)/PBCO (4 nm)//STO b) YBCO (50 nm)//STO. Ra: average roughness; Rq: root mean square roughness

We then optimised the growth conditions of BFO-Mn thin films on YBCO. The conditions were previously optimised for "thick" BFO-Mn films ($\sim 30\ nm$) but not for ultra-thin films. The optimal temperature and pressure for BFO-Mn films was $560{\sim}600\ °C$ and $0{,}01\ mbars$ of O_2, whereas the YBCO grows at $\sim 690\ °C$ an $0{,}34\ mbars$ of O_2. In order to maintain the oxygen doping in the YBCO films, after the growth of the latter we first lowered the temperature and then lowered the pressure once the temperature was stabilised. During the optimisation process, we focused on changing the pressure and temperature, on tuning the energy density of the spot and modifying the target to substrate distance. However, even though we usually kept a very flat background, the topography of our heterostructures exhibited numerous small defects and less frequent bigger precipitates. Figure IV.23 is a CT-AFM image of a BFO-Mn ($10\ nm$)/YBCO/PBCO//STO film:

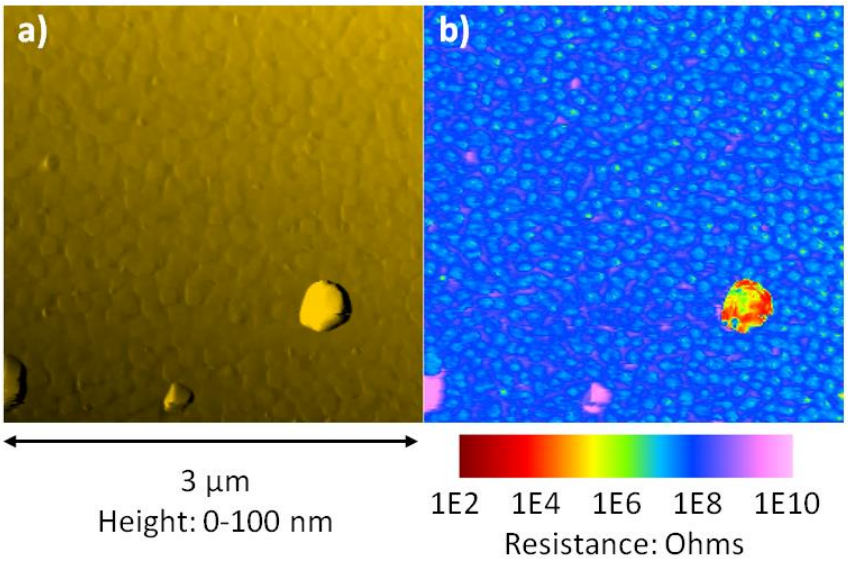

Figure IV.23: a) Topography and b) CT-AFM images showing conductive (in red) and insulating (in purple) defects of a BFO-Mn/YBCO/PBCO//STO structure

On this image, we can see that some defects (the precipitate that appears in red in the figure) are short-circuiting the BFO-Mn film and thus any eventual tunnel junction, whereas some other defects (in purple on the figure) are insulating.

IV.2.3 BFO-*Mn* epitaxy on YBCO films grown by PLD

As explained in section IV.1.4, the laboratory has two PLDs working with two different lasers: "Real" with an Excimer laser and "Abla" with a YAG laser. BFO-Mn in "thick" films (above $30\ nm$) is developed on both assemblies. Ultra-thin films of BFO-Mn were optimised on the PLD "Abla" on several substrates (LSMO, SRO…) but not on YBCO. We explored the possibility of growing the YBCO flat films in the usual PLD where this material is developed ("Real"), and optimising BFO-Mn in the PLD "Abla". The differences between the two PLDs and the process of growing an uncapped YBCO film and transferring it from one PLD to the other have been previously discussed in section IV.1.4.

We grew YBCO (7 u.c.)/PBCO (4 u.c.)//STO heterostructures as described before in section IV.2.2, and deposited BFO-Mn films of different thicknesses under the optimised conditions: $0{,}01\ mbars$ of O_2, at a temperature of $490°C$, with a target to substrate distance of $55\ mm$ at a rate of $2{,}5\ Hz$ ($P3w = 22\ mW$). The samples are then cooled under $300\ mbars$ of O_2.

We obtained good quality samples, but no significant increase in the quality of the sample in comparison with the best heterostructures obtained in situ in the first PLD. As the outcome of the optimisation process, we produced a serial of five samples with 4, 6, 9, 11 and $13\ nm$ of BFO-Mn. Figure IV.24 *a)* shows a typical X-Rays diffraction scan of a BFO-Mn ($11\ nm$)/YBCO (7 u.c.)/PBCO (4 u.c.)//STO heterostructure. The YBCO and PBCO signals are not distinguishable because of their close structures. The BFO-Mn peak is less sharp than the YBCO+PBCO peak. This means that the strain is not homogeneous over the thickness of the film. Figure IV.24 b) is a reflectivity scan of a BFO-Mn (4 nm)/YBCO (7 u.c.)/PBCO (4 u.c.)//STO heterostructure where the blue curve is the measured data and the red line is a simulation of the measurement expected with the parameters within the table.

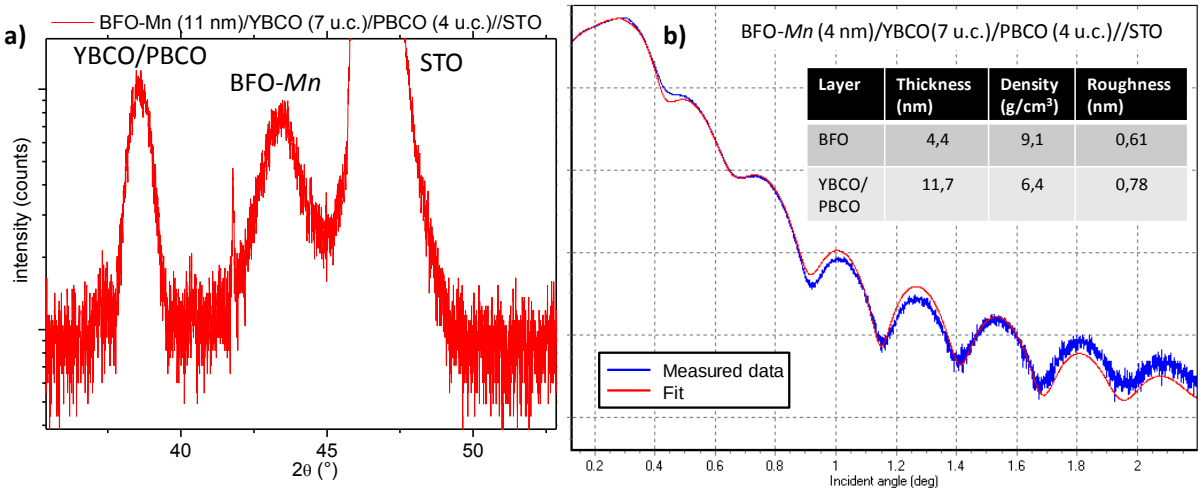

Layer	Thickness (nm)	Density (g/cm³)	Roughness (nm)
BFO	4,4	9,1	0,61
YBCO/ PBCO	11,7	6,4	0,78

Figure IV.24: a) θ/2θ and b) reflectivity scan of *ex situ* BFO-*Mn*/YBCO/PBCO//STO films

The films grew in a monodomain fashion, with the polarisation pointing downwards. Figure IV.25 shows PFM images of areas written by applying a DC voltage: the white areas are downwards and the black areas upwards. The five samples have a switchable polarisation.

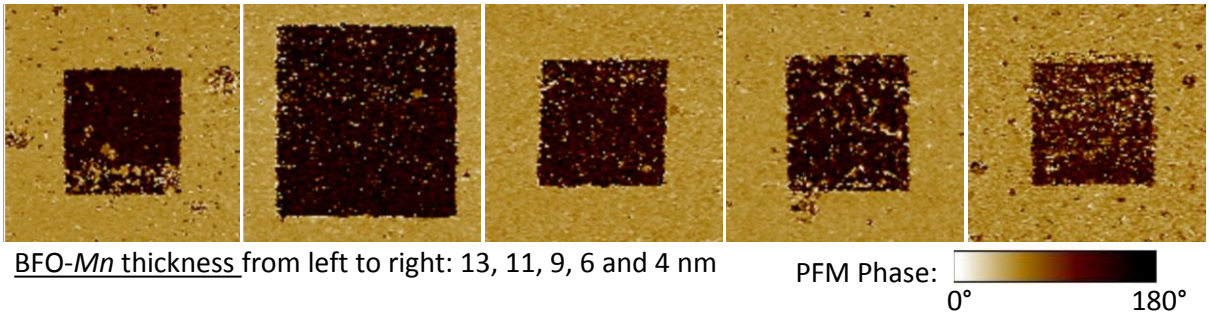

Figure IV.25: PFM switching of BFO-Mn/YBCO (7 u.c.)/PBCO (4 u.c)//STO samples

As in *in situ* heterostructures, CT-AFM images revealed the presence of defects either more conducting than the BFO-Mn film (green defects in Figure IV.26 *c)*), either more insulating (purple defects).

From the CT-AFM scan, it is possible to extract the mean value of the resistance of the film over the scanned area. Figure IV.26 *a)* represents this value for the five samples, measured with a setpoint of $2\ V$: the resistance increases exponentially with the thickness of the BFO-Mn film. This is the sign that the current tunnels through the BFO-Mn layer [24], [25], which makes these structures good candidates for vertical devices.

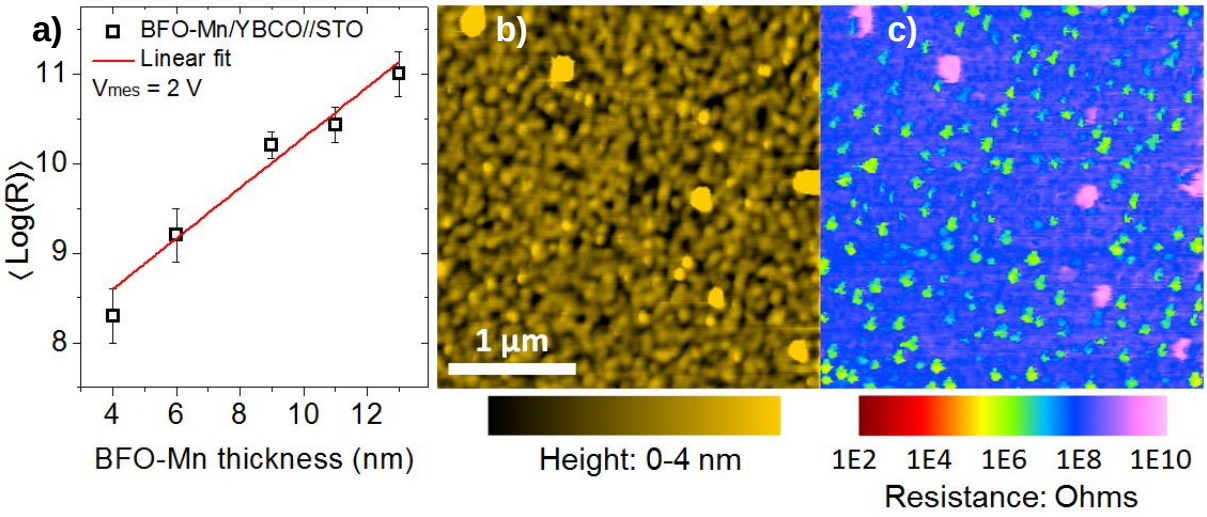

Figure IV.26: a) Mean resistance over the scanned area as a function of the BFO-*Mn* thickness; b) topographic image of a BFO-Mn (4 nm)/YBCO/PBCO//STO film and c) corresponding CT-AFM image measured at 2 V.

IV.2.4 BFO-*Mn* epitaxy on YBCO commercial films

In order to have more reproducible bottom electrodes and fewer defects we considered buying commercial YBCO films grown by sputtering by the company Ceraco. These films are $50\ nm$ thick. We compared films grown on YSZ (*Yttria-stabilised zirconia)* and STO, with and without a buffer of Cerium oxide (CeO_2). The $50\ nm$ thick buffer layer of CeO_2 allowed the YBCO films to be defect free and we systematically chose these films. Figure IV.27 shows AFM topography images of the surface of the films previously presented, *a)* and *b)*: grown by PLD at the laboratory and *c):* a commercial film (YBCO/CeO_2//YSZ). The roughness parameters R_a and R_q (average roughness and root mean square roughness) are comparable, but we can see that the morphology of the surface is different.

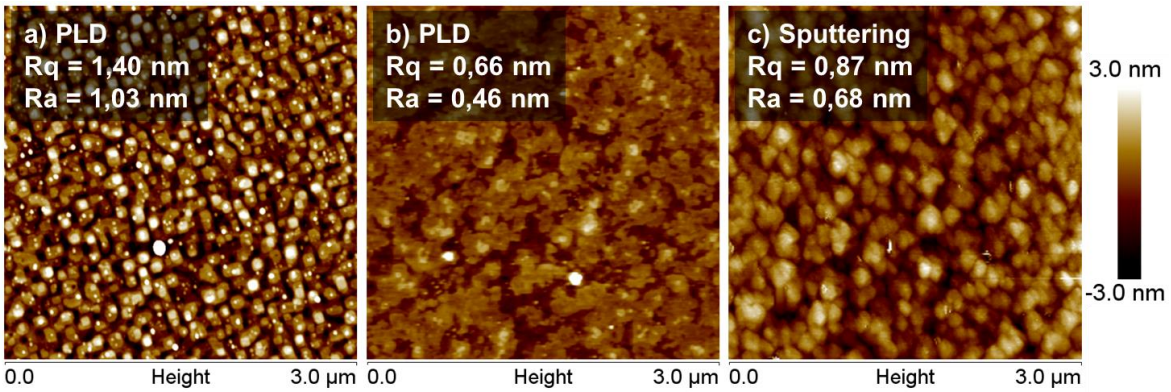

Figure IV.27: YBCO films grown by PLD a) YBCO (10 nm)/PBCO (4 nm)//STO b) YBCO (50 nm)//STO. c) Commercial sputtered YBCO film. R_a: average roughness; R_q: root mean square roughness

In order to compare how BFO-Mn grew on YBCO/CeO_2//YSZ layers *vs* YBCO/CeO_2//STO layers, we grew several BFO-Mn films simultaneously on both $5 \times 5\ mm^2$ samples. We also compared the BFO-Mn films grown on YBCO with the same films grown on bare STO substrates or LSMO//STO films. The main conclusions of these experiments are:

- BFO-Mn on STO or BFO-Mn on LSMO//STO is much flatter than BFO-Mn on YBCO. As an example, Figure IV.28 represents the topography images of the same BFO-Mn film deposited on a YBCO film (left) and a LSMO film (right). For this reason BFO-Mn has to be optimised specifically for YBCO substrates.

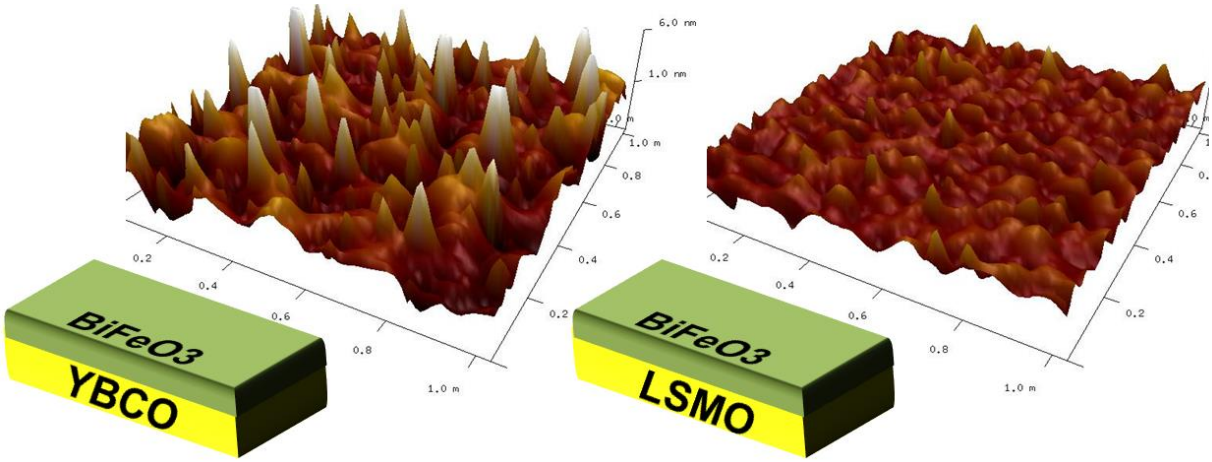

Figure IV.28: BFO ultra-thin film deposited simultaneously on YBCO (left) and on LSMO (right).

- Even though both the YBCO layer and the CeO_2 buffer are as thick as $50\ nm$, the BFO-Mn does not grow the same way on YBCO/CeO_2//YSZ and on YBCO/CeO_2//STO: as an example, Figure IV.29 represents XRD scans of the same BFO-Mn film deposited simultaneously on a the two structures: a parasite phase appears on the film grown on STO but not on YSZ.

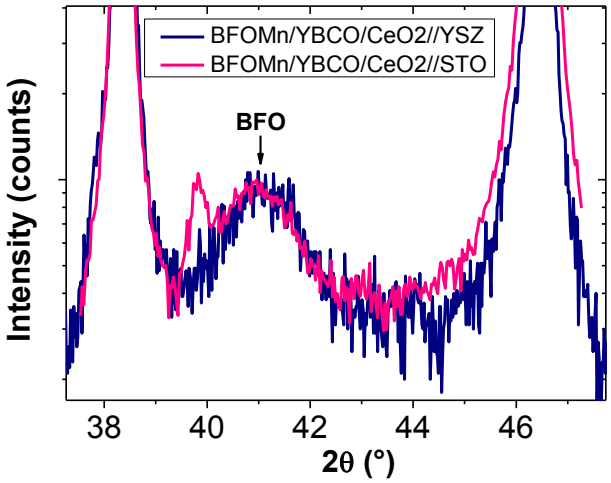

Figure IV.29: Comparison of two XRD scans of the same BFO-Mn film grown on YBCO/CeO2//YSZ and YBCO/CeO2//STO

In order to optimise the growth of BFO-Mn on commercial films, we first reproduced the growth conditions of the previous samples (BFO-Mn on YBCO deposited by PLD), but the BFO-Mn grew in a 3D mode, forming large and high precipitates. We explored a very wide range of temperatures ($350°C\ to\ 570°C$), pressure ($3{,}1 \cdot 10^{-3}\ to\ 2 \cdot 10^{-2}\ mbars$ of O_2), target to substrate distances (from 35 to $55\ mm$), and laser pulse frequency (from 1 to $5\ Hz$). We observed no clear phase diagram for the BFO-Mn films. The thickness of the BFO-Mn layer was usually hard to determine directly from reflectometry scans of the heterostructures, on one hand because of the roughness of the BFO-Mn film and on the other hand because the "low frequency" contribution of the ultra-thin film is convoluted with the high-frequency signal of the $50\ nm$ YBCO film and with the signal of the $50\ nm\ CeO_2$ film. However, a simulation program such as X'Pert reflectivity allows us to fit the measured data and estimate the thickness of the layers (see for example Figure IV.30 *b)*). In order to know more precisely the thickness of the BFO-Mn film, we usually stick a bare STO substrate next to the YBCO film prior to the growth, and proceed to an X-Rays reflectometry measurement on the BFO-Mn//STO film (see for example Figure IV.30 *a)*).

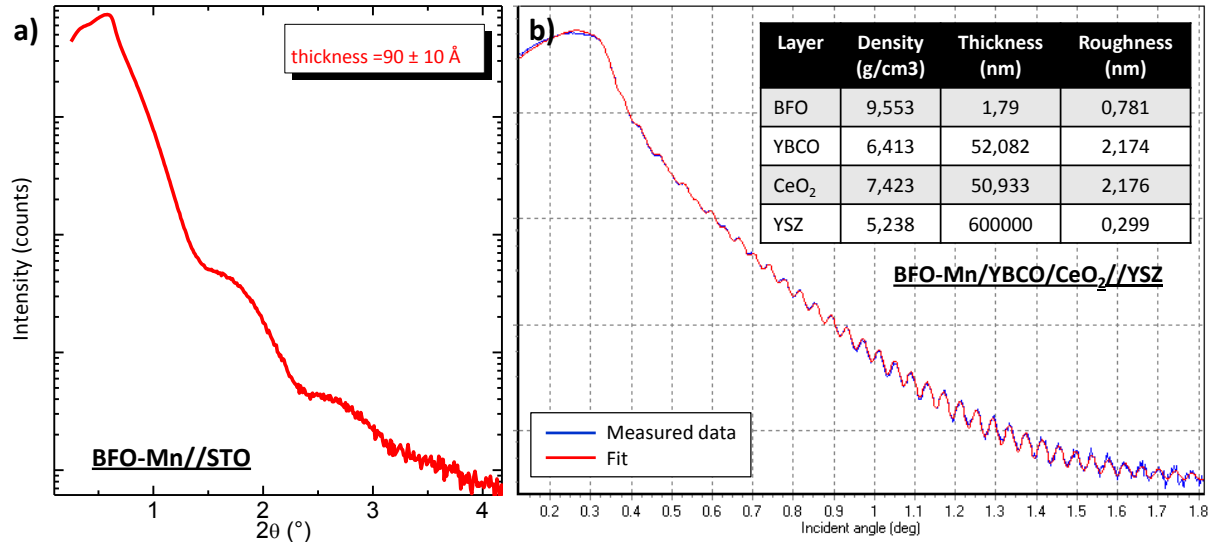

Figure IV.30: X-Rays reflectometry scan of a) a BFO-*Mn*//STO film and b) a BFO-*Mn*/YBCO/CeO2//YSZ film (in blue) and a fit obtained by X'Pert Reflectivity simulation

CT-AFM scans of the BFO-Mn surface were done in order to characterise the electric transport through the film. The same pattern as before was observed: several conducting and insulating defects (see Figure IV.31 *b)* and *c)*), as well as an exponential dependence of the mean resistance as a function of the thickness of the film (see Figure IV.31 *a)*), indicating that the electrons tunnelled through the BFO-Mn films.

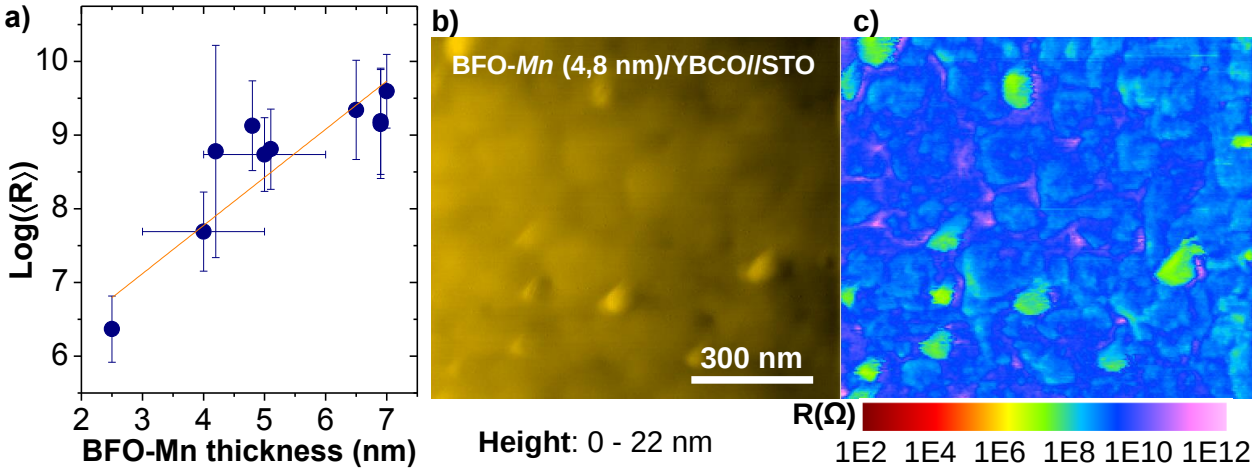

Figure IV.31: a) Mean resistance over the scanned area as a function of the BFO-*Mn* thickness on commercial YBCO; b) topographic image of a BFO-Mn ($4\ nm$)/YBCO/PBCO//STO film and c) corresponding CT-AFM image measured at 2 V.

PFM measurements showed a good ferroelectricity of the BFO-Mn films. Figure IV.32 shows a typical PFM image of background, upwards and downwards areas. The background is mainly downwards (surrounding white square in the left image). The amplitude (right-hand image) is lower for the domains pointing upwards (black square in the left image) than for the domains pointing downwards (surrounding and inner squares). These two trends are characteristic of our BFO-Mn/YBCO films, and are widely discussed in Chapter V.

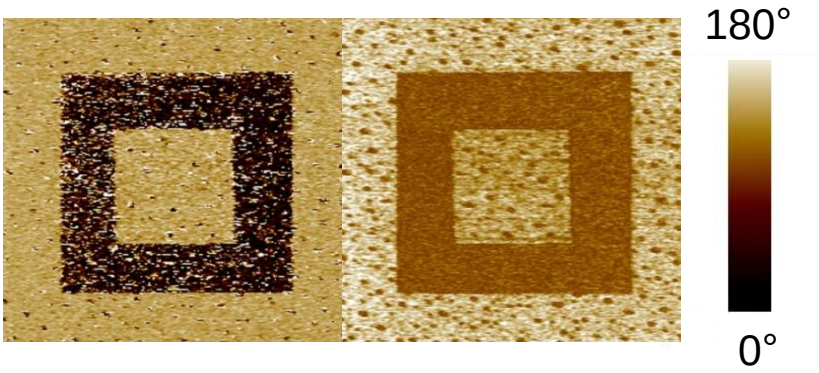

Figure IV.32: PFM measurement of a BFO-*Mn* (7,0 nm)/YBCO/CeO_2//STO (left: phase ; right: amplitude)

To conclude, we achieved to grow ultra-thin BFO-Mn films with good transport and ferroelectric properties on commercial YBCO films. However, after several tens of samples we did not achieve to establish a set of growth conditions that gives reproducible films. This could be due to the fabrication of the commercial YBCO films.

V. BFO/YBCO ferroelectric properties

Index

V. BFO/YBCO ferroelectric properties 110

V.1 Stability of the ferroelectric domains 111

V.1.1 Samples not exposed to an O_2 plasma 111

V.1.2 Samples exposed to an O_2 plasma 114

V.1.3 Asymmetry of the ferroelectric characteristics of BFO films on YBCO 115

V.1.3. a) Electrostatic interactions 116

V.1.3. b) Pinned ferroelectric layer 117

V.1.3. c) Pinned ferroelectric domains 118

V.2 Structure of the BFO-*Mn*/YBCO interface 119

V.3 Ferroelectric switching inside a cryostat 121

V.3.1 Ferroelectric switching in Helium atmosphere 121

V.3.2 Ferroelectric switching at low temperature 123

In the previous chapter, we detailed the growth of different BFO-Mn/YBCO epitaxial structures and gave general characterisations of the obtained films. Two kinds of devices are investigated in this thesis:

- "Planar" structures, where the YBCO film is very thin (few unit cells) whereas the BFO-Mn film is thick ($30\ nm$);
- "Vertical" structures, where the YBCO electrode is thick whereas the BFO-Mn barrier is nanometric and coated by a top electrode.

Prior to the fabrication of the solid-state devices, further experiments were carried on the BFO-Mn/YBCO films in order to characterise the stability of the ferroelectric domains. In particular, we figured out the presence of an electric dipole at the BFO-Mn/YBCO interface, and investigated the strong asymmetry of the ferroelectric characteristics observed in our samples.

V.1 Stability of the ferroelectric domains

The planar devices consist in a $30\ nm$ BFO-Mn film on top of an ultra-thin YBCO film. These samples are patterned into measurement bridges. Then, using a PFM set-up, the polarisation is set upwards on most of the channel except on a thin band across the bridge – in order to define a junction. It is thus critical to make sure that both the upwards and the downwards areas are stable within a long period of time. In this section, we present two types of samples that have the same structure (BFO-Mn/YBCO/PBCO//STO) but that did not undergo the same lithography process. Their patterns are both defined by optical lithography and Ion Beam Etching (IBE), but in the first case the sample is only cleaned with acetone whereas in the second case the sample is exposed to an O_2 plasma. Details on the lithography process can be found in section II.3.2.

V.1.1 Samples not exposed to an O_2 plasma

Early experiments were carried on BFO-Mn/YBCO/PBCO//STO heterostructures. The devices were lithographied according to the process described in section II.3.2, at the exception that they were not exposed to an O_2 plasma after the IBE step. The whole channel was first polarised upwards by applying a DC voltage of +7 V_{DC} between the YBCO layer and the CT-AFM tip. Then, a thin band was written downwards in the middle of the bridge, by applying -7 V_{DC} between the YBCO and the tip. Several "junctions" were written; their width was measured by imaging the junction in PFM mode, with an AC voltage of $2\ V_{PP}$. A typical PFM image of a junction is represented in Figure V.1: in *a)* the phase of the signal is represented: black domains are upwards and white domains downwards. Figure V.1 *b)* is the amplitude of the signal. We can see that the borders are not straight, because of the ferroelectric domains of BFO-Mn that are typically $30\sim80\ nm$ large in our samples. The width of the junction is taken as the average value line by line over the image. Note that the amplitude if the upwards domains is lower than the downwards domain: we will discuss this in section V.1.3.

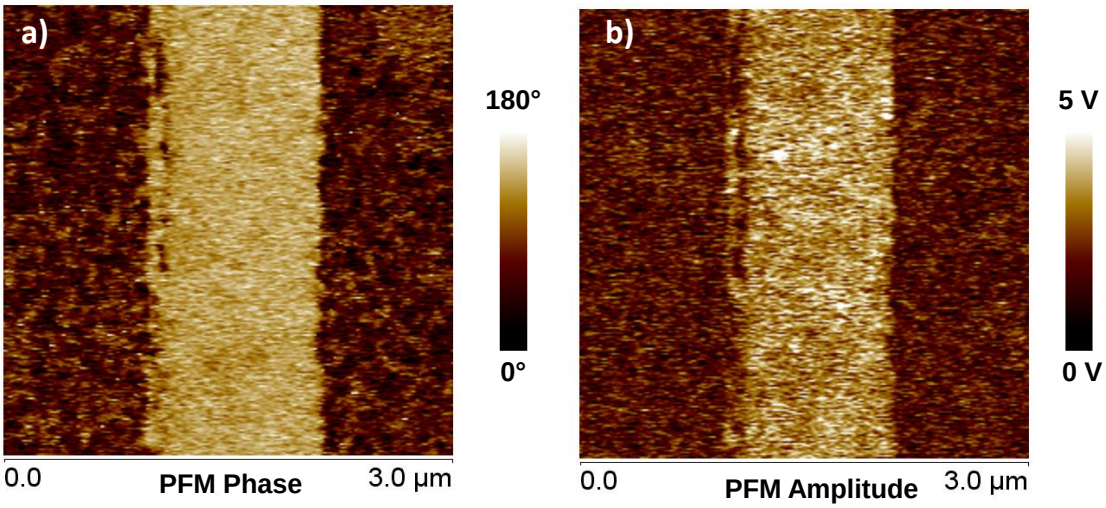

Figure V.1: PFM image of a planar device with a junction. a) Phase; b) Amplitude

The same junctions were re-measured two weeks later. The measured widths at day *D* and *D+14* are reported in Table V.1:

Bridge	Width day D	Width day D+14	Absolute	Relative
1	3,14 µm	3,75 µm	+0,61 µm	+19%
2	6,06 µm	7,02 µm	+0,96 µm	+16%
3	0,40 µm	0,50 µm	+0,10 µm	+25%
4	0,93 µm	1,20 µm	+0,27 µm	+29%

Table V.1: Evolution of the width of planar junctions with no 0_2 treatment with time

The downwards domain expanded – from $100\ nm$ for the most stable one to $1\ \mu m$ for the worst. However, no downwards isolated domains appeared in the upwards area, which remained uniform. **This indicates that the downwards direction is energetically more favourable but that the vicinity with downwards domains is necessary for an upwards domain to switch spontaneously**.

To investigate the effect of the neighbourhood on the stability of the domains, we proceed to local switching of the ferroelectric polarisation with the tip of a CT-AFM in static mode: the tip is grounded and immobile, whereas the YBCO layer is connected to the positive electrode of a voltage source. We apply successively *DC* pulses to modify the polarisation and *AC* short sequences to measure the polarisation (the microscope is in the PFM set-up). We compare the behaviour of a domain surrounded by downwards domain with the behaviour of a domain surrounded by upwards domains (Figure V.2), on a BFO-Mn ($30\ nm$)/YBCO ($5\ u.c.$)/PBCO//STO patterned sample:

- In the first case, the probed domain is initially downwards, and is surrounded by downwards domains (Figure V.2, left). We apply *DC* pulses with increasing values of voltage (in abscise of the graphs) and apply an *AC* sequence to measure the PFM response of the domain. From the PFM signal, we extract a phase (that is 0 or π depending on the direction of the polarisation) and the amplitude of the piezoresponse

of the domain. The blue ("1st pass") curve represents the first measurement of a zone and the green ("2sd pass") curve a subsequent measurement of the same zone. From the *phase vs applied voltage* graph, we observe that **the upwards direction is not stable**: the phase switches back to $+90°$ well before a downwards electric field is applied. The amplitude (upper graph) indicates that the upwards direction gives a weaker signal than the downwards direction, and, contrary to the phase, is hysteretic: this lets us think that the polarisation might switch upwards when the field is applied, but switches back during the reading process. This could happen either spontaneously or because of the AC excitation, even though the amplitude is small ($1\ V_{PP}$).

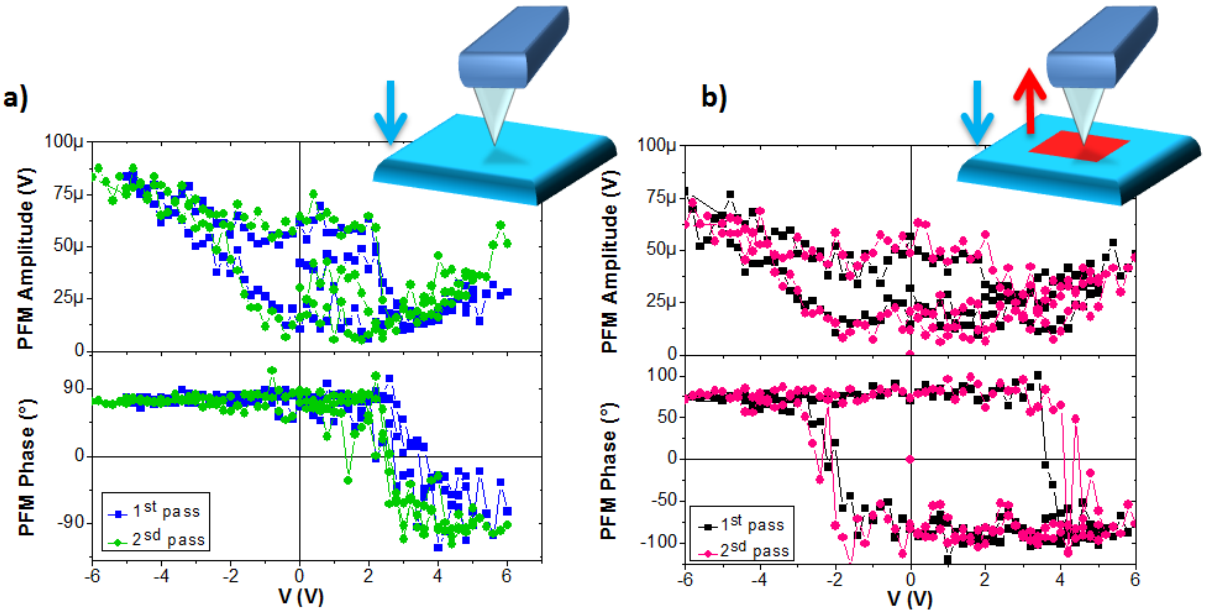

Figure V.2: Stability of a domain with respect to its environment. The probed domain is mainly surrounded in a) by downwards domains and in b) by upwards domains

- We then polarised a large area ($5 \times 5\ \mu m^2$) upwards by scanning the zone while applying $+6\ V_{DC}$ between the YBCO and the tip. We verified with a PFM image that the area was well written and stable. Even though we were not able to stabilise the polarisation upwards on a single domain, **the writing process in which we first write a large area without applying any AC voltage allows the upwards switching of the polarisation**.
- We then probed local domains within this zone (the domain is thus surrounded by upwards domains). Data are presented in Figure V.2–right, for four different areas. We can see from the phase *vs* applied DC voltage that **when the domain is surrounded by upwards domains, the polarisation is much more stable in both directions and can be switched following a usual ferroelectric hysteretic cycle**. We notice that the coercive fields are asymmetric: the domains need a smaller electric field to switch from the upwards to the downwards direction than the opposite, and that the amplitude of the piezoresponse of the upwards domains is smaller than for the downwards domains.

These experiments emphasise the strong competition between the different mechanisms in the switching process:

- **The downwards direction is energetically more favourable than the upwards direction;**
- **The stability of a domain is directly related to its environment.**

V.1.2 Samples exposed to an O_2 plasma

Later, the lithography process was modified in order to improve the quality of the patterned devices. As described in section II.3.2, we observed that proceeding to a cold O_2 plasma after the IBE step significantly increased the robustness of our samples. On these exposed samples, we carried on similar experiments than those presented in section V.1.1. On long timescales (four months in the example shown in Figure V.3 *a)* and *b)*), the upwards domains nucleated into downwards domains, like represented in Figure V.3 *a)* and *b)*. The junction, which has an initial width of $2{,}02\ \mu m$, did not expand.

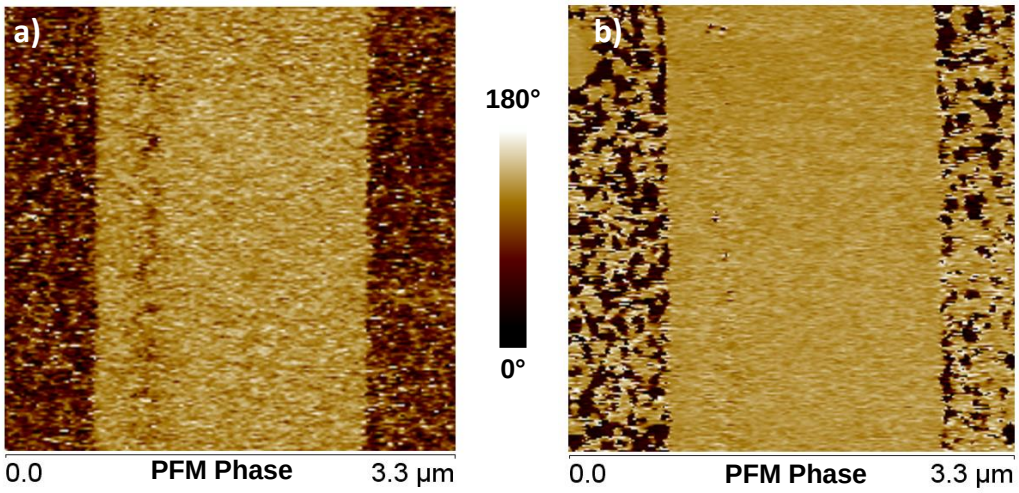

Figure V.3: PFM image (phase) of a junction a) the day it was written and b) four months later

During the four months that separate the two images, the sample was kept at room temperature: this spontaneous switching might be significantly slower at low temperature.

If we now compare two images taken after three weeks – see Figure V.4 *a)* and *b)* – we observe that the upwards domains did not switch back downwards. *c)* and *d)* represent the average width of the barrier over the image: **the width of the downwards domains remained unchanged after several weeks**, which was not the case on the unexposed samples.

The bottom electrode (ultra-thin YBCO) is a rather bad metal and has poor screening abilities. By exposing the sample to an O_2 plasma, the YBCO film might have been reoxygenated: it thus has a higher hole concentration, which is consistent with the higher T_cs measured on these bridges. **Therefore a larger number of free carriers are available to screen the ferroelectric polarisation and stabilise it**.

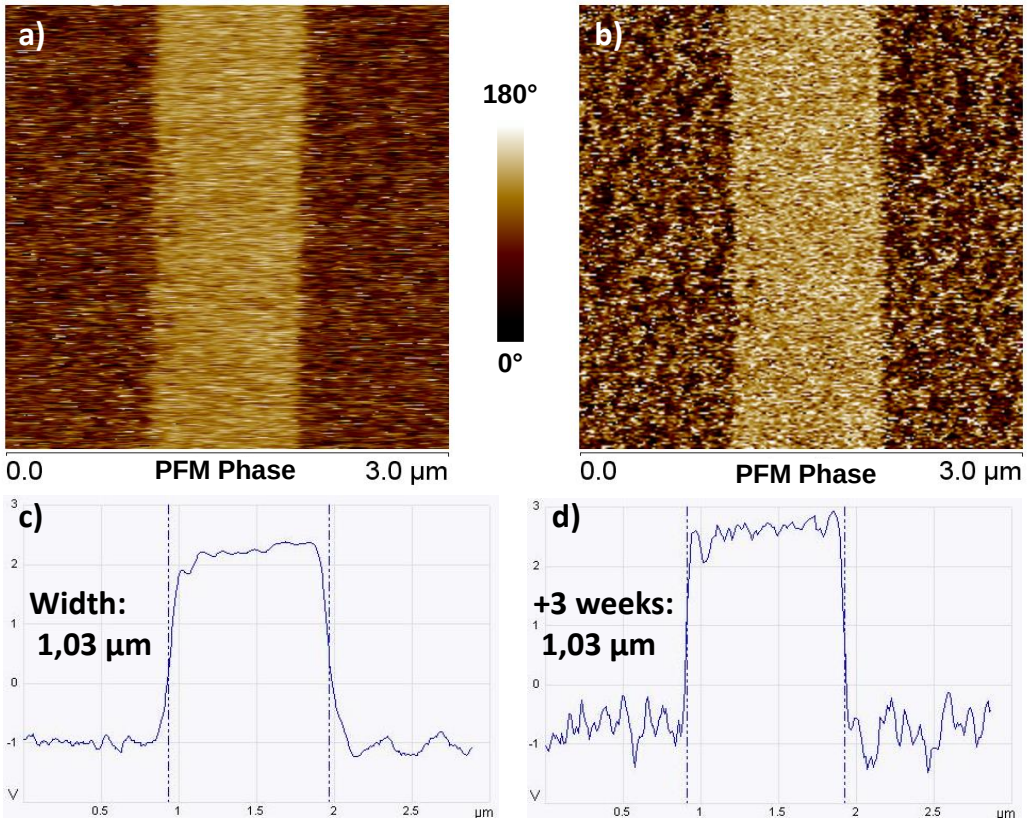

Figure V.4: PFM image (phase) of a junction a) the day it was written and b) three weeks later. c) and d) Average line by line phase profile over the image.

To conclude, thanks to a modification in the lithography process that improves the quality of our devices, we are able to define junctions with width of stable size.

V.1.3 Asymmetry of the ferroelectric characteristics of BFO films on YBCO

Both at the nanoscale and in bigger PFM scans, we observe three asymmetries:

- **The as-grown polarisation is usually downwards**, or predominantly downwards;
- **The negative coercive field** (the field that has to be applied to switch from the upwards to the downwards polarisation) **is always smaller than the positive coercive field**. This is observed when we switch locally the polarisation, as well as when we write large areas like in Figure V.5, left: the voltage necessary to switch completely the polarisation of an area is smaller to write downwards areas (here -2 V_{DC}) than to write upwards areas (here +3 V_{DC});
- **The piezoresponse amplitude of domains or areas in the upwards direction is always smaller than in the downwards direction** (see Figure V.5, right: upwards domains have almost zero amplitude).

These asymmetries are not observed to that extent in similar systems when BFO-Mn is grown on different electrodes such as LSMO, LCMO… but have been observed on the BTO/YBCO films. They occur on the three different PFM set-up of the laboratory. Understanding the origin of this asymmetry is critical for our understanding of the electrostatic interactions between the YBCO and

the BFO-*Mn* film, and thus the field-effect. In the following paragraphs, we discuss the difference of amplitude between the upwards and the downwards domains.

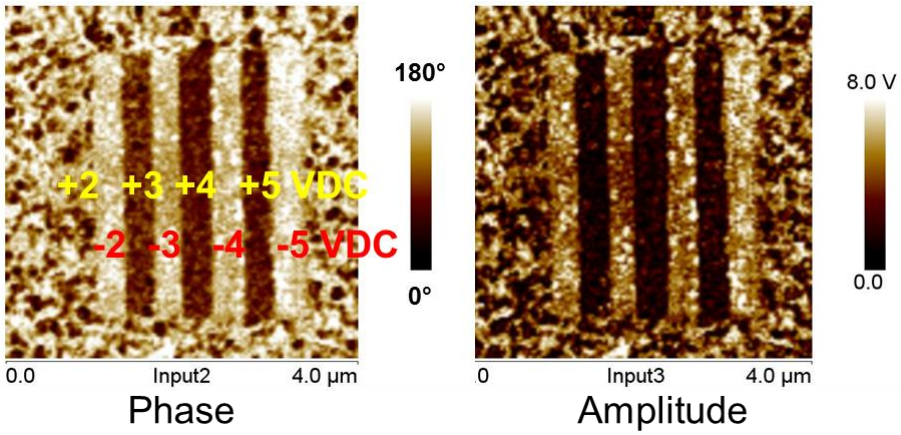

Figure V.5: Local modification of the polarisation of a BFO-*Mn*/YBCO layer with PFM (read with 1 V_{pp})

V.1.3. a) Electrostatic interactions

PFM is based on the detection of bias-induced surface deformation: the piezoresponse of the surface is detected as the first harmonic component of the tip deflection, $d = d_0 + A\cos(\omega t + \varphi)$, where the phase φ directly depends on the direction of the polarisation, and the piezoresponse amplitude $PR = A/V_{AC}$ defines the local electromechanical activity of the surface. For a pure piezoelectric response, it should be equal for down and up domains. However, long range electrostatic forces and non-local contributions due to capacitive cantilever-surface interactions might contribute to the PFM amplitude [176].

To investigate this asymmetry, we first checked that it was not due to a capacitance effect between the cantilever and the bottom electrode. To do this, we compared the PFM amplitudes for both direction of a BFO-*Mn*/YBCO heterostructure at the centre or the sample and on the border of the sample. Figure V.6 *c)* is a picture of the cantilever at the border of the sample: the tip is below the left side of the cantilever, the main body of which is above an area of the substrate (STO) where no YBCO was deposited. In both regions, we pole a square in the upwards direction, then pole a smaller square in the downwards direction.

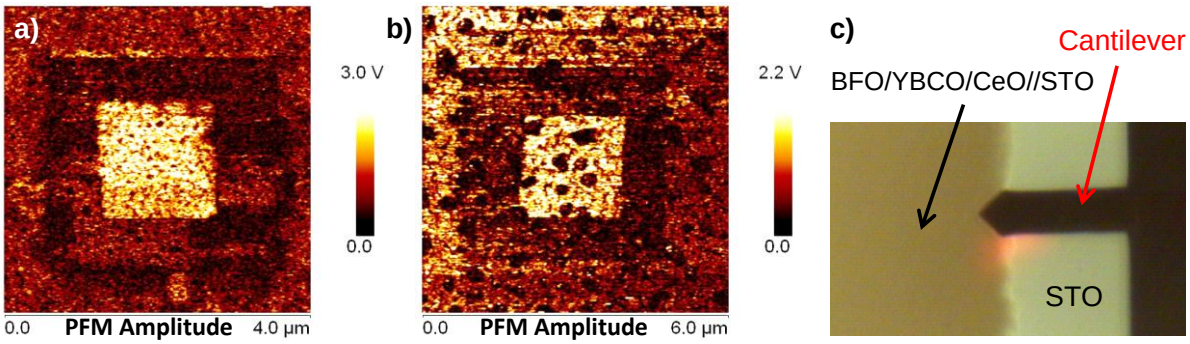

Figure V.6: Comparison of PFM amplitudes a) in the center and b) at the border of a BFO-*Mn*/YBCO/CeO2//STO sample. c) Photograph of the set-up with the tip at the border.

We then image the area with an AC voltage. Figure V.6 *a)* shows the amplitude of the PFM scan at the centre of the sample (with the cantilever above the YBCO electrode) and Figure V.6 *b)* shows the amplitude of the PFM scan at the border of the sample. The topography of this area was rather bad and presented a lot of defects with no ferroelectric contributions. In the two cases, the piezoresponse of the downwards square has a bigger amplitude than for the upwards area, which suggests that **this asymmetry does not come from a capacitance effect between the main body of the cantilever and the YBCO.**

V.1.3. b) Pinned ferroelectric layer

The asymmetry could come from a pinned layer in the BFO-Mn film: if two ferroelectric blocks have the same polarisation, their piezomechanical response will both contribute to the amplitude with the same sign, whereas in the case of an upwards domain superposed to a downwards domain, one domain will expand while the other retracts and the total amplitude will be very low, as schematically explained in Figure V.7.

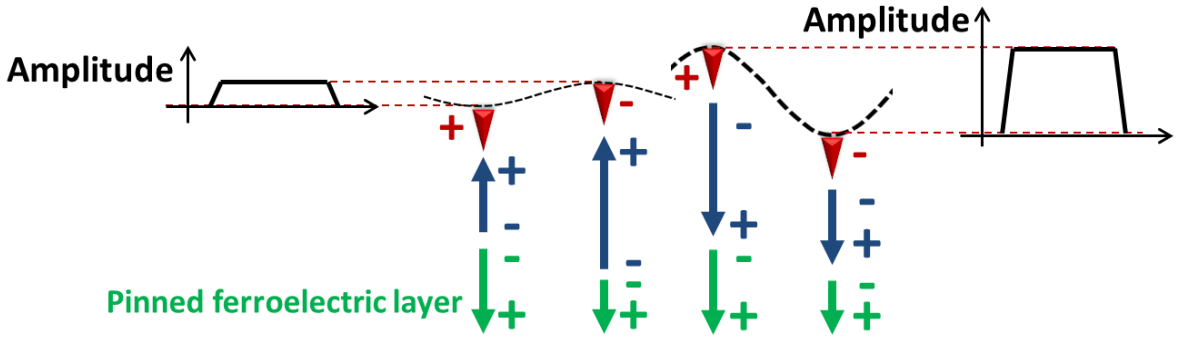

Figure V.7: PFM contribution of a pinned ferroelectric layer

In principle, if we suppose that the pinned layer has a thickness that does not depend on the total thickness of the ferroelectric film, this effect should increase as the total thickness of the film decreases. We measured the amplitude in the up and down directions from several samples with thicknesses down to $4\ nm$, but we observed no correlation between the thickness and the difference of amplitudes (Figure V.8).

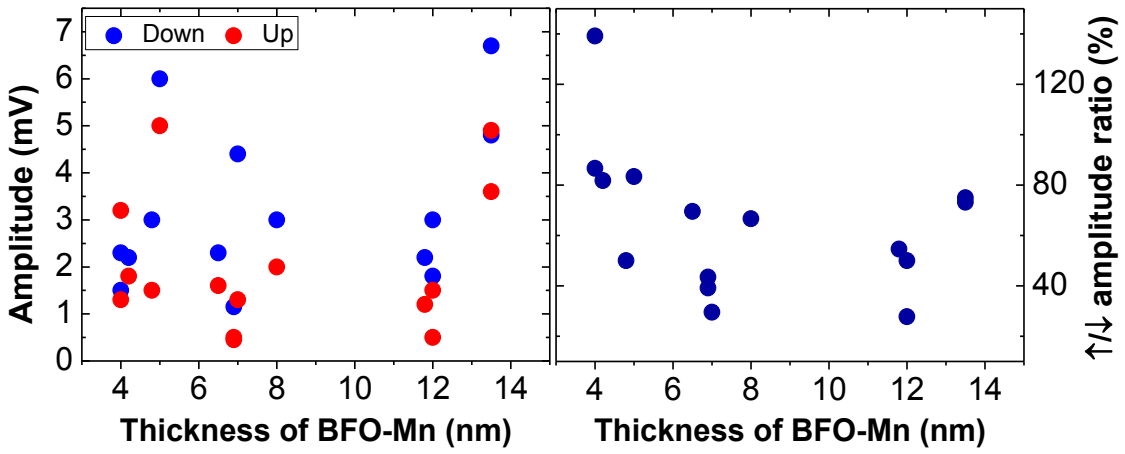

Figure V.8: PFM amplitude for BFO-Mn/YBCO structures for up and down directions (left) and ratio (right)

This signifies that the asymmetry might not arise from a pinned layer at the interface.

V.1.3. c) Pinned ferroelectric domains

Finally, a reason why the amplitude of the upwards direction is smaller than the amplitude of the downwards could lie in small pinned domains that do not switch upwards, but that contribute to the total amplitude in a positive or in a negative way, as represented in Figure V.9.

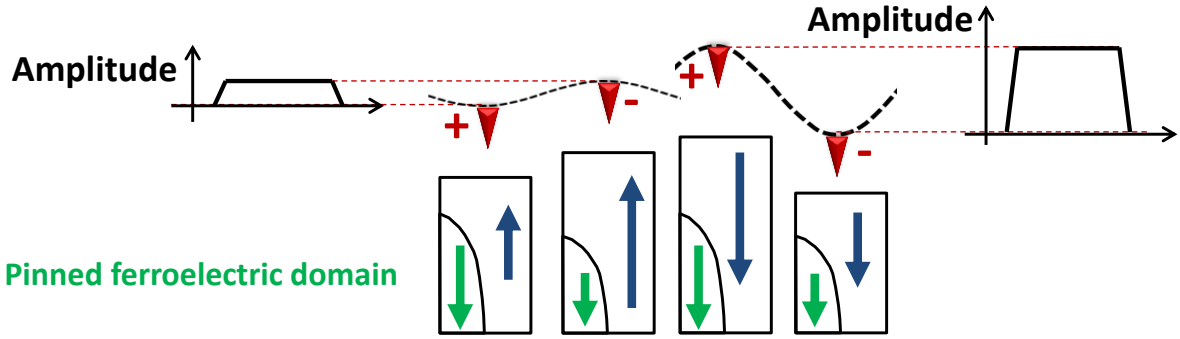

Figure V.9: PFM contribution of a pinned ferroelectric domain

This scenario is consistent with the large dispersion observed from one domain to the other when measuring PFM local cycles. Indeed, some areas switch "easily" i.e. with small coercive fields – for example the zone corresponding to the blue curve in Figure V.10, whereas other areas seem pinned by downwards domains – for example the zone corresponding to the red curve in Figure V.10.

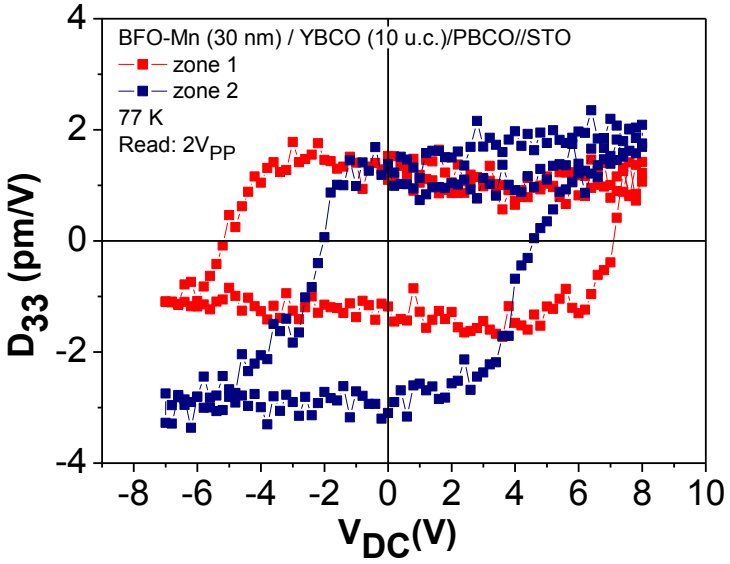

Figure V.10: PFM contribution of a pinned ferroelectric domain

To conclude, the difference of amplitude between the upwards and downwards BFO-*Mn* domains on YBCO might be the sign that some small domains are pinned in the downwards direction. These domains might reduce the amplitude of the field-effect in our device: the charge transfer will thus be smaller than the polarisation of $70\ \mu C/cm^2$ expected for "thick" BFO-*Mn* films.

V.2 Structure of the BFO-Mn/YBCO interface

Thanks to the collaboration of Maria Varela, we were able to obtain Scanning Transmission Electron Microscopy (STEM) images of our heterostructures. Electron Energy Loss Spectroscopy (EELS) maps were established for two different BFO-Mn/YBCO/PBCO//STO samples with thickness of 3 u.c. and 13 u.c. for the YBCO layer. Figure V.11, *a)* shows the EELS maps obtained from targeting the $Fe\ L_{2,3}$ in green, the $Ba\ M_{4,5}$ in red, the $Pr\ M_{4,5}$ in blue, and the $Ti\ L_{2,3}$ in yellow for the 2 u.c. sample. Together with the High-Angle Annular Dark Field (HAADF) image (Figure V.11, *b)*) on which the atomic structure clearly appears, we were able to determine the composition of the BFO-Mn/YBCO interface. The maps were identical for both samples.

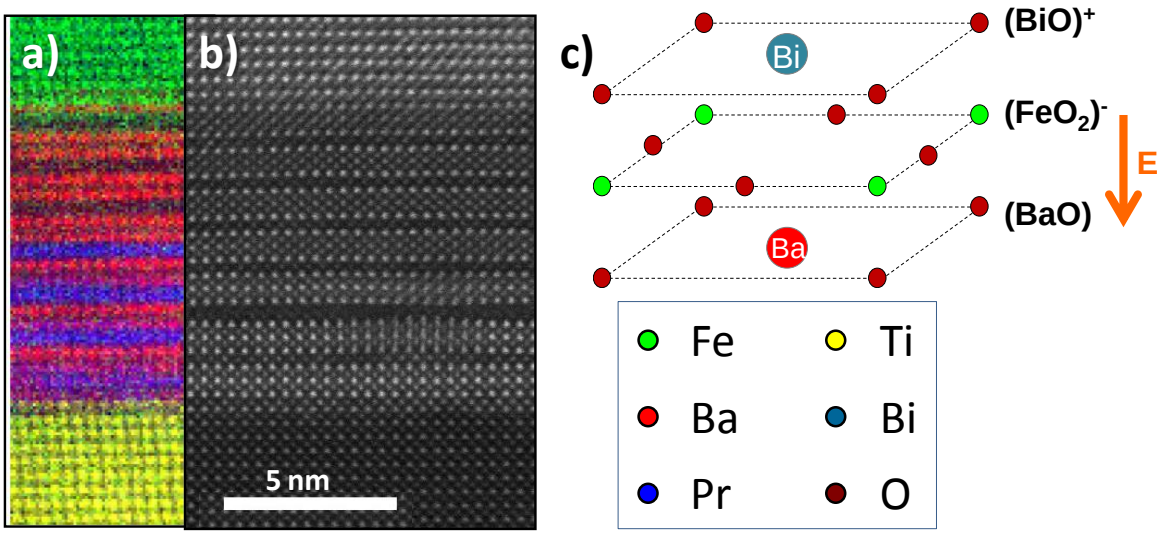

Figure V.11: a) EELS map and b) STEM-HAADF images of BFO-Mn (30nm)/YBCO(3 u.c.)/PBCO(4 u.c.)//STO. c) Permanent dipole at the BFO-Mn/YBCO interface

We observed that the YBCO upper layer is terminated by a neutral BaO plane, which suggests that the first BFO-Mn plane is $(FeO_2)^-$: a permanent dipole pointing downwards – towards the YBCO film – exists at the interface. Because of this dipole, the downwards direction is favourable for the polarisation: in this configuration, the depolarising field at the interface compensate the dipole [124], [177].

The STEM images enable us to estimate the displacement of Fe atoms with respect to Bi atoms. Figure V.12 represents a STEM-HAADF image of a BFO-Mn $(30\ nm)$/YBCO(5 u.c.)/PBCO(4 u.c.)//STO sample. On the right, the colour of each pixel represents the measured displacement of the Fe atom with respect to the centre of the cell formed by the four surrounding Bi atoms. We can see that in this area, the Fe atom is usually above the centre of the Bi atoms, and on the left.

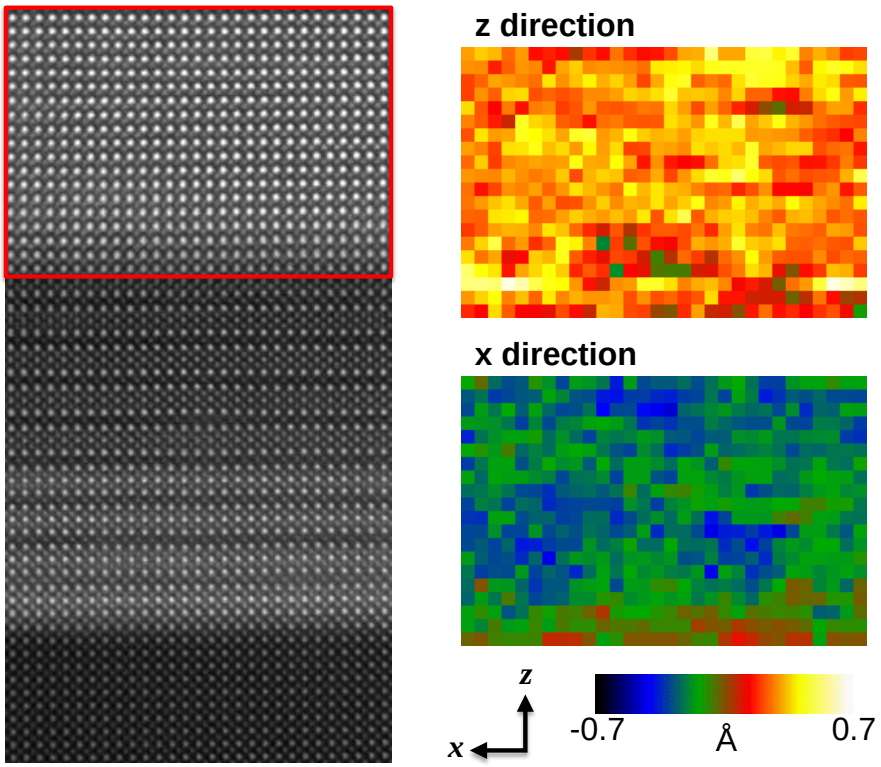

Figure V.12: STEM map showing the displacement of Fe atoms with respect to the centre of the cell, in a BFO-Mn (30 nm)/YBCO(5 u.c.)/PBCO(4 u.c.)//STO sample

This gives us precious information on the polarisation of the BFO-Mn next to the interface. As detailed in the chapter I, and represented in Figure V.13 *a)*: the polarisation in BFO-Mn results of the displacement of both the Bi atoms and the Fe atom (both carrying a positive charge) in one direction along the [111] axis, and the displacement of the oxygen octahedron (carrying a negative charge) along the same axis but in the opposite direction. The centre of the cell formed by the Bi atoms moves more than the Fe atom. For this reason, the vector $\overrightarrow{D_{FB}}$ representing the displacement of the Fe atom with respect to the centre of the Bi cell has an opposite direction to the polarisation $\vec{P}$.

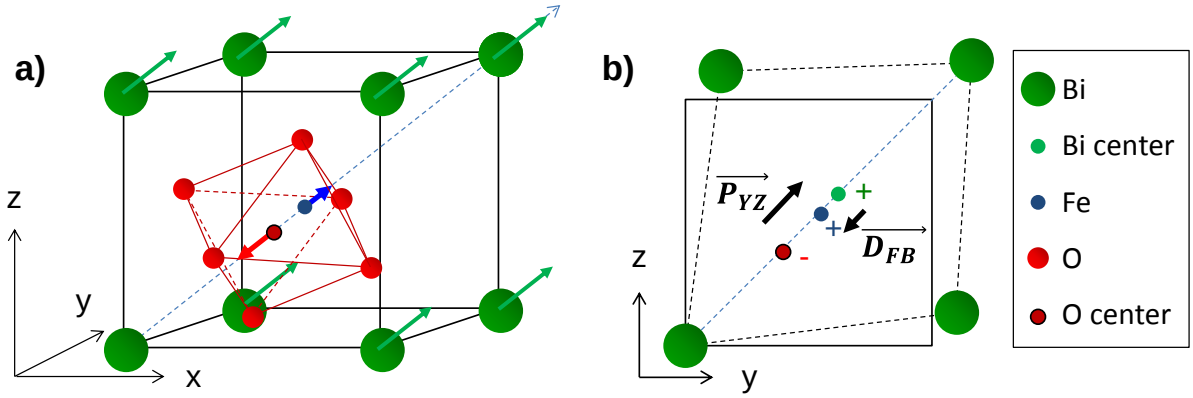

Figure V.13: a) Displacement of the atoms in the BFO unit cell along the [111] direction. b) Projection of the displacement of the charge barycentres on the *yz* plane.

Figure V.13 *b)* represents these two vectors projected along the *yz* plane; as the displacement occurs along the [111] direction, this projection is equivalent along the *xy* and *xz* planes. **The displacement**

map in Figure V.12 shows a $\overrightarrow{D_{FB}}$ pointing upwards, which is thus consistent with a polarisation pointing downwards.

Quantitative displacements maps along the [111] direction for two samples can be found in Figure V.14. The mean displacement is $0{,}32 \pm 0{,}10$ Å for sample *a)* and $0{,}36 \pm 0{,}12$ Å for sample *b)*.

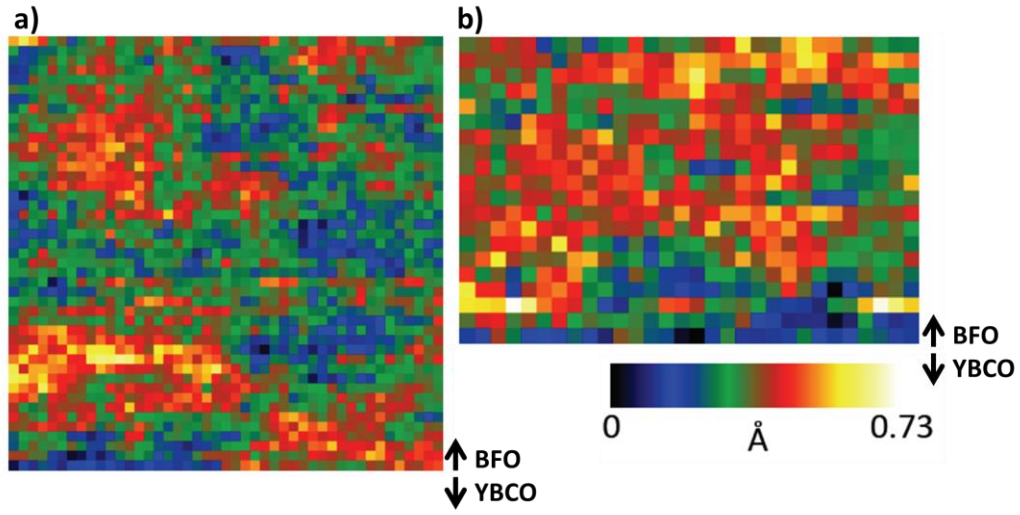

Figure V.14: displacement of the Fe atoms with respect to the Bi center in the BFO unit cell in a BFO-Mn (30 nm)/YBCO(n u.c.)/PBCO(4 u.c.)//STO sample with a) n=8 and b) n=5. The BFO/YBCO interface is at the bottom.

From this displacement, one can estimate the value of the polarisation in the image plane $\boldsymbol{P}$ according to the simple relationship [178]:

$$\boldsymbol{P} = -2{,}5 \frac{\mu C}{cm^2.pm} \cdot \boldsymbol{D_{FB}} \qquad \text{(V.1)}$$

This leads to $P = 80 \pm 25$ $\mu C/cm^2$ for sample *a)* and $P = 90 \pm 30$ $\mu C/cm^2$ for sample *b)*, which is consistent with the values measured with $P(E)$ loops on thicker samples (see Figure IV.16).

V.3 Ferroelectric switching inside a cryostat

In the context of the planar devices, we define Superconductor/Normal Metal/Superconductor junctions by modifying locally – with a PFM scan – the direction of the polarisation of BFO-Mn in BFO-Mn/YBCO heterostructures. These devices operate at low-temperature; we expect a change in the transport characteristics when modifying the width of the junction, defined by a PFM scan. For these reasons, **we aim at fabricating devices in which the ferroelectric polarisation can be switched directly inside the operating cryostat**, i.e. at low temperature and in a He atmosphere. With this in mind, we characterised the ferroelectric switching in these specific conditions, using an Attocube commercial set-up.

V.3.1 Ferroelectric switching in Helium atmosphere

We compared ferroelectric local measurements in the air and in a chamber that was first pumped down to 10^{-6} $mbars$, then filled with 17 $mbars$ of He. Figure V.15 presents the data for

three zones in Helium atmosphere (left) and two other zones in air (right). In air, the ferroelectric polarisation is screened by ionic species. In vacuum or in an inert atmosphere like Helium, it can be expected to be screened by intrinsic charge carriers rather than mobile adsorbates [179]. Moreover, the contact between the tip and the surface is strongly affected by humidity, as water can form a meniscus around the tip [180]. The impact of the meniscus is system dependent; in some cases it was reported to hamper the switching [181], whereas in other cases it supports switching and leads to formation of bigger domains [180].

Figure V.15 shows typical measurements in Helium (on the left) and in air (on the right) for the same sample, with the same tip and the same set-up. The labels of the data plots "*zone i-j*" shall be read as "measurement n°*j* of zone n°*i*". As previously described, we apply a DC voltage (in abscise of the graphs) and then apply an AC sequence to measure the phase and the amplitude of the piezoresponse (bottom graphs). From these signals, we calculate the longitudinal piezoelectric coefficient d_{33} (upper graphs).

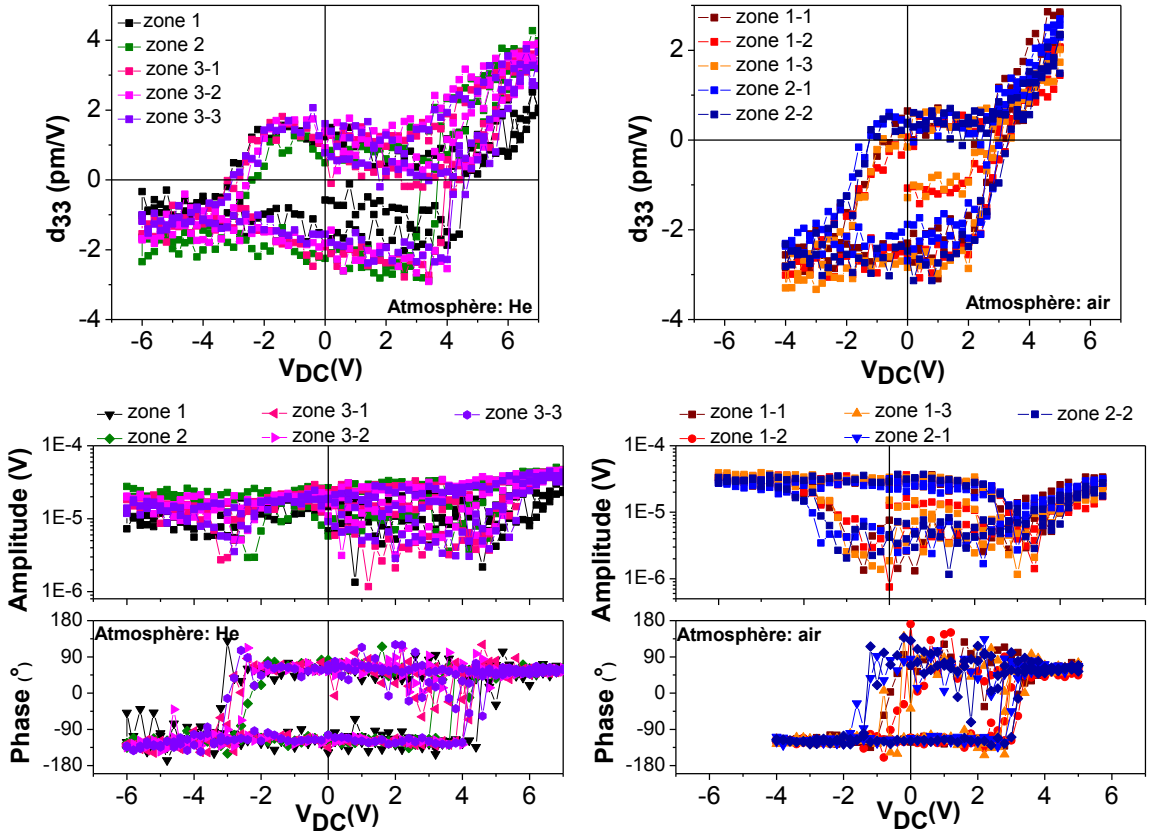

Figure V.15: Local PFM measurements under 17 mbars of He (left) and air (right)

We can see that in our system, the coercive fields are higher in Helium than in air: the switching mechanism needs more energy to change the direction of the polarisation. This is not always the case in other systems: as a comparison, we reproduced the same experiments on BFO grown on $SrRuO_3$ (SRO) as a bottom electrode. Figure V.16 represents the d_{33} coefficient for both systems, in Helium and in the air: contrary to the BFO-*Mn* on YBCO, for the BFO-*Mn* on SRO the coercive fields are smaller in the air than in Helium.

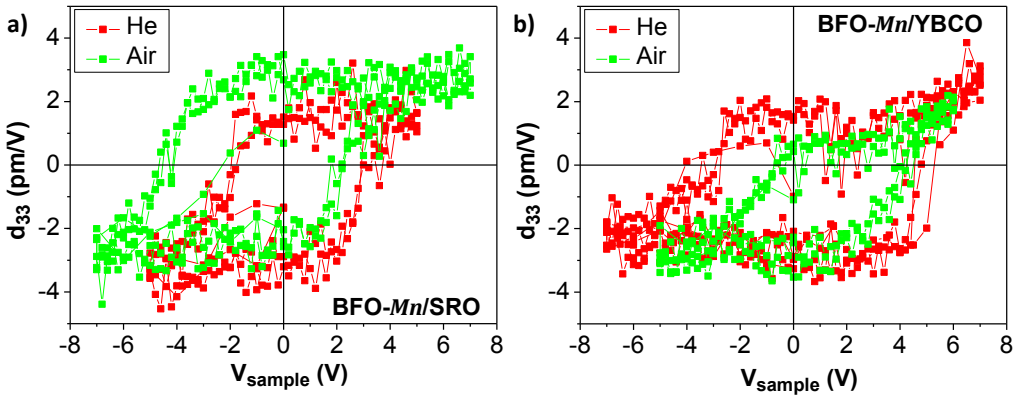

Figure V.16: Local PFM measurements under 17 *mbars* of *He* (red data plots) and air (green data plots) for a) BFO-*Mn*/SRO and b) BFO-*Mn*/YBCO

We showed that we were able to switch the polarisation of nanoscale domains of BFO-Mn/YBCO in an atmosphere without any water or ionic species. We now investigate the feasibility of ferroelectric switching at low temperatures.

V.3.2 Ferroelectric switching at low temperature

We investigated the ferroelectric switching of BFO-*Mn* (30 *nm*)/YBCO (10 *u.c.*)/PBCO(4 *u.c.*)//STO with a PFM set-up at low temperature. The experiments were carried on a commercial Attocube microscope. The critical temperature of the YBCO film was 81 K. We were able to switch the polarisation of the BFO-*Mn* film at room temperature, at 100 K and when the electrode was in the superconducting state at 77 K. As an example, Figure V.17 represents a PFM image at 77 K of the film. Figure V.17 *a)* is the phase of the PFM signal. The black domains represent the downwards domains and the white ones the upwards domains. The background is mainly downwards, with some upwards domains. By applying +5 V_{DC} between the sample and the tip, we write an upwards area (blue rectangle); we then apply -4 V_{DC} to write a downwards area (yellow rectangle). The written areas are then read by applying an AC voltage between the YBCO and the tip (2 V_{PP}).

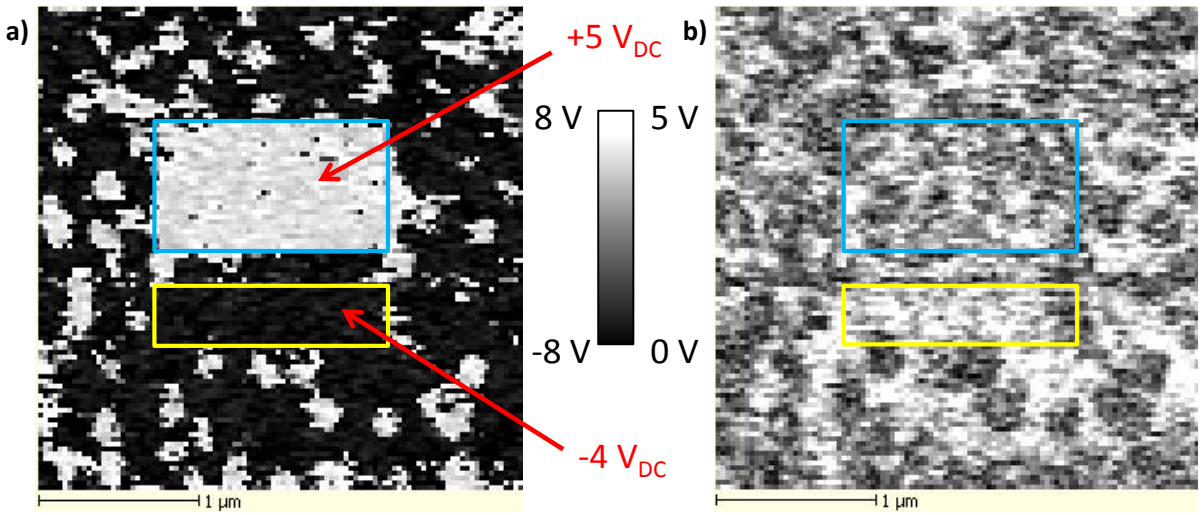

Figure V.17: PFM writing and reading of a BFO-*Mn*/YBCO layer at 77 K. a) Phase b) Amplitude

We observe that we successfully switched the polarisation at low temperature, below the superconducting transition of the bottom electrode. Figure V.17 *b)* is the amplitude of the PFM signal. Like at room temperature, the amplitude of the downwards area is higher than the amplitude of the upwards area. A second reading of the same image shows that the domains are stable.

We also proceeded to local switching of the film. Figure V.18 *a)* and *b)* is an example showing two PFM cycles on different zones at 77 K. The cycles are highly asymmetric: the film switches from downwards to upwards with $\sim$+2 V whereas it switches back downwards for only -0,6 V. We studied the evolution of the coercive fields with the temperature: they are represented for several PFM local cycles in Figure V.18 *c)*. The noise of the measurement set-up and the natural dispersion of the local measurement did not allow us to identify a clear trend.

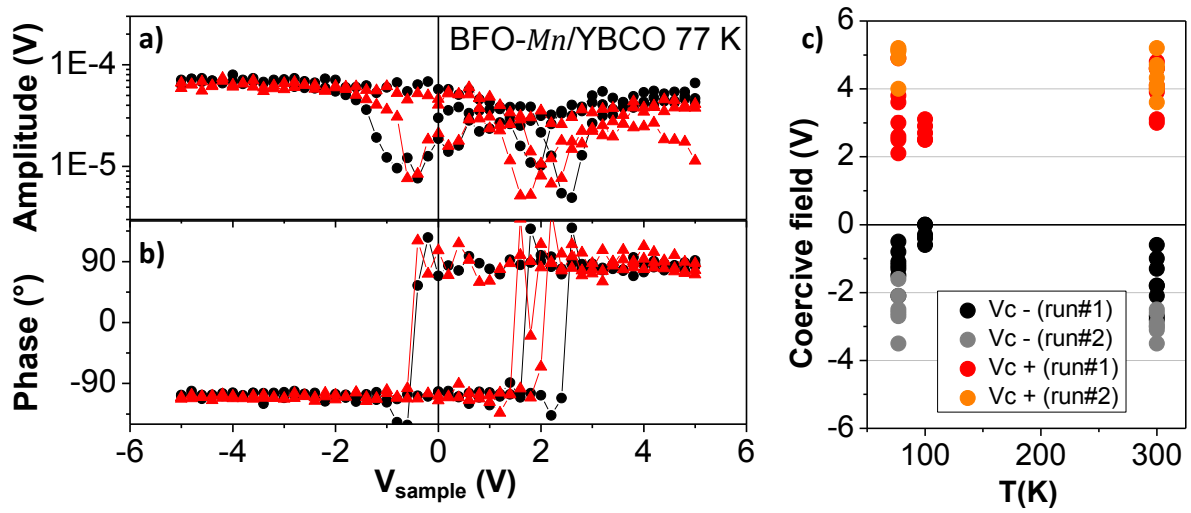

Figure V.18: Coercive fields measured from local PFM measurements under 17 *mbars* of *He* at different temperatures

To conclude, we were able to switch the polarisation of BFO-*Mn* films in both directions, over areas remaining stable for several weeks. The resulting transport measurements are detailed in section VI. We were able to polarise BFO-*Mn* at various temperatures, within an atmosphere containing no ionic species. This opens the possibility of proceeding to the transport measurement and the PFM switching in the same set-up and at low temperature.

VI. Planar field-effect devices

Index

VI. Planar field-effect devices 125

VI.1 Field-effect measurements 126

VI.1.1 Characterisation of the devices 126

VI.1.2 Electrostatic modulation of the carrier density 130

VI.1.3 Experiments with a top-gate electrode 133

VI.2 Planar S/S'/S junctions 135

VI.2.1 Resistive transition of S/S'/S junctions 136

VI.2.2 Voltage-current characteristics of the junctions 138

VI.2.2. a) General shape of the voltage-current characteristics 139

VI.2.2. b) Cross-over regime from the dissipative to the non-dissipative state 140

VI.2.2. c) Voltage-current dependence on the magnetic field 141

VI.2.3 Magnetotransport 142

VI.2.4 Interpretation of the experimental observations 147

VI.3 Conclusion 151

In this chapter we investigate an approach to fabricate planar superconductor/normal metal/ superconductor (S/N/S) junctions via ferroelectric field-effects. The pursued concept is shown in Figure VI.1. It consists of a ferroelectric/superconductor heterostructure, in which the ferroelectric has a strong, switchable out-of-plane polarisation and the superconductor thickness is comparable to the electric-field screening length (Thomas-Fermi length). A particular ferroelectric domain structure is set using a conductive tip AFM: the ferroelectric polarisation is set upwards over most of the channel except in the central part, in which a "band" on downwards polarisation is set. Under the upwards polarised ferroelectric, the electrostatically produced charge carrier (hole) accumulation dopes the superconductor and enhances its critical temperature and $T_c^{\uparrow}$. Conversely, under the downwards polarised area, the superconductor is locally depleted in carriers and its critical temperature $T_c^{\downarrow}$ is locally depressed. Thus, at a temperature above $T_c^{\downarrow} < T < T_c^{\uparrow}$, one expects that the channel consists of two superconducting blocks separated by a normal region, forming an S/N/S junction whose electrical characteristics will depend on the width of the depleted zone, tuneable by a simple CT-AFM scan – this technique is described in section III.2.3. b).

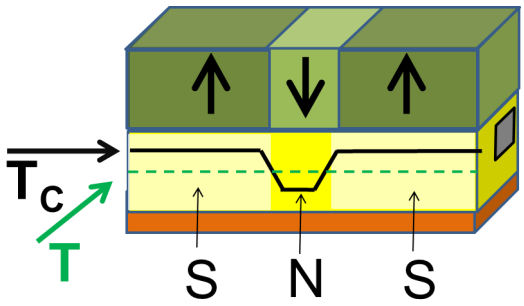

Figure VI.1: Scheme of a field-effect based Josephson junction

The studied devices are microbridges patterned out of BFO-Mn $(30\ nm)$/YBCO (few u.c.)/PBCO (3 u.c.)//STO films. First, the transport properties of these ultra-thin films are characterised in the as-grown state. Then, the field-effect is observed by polarising the whole bridge in one direction or the other. Finally, we investigate the transport properties of bridges in which a junction is "written" by conductive-tip AFM.

VI.1 Field-effect measurements

VI.1.1 Characterisation of the devices

Field-effect is the keystone of these planar junctions. It is characterised by comparing the transport properties of the measurement channel when it is entirely polarised upwards (accumulation of holes – carriers – in the superconducting layer near the interface) and when it is entirely polarised downwards (depletion of holes in the channel). The ferroelectric poling, upwards

or downwards, is set by applying a voltage pulse; either locally using a conductive-tip AFM (as in section IV.1.5. c)) or using a solid state micro-electrode (Section VI.1.3).

Transport measurement methods

Electric properties of the devices are characterised from in plane transport measurements. The resistivity of the three layers (BFO-Mn, YBCO, PBCO) and the substrate (STO) are measured in parallel. For every range of temperature, the resistivity of the YBCO film is much lower than that of the other materials of the heterostructures, so that in practice this is the resistance being measured.

Resistance vs temperature measurements: Resistance measured as a function of the temperature gives access to the T_c of the superconductor. As the YBCO films are very thin ($2{\sim}6\ nm$), the $R(T)$ measurements presented in this thesis were done with a low current ($100\ nA$) in order to achieve small current densities. The set-up is described in section III.3.6. The procedure is the following: the cryostat is thermalised at its lowest temperature (${\sim}6\ K$) during at least fifteen minutes, then the compressor is turned off and the measurement starts.

Carrier density measurements: In order to determine the carrier density in our devices, Hall measurements were done by measuring resistance as a function of the magnetic field, in a configuration where the magnetic field is perpendicular to the direction of the current (parallel to the *c*-axis). The voltage probes are either facing each other (Hall bar configuration) either slightly shifted from several micrometres along the x direction (this does not affect the measure of the Hall resistance in the y direction). Measurements were done at $100\ K$ with a current of $10\ \mu A$. The Hall resistance R_{Hall} is extracted from the measured data by a linear fit of the $R(H)$ curve. The carrier density n is given as a function of the thickness t of the superconducting film by:

$$n = \frac{1}{R_{Hall} \cdot e \cdot t} \qquad \text{(VI.1)}$$

with n in m^{-3}, R_{Hall} in Ω/Oe, e the elementary charge ($e = 1{,}6 \cdot 10^{-19}\ C$), t the thickness of the YBCO layer in m. The previous relations between the carrier density and the Hall resistance are given for a metal. In complex oxides such as YBCO, the mechanisms at the origin of the Hall resistance are not fully understood; they are biased by the opening of a pseudo-gap in the underdoped regime [182]. However, it gives a quantitative approximation of the carrier density and its modulation in our samples.

Correlation between carrier density and superconducting properties:

Figure VI.2 *b)* represents a typical resistance *vs* temperature measurement of a lithographied bridge (a description of the bridges can be found in section III.3.2, and a microscope image is represented in Figure VI.2 *a)*). In our devices, because of the reduced thickness of the YBCO film, the metal/superconducting transition is large [171]. In the literature, the usual criterion to define the critical temperature of a superconductor is the temperature at which the resistivity dropped by 90% of the resistivity of the film at the onset of the transition. As we can see on the example of Figure VI.2, which is a resistance *vs* temperature measurements for a typical $10\ \mu m$ wide and $40\ \mu m$ long bridge patterned on a 4 u.c. thick sample, the studied samples sometimes observe two slopes in the $R(T)$ transition. This makes it difficult to define the onset of the transition. Thus we chose the

criterion to define the critical temperature of our samples as the temperature above which the voltage across the bridge is bigger than the noise.

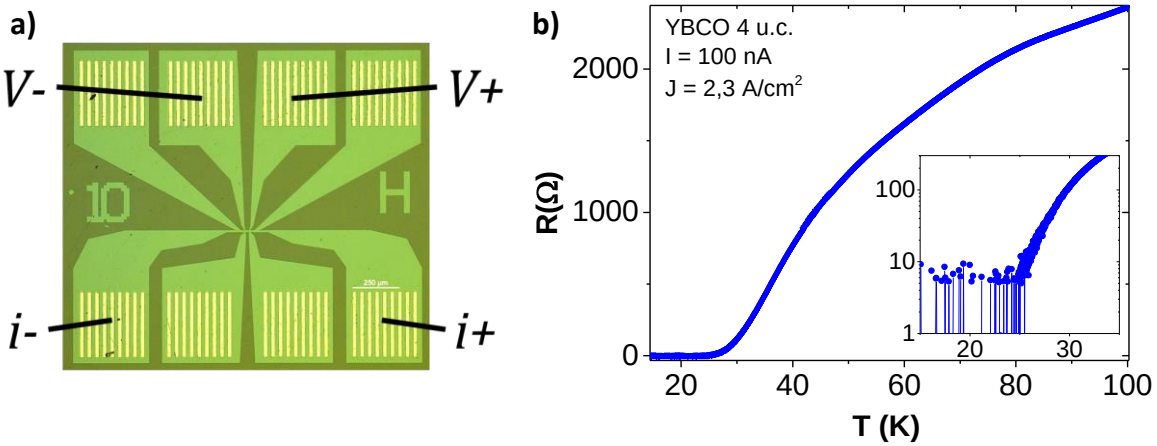

Figure VI.2: a) Microscope image of a measurement bridge. The current is injected by the lateral pads and the voltage is measured between two inner probes. b) Resistance as a function of temperature of a 4 u.c. device in the virgin state

We saw in section IV.1.5. a) that the diminution of the T_c and the broadening of the transition were gradual with the diminution of the thickness of the YBCO unpatterned films. However, in patterned devices (bridges as shown in Figure VI.2 *a)*), no clear trend correlates the critical temperature to the thickness of the YBCO film in our devices. Indeed, we often found different critical temperatures in different micro-bridges lithographied on a single ($5\ mm \times 5\ mm$) BFO/YBCO sample. This suggests that the ultrathin YBCO films (2 to 5 unit cells thick) are inhomogeneous on a millimetre length scale.

Despite that, the critical temperature correlates as expected with the carrier density measured in each bridge. Figure VI.3 represents the critical temperature of bridges in the virgin state (before any ferroelectric poling was conducted), plotted as a function of the carrier density measured by Hall measurement at $100\ K$ under $10\ \mu A$. The obtained dependence **scales accurately with the observations published on thicker YBCO films**, represented in this figure by the purple line (see appendix for further details).

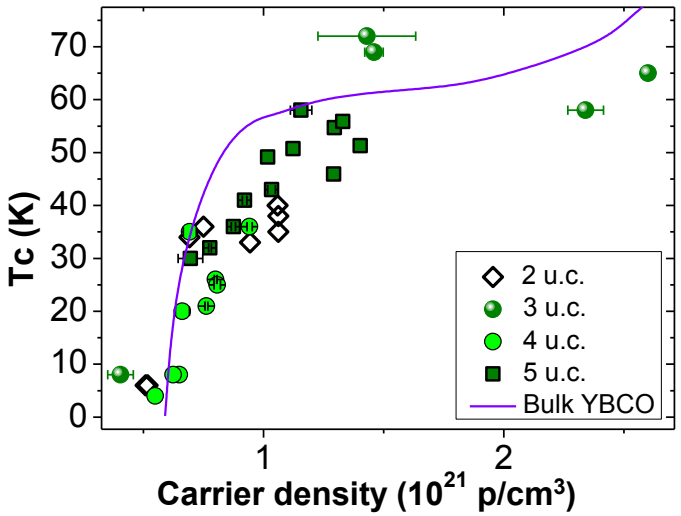

Figure VI.3: Critical temperature as a function of the hole density, measured by Hall effect at T=100 K, for different BFO-*Mn*/YBCO (*n* u.c.)/PBCO//STO patterned devices.

Ageing:

The polarisation of the BFO-Mn is switched using a PFM: to measure the devices in the accumulated (upwards polarisation) and depleted (downwards polarisation) states the sample has to be poled with a CT-AFM set up, measured in a cryostat, then removed from the cryostat, poled in the other direction, and reintroduced again in a cryostat for the transport measurement. We find that this process leads to ageing effects which can be attributed to different mechanisms:

- Ageing due to the thermal cycles: Each time the sample is measured it is thus cooled down and warmed up in a cryostat. In section II.3.2, we showed that for poorly oxygenated samples – samples that had not been exposed to an O_2 plasma after the ion beam etching step – such cycles would deteriorate the superconducting properties of the YBCO. As an example, Figure VI.4 *a)* shows two successive resistance *vs* temperature measurements of a device not exposed to an O_2 plasma. It was not removed from the cryostat between the two measurements. We can see that the critical temperature of the film is lower after the first thermal cycle. As explained in section II.3.2, **exposing the sample to an O_2 plasma after the ion beam etching step during the lithography made much more robust samples.**

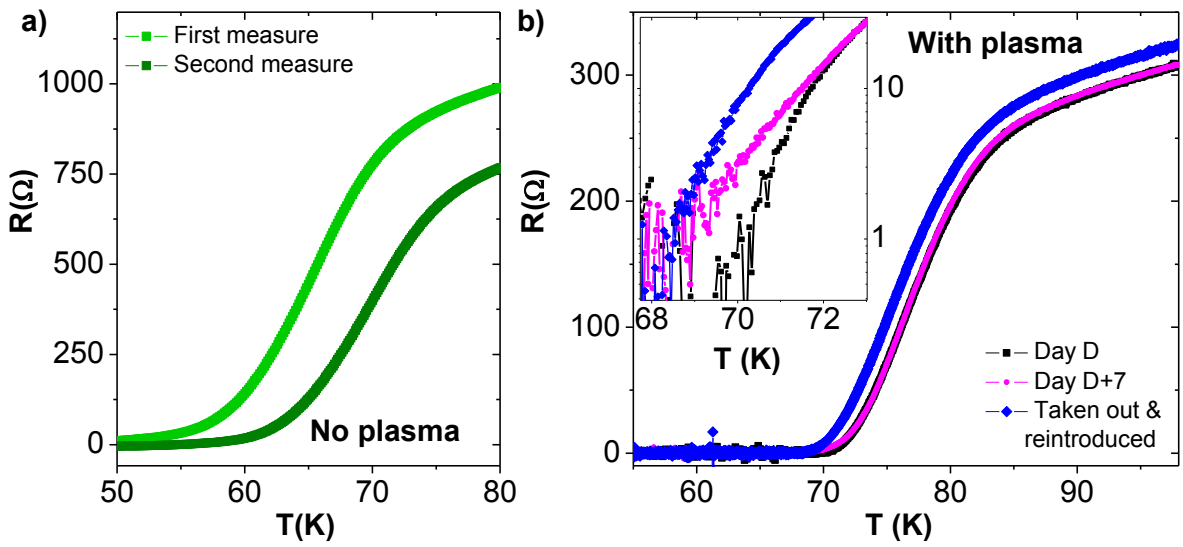

Figure VI.4: Ageing on a device that was a) not exposed and b) exposed to an O_2 plasma during the lithography.

As an example, Figure VI.4 *b)* represents three subsequent $R(T)$ measurements of a bridge exposed to an O_2 plasma: the black curve is the measurement the day the sample was introduced in the cryostat; the magenta curve is the same measurement seven days after (during these seven days the sample stayed at temperature comprised between 5 and 100 K); the blue curve is an $R(T)$ measured after removing the sample from the cryostat and reintroducing it without modifying the ferroelectric state of the bridge. We observe that even if the sample is more robust, the ageing is still present. It is less when the sample remains at low temperature, indicating that the ageing is thermally activated. This ageing might be due to the desorption of the oxygen atoms from the surface of the BFO-Mn or the STO and a migration of the oxygen atoms of the YBCO, either towards the edge of the layer, either towards the BFO-Mn and the STO [183].

- Ageing due to the PFM poling: the polarisation of the BFO-Mn is switched by scanning the bridge with a PFM in contact mode with a conductive tip meanwhile a voltage is applied between the tip and the YBCO layer. This procedure is detailed in section III.2.3. b). After the poling, we sometimes observe on topographic images that the electric field damaged the bridge locally, especially on the edges. This contributes to a lower critical temperature and a higher normal resistance.

The ageing of the sample thus has to be taken into account when comparing two measurements. In particular, when a sample is switched from the depleted to the accumulated state, the field-effect tends to increase the T_c whereas the ageing tends to decrease the T_c. When a sample is switched from the accumulated to the depleted states, the two effects tend to decrease the T_c. This prevents us from determining the exact value of the T_c shift due to the field-effect only; however, the latter can be estimated by comparing subsequent T_c shifts on the same sample and its determination is not mandatory for the study of the junctions defined by field-effect.

VI.1.2 Electrostatic modulation of the carrier density

In a free-electron model, the modulation of the number of carriers Δn by a ferroelectric gate is proportional to the switching of the polarisation ΔP and inversely proportional to the thickness t of the layer [120]:

$$\Delta n = \frac{\Delta P}{e \cdot t} \qquad \text{(VI.2)}$$

In principle, the electric field exponentially decays within the superconductor over a distance equal to the Thomas-Fermi length, that is $\sim 1\ nm$ in YBCO [104]. We saw in the previous section that the superconducting properties of YBCO strongly depend on the carrier density. According to these results, depending on the direction of the polarisation of the BFO-Mn film, we should observe a modulation of the critical temperature of the YBCO channel, and this modulation should be stronger for thinner samples. Figure VI.5 shows the typical signature of the field-effect in our sample:

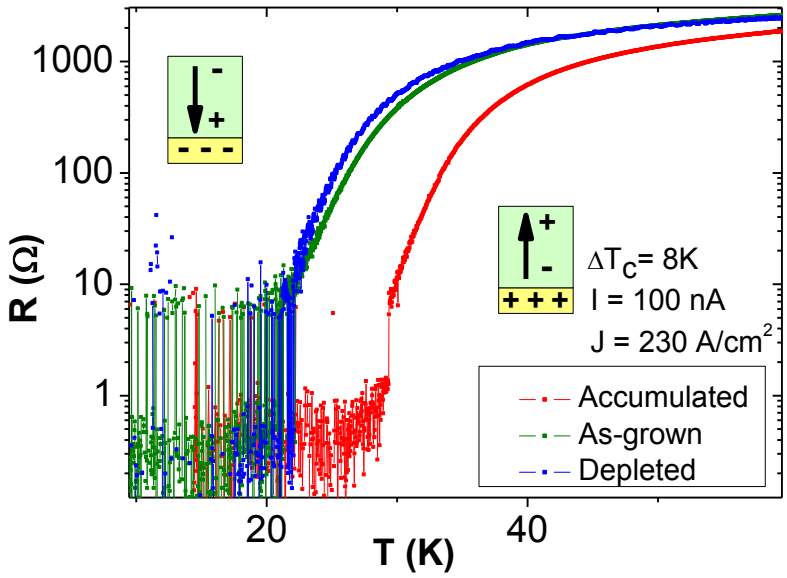

Figure VI.5: Resistance as a function of temperature for a BFO-*Mn*/YBCO (4 u.c.)/PBCO//STO device.

In the as-grown state (green curve) the critical temperature is low. PFM reading of the as-grown state reveals that the BFO-Mn polarisation mainly points towards the interface, *i.e.* the induced electric field tends to deplete the holes (the carriers) in the YBCO layer. **After poling the BFO-Mn film upwards, the channel exhibits a higher conductance and critical temperature (red curve): the holes are accumulated in the YBCO channel. After poling the BFO-Mn downwards, the critical temperature is shifted from several degrees to the low temperatures, as the channel is** – again – **depleted in charge carriers.**

Figure VI.6 represents the T_c as a function of the carrier density of several devices measured in the as-grown, depleted and/or accumulated states. In this figure, each symbol stands for a device; the green colour signifies that the device is in the as-grown state, the blue colour in the depleted state and the red colour in the accumulated state. As expected, the strongest modulation is observed for the thinnest sample (2 u.c. – squares on Figure VI.6): we measured a ΔT_c of $14\ K$. This shift is smaller than previously reported in our group by Crassous *et al.*, which was as big as $30\ K$ on a 2 u.c. thick sample [139].

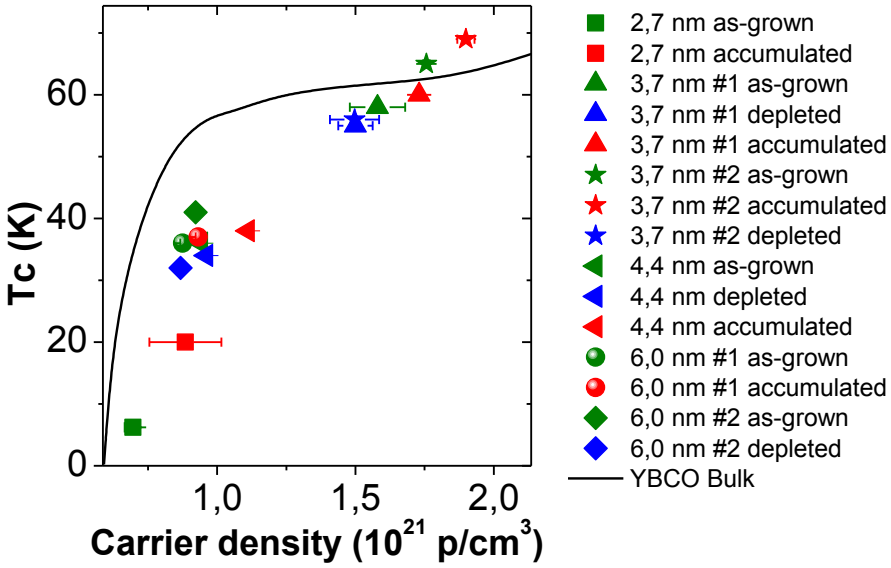

Figure VI.6: Critical temperature measured with I=100 nA, as a function of the carrier density measured by Hall effect at 100 K with 10 µA. Each symbol corresponds to a device in the green: as-grown state; red: accumulated state; blue: depleted states.

Figure VI.7 represents the associated relative shifts: $\frac{\Delta T_c}{T_c}$ for the critical temperature, $\frac{\Delta p}{p}$ for the carrier density measured at 100 K and $\frac{\Delta R}{R}$ for the resistivity of the channel measured at 300 K. The red lines $y = x$ are guides to the eye. From Figure VI.7 *a)*, we see that $\frac{\Delta T_c}{T_c}$ **scales with** $\frac{\Delta p}{p}$**, *i.e.* the relative variation of the critical temperature depends on the carrier density variation, as expected** [132]**.** In Figure VI.7 *b)*, a similar trend is observed: $\frac{\Delta R}{R}$ is roughly proportional to $\frac{\Delta p}{p}$, which dictates that the transport in these films approximately follows a free electron model behaviour.

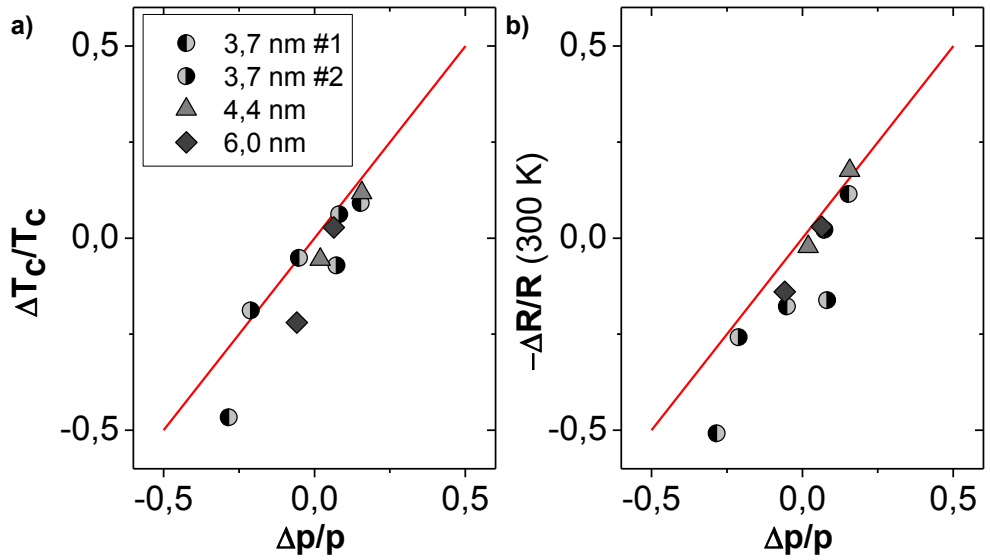

Figure VI.7: a) Relative critical temperature shift *vs* relative carrier density shift measured at 100 K; b) relative resistivity shift measured at 300 K *vs* the relative carrier density shift for several BFO-*Mn*/YBCO/PBCO//STO devices

In Figure VI.8, the shift in the inverse of the Hall resistance is represented as a function of the associated T_c shift. From equation (VI.1) and (VI.2) we obtain:

$$\Delta P = \Delta n \cdot e \cdot t = \Delta\left(\frac{1}{R_{Hall}}\right) \qquad \text{(VI.3)}$$

i.e. assuming a free-electron model, the ordinate of Figure VI.8 is also the change in polarisation in the ferroelectric. The green/blue symbols indicate shifts measured from the as-grown to the depleted state (the latter is set upon polarising the ferroelectric downwards). We observe that the change in polarisation ΔP ranges between 0 and $-4\ \mu C/cm^2$.

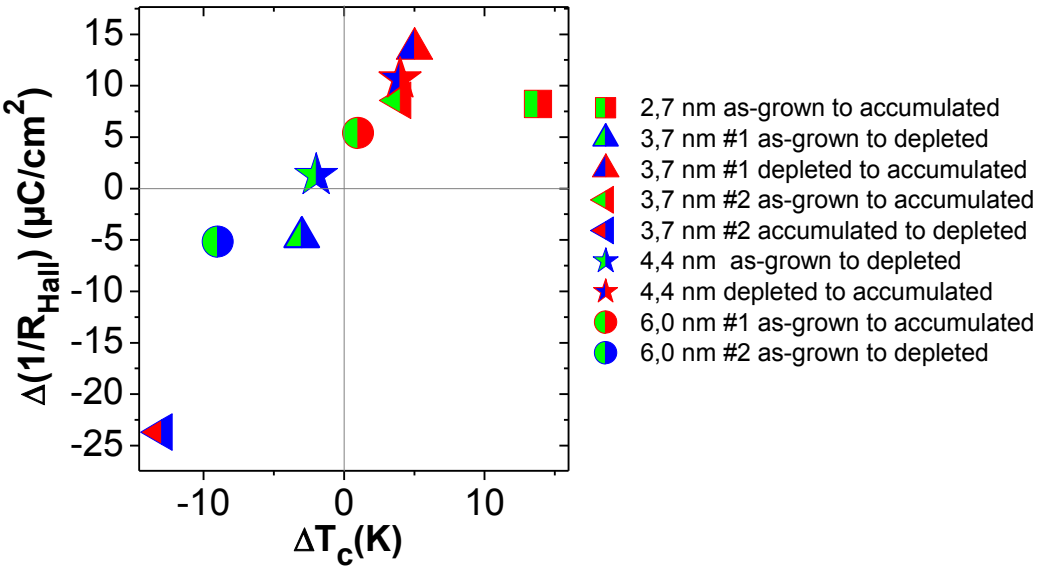

Figure VI.8: Hall resistance variation with respect to the T_c shift for several BFO-*Mn*/YBCO/PBCO//STO devices.

This indicates that, although the polarisation predominantly points downwards in the as-grown state – as expected from the phase measured during PFM scans – **some small domains might initially point upwards until they are reversed by poling the ferroelectric, yielding that small** ΔP.

The green/red symbols indicate shifts measured from an as-grown to an accumulated state: in this case the polarisation change is larger: ΔP ranges from 6 to 9 $\mu C/cm^2$. This is in agreement with the above scenario, as it corresponds to a change from a predominantly downwards polarisation state towards an upwards polarisation state. Finally, we observe that the blue/red symbols, representing the shift from a depleted to an accumulated state, represents a polarisation shift of range 11 $\mu C/cm^2$ to 14 $\mu C/cm^2$, which is roughly the sum of the two precedent values. The maximal effective polarisation was obtained for a device in the accumulated state, then poled in the downwards direction : $\Delta P = -24\ \mu C/cm^2$. As discussed in section VI.1.1, in this case, both the field-effect and ageing contribute to a smaller carrier density. However, even in this situation, the ΔP obtained is much smaller than the polarisation maximum $\Delta P = 140\ \mu C/cm^2$ expected from the measured polarisation of our BFO-Mn films, which is $\sim 70\ \mu C/cm^2$. This relatively low efficiency is as usually observed in ferroelectric field-effect devices [120], [124]. It may be due to the presence of residual nanoscale domains with opposite polarisation after poling, as discussed in section V.1.3. c).

To conclude, we were able to shift the critical temperature of our YBCO channels by several Kelvins by switching the direction of the BFO-Mn polarisation. This shift comes along with a modulation of the free carrier density in the channel, and is attributed to the ferroelectric field-effect. The strength of the field-effect is less than the maximal expected value: this might be due to different mechanisms of screening of the electric field at the interface. Nevertheless, these results are promising for planar junctions devices, based on the local modification of the superconducting properties.

VI.1.3 Experiments with a top-gate electrode

In order to characterise the field-effect in our thin films without handling the ageing due to the removal of the sample from the cryostat, we fabricated samples with a top-gate electrode. To do so, we grew heterostructures with a thicker BFO-Mn layer (150 nm compared to 30 nm) in order to reduce leakages, and grew a metallic top electrode (Au) above the channel. To be in the same configuration than with the PFM, we ground the top electrode and biased the YBCO layer. A scheme of the device is represented in Figure VI.9 *b)*; its fabrication is detailed in section III.3.3.

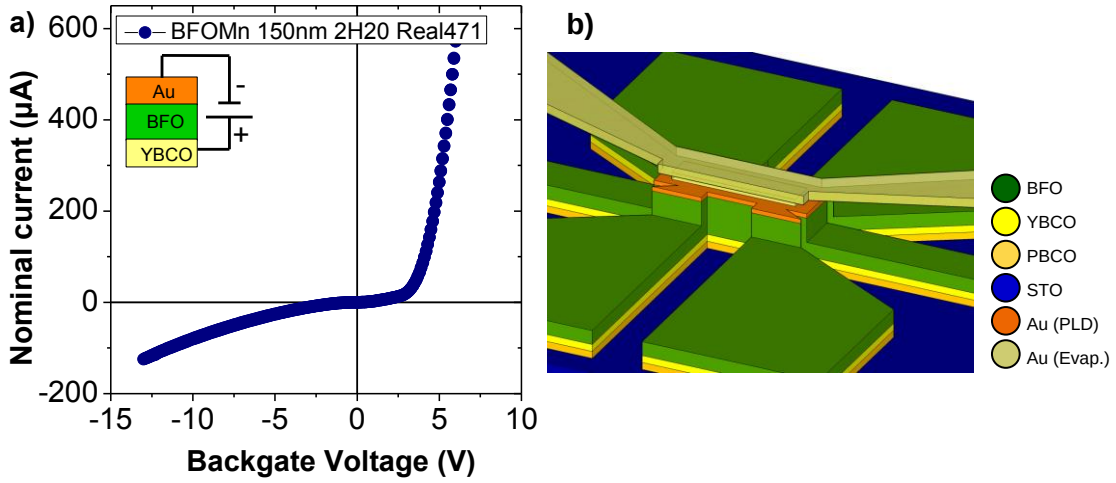

Figure VI.9: a) Current through BFO-*Mn* layer when gate voltage is applied; b) Scheme of the device

We measured the resistance of the channel after applying the gate voltage, setting the gate voltage to zero, and then waiting $200\ ms$. Figure VI.9 *a)* represents the current measured by the voltage source during the application of the gate voltage, at room temperature. This measure gives an indication of the leakage currents flowing though the BFO-Mn.

- We observe that the $I-V$ characteristic is asymmetric. This can be explained by the fact that the conduction mechanisms in ferroelectric oxides are interface-dependant, it is thus not the same to inject electrons in one direction or the other if the electrodes are different – these mechanisms are detailed in section I.3.3.
- From Figure VI.9 *a)* we observe that the leakage currents through the BFO-Mn layer are high, up to $600\ mA$ for $6\ V$. This is unexpected: as we saw in Section IV.1.5. c), BFO-Mn film of thicknesses of $150\ nm$ patterned with Pt/Co pads of comparable surfaces ($2500\ \mu m^2$ pads compared to $2400\ \mu m^2$ for the biggest gates) are 90% switchable. These leakage currents could occur along the borders of the bridge, which were exposed to the ion beam etching during the lithography.

Figure VI.10 *a)* represents $R(T)$ measurements of the channel in the as-grown state (before any voltage is applied on the gate – black curve), and after a voltage of $-11\ V_{DC}$ (resp. $9\ V_{DC}$) being applied at room temperature (blue, resp. red curves).

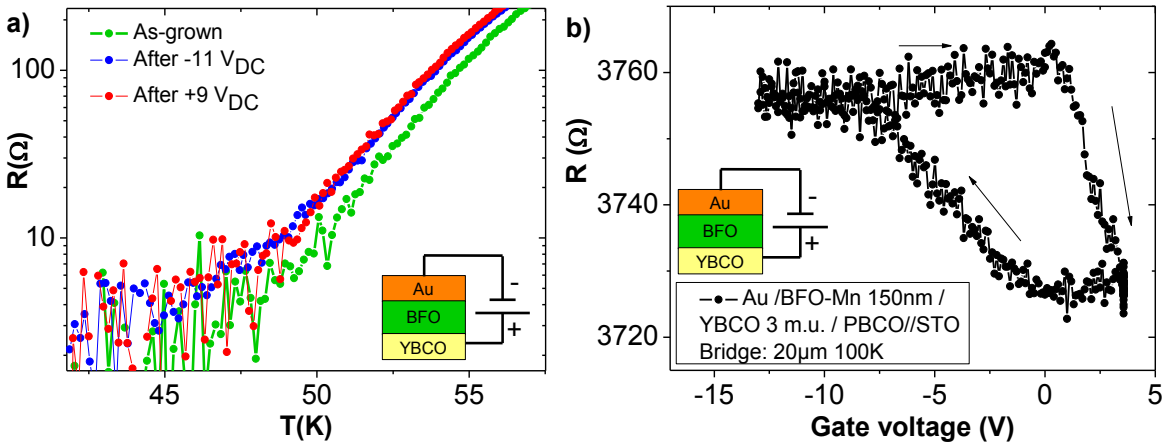

Figure VI.10: a) Resistance *vs* temperature measurements of an Au/BFO-Mn/YBCO (3 u.c.)/PBCO//STO bridge in the as-grown state (black curve), after applying $-11\ V_{DC}$ (blue curve), and after applying $9\ V_{DC}$ (red curve) between the YBCO film and the gate. b) Resistance at 100 K as a function of the gate voltage applied prior to the measure.

Finally, Figure VI.10 *b)* represents the resistance of the channel at $100\ K$, measured with a current of $1\ \mu A$, as a function of the gate voltage pulse applied prior to the resistance measurement (no bias is applied during the resistance measurement).

- In Figure VI.10 *a),* the bridge is first measured in the virgin state (green curve) *i.e.* no voltage is applied on the gate prior to the resistance vs temperature measurement. Then, at room temperature, $-11\ V$ is applied between the YBCO and the gate, which corresponds to a downwards polarisation of the ferroelectric film. The subsequent $R(T)$ measurement (blue curve) shows a slight shift towards lower critical temperature. Then, at room temperature, $9\ V$ is applied between the YBCO film and the gate, and the temperature dependence of the resistance is measured (red curve): it is identical to the previous measurement, indicating that no field-effect occurred in the YBCO film, *i.e.* that the polarisation of the BFO-Mn might

not have switched. This could be because of strong leakage currents when the electric field is in the other direction. However, a hysteretic cycle (Figure VI.10 *b)*) was obtained at $100\ K$ with a YBCO 3 u.c. thick sample, where a modulation of $30\ \Omega$ was obtained.

To conclude on these experiments, we were not able to reversibly polarise the BFO-Mn in these devices with top electrodes, because of high leakage currents. In order to obtain further results, efforts shall be made to improve the technology, in particular to remove the IBE step. This could be done by first growing an amorphous material (for example amorphous STO) on the substrate, then etching holes with the shape of measurement bridges inside this film, and finally filling them with the PBCO, YBCO and BFO-Mn materials by PLD.

VI.2 Planar S/S'/S junctions

In the previous section, we showed that we were able to shift the critical temperature of our YBCO films, by modulating the carrier density thanks to ferroelectric field-effect. In this chapter, we investigate the behaviours of junctions defined by field-effect. As represented in Figure VI.11, **the channel is mainly in an accumulated state (BFO-*Mn* polarisation points upwards) except in a thin band where the superconductivity is depressed (the junction)**. This configuration is obtained by polarising the ferroelectric film locally with a CT-AFM tip.

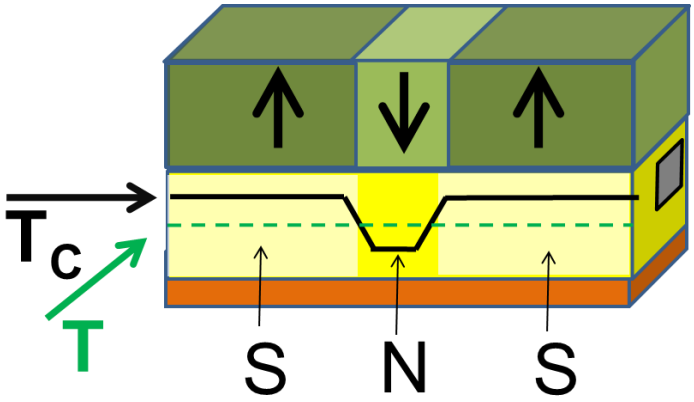

Figure VI.11: Scheme of a field-effect based Josephson junction

It is intended that, in these junctions, the coupling between the two superconducting parts is made through a region that has a critical temperature T_c', lower than the critical temperature T_c of the rest of the film. The main goal of this part of the work is to determine whether these planar "S/S'/S" junctions (where S and S' refer to two superconductors) behave as "S/N/S" (where N refers to a normal metal) Josephson junction when the temperature is above T_c' and below T_c.

The junctions designed in this work are very long ($\sim 1\ \mu m$) as compared to the case of usual S/I/S junctions, in which the dominant mechanism is the direct tunnelling of Cooper pairs through the insulating (I) barrier. The conduction mechanisms involved in our system, as well as in S/N/S junctions, is different. In the case of S/N/S and S/S'/S junctions – with S' in the normal state – the proximity effect is possible thanks to the existence electronic states inside the barrier. At the interface with S, a Cooper pair $|k\uparrow, -k\downarrow\rangle$ can transform into an electron $|-k\downarrow\rangle$ and a hole $|k\uparrow\rangle$, thus forming an Andreev pair in the N or S' part, where this pair progressively loses its phase. The

characteristic length over which the pair loses its correlation is the normal coherence length of the N or S' part, ξ_N. The number of Andreev pairs at a distance x from the interface is given by the pair condensation amplitude $F_N(x)$:

$$F_N(x) = F_N(0)e^{-|x|/\xi_N} \quad \text{(VI.4)}$$

Our junctions have very faded interfaces, as there are no chemical discontinuities in the material. The physical properties of the material, such as the mean free path of the particles, the Fermi velocity, or even the Cooper pair condensate density, vary continuously. Nevertheless, as we show below, the obtained spatial modulation of the superconducting properties make it possible to modulate supercurrents across the device via a magnetic field which is reminiscent of that expected in Josephson junctions [28].

VI.2.1 Resistive transition of S/S'/S junctions

In the previous section, we showed that the ferroelectric field-effect induced a shift of the critical temperature of the whole channel. In this section, we investigate the temperature dependence of the resistance of a channel which is poled upwards everywhere, except in a thin band that is poled downwards, as represented by the PFM image in Figure VI.12 *a)*. A scheme of the device is represented in Figure VI.12 *b)*:

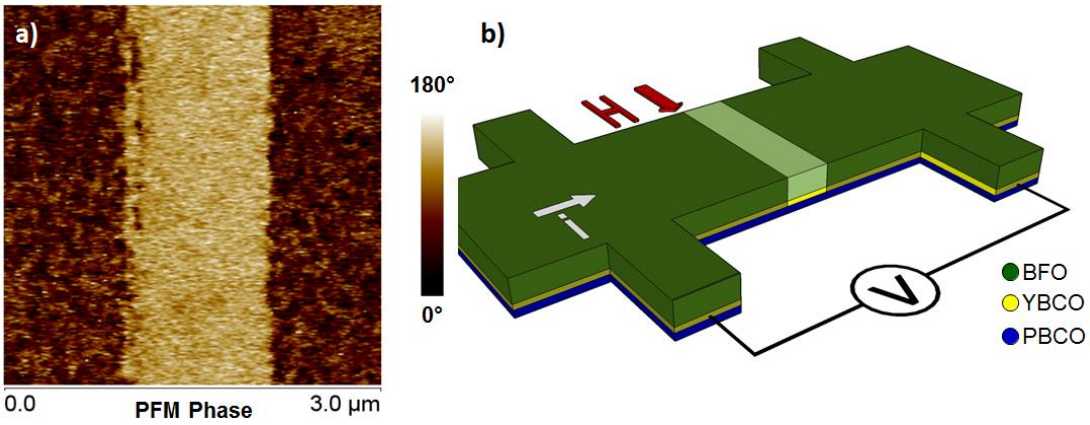

Figure VI.12: a) PFM image (phase) of a 1 µm junction. b) Scheme of the device

Let us start by discussing the behaviour of S/S'/S junctions created via ion irradiation in single YBCO layers. To create these junctions, a spatial modulation of the critical temperature is used, similarly as sketched in Figure VI.11, which is produced via local irradiation damage instead of the ferroelectric field-effect. Figure VI.13, taken from [184], represents the resistance *vs* temperature measurement of an irradiated junction. In these junctions, the $R(T)$ curve exhibits two transitions. This behaviour is understood as follows: at high temperature, the whole device is normal and the resistance decreases slowly with decreasing temperature. When the superconducting electrodes S transit at T_C, the resistance drops sharply to a residual resistance that keeps decreasing linearly with temperature. The residual resistance corresponds to the resistance of S' in the normal state. As the temperature is further lowered, Josephson coupling eventually occurs across S', and the device resistance drops to zero.

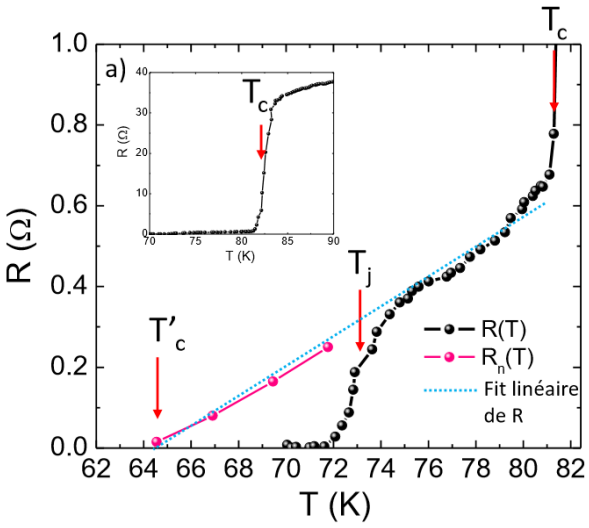

Figure VI.13: Resistance as a function of temperature of an irradiated SS'S junctions, taken from [184]

This occurs at a temperature T_J called "coupling temperature". At lower temperatures, in particular below the critical temperature T_c' of the S' region, the whole device becomes superconducting. As detailed in section I.2.2, the Josephson effect occurs in the regime where the wavefunctions of the two electrodes overlap, and is observable above the critical temperature of the barrier T_c' and below the coupling temperature T_J.

Figure VI.14 shows the measurement of a YBCO/BFO device (the YBCO thickness is 3 u.c., *i.e.* $\sim 3{,}7\ nm$) in three different ferroelectric states. The three $R(T)$ measurements correspond to different ferroelectric states of the same bridge, which was subsequently in the accumulated state (BFO-Mn was polarised upwards – red curve), then depleted (blue curve), and finally (black curve) accumulated again except on a 1 µm band to create an S/S'/S structure as that in Figure VI.11.

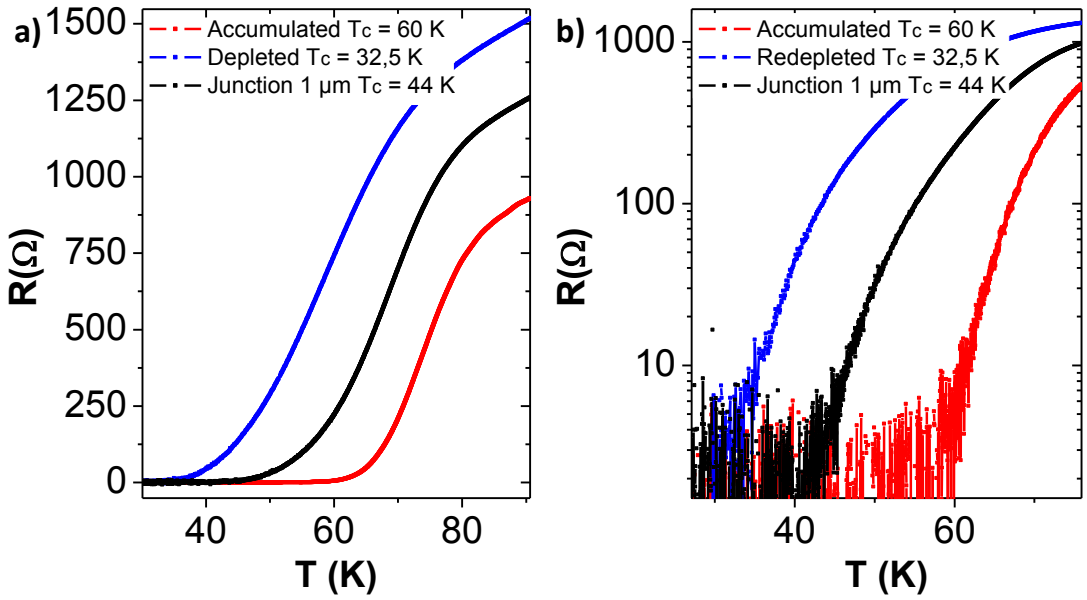

Figure VI.14: Resistance as a function of temperature of a device which has subsequently been measured in the accumulated (red curve), depleted (blue curve) states and with a 1 µ*m* large junction (black curve); a) in linear scale and b) in logarithmic scale. YBCO thickness is 3 u.c..

The $R(T)$ of the S/S'/S device created by ferroelectric field (black curve in Figure VI.14) is representative of the similar devices measured during this thesis, and differs from that seen for the irradiation created S/S'/S. In particular, and while the zero-resistance temperature (putatively T_J) is above T_C' and below T_C as expected, we do not observe the two-steps transition seen in Figure VI.13. This is probably because the width of the superconducting transition of both S' and S is large compared to the difference between T_C' and T_C. Thus, as the device is cooled down, the superconducting transition of the depleted area (junction barrier) starts before the accumulated electrodes have reached the zero-resistance state.

However, it is also clear that the S and S' regions do not simply behave as two "isolated" superconductors undergoing a superconducting transition at different temperatures. To show this, in Figure VI.15, one can find a model showing the expected $R(T)$ behaviour in that case. We consider a $39\ \mu m$ long area in the accumulated state (red curve) in series with a $1\ \mu m$ long depleted area (blue curve), without any coupling between them. The distances correspond to those of the bridge measured in Figure VI.14. **The output of this simplified model (grey curve in Figure VI.**15**) is an $R(T)$ curve with a smooth step in the foot of the transition, with a critical temperature equal to the T_c of the superconductor in the depleted state:**

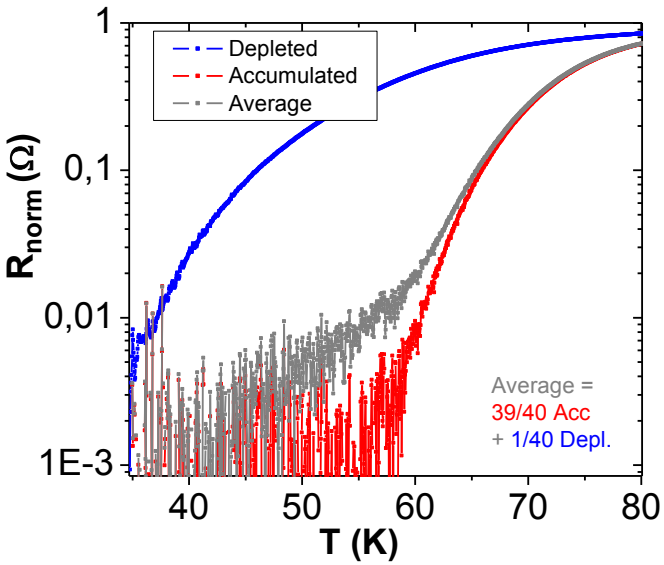

Figure VI.15: In grey: expected resistance vs temperature measurement for a 1 µm long depleted area (blue curve) in series with a 39 µm long accumulated area (red curve). The curves are normalized to their value at 100 K.

In the resistance *vs* temperature measurements of our junctions, we do not observe such behaviour, but a rounded foot, as well as a higher critical temperature. **This indicates that our channel does not consist of two superconducting electrodes and a depressed region simply electrically connected in series, but that these blocks are coupled together.**

VI.2.2 Voltage-current characteristics of the junctions

From the resistance *vs* temperature measurements, we were only able to have an estimation of the zero-resistance temperature of the channel, as it strongly depends on the current bias and on the noise of the measurement. To further investigate the transition, we study the temperature dependence of the voltage-current characteristics of our devices.

VI.2.2. a) General shape of the voltage-current characteristics

Junctions are current biased, and the average voltage is measured during a long integration time ($500\ ms$). Figure VI.16 represents the V-I curves for a $870\ nm$ junction on a 2 u.c. thick device:

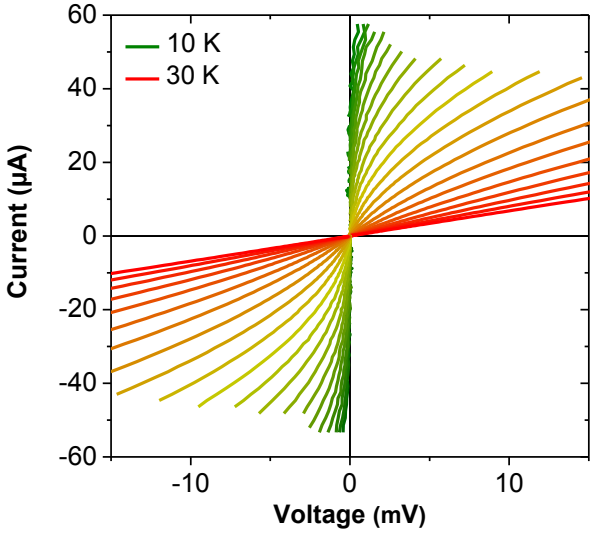

Figure VI.16: I-V characteristics for a) a $870\ nm$ thick junction on a 2 u.c. sample at different temperatures.

For high temperatures, the channel is Ohmic and the characteristics are linear (red curves). As the temperature gets lower, the curve progressively becomes non-linear (green curves) indicating that the channel undergoes a normal/superconducting transition. The value of the critical current – the minimal current necessary to measure a voltage across the channel – becomes higher as the temperature decreases.

For comparison, one can find in Figure VI.17 *a),* taken from [185], some $I-V$ curves measured on YBCO irradiated junctions:

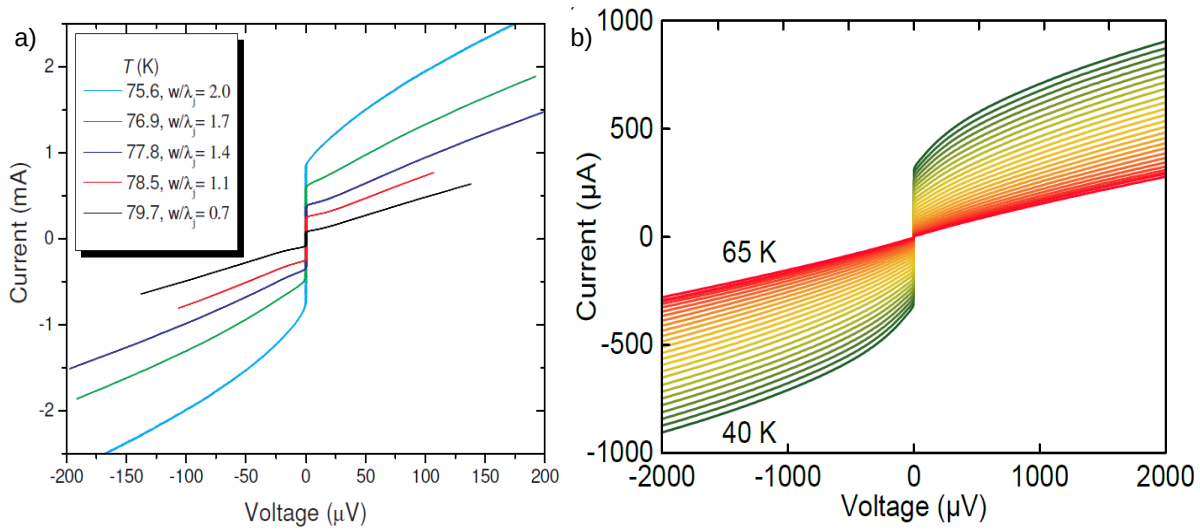

Figure VI.17: I-V characteristics for YBCO irradiated Josephson junctions a) taken from [185] and b) taken from [186], at different temperatures.

In this figure, two regimes are seen: at high temperature (T_j>T>T_c'), the irradiated junction has a typical RSJ (resistively shunted junction) shape. As the temperature gets lower – closer to T_c' – the

junction becomes strongly coupled and the $I-V$ curves becomes rounded. At this point the weak-link undergoes the superconducting transition and the junction enters the "flux-flow" regime. This change in the curvature of the $I-V$ curves is not always seen: in some case, the thermal noise is high and even though the junction is in the Josephson regime, the feet of the $I-V$ curves are rounded. It is for example the case in Figure VI.17 *b)* taken from [186].

As in Figure VI.17 *b)*, in our devices the curvature of the *V-I* characteristics is positive in the whole range of temperature. This can be due to the thermal noise becoming comparable to the Josephson energy.

VI.2.2. b) Cross-over regime from the dissipative to the non-dissipative state

In Figure VI.18 are represented the *V-I* characteristics of the $1\ \mu m$ junction, the resistance *vs* temperature dependence of which was represented in Figure VI.14. Note that in this figure the curves are shown in double logarithmic scale.

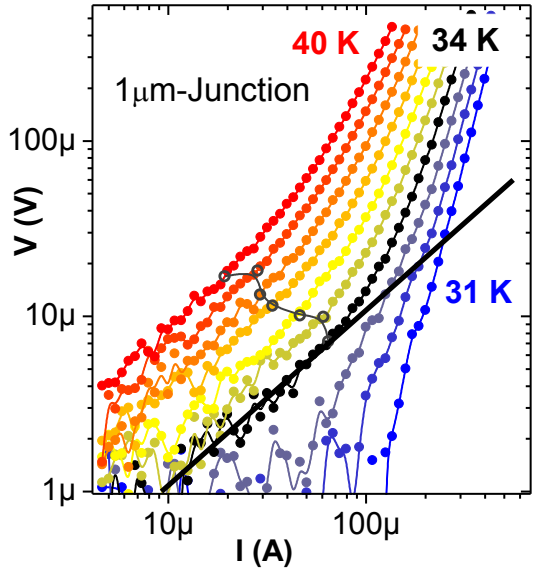

Figure VI.18: *V-I* characteristics for a $1\ \mu m$ junction at 0 applied magnetic field

For temperatures above $\sim 34\ K$, we observe a nearly Ohmic tail at low currents and a non-linear behaviour at higher currents. For lower temperatures, the nearly Ohmic tail is no longer visible, and yields a steep *V-I* at the lowest temperature ($31\ K$), with seemingly vanishing resistance in the low current limit. Qualitatively, this is as commonly observed in YBCO thin films as they undergo a 2nd order vortex glass transition [187] in the presence of applied magnetic field. However, there are quantitative disagreements between the theoretical expectations for that scenario and the data shown in Figure VI.18. For instance, the current above which nonlinear behaviour is observed I_{nl} – marked with open symbols in Figure VI.18 – increases with decreasing temperature. This is opposite to the theoretically expected behaviour, since in the case of a vortex glass transition I_{nl} should scale as:

$$I_{nl} \approx S \frac{k_B T}{\Phi_0 \xi_c \xi_{ab}} \qquad \text{(VI.5)}$$

with S the cross sectional area of the film, and ξ_c and ξ_{ab} the coherence lengths in the c and a or b directions [19], [20], [188].

As we discuss further below, the different regimes observed in the *V-I* characteristics and the disagreement of the observed behaviour with that of single YBCO films are the signature of the S/S'/S structure, in which the contribution of the junction to the electrical transport is observed as S' shows a dissipative to non-dissipative transition at lower temperatures than the electrodes.

VI.2.2. c) Voltage-current dependence on the magnetic field

By probing the *V-I* characteristics of the devices at different temperature and magnetic fields, we can identify the range of temperature around which the critical current is the most sensitive to the magnetic field. The V-I characteristics are shifted to lower temperatures when a magnetic field is applied: as an example, Figure VI.19 represents the V-I characteristics for a $950\ nm$ junction on a 4 u.c. thick sample. Bold lines are the characteristics under no external magnetic field, and thin lines (open symbols) are the same measurements under $9000\ Oe$, applied perpendicular to the current and to the c-axis.

We observe three different regimes, which are better seen in the *log-log* representation of Figure VI.19 *b)*. At high temperatures (red curves), in the normal state, the V-I characteristics are Ohmic in the entire current range, and the application of the magnetic field does not modify the characteristics (no magnetoresistance).

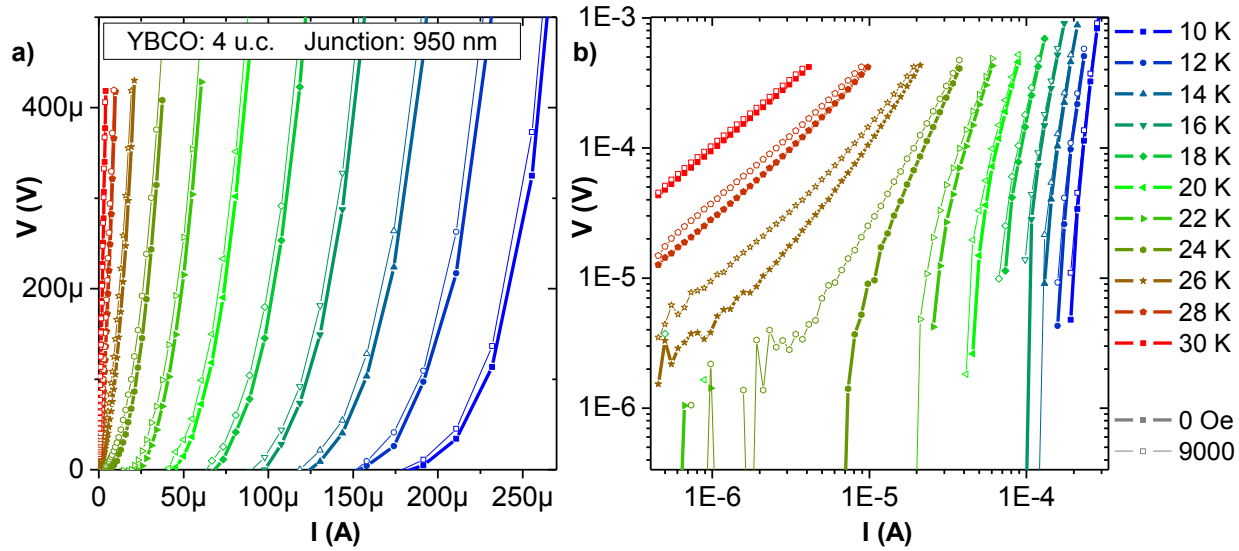

Figure VI.19: *V-I* characteristics for a $950\ nm$ thick junction on a 4 u.c. sample under 0 and $9000\ Oe$ in *a)* linear scale and *b)* log-log scale

In the superconducting state (green and blue curves), two different behaviours are observed. At high temperatures, the V-I characteristics show an Ohmic tail at low current (no finite critical current) and nonlinear behaviour above some threshold current I_{nl}, beyond which the curves show positive curvature.

Below some temperature, the Ohmic tail disappears, the characteristics are non-linear in the entire current range and the curvature of the V-I is negative. This means that there is vanishing voltage in the low-current limit, and that a finite critical current exists. We note, when comparing the V-I characteristics measured in magnetic field ($9\ kOe$, open symbols) to those measured at zero field (filed symbols), that the magnetic field-effects are stronger in the intermediate temperature range in which we observe the change of curvature in the V-I characteristics.

VI.2.3 Magnetotransport

As detailed in section I.2.3, in superconductor/normal metal/superconductor Josephson junction the critical current shows characteristic field dependence. For instance, in case of a uniform, rectangular junction, the maximum superconducting current that can flow through the junction oscillates as a function of the applied magnetic field, following the so-called Fraunhofer pattern, with extinctions of the Josephson current when the flux through the junction is an integer of the magnetic flux quantum. The field modulation of the critical current in Josephson junctions is also evident in transport measurements in which the current exceeds I_C and a finite voltage appears across the junction. In particular, unless $I >> I_C$ and the junction resistance is nearly the normal-state one R_N, the DC current required to generate a given DC voltage across the junction will oscillate as a function of the applied field. To investigate whether the intended nanoscale modulation of T_C displayed in Figure VI.19 yields this type of magnetic field-effects, we performed sets of $V - I$ measurements for a number of fields in the range $[-9\ kOe, 9\ kOe]$ at different temperatures.

Figure VI.20 represents these measurements for the $1\ \mu m$ junction in the 3 u.c. thick device presented above:

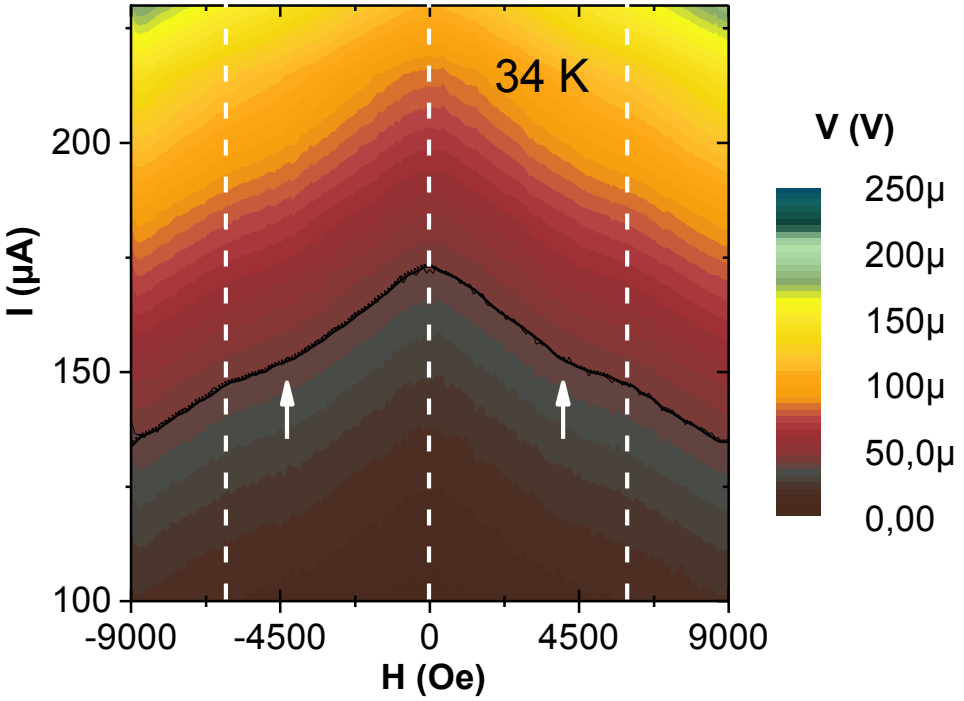

Figure VI.20: Modulation of the critical current with the applied magnetic field, for a 1 μm thick junction in a 3 u.c. YBCO thick device at 34 K. Black curve: $I_c(H)$ defined by a $40\ \mu V$ criteria.

The magnetic field is applied perpendicular to the current, and nearly parallel to the ab planes (the disorientation is $5 \pm 1º$). A contour plot is used in which the colour scale is associated to the measured voltage V as a function of the injected current and applied field. As an example, the black line highlights the contour level for $V = 40\ \mu V$ criteria.

In agreement with the observations in section VI.2.2, the critical current decreases when the magnetic field increases. **We observe that this modulation is not linear but presents oscillations**, which is emphasised by the arrows indicating the local minima at $H = \pm\sim 4300\ Oe$.

We investigated the temperature dependence of these oscillations. Figure VI.21 represents the same measurements at 31, 32, 34, 38 and $40\ K$.

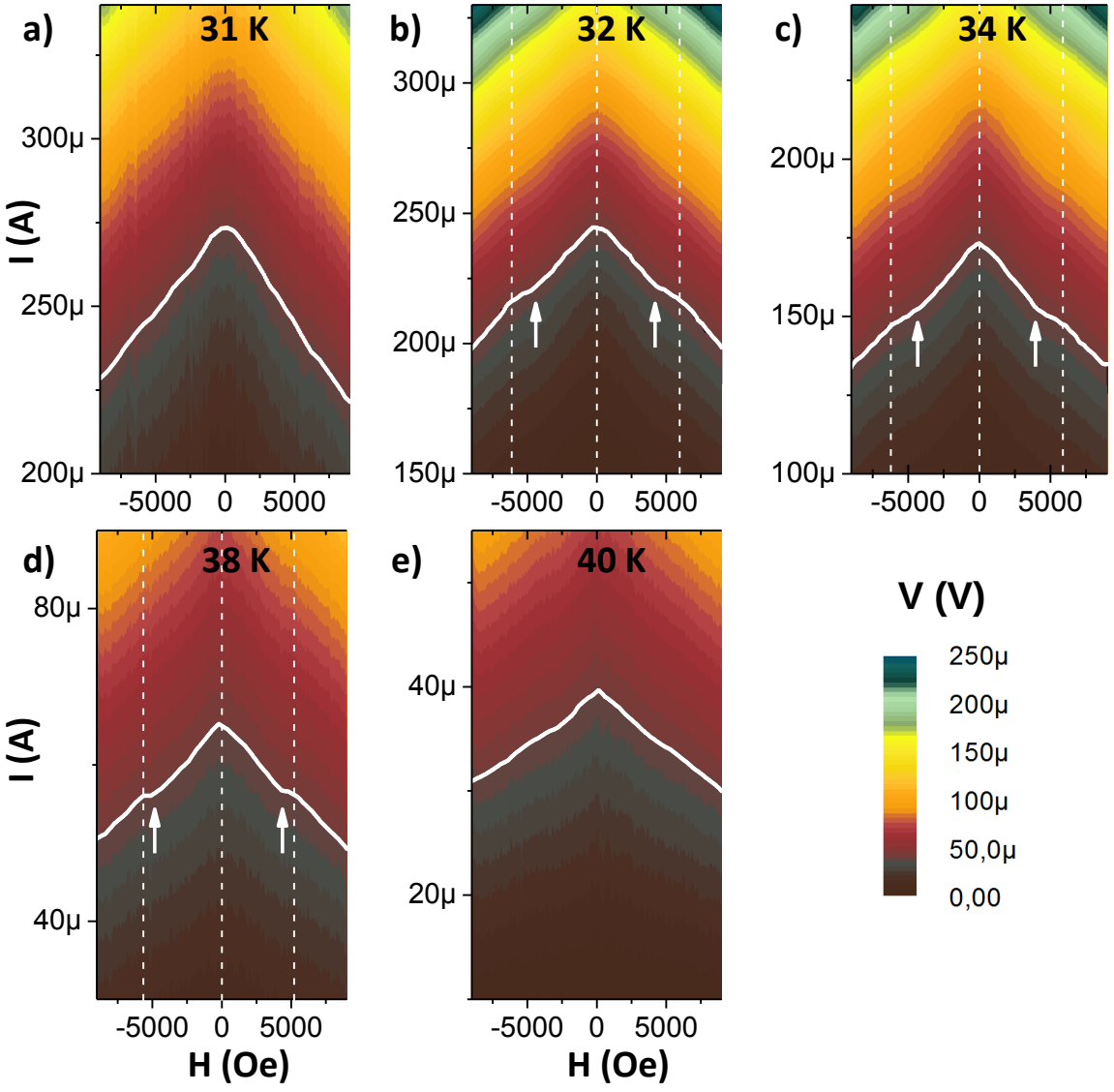

Figure VI.21: Modulation of the critical current of a 1 µm thick junction in a 3 u.c. YBCO thick device with the applied magnetic field for different temperatures

We observe that the oscillations are the most visible around $33\ K$, and disappear (rapidly) for lower and (more progressively) for higher temperatures. Note that the low temperature range in which the oscillations rapidly disappear correspond to that in which the V-I characteristics are nonlinear within the whole experimental window (*cf* Figure VI.18 *a)*).

Indeed the temperature at which the oscillations are larger roughly corresponds to the transition temperature between V-I showing a low-current Ohmic tail and V-I showing vanishing resistance in the low-current limit.

The oscillatory magneto-transport described above can be also evidenced through magneto-resistance measurements. Figure VI.22 presents measurements for the previous $1\ \mu m$ thick junction in the 3 u.c. device, presented earlier in Figure VI.20 and Figure VI.21. The orientation of the magnetic field with respect to the device is unchanged.

We observe that at low temperature (blue curve in Figure VI.22 *a)*), the background resistance increases weakly with the applied magnetic field. This is as expected when the magnetic field is nearly parallel to the ab planes (the small resistance increase is possibly due to the small component of the magnetic parallel to the c-axis of YBCO). As the temperature is increased (green curves), the non-monotonic behaviour gradually appears, becomes the **most pronounced around $T = 32{\sim}34\ K$**, and tends to vanish at higher temperatures. **As in the $V(H, I)$ contour plot, the maxima appear around $= \pm 4300\ Oe$** , which is more clearly seen in Figure VI.22 *b)*, where the magneto-resistance at $34\ K$ is represented alone.

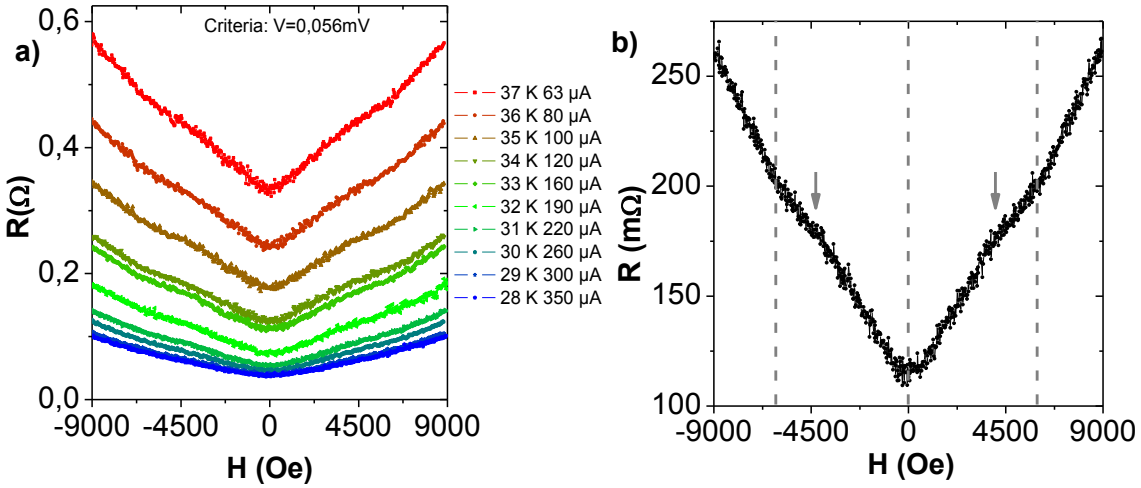

Figure VI.22: a) Resistance vs applied magnetic field at different bias current and temperatures for a 1 µm thick junction in a 3 u.c. YBCO thick device. b) Measurement at 34 K represented alone.

We investigate the amplitude of this effect at different bias currents, at a given temperature. Figure VI.23 *a)* represents the normalized resistance as a function of the applied field, at $34\ K$, for different bias currents (the current levels are marked by dashed lines on the $V - I$ characteristics in Figure VI.23 *b)*). We observe in Figure VI.23 *a)* that **the field-effect modulation is the strongest at low bias (black curve), and vanishes at high currents (blue curve)**. However, the noise of the measurement is bigger at low currents, which implies a compromise on the value of the current in order to observe these oscillations.

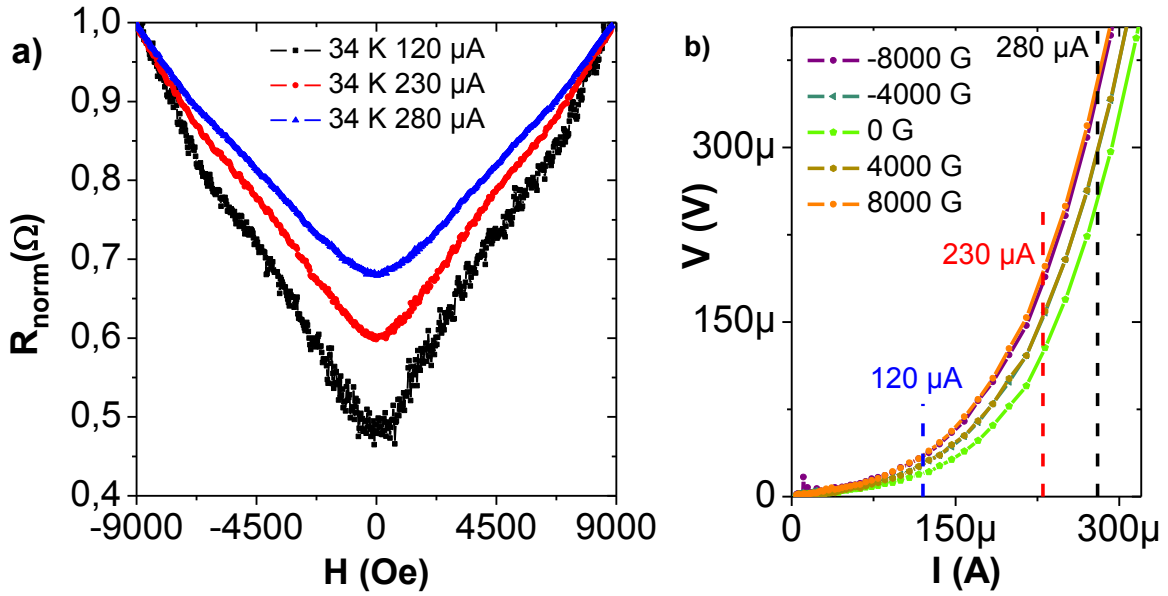

Figure VI.23: a) Normalized resistance vs applied magnetic field at different bias currents, corresponding to the dashed lines in b) *V-I* characteristics. Data measured at 34 *K* for a 1 µ*m* thick junction in a 3 u.c. YBCO thick device.

Measurements similar to those reported above were made with the magnetic field applied at different angles θ with respect to the ab planes, see Figure VI.24 *a)*:

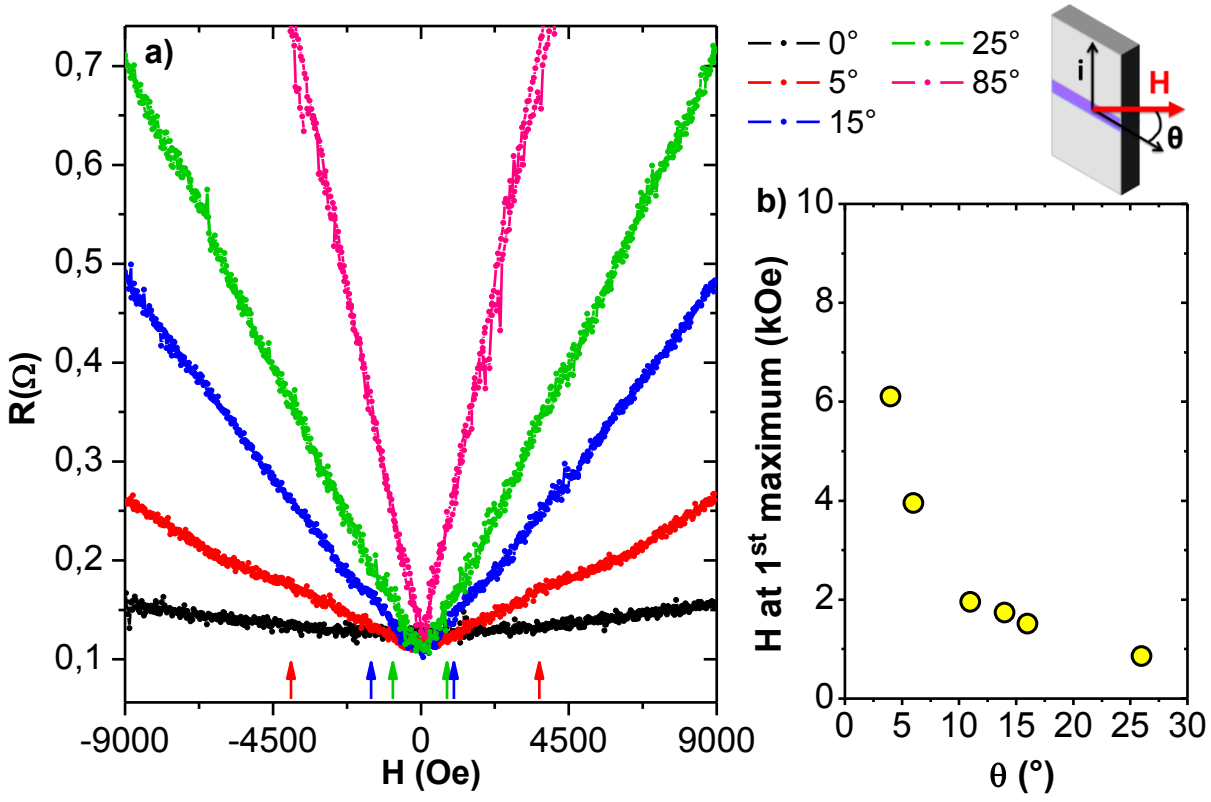

Figure VI.24: Resistance *vs* applied magnetic field at different orientations of the magnetic field for a 1 µm thick junction in a 3 u.c. YBCO thick device, at 34 K and 120 µA

A much stronger magneto-resistance is observed as the field is rotated out-of-plane, as expected from the very anisotropic nature of YBCO ultrathin films [171], [189]. When the magnetic field becomes parallel to the *c*-axis, the number of dissipating vortices and thus the resistance increases. Simultaneously, the curve features shift to lower fields. The arrows in Figure VI.24 *a)* represent the inflexion points (local "maxima") for several angles. The corresponding fields are displayed in Figure VI.24 *b)* as a function of θ. One sees that the characteristic fields rapidly decrease with increasing angle. The observed trend allows understanding why the non-linear modulation of the resistance is only evident in the magnetoresistance $5º < \theta < 25°$: for high angles the characteristic field falls below the measuring resolution, for $\theta \sim 0°$ it grows out of the experimentally accessible window.

The behaviour of homogeneous, rectangular junctions in an oblique field is simplified in ref. [30] where it is described as the product of the contribution in both directions. As explained in the discussion section below, trying to quantitatively analyse the above angular dependence from a Josephson effect perspective is difficult, since one dimension of the junction is small compared to the magnetic penetration depth and since our material is highly anisotropic. We show below measurements in which YBCO is thicker, which allows observing modulation effects in strictly parallel applied fields within the experimentally accessible window.

Figure VI.25 shows resistance *vs* applied magnetic field measurements in a thicker sample (YBCO thickness was $4{,}4\ nm$), for a junction of a comparable width ($d = 1\ \mu m$), which shows a qualitatively similar behaviour to that of the 3 u.c. sample . For this sample, **the non-monotonic field modulation was present at temperatures comprised between 19 and $21\ K$ and vanished at lower and higher temperatures** (see Figure VI.25 *b)* – the different currents are chosen to correspond to the same voltage from one temperature to another). Figure VI.25 *a)* represents the resistance *vs* applied magnetic field at $20\ K$ for different currents, showing that the oscillations remained even once the channel starts to dissipate. Similarly as for the 3 u.c. sample, both the amplitude of the oscillation and the noise are weaker when the current increases.

In this example, the magneto-resistance local maxima appear at $\sim \pm 5000 \pm 500\ Oe$ are well defined. If we try to understand this from a Josephson perspective, assuming that the field is perpendicular to the surface of the junction as defined by the effective width D of the junction and the thickness $t = 4{,}4 \pm 1\ nm$ of the film, and assuming a rectangular, homogeneous junction, the effective width of the junction would be:

$$D = \frac{\Phi_0}{H \times t} = \frac{2{,}1 \cdot 10^{-11}}{5 \cdot 10^3 \times 4{,}4 \cdot 10^{-9}} = 940 \pm 300\ nm \qquad \text{(VI.6)}$$

This value is consistent with the width of the junction defined by PFM, which was $d = 1\ \mu m \pm 50\ nm$.

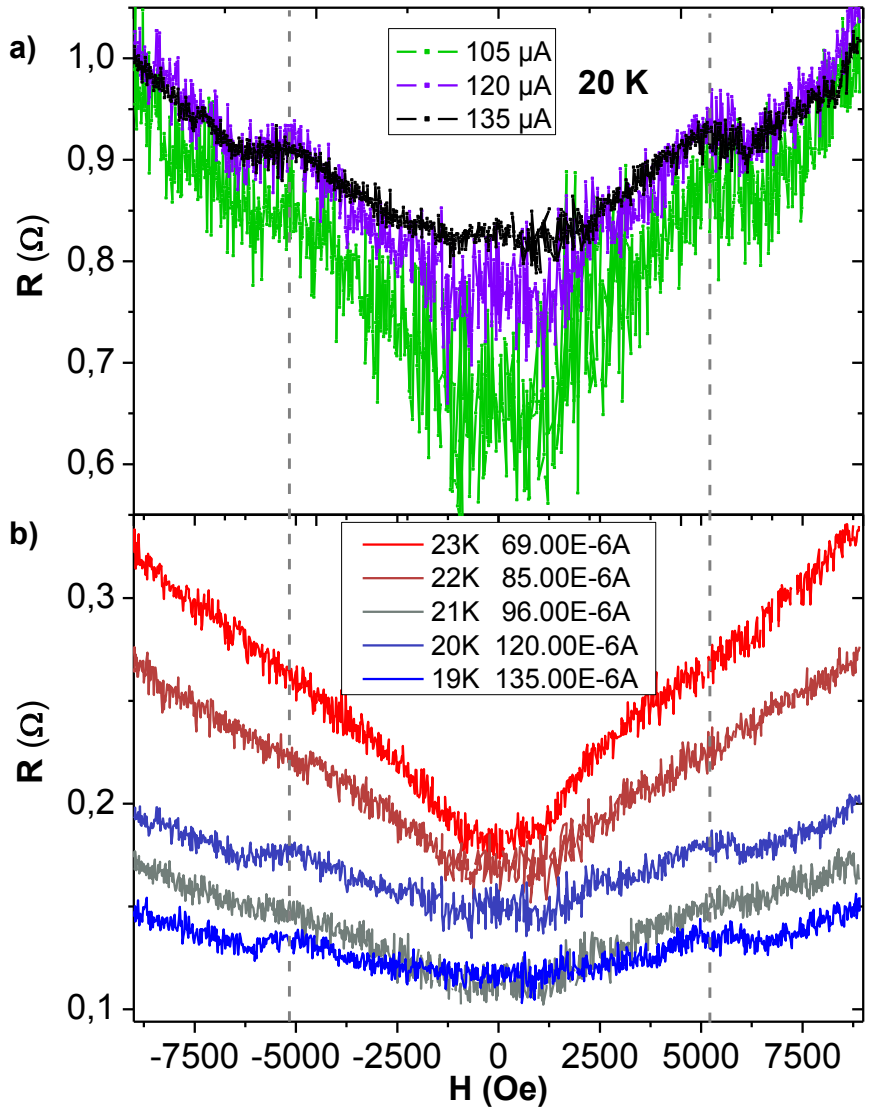

Figure VI.25: Resistance vs field measurements for a 1 μm thick junction in a 4 u.c. thick device for a) different bias currents (normalized to the maximal value) and b) different temperatures but same levels of voltage.

VI.2.4 Interpretation of the experimental observations

The key experimental results can be summarised as follows:

I) The resistance vs. temperature of field-effect S/S'/S junctions does not show a two-step transition as observed in the case of irradiation-defined junctions (see Figure VI.14). However, the zero-resistance temperature does lie in between the critical temperature of the depleted and accumulated regions, as expected.

II) Within the experimentally accessible window, the V-I characteristics of field-effect S/S'/S junctions show a nearly Ohmic tail at high temperatures. Below some temperature T_C',

the Ohmic tail disappears, yielding V-I of negative curvature and vanishing resistance in the low-current limit. While qualitatively reminiscent of it, this behaviour does not quantitatively correspond to that of plain superconducting YBCO. In particular, the current level at which the V-I becomes non-linear at high-temperatures (I_{nl}) does not follow the expected temperature dependence.

III) In the temperature range $T>T_C'$, the electrical transport depends non-monotonically on the applied magnetic field. In particular, two maxima (minima) appear in the magneto-resistance symmetrically around $H = 0\ Oe$.

IV) This modulation is observed for different orientations, and the field at which it occurs varies with the angle. Note that when the field has a component parallel to the c-axis of YBCO, the background magneto-resistance shows a strong dependence on the magnetic field due to the penetration and dynamics of vortices.

V) In strictly parallel magnetic fields, the maxima (resp. minima) seen in the magneto-resistance (resp. current) as a function of the applied magnetic field corresponds to one flux quanta over the area of the intended junction.

The above experimental facts can be understood if we consider that the device with a written junction effectively behaves i) as decoupled S/N/S junction, ii) a proximity coupled S/N/S junction or iii) a superconducting film S/S'/S as a function of temperature. In particular, taking as an example the junction defined in the 3 u.c. sample, the measurements of which are shown in Figure VI.20 through Figure VI.23:

- At high temperatures $\sim 80\ K$, the entire device is in the normal state. Upon decreasing temperature, the superconducting transition of the electrodes "S" occurs. Because of the reduced dimensionality of the film, the transition occurs over a very large temperature range. Down to $\sim 38\ K$, the measured device resistance essentially corresponds to the electrodes' ("S") resistance.
- **Around $\sim 40\ K$**, the "S" electrodes approach the zero-resistance state (vanishing current in the low-current limit). The device behaves as a **decoupled S/N/S junction**, shows no magnetic field modulation, and low-current resistance starts being dominated by the "N" junction, which is Ohmic. The V-I curves become non-linear only in the high current regime, for which the resistance is again dominated by that of the "S" electrodes.
- **Below $T \sim 38\ K$**, the coupling of the "S" electrodes across the "N" junction develops, which yields the onset of the non-monotonic magneto-transport. **The device starts behaving as a coupled S/N/S junction** due to proximity effect between the two electrodes, *i.e. via* the coherent transport of Andreev bound states across N. In this regime:
    - The amplitude of the resistance (current) modulation with magnetic field increases with decreasing T (Figure VI.21), because the junctions' critical current increases with decreasing T.
    - Down to $\sim 34\ K$, the V-I curves (Figure VI.18) are Ohmic in the low-current regime. The junction critical current is zero in the whole experimental window. The nearly Ohmic tail corresponds to the junction response above its critical current. This explains why the cross-over into the non-linear regime occurs at increasing currents

I_{nl} with decreasing temperatures, which does not correspond to a plain thin film behaviour. In this scenario, I_{nl} corresponds to the current above which the device resistance is dominated by the non-linear "S" electrodes resistance.

- Between $34\ K$ and $32\ K$, the junction critical current has sufficiently increased so that it is observed in the low current regime, and consequently the Ohmic tail disappears. The *V-I* are thus steep in the whole experimental window (Figure VI.18).

- Below $32\ K$, the oscillatory magneto-transport disappears as the critical temperature of the "N" part is reached, *i.e.* the whole channel is superconducting (the conduction across "N" is no longer due to Josephson coupling, since it has become a superconductor on its own).

To conclude, the Josephson effect can only be observed in a range of temperature $T_c^{\downarrow} < T < T_J < T_c^{\uparrow}$ where $T_c^{\downarrow}$ (resp. $T_c^{\uparrow}$) is the critical temperature of the whole bridge measured in the depleted (resp. accumulated state), and T_J is the coupling temperature of the accumulated region ("S") across the depleted one ("S'"). Knowing that $T_c^{\downarrow}$ and $T_c^{\uparrow}$ are relatively close ($\Delta Tc = 5{\sim}15\ K$ in the studied junctions), **the range of temperature in which the Josephson effect can occur is relatively narrow.**

Finally let us briefly discuss the characteristic field at which maxima (minima) are observed in the magneto-transport, and its angular dependence.

The equations leading to the expected Fraunhofer pattern in the case of a homogeneous, rectangular Josephson junction are described in section I.2.3. b). One has to keep in mind that in this simple calculation, the extinctions of the critical current occur when the flux through the effective magnetic section of the junction is an integer of the flux quantum.

In ultra-thin films, the effective width of the junction depends on the orientation of the magnetic field:

- Field perpendicular to the film plane: the effective penetration length is longer than λ if the thickness $t < \lambda$ [190]. For a film of thickness t, the distance over which the field penetrates the superconducting layer, the Pearl length Λ, becomes as big as:

$$\Lambda = \frac{2\lambda^2}{t} \qquad \text{(VI.5)}$$

  where λ is the London penetration depth. Thus, for a thickness of few nanometres, and considering the YBCO in-plane $\lambda = 150\ nm$, one obtains $\Lambda{\sim}10\ \mu m$, and a situation like that represented in Figure VI.26 *a)* is expected. If $d \sim 1\ \mu m$ is the width of the written junctions, one expects an effective junction area $D \times W = (2\Lambda + d) \times W \approx 2 \cdot 10^{-10}\ m$ and the period of the associated Fraunhofer pattern is $\frac{\Phi_0}{D \times W} \sim \frac{2 \cdot 10^{-11}}{2 \cdot 10^{-10}} = 10^{-1}\ G$, which is below the precision of our set up.

- Field parallel to the ab planes: With the field parallel to the ab planes (Figure VI.26, *b)*), the section of the film is thinner than the London penetration depth, ***i.e.*** **screening currents circulate in the whole film and the field penetrates both the normal region and the rest of the film.** This makes the calculation of the effective junction area challenging. If we assume that this is given by the section shown in Figure VI.26, *b)*, we expect $\frac{\Phi_0}{t \times d} {\sim} 5\ kG$, in good agreement with the experimental observation.

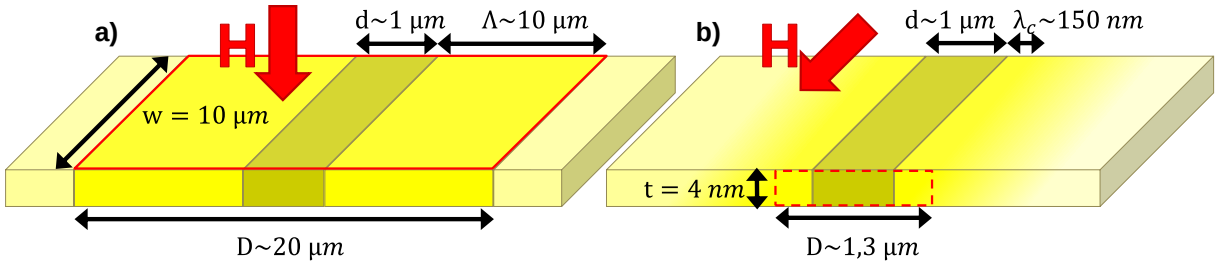

Figure VI.26: Surface of the junction for a field a) Parallel to the c-axis and b) Parallel to the ab planes.

In conclusion, **when a magnetic field is applied, the effective width of the junction depends on the orientation of the magnetic field with respect to the junction. The effective junction area for angles other than strictly perpendicular to the film is not well determined.** Thus, Figure VI.24 cannot be explained by a simple model describing a rectangular junction in a magnetic field, but necessarily depends on the sharp geometry of our devices. Explaining quantitatively the results would require a model able to deal with extremely high aspect ratio of the junctions (to give a graphical example, this is comparable to a $1\ m$ long, $10\ cm$ wide and $0{,}1\ mm$ thick sheet). Furthermore, this also shows that minor misalignment during sample measurements (the sample is stuck on the sample holder with tape, and only one out of three rotation axes is precisely controlled by the goniometer) may limit the operation and measurement of this type of ferroelectric field-induced junctions.

Finally, to conclude on the experimental observation, we shall briefly recall the limitation imposed by the depth profile of the junction. In the YBCO film, the field-effect is expected to occur only very close to the interface with the BFO-Mn, on a distance comparable to the Thomas-Fermi length, which is $\sim 1\ nm$ in YBCO. While the actual length over which charge accumulation and field-effect doping is probably somewhat larger (as shown in section VI.1.2, we are able to modulate the T_c of five unit cells thick samples), as shown in section III.2 via experiments in a similar system (BFO/CMO), the carrier density profile might not be homogeneous along the c-axis.

This may have effects on the junction behaviour. For example, close to the critical temperature T'_c of the barrier, the normal region close to the interface might be larger than far from the interface. **This would result in a junction with a variable width. Regarding our results, this may contribute to $I_c(H)$ and $R(H)$ patterns differing from the Fraunhofer pattern expected for a homogenous, rectangular junction.**

In summary, while the overall behaviour of the studied S/S'/S junctions can be successfully interpreted in terms of a simple model that considers a homogeneous junction in a well-defined magnetic field orientation, a detailed quantitative explanation of the experimental details would require a more elaborate model that considers the various points discussed above.

VI.3 Conclusion

We demonstrated remanent and switchable ferroelectric field-effect in BFO-Mn/YBCO heterostructures. By reversing the polarisation of BFO-Mn domains with a CT-AFM tip, we induced an electrostatic modulation of the carrier density modulation in the YBCO film. This modulation was measured in the normal state by Hall effect measurements; the corresponding value of the polarisation was one order of magnitude lower than expected for our BFO-Mn films, in which large out-of-plane polarisation was measured during the characterisation process. This confirms the hypothesis made in section V.1.3. c) that some ferroelectric domains are pinned at the interface in the downwards direction, probably because of the intrinsic electric dipole at the interface which favours this orientation.

We then investigated the transport properties of devices consisting of S/S'/S junctions defined by ferroelectric field. From the resistance vs temperature and voltage-current measurements, we demonstrated that the device neither behaved as a decoupled S/N/S barrier, nor a plain superconducting film, but as an S/S'/S junction in which a strong proximity effect occurred despite the length ($1\ \mu m$) of the weak link.

As predicted by the theory of the DC Josephson effect, in presence of a magnetic field, the phase difference between the two "S" electrodes led to oscillations in the $I_c(H)$ and $R(H)$ patterns. Because of the reduced T_c shift between the depleted region and the accumulated electrodes, this effect is only observable in a reduced temperature range. We did not obtain a complete extinction of the critical current, like predicted by the Josephson theory: this might be because of inhomogeneities in the depth profile of the junction as well as the faded interface of the region in which the magnetic field penetrates. Nevertheless, we demonstrated the existence of the DC Josephson effect in a weak link defined by electrostatic depletion of free carriers.

In the following chapter, we investigate a completely different type of junctions, in which the superconducting electrodes are separated by an insulating ferroelectric film.

VII. Out-of-plane field-effect devices

Index

VII. Out-of-plane field-effect devices 152

VII.1 Room-temperature measurements 154

VII.1.1 Description of the set-up 154

VII.1.2 Characterisation of *Pt*/*Co*/BFO-*Mn*/YBCO junctions 155

VII.1.3 Characterisation of *Nb*/BFO-*Mn*/YBCO junctions 158

VII.1.4 Characterisation of *NbN*/BFO-*Mn*/YBCO junctions 159

VII.1.5 Characterisation of *MoSi*/BFO-*Mn*/CMO junctions 160

VII.2 Low-temperature measurements 161

VII.2.1 Characterisation of the junctions 161

VII.2.2 Field-effect measurements 164

VII.2.3 Conclusions 166

VII.3 Conclusion 167

In this chapter, we investigate the feasibility of a Ferroelectric Tunnel Junction (FTJ) with two superconducting electrodes, one made out of a high-T_c superconductor and one out of a low-T_c superconductor. FTJs raise a considerable interest in the solid-state devices community, as they are potential candidates for future generations of Random Access Memories. The principle is the following: an insulating ferroelectric ultra-thin film is sandwiched between two metallic electrodes. Its thickness is small enough so that when a current is applied, the electrons tunnel through it. Depending on the direction of the polarisation, the Tunneling Electro-Resistance (TER) is different – we talk of "resistive switching". As explained in section I.3.4. c), and described by many examples in section II.4.3, this arises from different phenomena. Among them, in our High-T_c Superconductor / Ferroelectric / Low-T_c Superconductor junctions, we explore the following effects:

- High-T_c superconductors have smaller carrier densities than low-T_cs. Consequently the Thomas-Fermi length (introduced in section II.1.2) is much larger in high-T_c superconductors. We saw in section I.3.4 that when the electrodes of an FTJ have different screening lengths, then **the electrostatic height of the barrier and thus its TER is different for the two directions of the polarisation.**
- We saw in the previous chapter that a small change in the carrier density – induced by ferroelectric field-effect – caused large changes in the superconducting properties of the material over a distance equal to the Thomas-Fermi length. Like represented in Figure VII.1, **the interfacial layer of the high-T_c superconductor might undergo a metal/insulator transition depending on the direction of the ferroelectric polarisation. This would modify the effective thickness of the barrier, and thus the TER**.

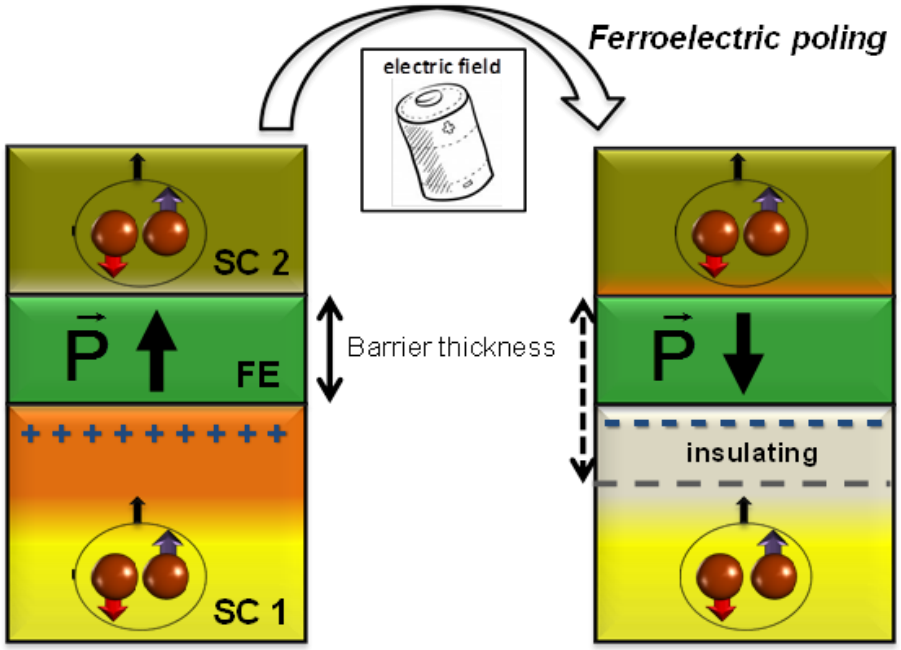

Figure VII.1: Principle of the vertical field-effect junctions

VII.1 Room-temperature measurements

VII.1.1 Description of the set-up

In order to characterise the resistance of our films and scale the resistance of our junctions with their size, we proceeded to the measurement of several junctions of different areas, for different BFO-Mn film thicknesses. To do this, we fabricated simple junctions where the top electrode is a pad deposited on a BFO-Mn/YBCO//STO bilayer. The technology is described in section II.3.6. The sample is patterned with pads of sizes from $300\ nm$ to $1\ \mu m$. Figure VII.2 is a microscope image of the matrices of pads: each square represents an area where the pads are of the same size.

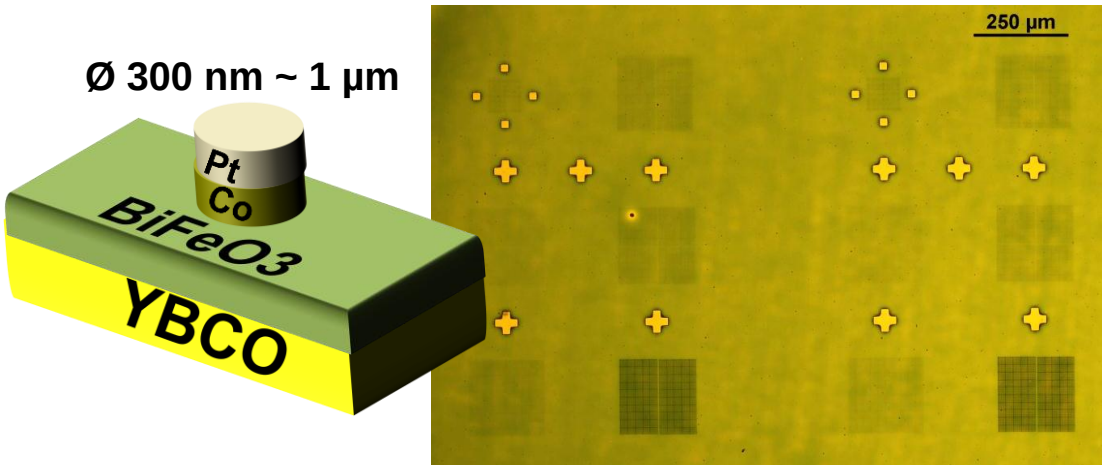

Figure VII.2: Optical image of matrices of pads on a device and schematic representation of the structure of a pad

The device is then contacted using a CT-AFM microscope like schematized in Figure VII.3. The YBCO layer is electrically connected to a low-noise generator, and the CT-AFM tip, connected to the other pole of the generator, is placed above a random pad.

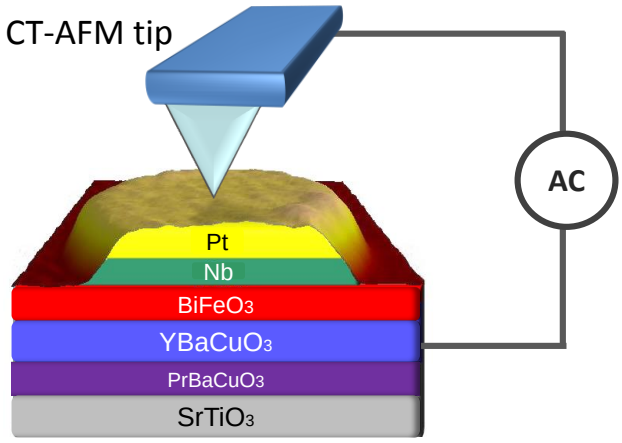

Figure VII.3: Scheme of a Pt/Nb/BFO-Mn/YBCO/PBCO//STO nanodevice

To investigate the resistive switching of the device and the ferroelectric properties of the BFO-Mn films, we combined PFM and CT-AFM measurements. The CT-AFM tip used for the two kinds of measurement is the same, but it is connected to one set-up or the other:

- In PFM mode, we image either the BFO-Mn film surrounding the pad, either the pad itself. The pad is thin enough so that the piezoresponse of the ferroelectric film underneath is felt by the tip.
- In CT-AFM mode, a voltage of $200\ mV$ is applied between the tip and the YBCO film, and the resistance is deduced from the current necessary to apply this voltage. The resistance of the tip is typically $10\ k\Omega$.

We carried out experiments on several types of junctions: with a well-known electrode, Pt/Co – which was previously used at the laboratory to study ultra-thin BTO barriers on LSMO: see [81] – and with low-T_c superconducting electrodes: Niobium (Nb), Niobium Nitride (NbN) and Molybdene Silicium ($MoSi$).

VII.1.2 Characterisation of Pt/Co/BFO-Mn/YBCO junctions

In these junctions, the top-electrode consists of a $10\ nm$ layer of Co. This metal is chosen because it bonds well with the BFO: if the mechanical contact between the top-electrode and the ferroelectric is not good enough, the pad might be scratched during the contact-mode scans of the AFM. It is covered by $10\ nm$ of Pt, which ensures a good electrical contact between the tip and the pad.

In order to characterise the homogeneity of the barrier, we measure the resistance of several pads in CT-AFM mode with a bias of $200\ mV$. The resulting resistance × area products are represented in Figure VII.4.

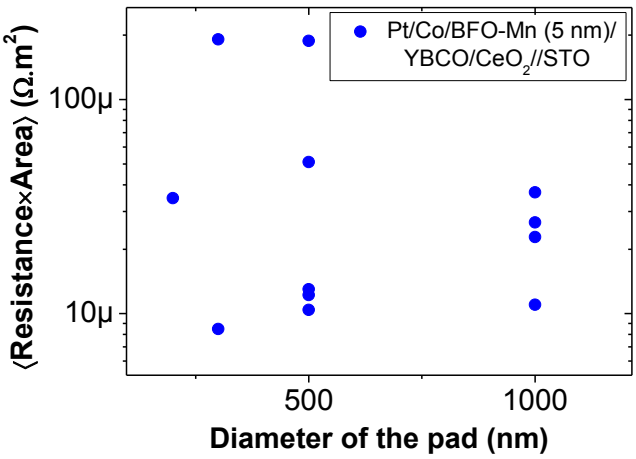

Figure VII.4: Product of the measured resistance by the surface of the pad as a function of the diameter of the Pt/Co pads on a BFO-Mn ($5\ nm$)/YBCO/CeO_2//STO film

The dispersion from one pad to the other is large: there is sometimes one order of magnitude between the resistances of two pads with the same area. This can be due to the presence of hot spots short-circuiting the ferroelectric film.

To investigate resistive switching in these pads, we first image the pad in PFM mode in order to make sure that the BFO-Mn has an out-of-plane polarisation underneath the pad and to determine the direction of the polarisation. An example of a PFM image of a pad in the initial state is reproduced in Figure VII.5 (left images). On this example the phase is downwards both underneath the pad and around the pad. We can see that underneath the pad, the signal is stronger: when the voltage is applied, the electric field is established underneath the entire pad and every domain responds mechanically to this excitation. The probed domain is thus surrounded by domains that also expand or retract. Outside the pad, the probed domain is pinned by its neighbouring domains, which do not feel the electric field: its piezoresponse has a smaller amplitude.

We then apply a DC voltage pulse V_{pulse} during $100\ \mu s$ between the YBCO layer and the tip, and subsequently measure the resistance of the barrier by applying a DC voltage of $200\ mV$ in CT-AFM mode. A typical sequence is represented by the blue curve in Figure VII.5. After each V_{pulse} is applied, the resistance of the pad is measured (black curve).

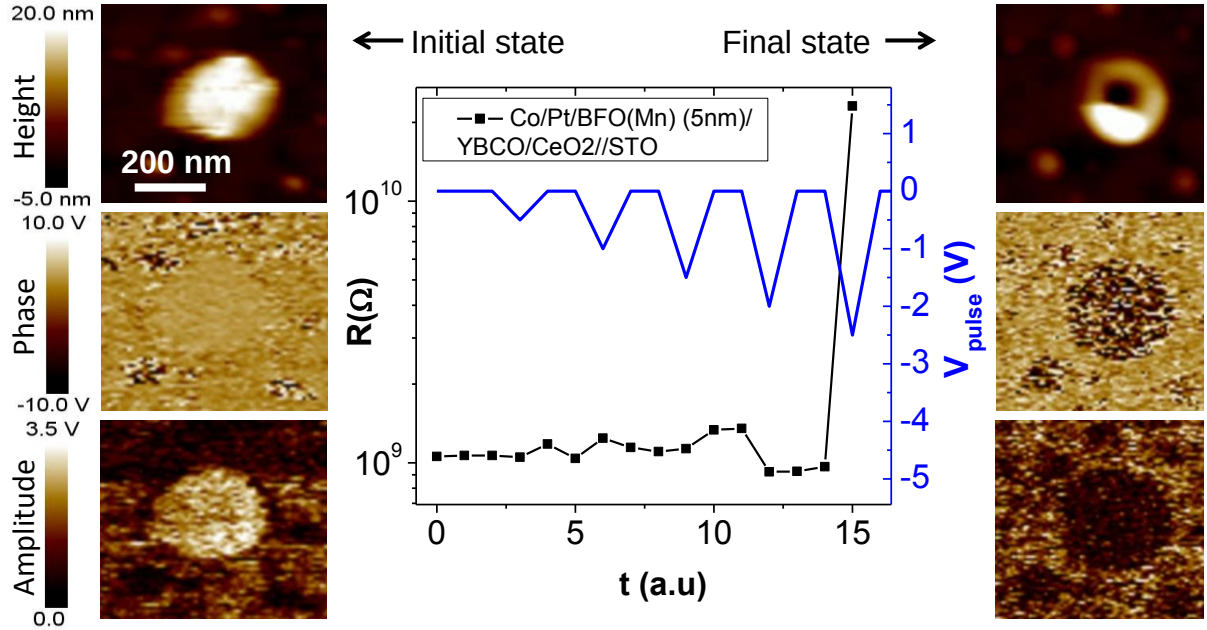

Figure VII.5: PFM image of a small pad in its initial state (left) and after applying -2,5 V_{DC} (right). The resistance (black data points) is measured after each DC pulse (blue curve)

For pads smaller than $1\ \mu m$, no resistive switching was observed; for increasing DC voltage of one sign or the other, the resistance would remain the same until it suddenly increases by several orders of magnitude, as represented in Figure VII.5: after applying $V_{pulse} = -2{,}4\ V_{DC}$, the resistance of the pad increases from $1\ G\Omega$ to $10\ G\Omega$. Topography images of the pads after such measurements usually exhibit a deterioration of the pad, and the absence of PFM signal: zero amplitude and undefined phase, as represented by the images on the right in Figure VII.5.

This indicates that on the submicrometric junctions, at room temperature the breakdown field of the capacitor is below the electric field necessary to switch the ferroelectric polarisation.

We were able to observe a resistive switching on several $1\ \mu m$ pads. Figure VII.6 shows an example of a Pt/Co/BFO-Mn $(5\ \ nm)$/YBCO/CeO_2//STO pad that exhibited three states of resistivity. The following description is chronologic:

- The pad is imaged with PFM in its initial state. Figure VII.6 *a)-left* represents the phase of the piezoresponse and Figure VII.6 *a)-right* the amplitude: again, we can see that the phase is downwards both underneath the pad and around the pad. The initial resistance of the barrier, measured with $200\ mV$, is $6 \cdot 10^7\ \Omega$.
- Negative DC pulses are then applied between the pad (grounded) and the YBCO layer. The resistance of the barrier is measured after each DC pulse and remains constant.
- The resistance of the barrier suddenly drops by an order of magnitude for $V_{pulse} = -2{,}5\ V$. We then switch to the PFM mode and image the pad (see Figure VII.6 *b)*): we observe that an area with no amplitude and with an undefined phase nucleated at the border of the pad.
- We then apply several pulses of small DC negative voltages and observe that the area with the undefined phase propagated (see Figure VII.6 *c)*).
- Positive DC pulses are then applied in order to eventually switch the barrier back into its initial state. The level of resistance remains constant.
- The resistance of the barrier suddenly increases by two orders of magnitude for $V_{pulse} = 2{,}5\ V$. PFM image of the pad reveals that the piezoelectric signal is null over the whole pad.
- We then apply negative DC pulses above $V_{pulse} = -2{,}5\ V$ but the resistive switching previously observed does not occur.

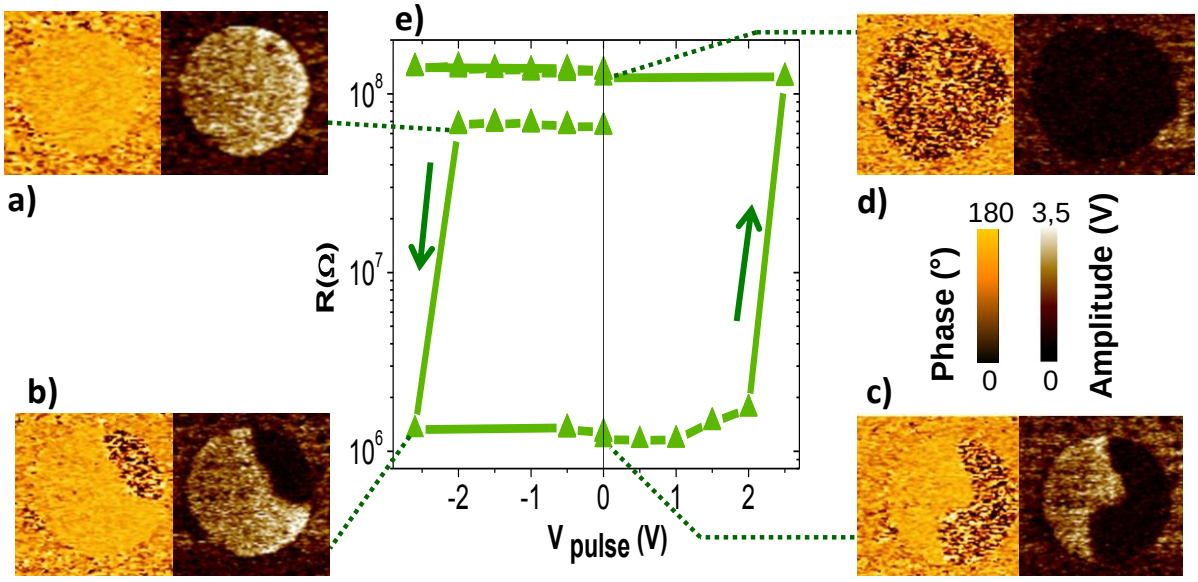

Figure VII.6: Variation of the resistivity and the ferroelectric state of a Pt/Co/BFO-Mn (5nm)/YBCO/CeO_2//STO pad. PFM image of the pad in a): initial, b) and c): intermediate and d): final states. e): measured resistivity as a function of the applied DC pulse.

We saw in precedent chapters that the piezoresponse of the upwards direction of our BFO-Mn/YBCO films was usually very weak, but at least the phase was defined in the upwards areas. In the PFM images of the pad, we can see that in the areas that are not downwards the amplitude drops and that the phase is not defined at all, indicating that there is no out-of-plane polarisation in this area.

The fact that the resistance is smaller when the pad is in a mixed state suggests that the drop of resistance might occur through the domain wall between the two areas.

These experiments raise two questions:

- Why are we not able to switch the polarisation underneath the pads at room temperature? All the measured samples with thicknesses down to 2,7 nm were switchable in both directions when using the PFM in writing mode (outside the pads). In the case of the small pads, the breakdown field of the capacitor was smaller than the field necessary to switch the polarisation. **In both cases the depolarising field generated when there is a top-electrode might be too strong and destabilises the polarisation in the upwards direction.**
- Why have we lost the polarisation in the micrometric pads? The application of a voltage through the pad might have temporarily removed screening charges and left unscreened bound charges at the surface of the ferroelectric field, generating a higher depolarising field and suppressing irreversibly the polarisation in BFO-Mn. Another possible explanation could be that some defects, generated while applying the electric field, pin the ferroelectric domain walls. If the resulting ferroelectric state is made of numerous tiny domains that are too small to be probed by the PFM, the resulting amplitude is null.

VII.1.3 Characterisation of Nb/BFO-Mn/YBCO junctions

We investigated the behaviour of similar junctions gated with a Niobium (Nb) electrode. This superconductor is a good candidate for the vertical Superconductor/Ferroelectric/Superconductor junctions because it has a high carrier density as well as a relatively high critical temperature ($\sim 9\ K$). We measured Nb pads in a range $300\ nm$ $\sim 1\ \mu m$ on a BFO-Mn ($4{,}4\ nm$)/YBCO/PCBO//STO. Figure VII.7 represents the resistance × area products of the measured pads, as a function of their diameter.

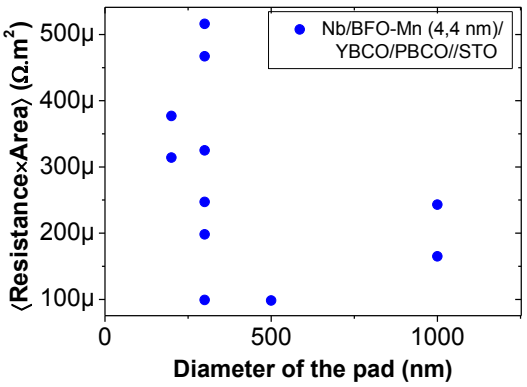

Figure VII.7: Product of the measured resistance by the surface of the pad as a function of the diameter of the Nb pads on a BFO-Mn ($4{,}4\ nm$)/YBCO/PBCO//STO film

Again, we observe a large dispersion of the resistance for pads of the same size. We were able to observe resistive switching in these devices: as an example, Figure VII.8 shows the resistance *vs* applied polarisation voltage for two pads of different diameters.

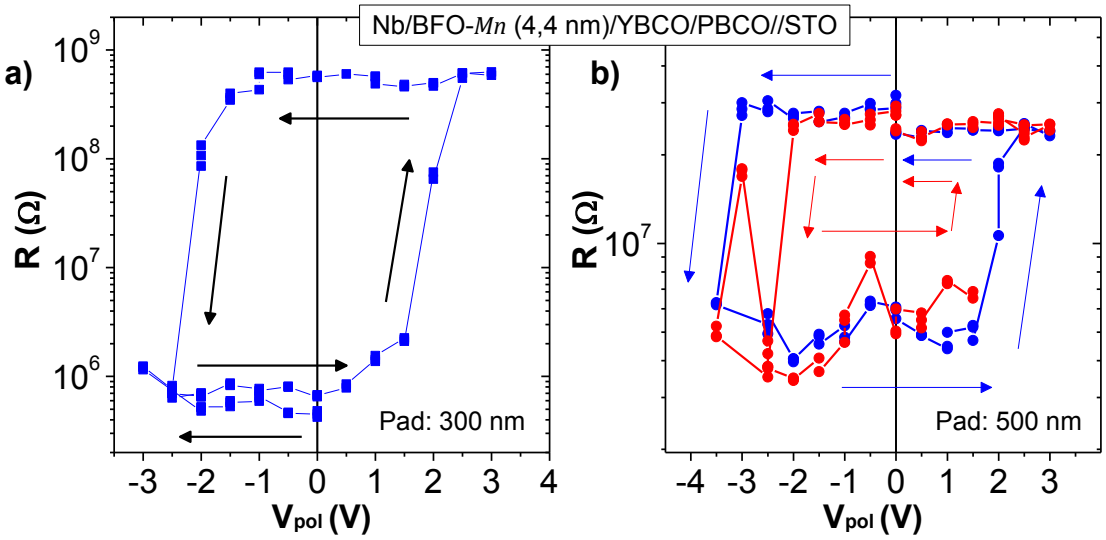

Figure VII.8: Resistive switching on an Nb/BFO-Mn ($4{,}4\ nm$)/YBCO/PCBO//STO film.
a) On a $300\ nm$ pad and b) on a $500\ nm$ pad.

In Figure VII.8 *a)* the pad has a diameter of $300\ nm$. The ratio between the OFF and ON state is $R_{\%} = \frac{R_{OFF} - R_{ON}}{R_{ON}} = 10^5\%$, which is comparable to the TER ratio obtained in other ferroelectric tunnel junctions (see examples in section II.4.3). In Figure VII.8 *b)* the pad has a diameter of $500\ nm$. In this case, the ratio between the OFF and ON state is $R_{\%} = 10^3\%$, two orders of magnitude smaller than the ratio obtained in the $300\ nm$ pad.

However, we observed that on many pads, the resistance was not stable and that it varied after each voltage pulse. This could be due to the fact that Nb reacts easily with oxygen: when a voltage is applied, chemical reactions might occur at the Nb/BFO-Mn interface. To avoid this, we decided to use Niobium Nitride, which is known to be less reactive with oxides than Nb.

VII.1.4 Characterisation of NbN/BFO-Mn/YBCO junctions

We investigated the behaviour of similar junctions gated with a Niobium Nitride (NbN) superconducting electrode. All the measured junctions (with diameters comprised between $300\ nm$ and $1\ \mu m$) showed the same behaviour: with increasing DC pulses, the resistance remained constant until the junction is damaged. No "resistive switching" comparable to the results obtained with the Co/Pt and Nb was observed.

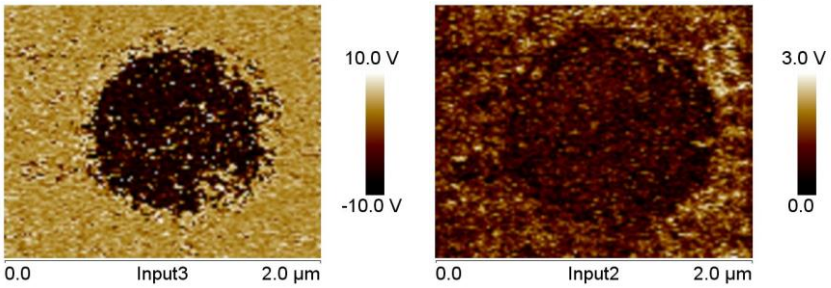

Figure VII.9: PFM image of an NbN/BFO-Mn ($4{,}2\ nm$) /YBCO/CeO_2//STO pad (left: phase, right: amplitude)

PFM images revealed a downwards polarisation, except in one sample (with a BFO-Mn thickness of $4{,}2\ nm$), where the polarisation was, as usual, downwards on the unpatterned layer but upwards underneath the NbN pads, as shown in Figure VII.9.
When a metal is in contact with a dielectric (here, the ferroelectric BFO-Mn), its wave function decays into the dielectric in the energy range where the metal conduction band overlaps with the band gap of the insulator. The presence of new states at the interface may induce a charge transfer at the interface, creating a dipole which stabilises one direction of the polarisation or the other. **This emphasizes the role the electrode material in aggravating or reducing the size effects in ferroelectric ultra-thin film** [82].

VII.1.5 Characterisation of $MoSi$/BFO-Mn/CMO junctions

Finally, we investigated $MoSi$ as a superconducting top electrode. In order to investigate the behaviour of $MoSi$ on thin BFO-Mn films, we compared $MoSi$/BFO-Mn/CMO junctions to Pt/Co/BFO-Mn/CMO junctions, which are well known structures previously characterised in our laboratory. Measurements on junctions with YBCO as a bottom electrode are reported in the next section.

Figure VII.10 represents the resistive switching obtained on the two kinds of junctions: *a)* for Pt/Co pads and *b)* for $MoSi$ pads. The resistive switching is reproducible and the ratio for $MoSi$ is high (up to $10^4\%$) and comparable to the resistive switching obtained with Pt/Co.

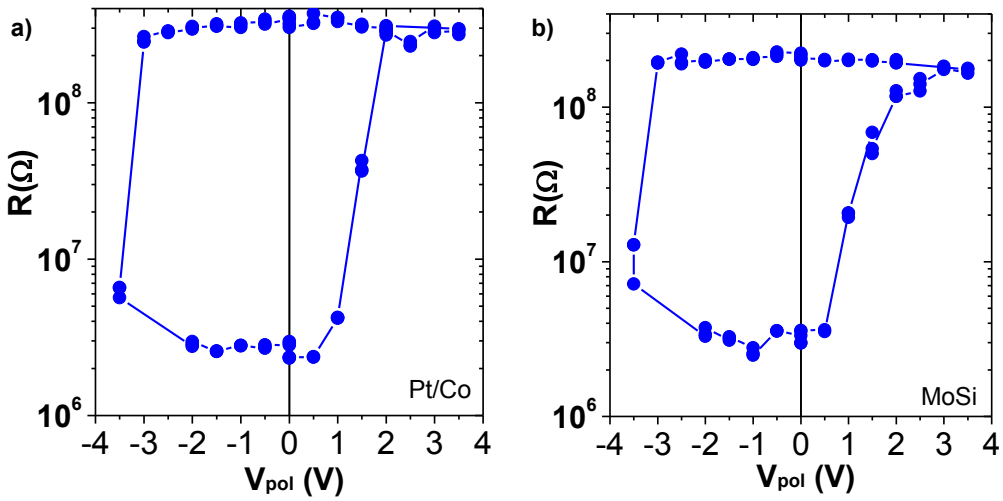

Figure VII.10: Resistive switching on a) Pt/Co/BFO-Mn ($4{,}4\ nm$)/CMO//STO pad and b) on a $MoSi$/BFO-Mn ($4{,}4\ nm$)/CMO//STO pad.

This experiment confirms that $MoSi$ is a good candidate for vertical devices. In the following section, we present the experiments carried on $MoSi$/BFO-Mn/YBCO junctions. In particular, we investigate the ferroelectric switching of our devices at low-temperature.

VII.2 Low-temperature measurements

In order to be able to measure junctions at low temperatures, we fabricated solid-state devices with junctions that had a surface of $5\sim15$ μm^2. The technology process is described in section II.3.6. They consist of BFO-Mn (few nm)/YBCO (50 nm) films gated with 100 nm of the low-T_c superconductor $MoSi$. The top-electrode of each junction as well as the common bottom electrode are wire-bonded to a measurement chip with Al wires.

VII.2.1 Characterisation of the junctions

VII.2.1. a) Room-temperature resistance of the junctions

In order to characterise the transport properties of the $MoSi$/BFO-Mn/YBCO junctions, we first measured the room-temperature resistance of the junctions. The devices are measured in two probes, *i.e.* the obtained resistance is the sum of the resistances of the contacts $R_{YBCO}^{contact}$ and $R_{MoSi}^{contact}$, the YBCO and $MoSi$ paths R_{YBCO} and R_{MoSi} and the BFO-Mn barrier R_{BFO}. We assume that the other resistances of the circuit (measurement wires, contacts between the aluminium wires and the measurement chip) are small in comparison. In this configuration, a Keithley K2450 sourcemeter measures the current necessary to apply a given voltage setpoint between the two probes. Figure VII.11 represents the resistance × area products of $MoSi$/BFO-Mn ($2{,}3$ nm)/YBCO junctions as a function of their characteristic dimension. The voltage setpoint is 100 mV.

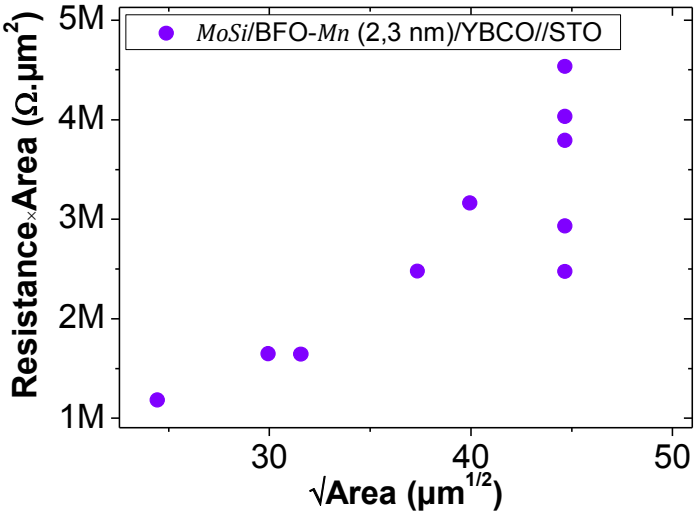

Figure VII.11: Resistance× area products as a function of the characteristic size of the junction for $MoSi$/BFO-Mn ($2{,}3$ nm)/YBCO junctions.

We can see that the resistance × area product is not constant but increases with the size of the junction. This is the sign that the current does not pass homogeneously across the BFO-Mn film, but that some hot spots might short-circuit the barrier. These defects are not necessarily conducting at low-temperature.

VII.2.1. b) Temperature dependence of the junctions

We then characterised the temperature dependence of the junctions. Figure VII.13 is an example of the temperature dependence of two devices, for several voltage setpoints. The curves with square symbols are measured from a $5\ \mu m^2$ junction and the curves with the round symbols are from a $15\ \mu m^2$ junction. The different colours correspond to different voltage setpoints: red: $3\ mV$, green: $5\ mV$, blue: $25\ mV$, black: $50\ mV$ and magenta: $100\ mV$. In Figure VII.13 *a)* is represented the resistance and in *b)* the current density.

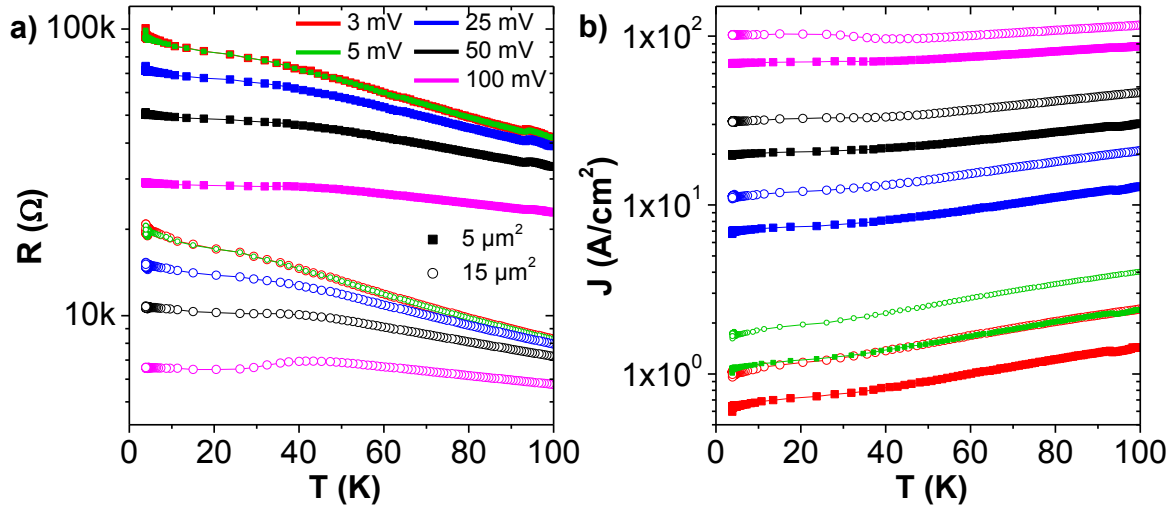

Figure VII.12: a) Resistance and b) Current density vs temperature of a $5\ \mu m^2$ junction (square symbols) and a $15\ \mu m^2$ junction (round symbols). Voltage setpoints: red: $3\ mV$, green: $5\ mV$, blue: $25\ mV$, black: $50\ mV$ and magenta: $100\ mV$.

The resistance of the circuit increases with decreasing voltage setpoint, indicating that the channel is not Ohmic. It also increases with decreasing temperature, as expected from an insulating barrier. In the low-voltage biased measurements, we do not observe the transitions of the superconducting electrodes. However, in the $100\ mV$ bias measurements the resistance flattens or slightly decreases with the temperature below $40\ K$, which suggests that we are measuring in series with the junction the YBCO electrode, which undergoes a normal/superconducting transition: this is confirmed by the resistance vs temperature measurements of the YBCO film represented in Figure VII.13.

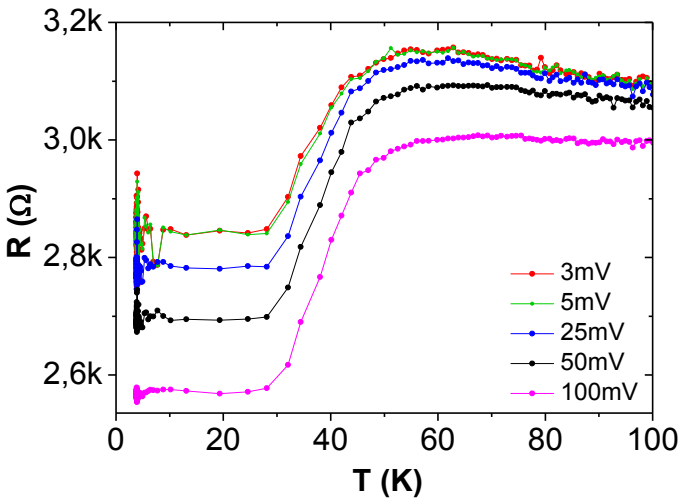

Figure VII.13: Resistance vs temperature for the YBCO layer for different voltage bias

In this measurement, the YBCO film is measured in a two probes geometry in which those are ~ 5 mm apart. This measurement shows the superconducting transition of YBCO, which occurs between $T_c^{onset} \cong 50\ K$ and $T_c \cong 30\ K$. Note that the low-temperature residual resistance corresponds to the contact resistance $2R_{YBCO}^{contact}$. Note also that the overall measured resistance $2R_{YBCO}^{contact} + R_{YBCO}$ is $\sim 3\ \mathrm{k}\Omega$ at room temperature, *i.e.* one order of magnitude smaller than the total resistance measured when the current is injected across the $5\ \mu m^2$ junction, and of the same order of magnitude than when the current is injected across the $15\ \mu m^2$ junction (see Figure VII.12 *a)*).

VII.2.1. c) Voltage-current characteristics of the junctions

We performed $I(V)$ measurements across the junction with low voltage-bias. This provides information about the T_c and the different superconducting gaps, Δ_{YBCO} and Δ_{MoSi}, present in the junction. Measurements are voltage-biased and the current across the junction is measured (two probes measurement). Figure VII.14 represents typical current-voltage characteristics of a $MoSi$/BFO-Mn $(2{,}3\ nm)$/YBCO junction at different temperatures:

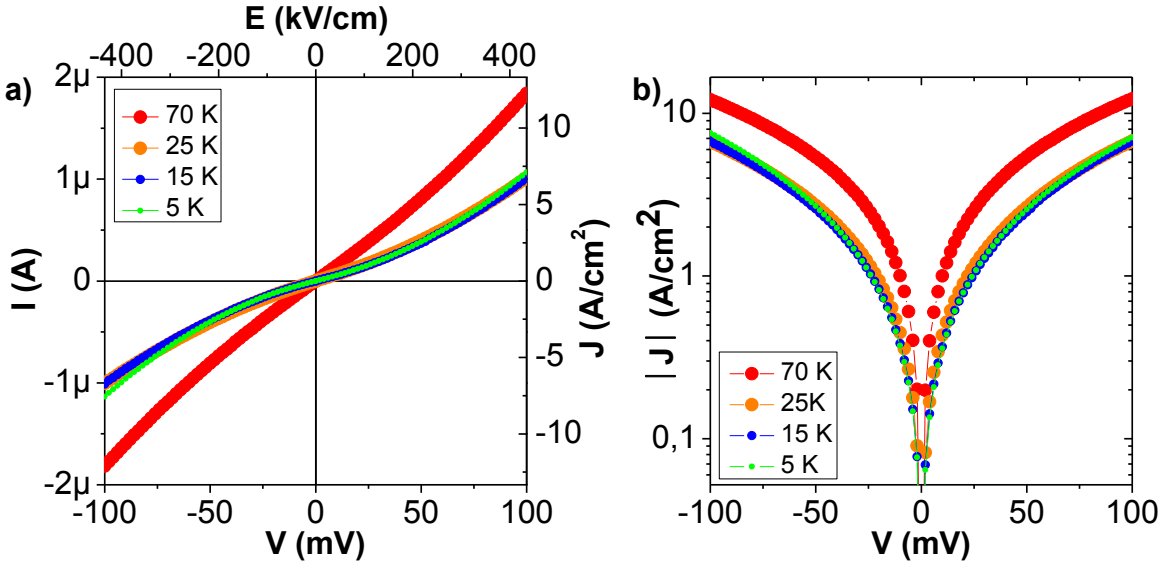

Figure VII.14: a) I-V characteristics of a $15\ \mu m^2$ $MoSi$/BFO-Mn $(2{,}3\ nm)$/YBCO junction at different temperatures. b) corresponding current densities.

The $I-V$ characteristics are symmetric. We observe no zero-resistance state through the barrier, even at low temperatures. Below the critical temperature of YBCO, the shape of the $I-V$ characteristics does not vary strongly with the temperature. However, by looking at the differential conductance $G(T,V) = \frac{dI}{dV}(T,V)$ we can have a closest look at the behaviour of the junction. $G(T,V)$ measures the conductivity of the junction. It is represented for the same junction in Figure VII.15, normalized by $G(T = 100\ K, V)$, as a function of the gate voltage, for several temperatures:

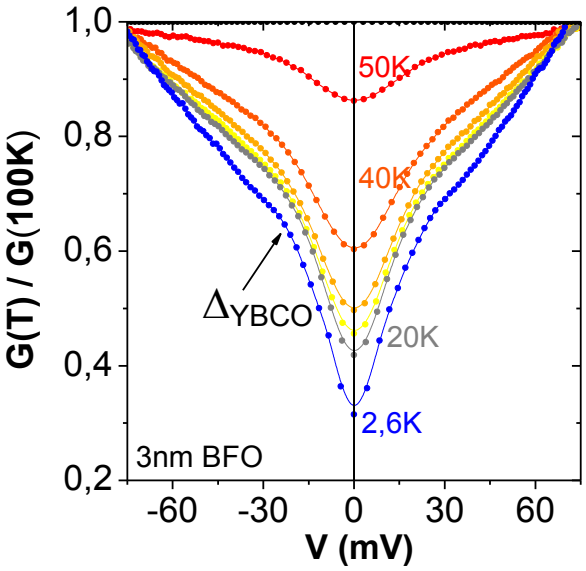

Figure VII.15: Conductivity as a function of the applied voltage for a 15 μm^2 $MoSi$/BFO-Mn (2,3 nm)/YBCO junction at different temperature, normalized by conductivity at 100 K.

We observe that for small voltages, the conductivity decreases in the range -25~25 mV. This phenomenon vanishes for temperatures above $40\ K$, the critical temperature of the YBCO film determined from Figure VII.13. The parabola shape is typical of Superconductor/Insulator/Normal metal tunnel junctions [191], [192].

To conclude, the two-probes measurements of the $MoSi$/BFO-Mn (2,3 nm)/YBCO junctions exhibit the following regimes:

- At high temperature (above the normal/superconducting transition onset of YBCO), the conductance of the channel increases when the voltage bias increases.
- Below $50\ K$, we observe the opening of the YBCO gap, which results in a conductance decrease for voltages below ~$25\ mV$. However, the finite electron (quasiparticle) tunnelling, due to the finite temperature and the availability of these states and the d-wave nodes, precludes full current suppression in this regime of the channel.

We now investigate the field-effect in these devices.

VII.2.2 Field-effect measurements

PFM measurements on the BFO-Mn/YBCO films before the lithography showed that BFO-Mn was ferroelectric with an out-of-plane polarisation (PFM images can be found in chapter IV.2). If an electric field is applied through the ferroelectric and is high enough, the direction of the polarisation can be switched.

In order to probe the ferroelectric switching in $MoSi$/BFO-Mn/YBCO junctions, we apply a polarisation voltage V_{Pol} through the barrier. The voltage is applied from zero to the setpoint with a rate of $0{,}2\ V/s$. Then, a bias voltage is applied and the current passing through the barrier is measured. Like previously, the conductivity is defined by $G(T,V) = \frac{dI}{dV}(T,V)$.

VII.2.2. a) Field-effect at low temperature

Figure VII.16 *a)* represents the measured conductivity after different polarisation voltages V_{Pol}. The red curves are obtained after applying a positive DC voltage up to $+5\ V_{DC}$ (the top-electrode is grounded: a positive voltage between the YBCO and the $MoSi$ corresponds to an electric field pointing upwards – outwards the BFO-Mn/YBCO interface). Then, negative DC voltages are applied, down to $-3\ V_{DC}$ (green curves).

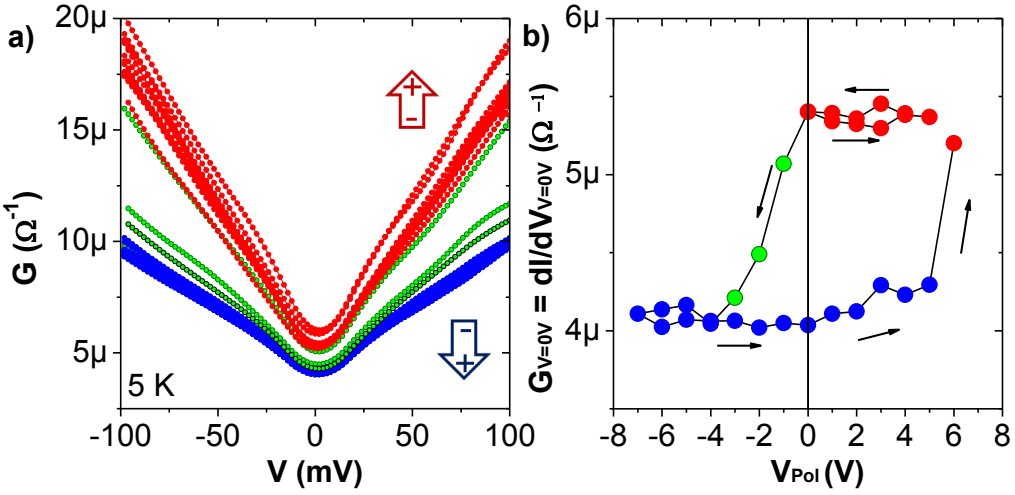

Figure VII.16: a) Conductivity after polarising a $MoSi$/BFO-Mn/YBCO junction upwards (red curves) and downwards (blue curves) for different polarisation voltages. b) Conductivity at zero bias as a function of the polarisation voltage.

We observe that the conductivity at zero bias and the conductivity at high bias get lower than the values obtained for positive V_{Pol} DC voltages. For lower values, down to $-7\ V_{DC}$, the conductivity is identical from one measurement to the other (blue curves). This remains true for increasing values of V_{Pol} up to $+5\ V_{DC}$. When $V_{Pol} = +6\ V$ is reached, the conductivity switches back to the first state (high conductivity).

In Figure VII.16 *b)* the conductivity at zero bias is represented as a function of the polarising voltage V_{Pol}. **This representation illustrates the hysteretic behaviour and switching between the two states described above: it suggests that the observed resistive switching is due to a switching of the BFO-*Mn* polarisation**. According to the sign of the polarisation voltages, **the "OFF" state** (low conductance, high resistivity) **corresponds to the downwards polarisation** (towards the BFO-Mn/YBCO interface) **and the "ON" state** (high conductance, low resistivity) **corresponds to the upwards polarisation** (outwards the BFO-Mn/YBCO interface).

VII.2.2. b) Temperature dependence of the field-effect

We analysed this switching at different temperatures. For each temperature, we measured the difference between the resistances in the "OFF" and "ON" states at zero bias (as represented in Figure VII.17 *a)*) and divided it by the resistance in the "ON" state, corresponding to a positive applied bias between the YBCO and the $MoSi$. The resulting ratio, "R%" is represented in Figure VII.17 *b)*.

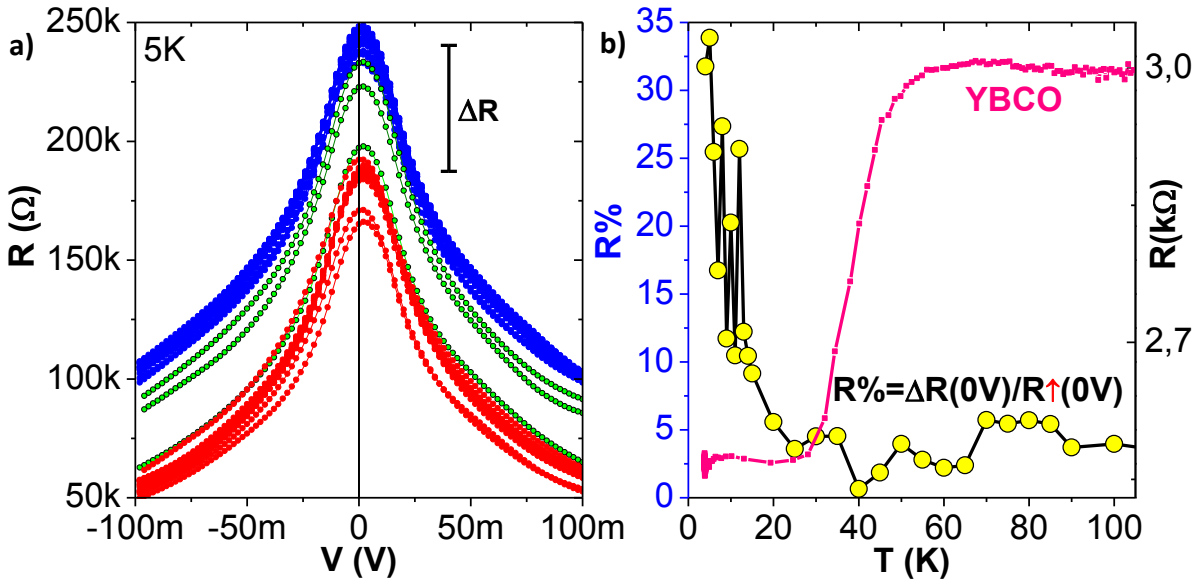

Figure VII.17: a) Resistance as a function of the applied voltage, calculated from the I-V characteristics. Blue curves correspond to the "OFF" state and red curves to the "ON" state. Green curves are intermediate states. b) Resistance ratio (yellow symbols) and resistance of the YBCO film (pink curve) as a function of the temperature.

We observe that the ratio is high at low temperatures (up to 30%) and decreases until the temperature reaches $30\ K$. It then remains constant. From the resistance *vs* temperature measurement of the YBCO film, we observe that this temperature corresponds to the superconducting/normal transition of the YBCO. This indicates that the field-effect might be linked to the superconducting properties of the bottom electrode.

VII.2.3 Conclusions

We were able to fabricate asymmetric ferroelectric junctions with two different superconducting electrodes. Our devices exhibit resistive switching, indicating that two states of polarisation are stable in the ultra-thin $MoSi$/BFO-Mn/YBCO structure. The temperature dependence of the resistive switching suggests that the mechanisms involved in the change of resistance might be linked to the superconductivity of the high-T_c electrode. In this conclusion, we discuss several mechanisms possibly involved in the resistive switching.

Modification of the electrostatic height of the barrier

As discussed in section II.4.3, several mechanisms can be at the origin of a resistive switching in ferroelectric junctions, in particular the modification of the electrostatic height of the barrier. In our experiments, the bottom electrode, YBCO, has a small number of carriers ($\sim 10^{21}\ holes/cm^3$). We showed in Chapter VI that the ferroelectric field-effect is strong in this material, and that the relative modulation of carrier density in the closest layers could be as high as 30% for a $30\ nm$ BFO-Mn film (Figure VI.6 in section VI.1.2). In section II.3.1, we saw that the electric screening length in superconductor depended on the carrier density p as $\lambda_{TF} \propto p^{-1/2}$. **Assuming that the switch in the polarisation of our ultra-thin BFO-Mn films induced a modification of the carrier density of the**

YBCO film close to the interface, the resulting change in the electric screening length modified the electrostatic height of the barrier and thus the resistance.

If the switch in the polarisation is complete, not only the density but also the sign of the carriers accumulated at the interface changes. In this case, the electrostatic height of the barrier is drastically modified, as explained in I.3.4. c).

Modification of the width of the barrier

We showed in chapter VI that close to the critical temperature of YBCO, a small change in the carrier density can induce a normal/superconducting transition. This could lead to the presence or the absence of a non-superconducting layer at the BFO-Mn/YBCO interface, depending on the direction of the BFO-Mn polarisation. In tunnel barriers, the resistance of the junction depends exponentially on the thickness of the barrier: this mechanism would thus lead to a change in the resistance of the junction. **This is consistent with the fact that the "ON" state corresponds to the upwards polarisation of the BFO-*Mn* film** (carriers are accumulated at the BFO-Mn/YBCO interface) **whereas the "OFF" states corresponds to the downwards polarisation of the BFO-*Mn* film** (carriers are depleted at the BFO-Mn/YBCO interface).

VII.3 Conclusion

We studied the behaviour of BFO-Mn ultra-thin ferroelectric films on YBCO bottom electrodes. By examining a large number of junctions with several different sizes and top-electrodes, we emphasised the strong dependence of the ferroelectric properties of ultra-thin films on the nature of the electrodes. Even though we were confronted to small breakdown voltages, we achieved to obtain resistive switching with both metallic and superconducting electrodes. Among the different low-T_c superconductors, we chose $MoSi$ for low-temperature applications. It shows good resistive switching properties on BFO-Mn at room temperature, has a relatively high critical temperature and does not oxidise.

We then fabricated solid-state devices in order to measure YBCO/BFO-Mn/$MoSi$ junctions at low temperature. We measured tunnelling current through the ferroelectric barrier. Moreover we were able to modulate the electroresistance of a ferroelectric junction by electrostatic field-effect on a superconducting electrode, only below the critical temperature of the latter. Further experiments have to be done in order to determine the exact mechanisms of the resistive switching in the devices.

Conclusion

The presented research project successfully led to the observation of novel ferroelectric field-effects. It began with the fabrication of high-quality epitaxial heterostructures by pulsed laser deposition. On one hand, we achieved to grow ultra-thin YBCO films showing robust superconducting properties. We maintained superconductivity in films as thick as two unit-cells, and were able to grow ferroelectric films with a strong and switchable out-of-plane polarisation ($\sim 70\ \mu C/cm^2$) on top of these ultra-thin YBCO films. Both X-ray diffraction techniques and STEM images confirmed the epitaxy and the high-quality of these heterostructures. On the other hand, we grew ultra-thin ferroelectric BFO-Mn films on YBCO electrodes. To do so we investigated several approaches, using different PLDs and procedures. We were able to maintain ferroelectricity in nanometric films of BFO-Mn, and could manipulate the out-of-plane polarisation by PFM in films as thick as a few nanometres. CT-AFM studies confirmed that the conduction mode through these films was mainly tunnelling.

The ferroelectric/superconductor interface was then carefully studied, especially with STEM and PFM techniques. We determined the existence of an electric dipole at the interface, favouring one direction of the polarisation with respect to the other. We studied the PFM response of films of different thicknesses, and concluded on the probable existence of pinned downwards domains. We achieved to reverse the ferroelectric polarisation, by scanning the surface of our samples with a PFM tip, in unfavourable thermodynamic conditions: in the absence of ionic species (Helium atmosphere) and at liquid nitrogen temperature. This opens the way to the fabrication of in situ modulable devices.

We then studied "planar" devices, *i.e.* measurement bridges in which the current flows within the YBCO film only. First of all, we developed a technology to fabricate Hall bar bridges, and analysed the effect of the different lithography steps on the samples. We made three main observations: first, the ion beam etching damages and weakens the ultra-thin YBCO films, probably by removing the oxygen atoms. Second, exposing the devices to an O_2 plasma right after the etching considerably improves the robustness of the films and limits their ageing. Third, the ion beam etching makes the border of the etched BFO-Mn film conducting, which limits the possibility of gating etched devices with metallic top electrodes. With this in mind, we optimised the technology with two objectives: maintaining good superconducting properties in the film and ensuring good contacts between the ultra-thin YBCO film and the bonding wires – ending on an original gold stripes patterns which allowed us to significantly reduce the noise in the devices.

In these devices, the direction of the polarisation was controlled by scanning the surface of the sample with a CT-AFM, while applying a voltage between the tip and the YBCO film. The out-of-plane polarisation, by electrostatic field-effect, induced a remanent modulation of the free carrier density in the superconducting film. This ferroelectric field-effect was demonstrated by successive critical temperature and Hall transport measurements for different directions of the polarisation. Critical temperature shifts over $15\ K$ and areal charge modulation – measured by Hall effect – over $10\ \mu C/cm^2$ were obtained.

Once the strength of the ferroelectric field-effect was demonstrated, we fabricated devices consisting of a measurement bridge in which the field-effect enhances the superconducting properties of the YBCO film everywhere, except in a thin band where it is depressed: the weak-link. This thin band is "written" with a PFM tip. Through magnetotransport and voltage-current characteristics studies, we studied the electrical behaviour of such devices. We identified a range of temperature in which the system showed an oscillatory magnetotransport, reminiscent of the Josephson effect in superconductors coupled through a weak-link. Compared to other Josephson junctions based on high-T_c superconductors, our weak-links have no chemical discontinuities at their interfaces with the electrodes, which allows the proximity effect to propagate over micrometric distances.

In this work, we demonstrated the feasibility of obtaining a Josephson coupling through a weak-link defined by simple electrostatic modulation of the free-carrier density. This is conceptually different from geometrical constrictions or ion irradiation, as there are no chemical interfaces delimiting the weak-link. In YBCO films, the broadening of the transition that occurs along with the diminution of the thickness prevented us from observing a sharp Josephson effect. However, the concept of the ferroelectric field-effect induced weak-link could be applied to other ferroelectric/superconductors systems, particularly low carrier-density-ones like Nb-doped $SrTiO_3$, where the contrast between accumulated and doped regions could be sharper.

In parallel, we studied "vertical" devices, in which the transport is measured through an asymmetric superconductor / ferroelectric / superconductor tunnel junction. We first fabricated devices that could allow us to measure a large number of junctions, modify the direction of the ferroelectric polarisation and image the phase of the polarisation. To do so, we fabricated matrices of pads by e-beam lithography. We compared several top-electrodes. This preliminary work allowed us to conclude on the strong dependence of the ferroelectric properties of ultra-thin films on the nature of the interfaces. Despite the fact that the breakdown field of the barrier was usually comparable to the coercive field of the ferroelectric film, we measured tunnelling electro-resistance modulation of several orders of magnitude at room temperature.

We then fabricated solid-state devices which allowed us to measure junctions at low-temperature. The ferroelectric field-effect was evidenced through two-states, hysteretic transport measurements across the barrier, dependent on the polarisation voltage. This hysteretic effect was only measurable below the critical temperature of YBCO, suggesting that a ferroelectric field-effect phenomena responsible for the electroresistance occurred at the BFO-Mn/YBCO interface.

Up to now, we did not achieve to measure a supercurrent trough the BFO-Mn barrier, which might be too thick to allow the tunnelling of Cooper pairs through it. However, such junctions combined to the ferroelectric field-effect would allow the electric control of the Josephson effect. Moreover, an additional Josephson current would be easily generated by the application of an electromagnetic radiation on the ferroelectric barrier through the photovoltaic effect. These last concepts are the subject of a patent registered in 2016 (in France, n°16 00816) of which I am one of the inventors.

As a general result, we fabricated two kinds of ferroelectric field-effect devices based on high-T_c superconductors, contributing to the study of the fascinating phenomena that occur at the interfaces between oxides.

Appendix

A) Josephson equations

Considering a superconductor/insulator/superconductor junction as described on Figure I.9, each superconducting block is described by a wave-function:

$$\psi_1 = \sqrt{n_1}e^{i\varphi_1} \text{ and } \psi_2 = \sqrt{n_2}e^{i\varphi_2} \tag{A.1}$$

where $n_1 = |\psi_1|^2$ and $n_2 = |\psi_2|^2$ represent the density of Cooper pairs in each superconducting part, and φ_1, φ_2 their phases. When the barrier is thin enough, the two wave-functions overlap, and the two blocks are coupled: the probability that a Cooper pair can go through the barrier thanks to tunnel effect becomes superior to zero. The system is then described by a linear combination of the two states:

$$|\psi\rangle = \psi_1|1\rangle + \psi_2|2\rangle \tag{A.2}$$

where ψ_i represents the probability that a Cooper pair is present in the block i.

The Hamiltonian of the junction can be described as a function of E_1 and E_2, the ground states energies of the superconductors far from the barrier, and the coupling constant K between these two states – that gives a measure of the coupling interaction between the two superconductors and depends of the junction – by the matrix:

$$\begin{bmatrix} E_1 & K \\ K & E_2 \end{bmatrix} \tag{A.3}$$

The temporal evolution of the system is driven by the Schrodinger equation:

$$\begin{bmatrix} E_1 & K \\ K & E_2 \end{bmatrix} \begin{bmatrix} \psi_1 \\ \psi_2 \end{bmatrix} = i\hbar \frac{\partial}{\partial t} \begin{bmatrix} \psi_1 \\ \psi_2 \end{bmatrix} \tag{A.4}$$

According to expressions (A.1):

$$\begin{bmatrix} E_1 & K \\ K & E_2 \end{bmatrix} \begin{bmatrix} \sqrt{n_1}e^{i\varphi_1} \\ \sqrt{n_2}e^{i\varphi_2} \end{bmatrix} = i\hbar \frac{\partial}{\partial t} \begin{bmatrix} \sqrt{n_1}e^{i\varphi_1} \\ \sqrt{n_2}e^{i\varphi_2} \end{bmatrix} \tag{A.5}$$

By choosing the zero of the energy equal to 0 and applying a voltage so that the chemical potentials are shifted by an amount eV, the energies of the blocks become:

$$E_1 = eV \text{ and } E_2 = -eV \tag{A.6}$$

In the absence of a vector potential $\vec{A}$, K can be assumed to be real. If we extract the real and the imaginary parts of equation (A.5), we obtain:

$$\frac{dn_1}{dt} = -\frac{dn_2}{dt} = \frac{2K}{\hbar}\sqrt{n_1 n_2}\sin(\varphi_1 - \varphi_2) \tag{A.7}$$

$$\frac{d\varphi_1}{dt} = \frac{K}{\hbar}\sqrt{\frac{n_1}{n_2}}\cos(\varphi_1 - \varphi_2) + \frac{eV}{\hbar} \tag{A.8}$$

$$\frac{d\varphi_2}{dt} = \frac{K}{\hbar}\sqrt{\frac{n_1}{n_2}}\cos(\varphi_1 - \varphi_2) - \frac{eV}{\hbar} \tag{A.9}$$

These three equations lead to the equations that describe the Josephson effects; they are expressed as a function of $\varphi = \varphi_1 - \varphi_2$, the phase difference between the two blocks.

B) Josephson junction in a magnetic field

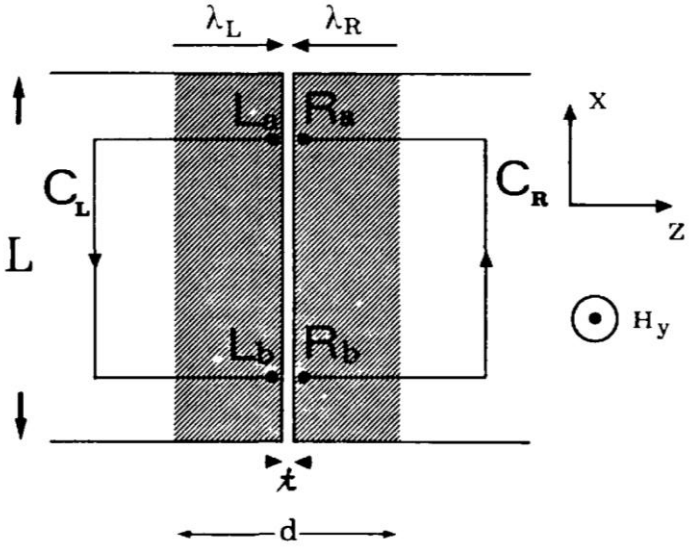

Figure B.1: Contours of integration for the derivation of the field dependence of the phase difference. The dashed areas indicate the regions where the field penetrates the superconductor. Taken from [30]

If we consider a junction plunged into a magnetic field H along the y direction, the presence of the field will induce a difference in the gauge invariant phase between two points of the barrier (either both on the left or both on the right of the barrier) and separated by a distance dx:

$$\nabla\varphi_{L,R} = \frac{2e}{\hbar c}\left(\frac{mc}{2e^2\rho}\vec{J_s} + \vec{A}\right) \tag{B.1}$$

with $\vec{A}$ the vector potential. By integrating it along the contours defined on Figure B.1 we obtain:

$$\begin{aligned} \varphi_{Ra}(x) - \varphi_{Rb}(x+dx) &= \frac{2e}{\hbar c}\int_{C_R}\left(\frac{mc}{2e^2\rho}\vec{J_s} + \vec{A}\right)d\vec{l} \\ \varphi_{Lb}(x+dx) - \varphi_{La}(x) &= \frac{2e}{\hbar c}\int_{C_L}\left(\frac{mc}{2e^2\rho}\vec{J_s} + \vec{A}\right)d\vec{l} \end{aligned} \tag{B.2}$$

The contour can be chosen to expand far away from the junction, until it reaches a region where the shielding current density $\vec{J_s}$ has vanished: it is possible only if the dimension along the z axis is bigger than the London penetration depth $\lambda_{L,R}$.

If the portions of the contour close to the barrier are chosen perpendicular to $\overrightarrow{J_s}$, the difference of these two equations lead to:

$$\begin{aligned}\varphi(x+dx)-\varphi(x) &= [\varphi_{Lb}(x+dx)-\varphi_{Rb}(x+dx)]-[\varphi_{La}(x)-\varphi_{La}(x)] \\ &= \frac{2e}{\hbar c}\left(\int_{C_R}\vec{A}\,d\vec{l}+\int_{C_L}\vec{A}\,d\vec{l}\right)\end{aligned} \tag{B.3}$$

By neglecting the barrier thickness t compared to the contour, and reminding that $\vec{\nabla}\,\vec{A}=\vec{H}$ the integrals can be replaced by a surface integral of the magnetic field:

$$\int_{C_R}\vec{A}\,d\vec{l}+\int_{C_L}\vec{A}\,d\vec{l}=\oint\vec{A}\,d\vec{l}=\ H_y(\lambda_L+t+\lambda_R)dx \tag{B.4}$$

which leads to:

$$\frac{d\varphi}{dx}=\ \frac{2e}{\hbar c}H_y(\lambda_L+t+\lambda_R)=\frac{2e}{\hbar c}H_y\mathrm{d} \tag{B.5}$$

where $d=(\lambda_L+t+\lambda_R)$ represents the magnetic static thickness of the junction. According to expression (I.54), the tunnelling current is then:

$$J(x)=J_c\sin(\frac{2e}{\hbar c}H_y dx+\varphi_0) \tag{B.6}$$

This equation implies that the current is spatially modulated along the direction parallel to the magnetic field, and that for some values of H_y, the net tunneling current in the channel is zero. The total current in the junction is given by the integration of the density over the junction area:

$$I=\iint J_c(x,y)\sin(\frac{2e}{\hbar c}H_y dx+\varphi_0)\,dxdy=\iint J_c(x,y)\sin(\,kx+\varphi_0)\,dxdy \tag{B.7}$$

with $k=2\pi d\frac{2e}{h}H_y=\frac{2\pi d}{\Phi_0}H_y$. The critical current density is given by the integration along the y direction:

$$\mathcal{J}_c(x)=\int dyJ_c(x,y) \tag{B.8}$$

and the critical current is obtained by integrating $\mathcal{J}_c$ along the largest junction dimension L along x:

$$I(k,\varphi_0)=\int_{-L/2}^{L/2}dx\mathcal{J}_c(x)\sin(kx+\varphi_0)=\mathrm{Im}\left\{e^{i\varphi_0}\int_{-L/2}^{L/2}dx\mathcal{J}_c(x)e^{ikx}\right\} \tag{B.9}$$

The maximum Josephson current is obtained by maximising equation (B.9) with respect to φ_0:

$$I_{max}(k)=\left|\int_{-L/2}^{L/2}dx\mathcal{J}_c(x)e^{ikx}\right| \tag{B.10}$$

$I_{max}(k)$ is thus the Fourier transform of the critical current density $\mathcal{J}_c(x)$ [38].

C) T_c as a function of the carrier density

The following figure presents the critical temperature as a function of the carrier density for several samples found in the literature. "PRL 70, 3995 (1993)" refers to [193], "PRL 69, 2855 (1992)" refers to [194], "PRB 69, 10 (2004)" refers to [195] and "PRL 93, 26 (2004)" to [196]. The purple line is a guide to the eye.

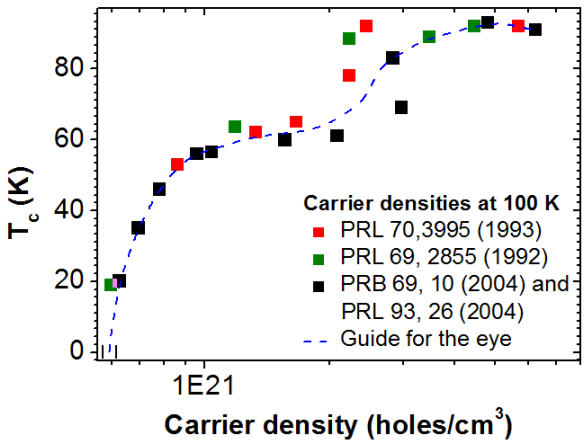

Figure B.1: T_c as a function of density for YBCO crystals.

Bibliography

[1] H. Kamerlingh Onnes, 'Communication from the Physical Laboratory of the University of Leiden', *Koninklijke Akademie van Wetenschappen te Amsterdam*, pp. 1479–1481, 28-Apr-1911.

[2] W. Meissner and R. Ochsenfeld, 'Ein neuer Effekt bei Eintritt der Supraleitfähigkeit', *Naturwissenschaften*, vol. 21, no. 44, pp. 787–788.

[3] F. London and H. London, 'The Electromagnetic Equations of the Supraconductor', *Proc. R. Soc. Lond. Ser. Math. Phys. Sci.*, vol. 149, no. 866, pp. 71–88, 1935.

[4] Shinobu Hikami and Takashi Hirai and Seiichi Kagoshima, 'High Transition Temperature Superconductor: Y-Ba-Cu Oxide', *Jpn. J. Appl. Phys.*, vol. 26, no. 4A, p. L314, 1987.

[5] J. Bardeen, L. N. Cooper, and J. R. Schrieffer, 'Theory of superconductivity', *Phys. Rev.*, vol. 108, no. 5, p. 1175, 1957.

[6] L. Gao *et al.*, 'Superconductivity up to 164 K in HgBa2Cam-1CumO2m+2+δ (m=1, 2, and 3) under quasihydrostatic pressures', *Phys. Rev. B*, vol. 50, no. 6, p. 4260, 1994.

[7] A. P. Drozdov, M. I. Eremets, I. A. Troyan, V. Ksenofontov, and S. I. Shylin, 'Conventional superconductivity at 203 kelvin at high pressures in the sulfur hydride system', *Nature*, vol. 525, no. 7567, pp. 73–76, Aug. 2015.

[8] Q. Si, R. Yu, and E. Abrahams, 'High-temperature superconductivity in iron pnictides and chalcogenides', *Nat. Rev. Mater.*, vol. 1, p. 16017, Mar. 2016.

[9] Philippe Mangin and Rémi Kahn, *Supraconductivité*. EDP Sciences, 2013.

[10] L. N. Cooper, 'Bound electron pairs in a degenerate Fermi gas', *Phys. Rev.*, vol. 104, no. 4, p. 1189, 1956.

[11] H. Fröhlich, 'Theory of the superconducting state. I. The ground state at the absolute zero of temperature', *Phys. Rev.*, vol. 79, no. 5, p. 845, 1950.

[12] J. W. Garland, 'Isotope Effect in Superconductivity', *Phys Rev Lett*, vol. 11, no. 3, pp. 114–119, Aug. 1963.

[13] M. Tinkham, *Introduction to superconductivity / Michael Tinkham*. New York: McGraw-Hill, 1975.

[14] L. P. Gor'kov, 'Microscopic derivation of the Ginzburg-Landau equations in the theory of superconductivity', *Soviet Physics JETP*, 1959.

[15] P.G. De Gennes, 'Superconductivity of metals and alloys', *Nucl. Phys. A*, vol. 90, pp. 706–706, Jan. 1967.

[16] G. Blatter, M. V. Feigel'man, V. B. Geshkenbein, A. I. Larkin, and V. M. Vinokur, 'Vortices in high-temperature superconductors', *Rev Mod Phys*, vol. 66, no. 4, pp. 1125–1388, Oct. 1994.

[17] H. F. Hess, R. B. Robinson, R. C. Dynes, J. M. Valles Jr, and J. V. Waszczak, 'Scanning-tunneling-microscope observation of the Abrikosov flux lattice and the density of states near and inside a fluxoid', *Phys. Rev. Lett.*, vol. 62, no. 2, p. 214, 1989.

[18] F. Bouquet *et al.*, 'An unusual phase transition to a second liquid vortex phase in the superconductor YBa2Cu3O7', *Nature*, vol. 411, no. 6836, pp. 448–451, May 2001.

[19] M. P. Fisher, 'Vortex-glass superconductivity: a possible new phase in bulk high-T c oxides', *Phys. Rev. Lett.*, vol. 62, no. 12, p. 1415, 1989.

[20] D. S. Fisher, M. P. Fisher, and D. A. Huse, 'Thermal fluctuations, quenched disorder, phase transitions, and transport in type-II superconductors', *Phys. Rev. B*, vol. 43, no. 1, p. 130, 1991.

[21] D. R. Nelson and V. M. Vinokur, 'Boson localization and pinning by correlated disorder in high-temperature superconductors', *Phys. Rev. Lett.*, vol. 68, no. 15, p. 2398, 1992.

[22] D. R. Nelson and V. M. Vinokur, 'Boson localization and correlated pinning of superconducting vortex arrays', *Phys. Rev. B*, vol. 48, no. 17, p. 13060, 1993.

[23] E. L. Wolf, *Principles of Electron Tunneling Spectroscopy*, Second Edition. Oxford University Press, 2011.
[24] W. F. Brinkman, 'Tunneling Conductance of Asymmetrical Barriers', *J. Appl. Phys.*, vol. 41, no. 5, p. 1915, 1970.
[25] J. G. Simmons, 'Generalized Formula for the Electric Tunnel Effect between Similar Electrodes Separated by a Thin Insulating Film', *J. Appl. Phys.*, vol. 34, no. 6, p. 1793, 1963.
[26] I. Giaever, 'Energy gap in superconductors measured by electron tunneling', *Phys. Rev. Lett.*, vol. 5, no. 4, p. 147, 1960.
[27] B. D. Josephson, 'Possible new effects in superconductive tunnelling', *Phys. Lett.*, vol. 1, pp. 251–253, Jul. 1962.
[28] B. D. Josephson, 'Supercurrents through barriers', *Adv. Phys.*, vol. 14, no. 56, pp. 419–451, Oct. 1965.
[29] P. W. Anderson and J. M. Rowell, 'Probable Observation of the Josephson Superconducting Tunneling Effect', *Phys Rev Lett*, vol. 10, no. 6, pp. 230–232, Mar. 1963.
[30] A. Barone and G. Paternò, 'Weak Superconductivity — Phenomenological Aspects', in *Physics and Applications of the Josephson Effect*, Wiley-VCH Verlag GmbH & Co. KGaA, 2005, pp. 1–24.
[31] A. F. Andreev, 'The Thermal Conductivity of the Intermediate State in Superconductors', p. 1228, 1964.
[32] K. K. Likharev, *Dynamics of Josephson junctions and circuits*. New York: Gordon and Breach Science Publishers, 1986.
[33] P. W. Anderson and A. H. Dayem, 'Radio-Frequency Effects in Superconducting Thin Film Bridges', *Phys Rev Lett*, vol. 13, no. 6, pp. 195–197, Aug. 1964.
[34] S. A. Cybart, K. Chen, and R. C. Dynes, 'Planar YBaCuO Ion Damage Josephson Junctions and Arrays', *IEEE Trans. Appiled Supercond.*, vol. 15, no. 2, pp. 241–244, Jun. 2005.
[35] N. Bergeal, X. Grison, J. Lesueur, G. Faini, M. Aprili, and J. P. Contour, 'High-quality planar high-Tc Josephson junctions', *Appl. Phys. Lett.*, vol. 87, no. 10, p. 102502, 2005.
[36] S. Shapiro, 'Josephson Currents in Superconducting Tunneling: The Effect of Microwaves and Other Observations', *Phys Rev Lett*, vol. 11, no. 2, pp. 80–82, Jul. 1963.
[37] R. C. Jaklevic, J. Lambe, A. H. Silver, and J. E. Mercereau, 'Quantum Interference Effects in Josephson Tunneling', *Phys Rev Lett*, vol. 12, no. 7, pp. 159–160, Feb. 1964.
[38] R. C. Dynes and T. A. Fulton, 'Supercurrent density distribution in Josephson junctions', *Phys. Rev. B*, vol. 3, no. 9, p. 3015, 1971.
[39] A. Barone and G. Paternò, 'Large Junctions – Static Self-Field Effects', in *Physics and Applications of the Josephson Effect*, Wiley-VCH Verlag GmbH & Co. KGaA, 2005, pp. 96–120.
[40] R. Cantor and F. Ludwig, 'SQUID Fabrication Technology', in *The SQUID Handbook*, Wiley-VCH Verlag GmbH & Co. KGaA, 2005, pp. 93–125.
[41] P. Chaudhari *et al.*, 'Direct measurement of the superconducting properties of single grain boundaries in Y 1 Ba 2 Cu 3 O 7- δ', *Phys. Rev. Lett.*, vol. 60, no. 16, p. 1653, 1988.
[42] J. Mannhart, P. Chaudhari, D. Dimos, C. C. Tsuei, and T. R. McGuire, 'Critical Currents in [001] Grains and across Their Tilt Boundaries in Y Ba 2 Cu 3 O 7 Films', *Phys. Rev. Lett.*, vol. 61, no. 21, p. 2476, 1988.
[43] H. R. Yi, M. Gustafsson, D. Winkler, E. Olsson, and T. Claeson, 'Electromagnetic and microstructural characterization of YBa2Cu3O7 step edge junctions on (001) LaAlO3 substrates', *J. Appl. Phys.*, vol. 79, no. 12, p. 9213, 1996.
[44] D. Koelle, R. Kleiner, F. Ludwig, E. Dantsker, and J. Clarke, 'High-transition-temperature superconducting quantum interference devices', *Rev. Mod. Phys.*, vol. 71, no. 3, p. 631, 1999.
[45] D. Stornaiuolo *et al.*, 'Submicron YBaCuO biepitaxial Josephson junctions: d-wave effects and phase dynamics', *J. Appl. Phys.*, vol. 107, no. 11, p. 113901, 2010.
[46] Y. A. Boikov, Z. G. Ivanov, A. L. Vasiliev, and T. Claeson, 'Biepitaxial Josephson junctions with high critical current density based on YBa2Cu3O7−δ films on silicon on sapphire', *J. Appl. Phys.*, vol. 77, no. 4, p. 1654, 1995.

[47] K. Petersen *et al.*, 'Biepitaxial Josephson junctions and SuFET technology for the preparation of HTS-JoFETs', *J. Phys. IV*, vol. 4, no. C6, pp. C6–205, 1994.
[48] S. E. Babcock *et al.*, 'A TEM-EELS study of hole concentrations near strongly and weakly coupled grain boundaries in electromagnetically characterized YBa2Cu3O7−δ bicrystals', *Phys. C Supercond.*, vol. 227, no. 1, pp. 183–196, Jun. 1994.
[49] J. Betouras and R. Joynt, 'Theoretical study of the critical current of YBa2Cu3O7−δ bicrystals with hole-deficient grain boundaries', *Phys. C Supercond.*, vol. 250, no. 3, pp. 256–264, Aug. 1995.
[50] S. S. Tinchev, 'Interface-engineered'high-Tc Josephson junctions: a possible mechanism of operation', *Supercond. Sci. Technol.*, vol. 12, no. 9, p. L5, 1999.
[51] M. B. Salamon, 'Thermodynamic properties, fluctuations, and anisotropy of high-temperature superconductors', in *Physical Properties of High Temperature Superconductors I*, World Scientific, 1998, pp. 39–69.
[52] W. E. Booij, A. J. Pauza, E. J. Tarte, D. F. Moore, and M. G. Blamire, 'Proximity coupling in high-Tc Josephson junctions produced by focused electron beam irradiation', *Phys Rev B*, vol. 55, no. 21, pp. 14600–14609, Jun. 1997.
[53] A. J. Pauza *et al.*, 'Electron-beam damaged high-temperature superconductor Josephson junctions', *J. Appl. Phys.*, vol. 82, no. 11, pp. 5612–5632, 1997.
[54] F. Kahlmann, A. Engelhardt, J. Schubert, W. Zander, C. Buchal, and J. Hollkott, 'Superconductor–normal–superconductor Josephson junctions fabricated by oxygen implantation into YBa2Cu3O7−δ', *Appl. Phys. Lett.*, vol. 73, no. 16, pp. 2354–2356, 1998.
[55] M. D. Strikovski *et al.*, 'Fabrication of YBa2Cu3Ox thin-film flux transformers using a novel microshadow mask technique for insitu patterning', *Appl. Phys. Lett.*, vol. 66, no. 25, pp. 3521–3523, 1995.
[56] M. E. Lines and A. M. Glass, *Principles and applications of ferroelectrics and related materials*. Oxford university press, 1977.
[57] S. Katzir, 'Who knew piezoelectricity? Rutherford and Langevin on submarine detection and the invention of sonar', *Notes Rec. R. Soc.*, vol. 66, no. 2, pp. 141–157, Jun. 2012.
[58] A. Rogalski, 'Infrared detectors: status and trends', *Prog. Quantum Electron.*, vol. 27, no. 2–3, pp. 59–210, Jan. 2003.
[59] P. A. H, 'Vera V. Daniel, dielectric relaxation . Academic press, London and New York, 1967, pp xiv + 281; price 75s', *J. Mol. Struct.*, vol. 2, pp. 424–424, Nov. 1968.
[60] 1927- Müller K. A.(Karl A. ., B. (Bruno) Dorner, and H. (Harry) Thomas, *Structural phase transitions*. Berlin ; New York : Springer-Verlag, 1981.
[61] R. E. Cohen, 'Origin of ferroelectricity in perovskite oxides', *Nature*, vol. 358, no. 6382, pp. 136–138, Jul. 1992.
[62] W. Cochran, 'Crystal stability and the theory of ferroelectricity', *Adv. Phys.*, vol. 9, pp. 387–423, Oct. 1960.
[63] W. Schottky, 'Halbleitertheorie der sperrschicht', *Naturwissenschaften*, vol. 26, no. 52, pp. 843–843, 1938.
[64] N. F. Mott, 'The Resistance and Thermoelectric Properties of the Transition Metals', *Proc. R. Soc. Lond. Math. Phys. Eng. Sci.*, vol. 156, no. 888, pp. 368–382, 1936.
[65] J. E. Rault *et al.*, 'Thickness-dependent polarization of strained BiFeO 3 films with constant tetragonality', *Phys. Rev. Lett.*, vol. 109, no. 26, p. 267601, 2012.
[66] I. P. Batra and B. D. Silverman, 'Thermodynamic stability of thin ferroelectric films', *Solid State Commun.*, vol. 11, no. 1, pp. 291–294, 1972.
[67] K. J. Choi, 'Enhancement of Ferroelectricity in Strained BaTiO3 Thin Films', *Science*, vol. 306, no. 5698, pp. 1005–1009, Nov. 2004.
[68] H. Béa, 'Croissance, caractérisation et intégration dans des hétérostructures de films minces du multiferroïque BiFeO3', 2007.
[69] D. Sando, B. Xu, L. Bellaiche, and V. Nagarajan, 'A multiferroic on the brink: uncovering the nuances of strain-induced transitions in BiFeO $ _3$', *ArXiv Prepr. ArXiv151205835*, 2015.

[70] V. Garcia *et al.*, 'Giant tunnel electroresistance for non-destructive readout of ferroelectric states', *Nature*, vol. 460, no. 7251, pp. 81–84, Jul. 2009.
[71] C. Li *et al.*, 'Ultrathin BaTiO3-Based Ferroelectric Tunnel Junctions through Interface Engineering', *Nano Lett.*, vol. 15, no. 4, pp. 2568–2573, Apr. 2015.
[72] H. F. Kay and J. W. Dunn, 'Thickness dependence of the nucleation field of triglycine sulphate', *Philos. Mag.*, vol. 7, pp. 2027–2034, Dec. 1962.
[73] V. Janovec, 'On the theory of the coercive field of single-domain crystals of BaTiO3', *Cechoslov-Fiz. Zurnal*, vol. 8, no. 1, pp. 3–15, 1958.
[74] James F. Scott, *Ferroelectric Memories*. Springer, 2000.
[75] R. R. Mehta, B. D. Silverman, and J. T. Jacobs, 'Depolarization fields in thin ferroelectric films', *J. Appl. Phys.*, vol. 44, no. 8, pp. 3379–3385, 1973.
[76] M. Zhuravlev, R. Sabirianov, S. Jaswal, and E. Tsymbal, 'Giant Electroresistance in Ferroelectric Tunnel Junctions', *Phys. Rev. Lett.*, vol. 94, no. 24, Jun. 2005.
[77] T. M. Shaw, S. Trolier-McKinstry, and P. C. McIntyre, 'The Properties of Ferroelectric Films at Small Dimensions', *Annu. Rev. Mater. Sci.*, vol. 30, no. 1, pp. 263–298, Aug. 2000.
[78] N. A. Pertsev and H. Kohlstedt, 'Depolarizing-field effect in strained nanoscale ferroelectric capacitors and tunnel junctions', *ArXiv Prepr. Cond-Mat0603762*, 2006.
[79] V. Garcia and M. Bibes, 'Ferroelectric tunnel junctions for information storage and processing', *Nat. Commun.*, vol. 5, Jul. 2014.
[80] Radaelli et al., 'Large Room-Temperature Electroresistance in Dual-Modulated Ferroelectric Tunnel Barriers'. 2015.
[81] A. Chanthbouala *et al.*, 'Solid-state memories based on ferroelectric tunnel junctions', *Nat. Nanotechnol.*, vol. 7, no. 2, pp. 101–104, Dec. 2011.
[82] N. Sai, A. M. Kolpak, and A. M. Rappe, 'Ferroelectricity in ultrathin perovskite films', *Phys. Rev. B*, vol. 72, no. 2, Jul. 2005.
[83] M. Kimura, M. Matsuo, M. Murakami, K. Sawano, and S. Matsuda, 'Characterization of oxide superconductor by means of X-ray diffractometry and X-ray absorption near edge structure', *ISIJ Int.*, vol. 29, no. 3, pp. 213–222, 1989.
[84] C. Bernhard and J. L. Tallon, 'Thermoelectric power of YCaBaCuO : Contributions from CuO planes and CuO chains', *Phys. Rev. B*, vol. 54, no. 14, pp. 10201–10209, Oct. 1996.
[85] J. R. Waldram, *Superconductivity of Metals and Cuprates*, Institut of Physics Publishing. London, 1996.
[86] J. Orenstein and A. J. Millis, 'Advances in the Physics of High-Temperature Superconductivity', *Science*, vol. 288, no. 5465, pp. 468–474, Apr. 2000.
[87] V. Breit *et al.*, 'Evidence for chain superconductivity in near-stoichiometric YBaCuO single crystals', *Phys Rev B*, vol. 52, no. 22, pp. R15727–R15730, Dec. 1995.
[88] D. Lebeugle, D. Colson, A. Forget, and M. Viret, 'Very large spontaneous electric polarization in BiFeO3 single crystals at room temperature and its evolution under cycling fields', *Appl. Phys. Lett.*, vol. 91, no. 2, p. 022907, 2007.
[89] Y. F. Popov, A. K. Zvezdin, G. P. Vorob'ev, A. M. Kadomtseva, V. A. Murashev, and D. N. Rakov, 'Linear magnetoelectric effect and phase transitions in bismuth ferrite $BiFeO_3$', *Sov. J. Exp. Theor. Phys. Lett.*, vol. 57, p. 69, Jan. 1993.
[90] P. Ravindran, R. Vidya, A. Kjekshus, H. Fjellv\a ag, and O. Eriksson, 'Theoretical investigation of magnetoelectric behavior in Bi Fe O 3', *Phys. Rev. B*, vol. 74, no. 22, p. 224412, 2006.
[91] D. Ricinschi, K.-Y. Yun, and M. Okuyama, 'A mechanism for the 150 μC cm $^{-2}$ polarization of $BiFeO_3$ films based on first-principles calculations and new structural data', *J. Phys. Condens. Matter*, vol. 18, no. 6, pp. L97–L105, Feb. 2006.
[92] T. Zhao *et al.*, 'Electrical control of antiferromagnetic domains in multiferroic BiFeO3 films at room temperature', *Nat. Mater.*, vol. 5, no. 10, pp. 823–829, 2006.
[93] C. Ederer and N. A. Spaldin, 'Effect of Epitaxial Strain on the Spontaneous Polarization of Thin Film Ferroelectrics', *Phys. Rev. Lett.*, vol. 95, no. 25, Dec. 2005.

[94] C. Ederer and N. A. Spaldin, 'Influence of strain and oxygen vacancies on the magnetoelectric properties of multiferroic bismuth ferrite', *Phys. Rev. B*, vol. 71, no. 22, Jun. 2005.
[95] D. Pesquera, X. Marti, V. Holy, R. Bachelet, G. Herranz, and J. Fontcuberta, 'X-ray interference effects on the determination of structural data in ultrathin La2/3Sr1/3MnO3 epitaxial thin films', *Appl. Phys. Lett.*, vol. 99, no. 22, p. 221901, 2011.
[96] J. Fontcuberta, B. Martinez, A. Seffar, S. Pinol, J. L. Garcia-Munoz, and X. Obradors, 'Colossal magnetoresistance of ferromagnetic manganites: Structural tuning and mechanisms', *Phys. Rev. Lett.*, vol. 76, no. 7, p. 1122, 1996.
[97] E. Dagotto, T. Hotta, and A. Moreo, 'Colossal magnetoresistant materials: the key role of phase separation', *Phys. Rep.*, vol. 344, no. 1, pp. 1–153, 2001.
[98] A. Urushibara, Y. Moritomo, T. Arima, A. Asamitsu, G. Kido, and Y. Tokura, 'Insulator-metal transition and giant magnetoresistance in La 1- x Sr x MnO 3', *Phys. Rev. B*, vol. 51, no. 20, p. 14103, 1995.
[99] C. Zener, 'Interaction between the d-shells in the transition metals. II. Ferromagnetic compounds of manganese with perovskite structure', *Phys. Rev.*, vol. 82, no. 3, p. 403, 1951.
[100] S. Kubo, 'Superconducting properties of amorphous MoX (X=Si, Ge) alloy films for Abrikosov vortex memory', *J. Appl. Phys.*, vol. 63, no. 6, pp. 2033–2045, 1988.
[101] A. S. Edelstein, S. R. Ovshinsky, H. Sadate-Akhavi, and J. Wood, 'Correlation Between the Superconducting and Normal State Properties of Amorphous Molybdenum-Silicon Alloys', in *Disordered Materials*, Springer, 1991, pp. 102–105.
[102] D. B. Kimhi and T. H. Geballe, 'Superconducting tunneling in the amorphous transition metals Mo and Nb', *Phys. Rev. Lett.*, vol. 45, no. 12, p. 1039, 1980.
[103] M. Imada, A. Fujimori, and Y. Tokura, 'Metal-insulator transitions', *Rev. Mod. Phys.*, vol. 70, no. 4, p. 1039, 1998.
[104] J. Mannhart, 'High-Tc transistors', *Supercond. Sci. Technol.*, vol. 9, no. 2, p. 49, 1996.
[105] C. H. Ahn, J.-M. Triscone, and J. Mannhart, 'Electric field effect in correlated oxide systems', *Nature*, vol. 424, no. 6952, pp. 1015–1018, 2003.
[106] S. Sakai, 'Theoretical study of electric-field effects in high-T c oxide superconductors using an ultrathin-metal-insulator superlattice model', *Phys. Rev. B*, vol. 47, no. 14, p. 9042, 1993.
[107] D. Matthey, N. Reyren, J.-M. Triscone, and T. Schneider, 'Electric-Field-Effect Modulation of the Transition Temperature, Mobile Carrier Density, and In-Plane Penetration Depth of NdBa2Cu3O7-δ Thin Films', *Phys. Rev. Lett.*, vol. 98, no. 5, Jan. 2007.
[108] H. Y. Hwang, Y. Iwasa, M. Kawasaki, B. Keimer, N. Nagaosa, and Y. Tokura, 'Emergent phenomena at oxide interfaces', *Nat. Mater.*, vol. 11, no. 2, pp. 103–113, Jan. 2012.
[109] C. H. Ahn *et al.*, 'Electrostatic modification of novel materials', *Rev. Mod. Phys.*, vol. 78, no. 4, pp. 1185–1212, Nov. 2006.
[110] J. T. Ye *et al.*, 'Liquid-gated interface superconductivity on an atomically flat film', *Nat Mater*, vol. 9, no. 2, pp. 125–128, Feb. 2010.
[111] Y. Lee *et al.*, 'Phase Diagram of Electrostatically Doped SrTiO3', *Phys Rev Lett*, vol. 106, no. 13, p. 136809, Apr. 2011.
[112] H. Shimotani, H. Asanuma, A. Tsukazaki, A. Ohtomo, M. Kawasaki, and Y. Iwasa, 'Insulator-to-metal transition in ZnO by electric double layer gating', *Appl. Phys. Lett.*, vol. 91, no. 8, 2007.
[113] A. T. Bollinger, G. Dubuis, J. Yoon, D. Pavuna, J. Misewich, and I. Božović, 'Superconductor–insulator transition in La2 − xSrxCuO4 at the pair quantum resistance', *Nature*, vol. 472, no. 7344, pp. 458–460, Apr. 2011.
[114] T. Timusk and B. Statt, 'The pseudogap in high-temperature superconductors: an experimental survey', *Rep. Prog. Phys.*, vol. 62, no. 1, p. 61, 1999.
[115] P. A. Lee, N. Nagaosa, and X.-G. Wen, 'Doping a Mott insulator: Physics of high-temperature superconductivity', *Rev. Mod. Phys.*, vol. 78, no. 1, pp. 17–85, Jan. 2006.
[116] X. Hong, A. Posadas, A. Lin, and C. H. Ahn, 'Ferroelectric-field-induced tuning of magnetism in the colossal magnetoresistive oxide La 1 − x Sr x MnO 3', *Phys. Rev. B*, vol. 68, no. 13, Oct. 2003.

[117] C. A. F. Vaz *et al.*, 'Origin of the Magnetoelectric Coupling Effect in Pb (Zr 0.2 Ti 0.8) O 3 / La 0.8 Sr 0.2 MnO 3 Multiferroic Heterostructures', *Phys. Rev. Lett.*, vol. 104, no. 12, Mar. 2010.
[118] M. Eblen-Zayas, A. Bhattacharya, N. E. Staley, A. L. Kobrinskii, and A. M. Goldman, 'Ambipolar Gate Effect and Low Temperature Magnetoresistance of Ultrathin L a 0.8 C a 0.2 M n O 3 Films', *Phys. Rev. Lett.*, vol. 94, no. 3, Jan. 2005.
[119] S. Mathews, R. Ramesh, T. Venkatesan, and J. Benedetto, 'Ferroelectric Field Effect Transistor Based on Epitaxial Perovskite Heterostructures', *Science*, vol. 276, no. 5310, pp. 238–240, Apr. 1997.
[120] K. S. Takahashi *et al.*, 'Local switching of two-dimensional superconductivity using the ferroelectric field effect', *Nature*, vol. 441, no. 7090, pp. 195–198, May 2006.
[121] S. M. Wu *et al.*, 'Reversible electric control of exchange bias in a multiferroic field-effect device', *Nat. Mater.*, vol. 9, no. 9, pp. 756–761, Sep. 2010.
[122] A. S. Dhoot, C. Israel, X. Moya, N. D. Mathur, and R. H. Friend, 'Large Electric Field Effect in Electrolyte-Gated Manganites', *Phys. Rev. Lett.*, vol. 102, no. 13, Mar. 2009.
[123] P.-H. Xiang *et al.*, 'Strain-Mediated Phase Control and Electrolyte-Gating of Electron-Doped Manganites', *Adv. Mater.*, vol. 23, no. 48, pp. 5822–5827, 2011.
[124] H. Yamada *et al.*, 'Ferroelectric control of a Mott insulator', *Sci. Rep.*, vol. 3, Oct. 2013.
[125] B. Y. Shapiro, 'The critical parameters and structure of the surface superconducting state induced by external electric field', *Solid State Commun.*, vol. 53, no. 8, pp. 673–676, 1985.
[126] A. T. Fiory and A. F. Hebard, 'Electron Mobility, Conductivity, and Superconductivity near the Metal-Insulator Transition', *Phys Rev Lett*, vol. 52, no. 23, pp. 2057–2060, Jun. 1984.
[127] T. G. Berlincourt, 'Large shifts of transition temperature with electric charging predicted for superconducting semiconductors', *Phys Lett 29A 308-9June 2 1969*, Jan. 1969.
[128] D. G. Naugle, 'The effect of very thin Ge coating on the superconducting transition of thin Sn and Tl films', *Phys. Lett. A*, vol. 25, no. 9, pp. 688–690, Nov. 1967.
[129] N. Marković, C. Christiansen, G. Martinez-Arizala, and A. M. Goldman, 'Electric-field effect in ultrathin films near the superconductor-insulator transition', *Phys. Rev. B*, vol. 65, no. 1, Nov. 2001.
[130] J. Mannhart, D. G. Schlom, J. G. Bednorz, and K. A. Müller, 'Influence of electric fields on pinning in YBa2Cu3O7-δ films', *Phys. Rev. Lett.*, vol. 67, no. 15, p. 2099, 1991.
[131] E. H. Taheri, J. W. Cochrane, and G. J. Russell, 'Electric field effects in superconducting YBa2Cu3O7−x thin films using field-effect transistor structures', *J. Appl. Phys.*, vol. 77, no. 2, p. 761, 1995.
[132] X. X. Xi, C. Doughty, A. Walkenhorst, C. Kwon, Q. Li, and T. Venkatesan, 'Effects of field-induced hole-density modulation on normal-state and superconducting transport in YBa 2 Cu 3 O 7-x', *Phys. Rev. Lett.*, vol. 68, no. 8, p. 1240, 1992.
[133] W. H. Brattain and C. G. B. Garrett, 'Experiments on the interface between germanium and an electrolyte', *Bell Syst. Tech. J.*, vol. 34, no. 1, pp. 129–176, Jan. 1955.
[134] X. Leng, J. Garcia-Barriocanal, S. Bose, Y. Lee, and A. M. Goldman, 'Electrostatic Control of the Evolution from a Superconducting Phase to an Insulating Phase in Ultrathin YBa_{2}Cu_{3}O_{7-x} Films', *Phys. Rev. Lett.*, vol. 107, no. 2, Jul. 2011.
[135] A. S. Dhoot, S. C. Wimbush, T. Benseman, J. L. MacManus-Driscoll, J. R. Cooper, and R. H. Friend, 'Increased Tc in Electrolyte-Gated Cuprates', *Adv. Mater.*, vol. 22, no. 23, pp. 2529–2533, May 2010.
[136] C. H. Ahn, S. Gariglio, P. Paruch, T. Tybell, L. Antognazza, and J.-M. Triscone, 'Electrostatic Modulation of Superconductivity in Ultrathin GdBa2Cu3O7-x Films', *Science*, vol. 284, no. 5417, pp. 1152–1155, May 1999.
[137] A. Crassous, 'Contribution à l'étude des effets de champ à l'échelle nanométrique dans des hétérostructures d'oxydes', 2011.
[138] H. L. Stadler, 'Changing Properties of Metals by Ferroelectric Polarization Charging', *Phys Rev Lett*, vol. 14, no. 24, pp. 979–981, Jun. 1965.

[139] A. Crassous *et al.*, 'Nanoscale Electrostatic Manipulation of Magnetic Flux Quanta in Ferroelectric/Superconductor BiFeO 3 / YBa 2 Cu 3 O 7 − δ Heterostructures', *Phys. Rev. Lett.*, vol. 107, no. 24, Dec. 2011.
[140] Crassous et al., 'BiFeO3/YBa2Cu3O7 heterostructures for strong ferroelectric modulation of superconductivity'. 2013.
[141] C. H. Ahn *et al.*, 'Local, Nonvolatile Electronic Writing of Epitaxial Pb(Zr0.52Ti0.48)O3/SrRuO3 Heterostructures', *Science*, vol. 276, no. 5315, pp. 1100–1103, 1997.
[142] Z. G. Ivanov, E. A. Stepantsov, A. Y. Tzalenchuk, R. I. Shekhter, and T. Claeson, 'Field effect transistor based on a bi-crystal grain boundary Josephson junction', *IEEE Trans. Appl. Supercond.*, vol. 3, no. 1, pp. 2925–2928, Mar. 1993.
[143] B. Mayer, J. Mannhart, and H. Hilgenkamp, 'Electric field controllable Josephson junctions of high quality in high-Tc superconductors', *Appl. Phys. Lett.*, vol. 68, no. 21, p. 3031, 1996.
[144] A. Beck, O. M. Froehlich, D. Koelle, R. Gross, H. Sato, and M. Naito, 'La1.85Sr0.15CuO4−δ bicrystal grain boundary Josephson junctions', *Appl. Phys. Lett.*, vol. 68, no. 23, p. 3341, 1996.
[145] Z. W. Dong, V. C. Matijasevic, P. Hadley, S. M. Shao, and J. E. Mooij, 'Electric field effect in Sm/sub 1-x/Ca/sub x/Ba/sub 2/Cu/sub 3/O/sub y/bicrystal junctions', *Appl. Supercond. IEEE Trans. On*, vol. 5, no. 2, pp. 2879–2882, 1995.
[146] K. Petersen, I. Takeuchi, V. Talyansky, C. Doughty, X. X. Xi, and T. Venkatesan, 'Electric field effect on ultrathin YBa2Cu3O7−δ grain boundary Josephson junctions', *Appl. Phys. Lett.*, vol. 67, no. 10, p. 1477, 1995.
[147] K. Nakajima, K. Yokota, H. Myoren, J. Chen, and T. Yamashita, 'Field effects on the dielectric property of YBCO bicrystal grain boundary junctions', *Appl. Supercond. IEEE Trans. On*, vol. 5, no. 2, pp. 2861–2864, 1995.
[148] J. J. Betouras, R. Joynt, Z.-W. Dong, T. Venkatesan, and P. Hadley, 'Ginzburg–Landau theory of Josephson field effect transistors', *Appl. Phys. Lett.*, vol. 69, no. 16, pp. 2432–2434, 1996.
[149] G. Kim, D. Mazumdar, and A. Gupta, 'Nanoscale electroresistance properties of all-oxide magneto-electric tunnel junction with ultra-thin barium titanate barrier', *Appl. Phys. Lett.*, vol. 102, no. 5, p. 052908, 2013.
[150] A. Gruverman *et al.*, 'Tunneling Electroresistance Effect in Ferroelectric Tunnel Junctions at the Nanoscale', *Nano Lett.*, vol. 9, no. 10, pp. 3539–3543, Oct. 2009.
[151] X. S. Gao, J. M. Liu, K. Au, and J. Y. Dai, 'Nanoscale ferroelectric tunnel junctions based on ultrathin BaTiO3 film and Ag nanoelectrodes', *Appl. Phys. Lett.*, vol. 101, no. 14, p. 142905, 2012.
[152] M. Y. Zhuravlev, S. S. Jaswal, E. Y. Tsymbal, and R. F. Sabirianov, 'Ferroelectric switch for spin injection', *Appl. Phys. Lett.*, vol. 87, no. 22, 2005.
[153] V. Garcia *et al.*, 'Ferroelectric Control of Spin Polarization', *Science*, vol. 327, no. 5969, pp. 1106–1110, Feb. 2010.
[154] J. P. Velev *et al.*, 'Magnetic Tunnel Junctions with Ferroelectric Barriers: Prediction of Four Resistance States from First Principles', *Nano Lett.*, vol. 9, no. 1, pp. 427–432, Jan. 2009.
[155] Y. W. Yin, M. Raju, W. J. Hu, X. J. Weng, X. G. Li, and Q. Li, 'Coexistence of tunneling magnetoresistance and electroresistance at room temperature in La0.7Sr0.3MnO3/(Ba, Sr)TiO3/La0.7Sr0.3MnO3 multiferroic tunnel junctions', *J. Appl. Phys.*, vol. 109, no. 7, 2011.
[156] D. Pantel, S. Goetze, D. Hesse, and M. Alexe, 'Reversible electrical switching of spin polarization in multiferroic tunnel junctions', *Nat Mater*, vol. 11, no. 4, pp. 289–293, Apr. 2012.
[157] H. Yamada *et al.*, 'Giant Electroresistance of Super-tetragonal BiFeO3-Based Ferroelectric Tunnel Junctions', *ACS Nano*, vol. 7, no. 6, pp. 5385–5390, Jun. 2013.
[158] Y. W. Yin *et al.*, 'Enhanced tunnelling electroresistance effect due to a ferroelectrically induced phase transition at a magnetic complex oxide interface', *Nat. Mater.*, vol. 12, no. 5, pp. 397–402, Feb. 2013.
[159] G. Radaelli, D. Gutiérrez, F. Sánchez, R. Bertacco, M. Stengel, and J. Fontcuberta, 'Large Room-Temperature Electroresistance in Dual-Modulated Ferroelectric Tunnel Barriers', *Adv. Mater.*, vol. 27, no. 16, pp. 2602–2607, 2015.

[160] Z. Wen, C. Li, D. Wu, A. Li, and N. Ming, 'Ferroelectric-field-effect-enhanced electroresistance in metal/ferroelectric/semiconductor tunnel junctions', *Nat. Mater.*, vol. 12, no. 7, pp. 617–621, May 2013.
[161] X. Liu, J. D. Burton, and E. Y. Tsymbal, 'Enhanced Tunneling Electroresistance in Ferroelectric Tunnel Junctions due to the Reversible Metallization of the Barrier', *Phys. Rev. Lett.*, vol. 116, no. 19, May 2016.
[162] A. N. Pargellis, 'Evaporating and sputtering: Substrate heating dependence on deposition rate', *J. Vac. Sci. Technol. Vac. Surf. Films*, vol. 7, no. 1, p. 27, Jan. 1989.
[163] F. C. Frank and J. H. van der Merwe, 'One-Dimensional Dislocations. III. Influence of the Second Harmonic Term in the Potential Representation, on the Properties of the Model', *Proc. R. Soc. Lond. Math. Phys. Eng. Sci.*, vol. 200, no. 1060, pp. 125–134, Dec. 1949.
[164] M. Volmer and A. Weber, 'Keimbildung in übersättigten Gebilden (Nucleation of supersaturated structures)', *Z. Physik. Chem. 119*, pp. 277–301, 1926.
[165] K. D. Vernon-Parry, 'Scanning electron microscopy: an introduction', *III-Vs Rev.*, vol. 13, no. 4, pp. 40–44, 2000.
[166] T. Lippmann *et al.*, 'Charge-density analysis of YBa2Cu3O6.98: Comparison of theoretical and experimental results', *Acta Crystallogr. A*, vol. 59, pp. 437–451, 2003.
[167] V. Scagnoli and S. W. Lovesey, 'Analysis of azimuthal-angle scans in resonant x-ray Bragg diffraction and parity even and odd atomic multipoles in the multiferroic modification of the terbium manganate TbMnO 3', *Phys. Rev. B*, vol. 79, no. 3, Jan. 2009.
[168] M. Hatzakis, B. J. Canavello, and J. M. Shaw, 'Single-Step Optical Lift-Off Process', *IBM J. Res. Dev.*, vol. 24, no. 4, pp. 452–460, Jul. 1980.
[169] A. Chanthbouala *et al.*, 'A ferroelectric memristor', *Nat. Mater.*, vol. 11, no. 10, pp. 860–864, Sep. 2012.
[170] H. Rogalla and P. H. Kes, *100 Years of Superconductivity*. CRC Press, 2011.
[171] J.-M. Triscone and Ø. Fischer, 'Superlattices of high-temperature superconductors: synthetically modulated structures, critical temperatures and vortex dynamics', *Rep. Prog. Phys.*, vol. 60, no. 12, p. 1673, 1997.
[172] H. M. Christen and G. Eres, 'Recent advances in pulsed-laser deposition of complex oxides', *J. Phys. Condens. Matter*, vol. 20, no. 26, p. 264005, Jul. 2008.
[173] X. H. Zhu *et al.*, 'Thickness-dependent structural and electrical properties of multiferroic Mn-doped BiFeO[sub 3] thin films grown epitaxially by pulsed laser deposition', *Appl. Phys. Lett.*, vol. 93, no. 8, p. 082902, 2008.
[174] T. Terashima, K. Shimura, Y. Bando, Y. Matsuda, A. Fujiyama, and S. Komiyama, 'Superconductivity of one-unit-cell thick YBa 2 Cu 3 O 7 thin film', *Phys. Rev. Lett.*, vol. 67, no. 10, p. 1362, 1991.
[175] R. E. Glover III and M. D. Sherrill, 'Changes in superconducting critical temperature produced by electrostatic charging', *Phys. Rev. Lett.*, vol. 5, no. 6, p. 248, 1960.
[176] M. Alexe and A. Gruverman, *Nanoscale Characterisation of Ferroelectric Materials*. Springer, 2004.
[177] P. Yu *et al.*, 'Interface control of bulk ferroelectric polarization', *Proc. Natl. Acad. Sci.*, vol. 109, no. 25, pp. 9710–9715, 2012.
[178] C. T. Nelson *et al.*, 'Spontaneous Vortex Nanodomain Arrays at Ferroelectric Heterointerfaces', *Nano Lett.*, vol. 11, no. 2, pp. 828–834, Feb. 2011.
[179] S. V. Kalinin and D. A. Bonnell, 'Screening Phenomena on Oxide Surfaces and Its Implications for Local Electrostatic and Transport Measurements', *Nano Lett.*, vol. 4, no. 4, pp. 555–560, Apr. 2004.
[180] D. Dahan, M. Molotskii, G. Rosenman, and Y. Rosenwaks, 'Ferroelectric domain inversion: The role of humidity', *Appl. Phys. Lett.*, vol. 89, no. 15, p. 152902, 2006.
[181] A. V. Ievlev, A. N. Morozovska, V. Y. Shur, and S. V. Kalinin, 'Humidity effects on tip-induced polarization switching in lithium niobate', *Appl. Phys. Lett.*, vol. 104, no. 9, p. 092908, Mar. 2014.

[182] D. Matthey, 'Field effect experiments in high Tc superconductors : a study of the transport properties in the underdoped regime', Ph.D. thesis, 2004.
[183] M. S. Islam, 'Computer simulation study of oxygen migration in YBa2Cu3O7', *Supercond. Sci. Technol.*, vol. 3, no. 11, p. 531, 1990.
[184] S. Ouanani-Sakhri, 'Etude de réseaux de jonctions Josephson à haute température critique', Paris-Saclay, 2015.
[185] S. A. Cybart, 'Planar Josephson junctions and arrays by electron beam lithography and ion damage', 2005.
[186] M. Malnou, 'High-Tc Josephson mixers for Terahertz detection', 2015.
[187] J. Trastoy *et al.*, 'Unusual magneto-transport of $YBa_2Cu_3O_{7-\delta}$ films due to the interplay of anisotropy, random disorder and nanoscale periodic pinning', *New J. Phys.*, vol. 15, no. 10, p. 103022, Oct. 2013.
[188] R. H. Koch, V. Foglietti, W. J. Gallagher, G. Koren, A. Gupta, and M. P. A. Fisher, 'Experimental evidence for vortex-glass superconductivity in Y-Ba-Cu-O', *Phys. Rev. Lett.*, vol. 63, no. 14, p. 1511, 1989.
[189] J. E. Villegas, Z. Sefrioui, M. Varela, E. M. Gonzalez, J. Santamaria, and J. L. Vicent, 'Interface barriers for flux motion in high-temperature superconducting superlattices', *Phys. Rev. B*, vol. 69, no. 13, Apr. 2004.
[190] J. Pearl, 'Current distribution in superconducting films carrying quantized fluxoids', *Appl. Phys. Lett.*, vol. 5, no. 4, p. 65, 1964.
[191] R. C. Dynes, J. P. Garno, G. B. Hertel, and T. P. Orlando, 'Tunneling study of superconductivity near the metal-insulator transition', *Phys. Rev. Lett.*, vol. 53, no. 25, p. 2437, 1984.
[192] F. Giazotto, T. T. Heikkilä, A. Luukanen, A. M. Savin, and J. P. Pekola, 'Opportunities for mesoscopics in thermometry and refrigeration: Physics and applications', *Rev. Mod. Phys.*, vol. 78, no. 1, pp. 217–274, Mar. 2006.
[193] T. Ito, K. Takenaka, and S. Uchida, 'Systematic deviation from T-linear behavior in the in-plane resistivity of YBa 2 Cu 3 O 7-y: Evidence for dominant spin scattering', *Phys. Rev. Lett.*, vol. 70, no. 25, p. 3995, 1993.
[194] A. Carrington, A. P. Mackenzie, C. T. Lin, and J. R. Cooper, 'Temperature dependence of the Hall angle in single-crystal YBa2(Cu1-xCox)3O7-d', *Phys Rev Lett*, vol. 69, no. 19, pp. 2855–2858, Nov. 1992.
[195] K. Segawa and Y. Ando, 'Intrinsic Hall response of the CuO 2 planes in a chain-plane composite system of YBa 2 Cu 3 O y', *Phys. Rev. B*, vol. 69, no. 10, Mar. 2004.
[196] Y. Ando, S. Komiya, K. Segawa, S. Ono, and Y. Kurita, 'Electronic Phase Diagram of High- T c Cuprate Superconductors from a Mapping of the In-Plane Resistivity Curvature', *Phys. Rev. Lett.*, vol. 93, no. 26, Dec. 2004.